# Génération et détection d'électrons chauds dans des dispositifs plasmoniques

Romain Hernandez

**THESE DE DOCTORAT DE L'ETABLISSEMENT UNIVERSITE BOURGOGNE FRANCHE-COMTE**

**PREPAREE AU LABORATOIRE INTERDISCIPLINAIRE CARNOT DE BOURGOGNE ET**

**AU POLITECNICO DI MILANO**

Ecole doctorale n°553

Carnot Pasteur

Doctorat de physique

Par

M. Romain HERNANDEZ

# Generation and Detection of Hot Carriers in Plasmonic Devices

Thèse présentée et soutenue à Dijon, le 10 décembre 2021

Composition du Jury :

| | | |
|---|---|---|
| Dr. Bouhelier Alexandre | Directeur de recherche, laboratoire ICB, Dijon | Président |
| Pr. Pineider Francesco | Associate Professor, University of Pisa | Rapporteur |
| Pr. Lheurette Eric | Professeur, Université de Lille | Rapporteur |
| Pr. Intonti Francesca | Associate Professor, University of Florence | Examinatrice |
| Pr. Finazzi Marco | Full Professor, Politecnico di Milano | Examinateur |
| Dr. Cluzel Benoît | Maître de conférence, Université de Bourgogne | Directeur de thèse |
| Pr. Biagioni Paolo | Associate Professor, Politecnico di Milano | Co-directeur de thèse |
| Dr. Demichel Olivier | Chargé de recherche, laboratoire ICB, Dijon | Co-encadrant de thèse |

ECOLE DOCTORALE
CARNOT - PASTEUR

**Title :** Generation and Detection of Hot Carriers in Plasmonic Devices

**Keywords :** plasmonic, hot electrons, photodetectors, multi-photon luminescence

**Abstract :** Hot carrier-based devices are quite promising for ultrafast photodetection and to set off enhanced physicochemical reactions. Controlling their generation at the nanoscale within plasmonic devices is a key for the future development of hybrid hot carriers technologies. Indeed, Surface Plasmon-Polaritons (SPPs) can be exploited to confine light and enhance the number of excited hot carriers. We aim at studying the excitation and dynamics of hot carriers, enhanced by plasmonics, with two different approaches. In a first approach, we aim at controlling the delocalized generation of hot carriers by a propagative SPP. A plasmonic waveguide with a grating coupler is employed. Hot electrons are indirectly probed by the multi-photon luminescence (MPL) collected in the near-field along with the waveguide propagation axis by hyperspectral nearfield imaging technique. We found that propagative SPPs control the spatial and energy distribution of hot electrons. Moreover, using propagating SPPs to produce hot electrons gives new insight in understanding hot carriers physics. In a second approach, the transfer and dynamics of hot carriers are studied by a plasmonic metal-semiconductor-metal device. Rigorous coupled-wave analysis (RCWA) method simulations demonstrate that Au gratings on SOI (silicon on insulator) wafers can resonantly enhance the absorption of light at 1.55 µm wavelength. With an optimization algorithm, perfect absorption has been reached for given filling factor and periodicity. The outcome is to increase the efficiency of hot carriers generation and thus the number of carriers transferred towards the semiconductor. This plasmonic device shows sub band gap absorption with a responsivity above 15 µA/W. Under pulsed excitation, we have demonstrated that a coexistence between two processes is occurring: a) the plasmonic linear absorption of Au and b) the non linear two-photon absorption (TPA) of Si. It has been shown that the relaxation time of hot carriers is in the ps range. Therefore, harvesting their energy efficiently and faster than their decay is a key challenge to detect photons at THz rates.

**Titre :** Génération et détection d'électrons chauds dans des dispositifs plasmoniques

**Mot clés :** plasmonique, électrons chauds, photodétecteurs, luminescence multiphotonique

**Résumé :** Les dispositifs basés sur les électrons chauds sont prometteurs pour la photodétection ultrarapide et le déclenchement de réactions physicochimiques. Contrôler leur génération à l'échelle nanométrique dans des dispositifs plasmoniques est important pour le développement futur de technologies hybrides basées sur les électrons chauds. En effet, les plasmons polaritons de surface (SPPs) peuvent être exploités pour confiner la lumière et accroître le nombre d'électrons chauds excités. Cette thèse a pour but l'étude de l'excitation et de la dynamique des électrons chauds, excités par SPPs, dans deux approches. Dans une première approche, notre but est de contrôler la génération d'électrons chauds à l'aide de plasmons de surface propagatifs. Un guide d'onde plasmonique avec un réseau coupleur est employé. Les électrons chauds sont indirectement sondés par la luminescence multiphotonique (MPL) collectée par champ proche le long du guide d'onde par imagerie hyperspectrale de champ proche. Nous avons trouvé que le plamon propagatif contrôle la distribution spatiale et énergétique des électrons chauds. De plus, produire des électrons chauds par plasmons propagatifs offre de nouvelles perspectives dans l'étude de la physique des électrons chauds. Dans une seconde approche, le transfert et la dynamique des électrons chauds sont étudiés à l'aide d'un dispositif hybride plasmonique métal-semiconducteur-métal. Des simulations basées sur l'analyse rigoureuse des ondes couplées (RCWA) ont démontré qu'un réseau d'or sur SOI (silicium sur isolant) peut augmenter de manière résonante l'absorption de la lumière à 1,55 μm. Avec des algorithmes d'optimisation, l'absorption totale par le réseau d'or a été obtenu pour certains paramètres du réseau. L'objectif est d'accroître l'efficacité de génération des électrons chauds et donc le nombre d'électrons transférés vers le semiconducteur. Ce dispositif plasmonique a présenté une absorption en dessous de la bande interdite du Si avec une responsivité de 15 μA/W. À l'aide d'excitations pulsées, nous avons démontré la coexistence de deux processus : a) l'absorption linéaire plasmonique et b) l'absorption non linéaire à deux photons (TPA) du Si. Il a été montré que le temps de relaxation des électrons chauds est de l'ordre de la ps. Ainsi, collecter l'énergie des électrons chauds plus rapidement que leur relaxation permettrait de développer des photodétecteurs avec une bande passante de l'ordre du THz.

**Titolo :** Generazione e rivelazione di elettroni caldi in dispositivi plasmonic

**Parole chiave :** plasmonica, elettroni caldi, fotorivelatori, luminescenza multi-fotone

**Abstract :** I dispositivi basati su elettroni caldi rappresentano una promettente opportunità per la rivelazione di fotoni ultraveloce e per l'accrescimento dell'efficienza nelle reazioni fisico-chimiche. Controllare la generazione di elettroni caldi alla nanoscala in dispositivi plasmonici è un elemento chiave per lo sviluppo di future tecnologie ibride basate su tali fenomeni. I plasmoni di superficie possono essere sfruttati per confinare la radiazione elettromagnetica e aumentare l'efficienza di eccitazione di portatori caldi. L'obiettivo del lavoro di tesi è studiare l'eccitazione e la dinamica di tali portatori con due diversi approcci plasmonici. In un primo approccio, puntiamo a controllare la generazione delocalizzata di portatori caldi da parte di un plasmone di superficie propagante. Utilizziamo a questo scopo una guida plasmonica unita a un accoppiatore basato su un reticolo plasmonico. Gli elettroni caldi vengono rivelati indirettamente attraverso la luminecsenza multi-fotone raccolta nel campo vicino lungo l'asse di propagazione della guida con una tecnica di microscopia a campo prossimo iperspettrale. Otteniamo evidenza che la distribuzione spaziale ed energetica degli elettroni caldi è governata dal plasmone propagante. Inoltre, la possibilità di utilizzare plasmoni propaganti per produrre elettroni caldi dà accesso a nuovi aspetti nella comprensione della fisica dei portatori caldi. In un secondo approccio, il trasferimento e la dinamica degli elettroni caldi sono studiati mediante un dispositivo plasmonico metallo-semiconduttore-metallo. Utilizziamo il metodo RCWA (rigorous coupled wave analysis) per verificare numericamente che un reticolo di oro su substrato SOI (silicon on insulator) può accrescere in maniera risonante l'assorbimento di luce a una lunghezza d'onda di 1.55 mm. Mediante un algoritmo di ottimizzazione, raggiungiamo assorbimento perfetto per specifici valori di periodicità e fattore di riempimento. Il risultato è un accrescimento dell'efficienza di generazione di portatori caldi e dunque del numero di portatori trasferito verso il semiconduttore. Il dispositivo plasmonico investigato mostra assorbimento per energie al di sotto della gap con una responsività di 15 mA/W. Mediante eccitazione con impulsi ultrabrevi, dimostriamo la coesistenza di due processi: a) assorbimento lineare plasmonico nell'oro e b) assorbimento nonlineare a due fotoni nel substrato di silicio. E' stato dimostrato che il tempo di rilassamento dei portatori caldi è dell'ordine dei picosecondi. Di conseguenza, raccogliere la loro energia efficientemente e più rapidamente del loro decadimento è una sfida chiave per raggiungere la possibilità di rilevare fotoni con tassi nei THz.

UBFC UNIVERSITE BOURGOGNE FRANCHE-COMTE

Université Bourgogne Franche-Comté
32, avenue de l'Observatoire
25000 Besançon

# Acknowledgements

I am deeply grateful to my supervisors, Dr. Benoît Cluzel, Dr. Olivier Demichel and Pr. Paolo Biagioni for their help at every stage of the research project, continuous support and invaluable advices. All our discussions influenced me to shape my experimental, modeling and simulation methodologies but also to push my limits. I would like to thank you for being present all the time during those PhD years.

My gratitude extends to the Université Franco Italienne for the funding opportunity to undertake my studies at the Department of Physics at the Politecnico di Milano and in the PRISM group at the Laboratoire Interdisciplinaire Carnot de Bourgogne (ICB) in Dijon.

I would like to offer my special thanks to the members of the jury: Pr. Francesca Intonti, Pr. Francesco Pineider, Pr. Marco Finazzi, Pr. Eric Lheurette and to the president of the jury Pr. Alexandre Bouhelier. Thank you for taking the time to read the manuscript and for the interesting scientific discussion during the defence.

I would like to thank all the colleagues I met during those PhD years. First, I would like to thank the colleagues from Italy for their warm welcome and the nice time at Politecnico: Dr. Monica Bolani (for the coffees in the morning in Como !), Dr. Michele Celebrano, Pr. Lamberto Duo, Dr. Federico Bottegoni, Dr. Carlo Zuccheti, Dr. Attilio Zilli, and all the students, Francesco, Erika, Adele, Greta, Guillermo, Alessandro, Madan and Virginia. Then, I would also like to thank the colleagues from France for those years spent together: Dr. Saïd Hamdi (thanks for all the discussions during the PhD !), Dr. Renato Juliano-Martins (for your support at the beginning of the PhD), Dr. Adrian Agreda, Dr. Meryem Ibnoussina, Dr. Malik Nafa, Marlène and all the students of the other research groups Jérémie, Marianne, Rémy and Anthony.

I would like to thank my father, for the curiosity he gave me in mathematics, physics and life in general, and my mother, we miss you everyday and especially in the good moments. I would like to give a special thanks to Jeanne for being present everyday and for the support she gave me and also to the Bianchi family. Nico, Clem, Guillaume and Elisa, thank you for so many good moments in Dijon. Gianluca, Auberie and Alicia thanks for the excellent time in Milano and also to Paolo, the great italian teacher. Charlotte, François, Cyril, Mailys, Clémentine, Julie and Flora, thank you for being here for so long ! Fusal, Carillal, Baptiste, Laura and Clément thank you for the amazing time during the master, and Robert and Anaïs for the fantastic moments during the Glasgow Erasmus.

# Table of contents

# Introduction

The nature of light, matter and their interactions intrigue humans since ancient time. In the mid-19th century, the classical electromagnetic theory of J. C. Maxwell supposed a continous exchange of energy between light and matter [1]. Such theory was questioned by the discovery of the photoelectric effect by H. Hertz in 1887 [2] when he found that kinetic energy of emitted carriers depends on the incident light frequency after a certain threshold. An explanation was yielded by A. Einstein in 1905: a quantized exchange of energy due to discrete packets of light (i.e. photon) produces excited "hot" carriers [3]. Hot carriers are carriers with kinetic energy that is higher than thermal fluctuations. Their production could eventually result in photoemitted carriers if their energy excess the work function. In the first quarter of 21st century, light-mater interactions still fascinate and the properties of such hot carriers in terms of energy, lifetime, photoemission and heat are explored.

Another facet of light matter interaction was discovered by R. Wood in 1902: reflection spectra of sub-wavelength metallic grating is anomalously attenuated for specific angle of incidence [4]. Such observation, known as Wood anomaly, led to enthusiastic debates started from J. W. Lord Rayleigh in 1907 [5] which first tried to solve it with the diffraction theory. In 1952, D. Pines and D. Bohm introduced the plasmons as the quantized collective oscillation of electrons [6] and, in 1956, U. Fano developed the concept of polaritons due to the coupling between electromagnetic fields and electric dipole-carrying excitations [7]. Those discussions led to discover the nature of Wood's observations by R. H. Ritchie in 1957 [8]: plasmon surface waves. Incident light can strongly couple at the interface between metallic structures and a dielectric called surface plasmon polariton (SPP) [9]. SPPs permit strong confinement of light and thus to enhance light matter interactions at the nanoscale. Such surface effect can then be used to highly produce hot carriers at nanoscale refering plasmon-induced hot carriers [10].

Moreover, SPPs oscillate very rapidly at optical frequency. Classical electronic components are small sized below hundred of nanometers but are limited in terms of bandwidth in the GHz and highly consume energy due to Joule heating. On the other hand, photonic components propagate light and permit very high bandwidth transmission above THz but are very bulky. Plasmonics permits to miniaturize components and to keep a high bandwidth [11]. Nanoobjects presenting SPP are thus very attractive for ultrafast phenomenon studies. Combined with the ultrashort lifetime of hot carriers in ps, ultrashort timescales are inverstigated. Engineering plasmonic circuitry offers remarkable perspectives to substitute classical electronic chips.

However, hot electrons excitation, relaxation and extraction mechanisms are still under debate. Indeed, after hot carriers are excited and relaxed, nonlinear photoluminescence is being measured. Such photoluminescence of gold nanoparticules is still under discussions and needs further insight to be understood.

Plasmon-induced hot carrier devices are impressive opto-electronic couplers which could also be employed in ultrafast photodetection. Indeed, classical photodetectors

made of semiconductors, are usually speed bandwidth limited by the time transit of carriers within a thick layer of semiconductor. Reducing the thickness of such semiconductor absorption layer increases the speed bandwidth but reduces the quantum efficiency. Usually, a trade-off is done depending on the photodetector application field (from fast to efficient photodetector). Plasmonic permits to cut down the size of the absorption layer: the carriers diffusion time is strongly reduced and the device keeps a high absorption. Furthermore, ultrashort lifetime of hot carriers within metals could be employed for photodetection if one can harvest them faster than their relaxation decay.

In addition, enhancing the informations processing and exchange in terms of speed, quantity from short to high distance becomes a social and ecological challenge. Such advances should be done to keep as low as possible electrical power consumption for ecological issues that we are already nowadays facing.

The **Chapter 1** presents the motivations and the context of this manuscript. I will present surface plasmons and define how they can be used to enhance hot carriers generation. I will also develop the dynamics of hot carriers: their spatial diffusion and temporal relaxation. Lastly, I will present plasmonic photodetectors and the state of the art strategies to enhance the speed of photodetectors.

The **Chapter 2** presents the remote generation of hot carriers at a distance from the excitation in gold plasmonic waveguide. Hyperspectral near-field imaging technique is being employed to determine the nonlinear photoluminescence emitted along the waveguide. In fact, such photoluminescence yields crucial information by indirectly probing hot carrier properties.

The **Chapter 3** presents the optimized incident light absorption by Au grating on top of silicon on insulator (SOI) substrate for photodetection applications. The SOI substrate enhances the field within the grating. The grating parameters are calculated to maximize the field absorption by Finite Element Method (FEM) and Rigourous Coupled Wave Analysis (RCWA) simulations. Perfect absorption within such structures is found by global optimization. The nanofabrication process will also be described within this chapter.

The **Chapter4** presents the opto-electronic characterization of the hot carriers Schottky photodetector. Confocal microscopy, with supercontinuum source and pulsed laser, permits photocurrent mapping technique to probe the yielded current. Autocorrelation technique is employed to explore the nonlinear photocurrent and the time dynamic of such photodetector.

The manuscript ends with conclusion and perspectives.

This PhD project has been supported by the VINCI program of the Franco-Italian University. The first year was done in the ICB laboratory in Dijon, France, the second year in Politecnico di Milano in Italy, and the two last years in the ICB laboratory. Strong interactions among the teams have been done to well carry on the project between the different stays.

# Chapter 1

# Ultrafast photodetection, hot electrons and plasmonic

*“ Le petit prince ne renonçait jamais à une question, une fois qu'il l'avait posée. ”*

Antoine de Saint-Exupéry, Le Petit Prince, 1943

## Contents



## 1.1 Interest for high-speed optical communications

### 1.1.1 High-data-rate optical communication

The information age represents our contemporary history. More and more datas are created, transfered and stored every single day. The Global Datasphere[1] performed 33 zettabytes[2] (ZB) in 2018 and is expected to grow to 175 ZB in 2025 according to a report

of the International Data Group and Seagate [12]. Furthermore, the number of internet users increases everyday. In 2020, they were 4.7 billions users [14] and they are expected to be 5.3 billions in 2023 [15]. The objects connected together (Machine-to-Machine) and to internet (Internet of Thing) are expected to grow exponentially (3.8 billions devices in 2018, 21.5 billions expected in 2025) [16]. An expansion of datas will most probably follow with all of the related applications: connected and self-driving vehicules, automated drones, biometrics, robotics, smart home devices and surveillance [15]. All the users and objects are or will be connected together or to data centers in a complex network via wireless (WiFi, 4-5G) and wire-based networks (Ethernet twisted pair wire, fiber optic). The internet data traffic, which represents the quantity of information exchanged, will increase to almost 400 exabytes[3] (EB) per month in 2022 [17] (Fig. 1.1). Thus, there is a strong social need to increase the network capacities. To face this rapid growth, the challenge is to transmit and process a maximal quantity of information over a long distance, with a low error rate, to keep the message safe (not be intercepted), and to be cost efficient.

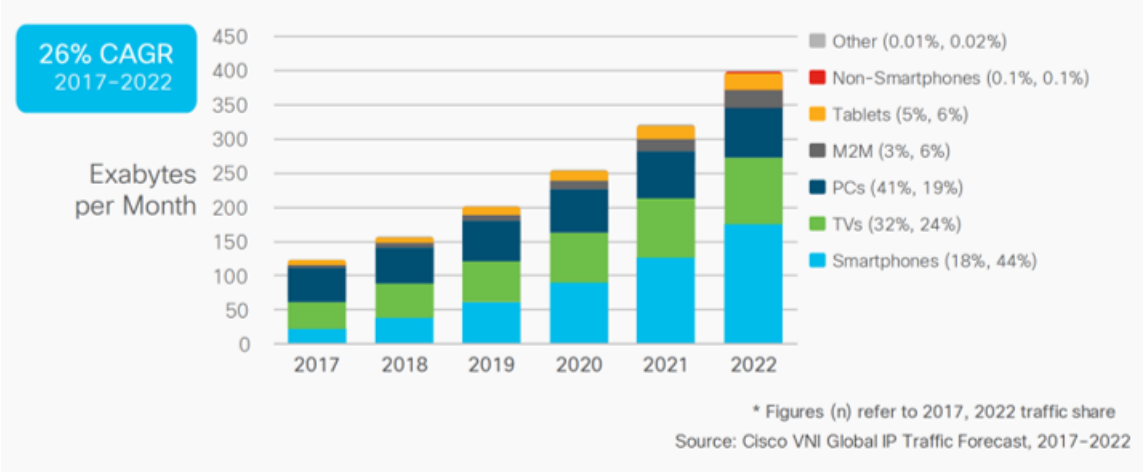


Figure 1.1: Global IP Traffic in Exabytes per Month between 2017 and 2022 for several types of device (Source Cisco [17]).

Nowadays, fiber optics communication is the highest capacity and fastest technology to transfer information [18]. Indeed, the use of light as carrier wave allows one to modulate at high frequency. Optical communication is composed of an optical transceiver or source, a guided medium for light and an optical receiver, plus optical amplifiers if needed. The optical sources are mainly solid-state semiconductor lasers. The datas are coded by direct modulation of the optical source varying the current injection or by electro-optical modulation (EOM) through fiber optics [19]. The coded light is then guided into a silica glass fiber [20] and is received by a high-speed photodetector usually made of semiconductor [21]. The demodulated information is then electronically processed. The infrared frequency domain around 1.55 µm is chosen because it corresponds to the lowest losses in silica glass (0.2 dB/km) (physical limit due to Rayleigh scattering and infrared absorption) [22]. Thus, the bandwidth-distance product[4] increases tremendously compared

[1] Global DataSphere: quantifies and analyzes the amount of data created, captured, and replicated in any given year across the world. It also looks at how much of that data is stored across various storage media (HDD, SSD, NVM-NAND, NVM-other, optical, and tape) in the Global StorageSphere [13].

[2] $10^{21}$ bytes

[3] $10^{18}$ bytes

to electrical or radio wave communication. Strong effort has been made to develop components working at 1.55 µm: laser sources with sharp lineshape [19], dispersion-shifted Single Mode Fibers (SMF) [23] and optimized photodetectors [21].

In 2004, Edholm's Law (represented Fig. 1.2 [24]) updated in 2014 by Ref. 25, predicted that bit rate technologies will double every 18 months. The Edholm's Law is following the famous Moore's law and those laws are linked together. Fig. 1.2 depicts the outstanding technological efforts made in optical components and communication protocols since the 1970's.

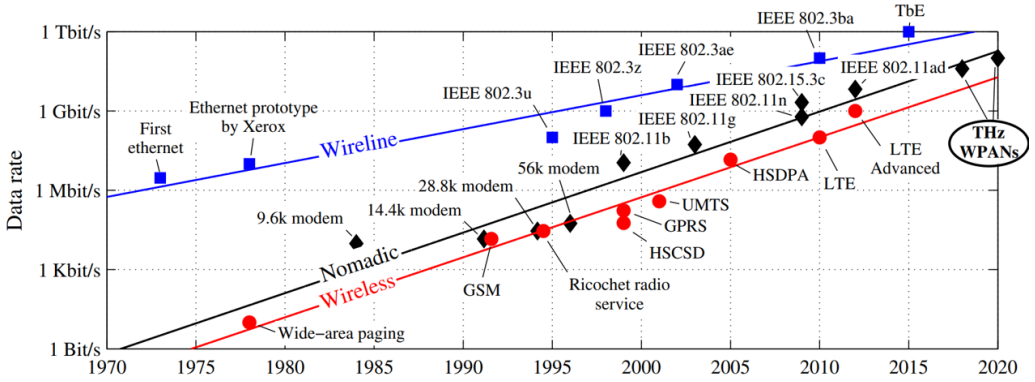


Figure 1.2: Edholm's law of increasing bandwidth as a function time ( [24, 25]

In fiber-optic communications, the bandwidth and data transfer rate naively seem to have an infinite growth. However, they are physically limited by the Shannon theory of information [26]. Indeed, the quantity of transmitted information through a channel for a certain bandwidth is limited by the Signal-to-Noise Ratio (SNR). In an optical fiber, if the information to be transmitted increases, then the power input has to increase (to keep a good SNR), increasing also the non linear effects. This effect is called the "nonlinear Shannon limit", reducing the bandwidth by Kerr-nonlinearity, noise and fiber chromatic dispersion [27]. The spectral efficiency[5] is thus reduced from the predicted value by Shannon. For instance, Ref. 28 estimated at 200 Tb/s the physical capacity limit within a single core fiber (for a bandwidth of 12.5 THz and a spectral efficiency of 16 bit/s/Hz). However, until now, the bandwidth remains limited by the laser modulation and the speed of the photodetector, not by the fiber itself.

In order to overcome the bandwidth limitations, the main popular technique is multiplexing. Since the 1990s, Wavelength Division Multiplexing (WDM) is adopted by slightly separating the wavelengths around 1.55 µm, each one of them being considered as a channel. In 1996, 1 Tb/s data transfer rate was reached by the WDM technique [29]. After 2000, the development of coherent receivers (heterodyne detection) has enabled more complex modulation formats with the constellation diagram: Amplitude-Shift Keying (ASK), Phase-Shift Keying (PSK), Quaternary PSK and later using digital processes and polarization, Quadrature Amplitude Modulation (QAM) [18, 28]. In 2011, Ref. 30 has reached 64 Tb/s using Polarization Division Multiplexing (PDM) coupled with QAM. To get over the bit rate capacity limit of SMF, since 2010 the strategy is to increase the number of cores per fiber (Multicore fiber, MCF) or to have several modes per fiber (Multimode

[4] Bandwidth-distance product: the bandwitdh is expressed in bit rate and the distance is the repeater spacing (i.e. the distance after which an optical signal must be regenerated to maintain its fidelity), this expression is used to compare different communication technologies.

[5] Spectral efficiency: number of bits transmitted in 1 s within a 1-Hz bandwidth.

fiber, MMF). The optical signals are then modulated/demodulated spatially by Space Division Multiplexing (SDM) [31]. The NICT in Japan have announced 172 Tb/s using SDM in 2020 [32]. Another argument for SDM is to reduce the energy cost per bit when using a parallel transport (100 times more energy-efficient according to Ref. 33).

A second strategy is to increase the speed of the photodetector to demodulate faster with a single channel (or wavelength). This approach is a Single-Input-Single-Output (SISO) without multiplexing and will be further developed in Sec. 1.3.

Within optical communication chains, improving each key components (optical transceiver, optical fiber, optical receiver and optical amplifer) is one of the key to increase data exchange between network nodes. Photodetectors need to reach a bandwidth above THz in order to demodulate at the state of the art of multiplexing approach and this is where this PhD thesis aims at contributing to the field. The literature, advantages/disadvantages and physical limits of the photodetector approach will be further developed later.

### 1.1.2 Chip-to-chip connection and photonics

Presently, tremendous quantities of data are exchanged and need to be treated by data centers. This has as a consequence that the energy power cost is becoming higher and higher. Indeed, in 2015, the data centers energy consumption was estimated at 3% of the world total electrical power supplied [34]. Computers used in data centers need to be cooled down because of Joule heating. Indeed, chips and other components in computers are interconnected by wires made of copper in which losses are significant. Moreover, electrical (metallic) interconnects can transmit signals with a limited bandwidth which reduces the parallelization computing capabilities. It is thus a serious challenge to overcome these limitations and optimize the data treatment.

Photonics interconnects are a strategy to reduce Joule heating and bandwidth limitations compared to electrical wire interconnects. Indeed, photonic waveguides or fiber optics don't produce heat during the propagation of light and possess almost no bandwidth limitation (compared to classical electrical interconnects). However, electrical outputs (or inputs) from a CPU or a motherboard need to be converted into light (or electrical signal). For that, one needs a ultrafast laser modulation and an opto-electronic convertor i.e. a photodetector.

In this area, Intel® has developed interconnects made of integrated silicon photonic components with optical fiber channels (Fig. 1.3.a). The output electrical signal from a classical circuit board is converted into light by four hybrid silicon lasers and optically multiplexed by wavelength division multiplexing (WDM). The optical signal then passes through a multimode fiber. The signal is received and optically demultiplexed by another circuit board made of four integrated high speed SiGe photodetectors converting the light to an electrical signal [35]. This interconnect is already on the market and works at 50 Gb/s.

Another strategy for communication between two chips is by directly integrating photonic connections on the same circuit board. Silicon photonics is quite promising due to the already developed capabilities offered by silicon on insulator (SOI) technologies [37, 38]. An array of processors are connected by silicon photonic waveguides (also called photonic bus) and permits new complex parallel computing [36]. Such a design is sometimes called photonic Networks-on-Chip (NoC). Bergman et al. [36] studied such NoC by the optical modulation made of ring resonators (Fig. 1.3.b). The conversion to electronic is done by a lateral Ge PIN photodetector. Silicon bus interconnect is one of the most advanced technology in terms of low energy cost, efficiency and cost effectiveness. Fukuda

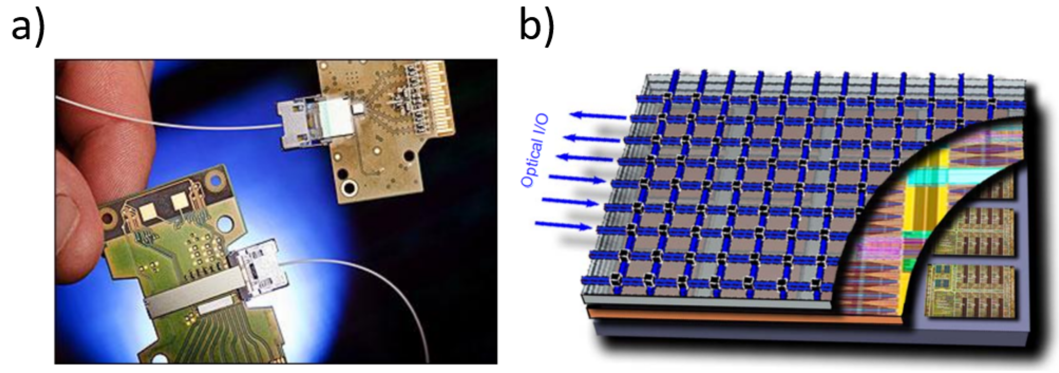


Figure 1.3: a) Intel's® Si photonics link working at 50 Gb/s (integrated lasers, wavelength division multiplexing and photodetectors) [35]. b) Integrated multi-core processors with photonic interconnects [36].

et al. [39] proposed to use plasmonic waveguides as interconnects between on-chip components. With less losses and higher speed than electrical wires, plasmonic buses present interesting perspectives [40].

All optical processing is also an encourageous field [41] to make all operations with optical switches and optical interconnects without the need of energy cost electrical components. Indeed, the converting operation of Eletrical / Optical / Electrical signals needs optical converters (transceiver, receiver and multiplexing elements) which adds system complexity and energy cost. The optical switches are mainly based on Mach-Zehnder interferometers, micro-ring resonators, liquid crystals on silicon (LCOS), Lithium niobate waveguides, III-IV semiconductor optical amplifiers (SOA) and micro-electro-mechanical-systems (MEMS) [42] or even with third-order nonlinearities [43]. Such devices would reduce the energetic cost of today's computers. Another alternative is integrating plasmonic chip processing that takes advantage of the low size of electronic components and the high speed of photonics [11].

For on-chip communication, enhancing the bandwidth, efficiency and reducing the power consumption is essential to improve data processing efficiency and environmental impact.

### 1.1.3 THz and high frequency current generation

Photodetectors are not only used to sense light but also to generate stable high frequencies such as THz or high frequency currents. THz waves are electromagnetic waves at frequencies between 0.3 THz (1 mm) and 30 THz (100 µm). These waves can penetrate through a lot of materials (wood, wall, cloths) and even slightly in bodies (without being ionizing rays). Tremendous applications emerge from THz waves: wireless communication, sensing in biology, food quality and non destructive testing, spectroscopy and imaging to cite a few [44].

The main drawback is that THz waves are difficult to generate. Plenty of strategies have been used to create them efficiently usually divided into two categories: electronic and optical approaches [45]. The electronic techniques usually suffer from low tunability and low efficiency (electronic up-converters through frequency multiplication, Gunn diodes, resonance tunneling diodes (RTDs), to cite a few). On the other hand, optical

techniques exhibit low power but are more tunable (THz quantum cascade lasers (QCLs), optical down-conversion by nonlinear or photoconductive mixing, to cite a few).

A promising approach presented in Fig. 1.4.a is to use an ultrafast photodetector connected to a THz antenna [46]. In fact, two continous wave (c.w.) lasers are mixed onto a plasmonic photodetector and generates THz electrical current. This structure is coupled to a THz antenna yielding THz waves. Such a device is referred as a Light-to-THz converter. In 2013, Koenig et al. [47] used similar principles to make a THz emitter for wireless communication applications (at a distance of 20 m with a data rate of 100 Gbit/s).

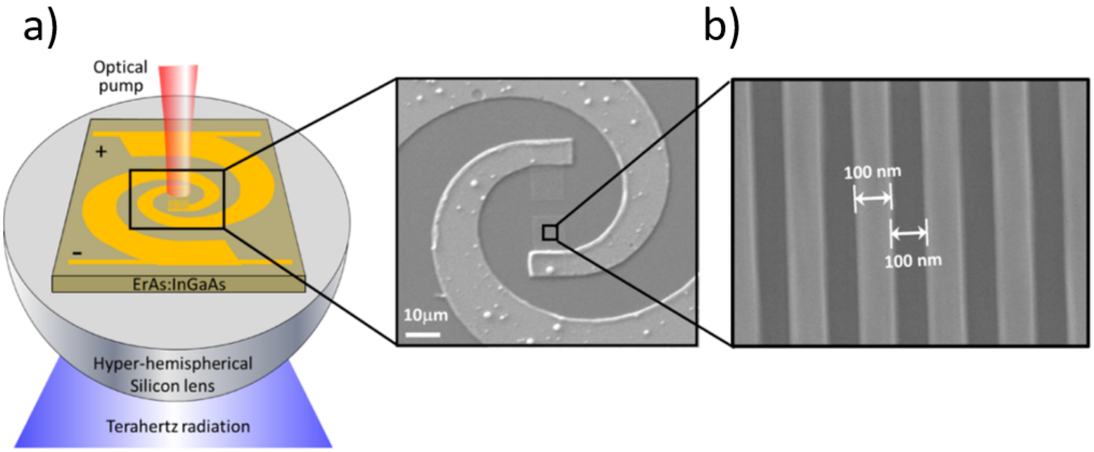


Figure 1.4: Plasmonic photodetector coupled to a THz antenna [46]. a) Scheme. b) SEM images.

Nowadays, local oscillators (LO) are commonly used in integrated circuits to generate oscillating currents. Though, generating a stable high electrical frequency above GHz is difficult. For instance, NASA needs to collect a very weak signal from the universe at 4.7 THz for the oxygen line [48]. Using a coherent detection (heterodyne) permits them to collect this weak signal with a proper signal-to-noise ratio. However, coherent detection needs a stable LO to compare the signal comming from the universe. Photomixing the signal and the local oscillator leads to an acceptable detection.

Finally, ultrafast data exchanges are of big interest in various fields: high data rate communications, chip-to-chip interconnects, THz generation, and LO for heterodyne detection.

## 1.2 Plasmonics for ultrafast opto-electronics

We have seen the scientific, technological and societal needs to increase information exchanges at low scale or long distance. Using light as a carrier wave allows to transmit more informations but needs bulky photonic components or optical fibers compared to classical electrical copper wires. On the other hand, electronic components can be smaller but are limited in bandwidth. The plasmonic approach allows one to face those difficulties by lowering the elements' size while maintaining high bandwidth [11]. Indeed, surface plasmons are light interactions with oscillations of carriers at the interface between a metal and a dielectric, enhancing light-matter interaction and strongly confining light in a small volume. This allows creating miniaturized photonic and electronic devices. Surface plasmons also present impressive underlying characteristics that allow

modulation at femtosecond time scales [49]. Because of high light-matter interactions, surface plasmons can transfer their energy to other carriers generating high energy carriers (compared to the Fermi energy), called hot carriers. Surface plasmons and hot carriers present outstanding features in terms of lifetime (tens of fs for the first ones and 1-2 ps for the second ones) and locally available energy. Those hot carriers can be advantageously extracted for ultrafast opto-electronic devices such as photodetectors benefiting from the compactness of plasmonics. The technological issue is to create carriers in small volumes and reduce their transport time (increasing the bandwidth).

This section will present how to define and represent surface plasmons. Then, hot carriers enhanced by surface plasmons will be detailed, followed by their extraction with a Schottky barrier.

### 1.2.1 Definition of plasmonics and light-matter interaction

Since the first observation in 1902 by Wood [4] of the anomalous diffraction in metallic gratings, an interesting debate emerged to understand the underlying physics. Indeed, for a given angle of incidence and wavelength, Wood anomaly was observed for TM polarization, depending on the metal and its shape. Thus, it could not be fully explained by Rayleigh's theory [50] until progresses due to Ugo Fano [51] and Hessel and Holiner [52] who introduced the "leaky waves supported by the grating". Moreover, in 1957, early work of Ritchie recognised the phenomenon in terms of surface waves [8]. In the 1970's, a more complete analysis was possible due to the development of computers and lasers [9], before being revisited by tremendous works since the 1990's permitted by advances in nanofabrication [53].

#### Propagative Surface Plasmon Polaritons (SPPs)

Surface plasmons (SPs) are defined as electromagnetic surface waves propagating at the interface between a metal and a dielectric. SPs are excited by the coupling between the far or near field and collective oscillations of free electrons at the metal's surface [8]. Such coupling between light and plasma oscillations refers as polaritons [7] yielding the term Surface Plasmon Polaritons (SPPs) [54]. SPPs are inherently lossy by Joule heating that occurs with charge oscillations. Thus, they are damped along their surface propagation within a certain distance length. At the interface along the propagation, the electric field is a longitudinal wave while the magnetic field is a transverse wave. Moreover, by nature, SPPs are evanescent orthogonally to the interface and slightly penetrate into the dielectric and the metal depending on their dielectric functions.

SPPs allow one to highly concentrate electromagnetic waves in subwavelength volumes. Another advantage is to propagate light in subwavelength structures rendering possible nanoscale circuitry based on SPPs and called plasmonics [55, 56]. Consequently, plenty of applications emerge from propagating SPPs especially in nano, chemical and bio sensors [53]. On the contrary, the SPPs' lossy nature limits applications and several strategies are applied to reduce losses [57]: reversible changes media due to heating [58], quandum dots as a gain medium [59] or electrical pumping [60]. Furthermore, additional loss mechanisms are: a) the unwanted SPPs coupling with the far field and b) the interband metal absorption for short wavelength excitation.

From classical Maxwell equations, SPPs emerge at the interface between two semi-infinite metal and dielectric media [61, 62]. The SPP dispersion relation for the $k_{SPP}$ vector

is then given by

$$k_{SPP} = \sqrt{\frac{\epsilon_D \epsilon_M(\omega)}{\epsilon_D + \epsilon_M(\omega)}} k_0 \tag{1.1}$$

with $\epsilon_D$ (resp. $\epsilon_M$) the dielectric function of the dielectric (resp. the metal which is usually frequency-dependent and complex: $\epsilon_M = \epsilon'_M + i\epsilon''_M$ with $\epsilon'_M < 0$ and $\epsilon''_M$ rendering account of the Joule effect or absorption of the metal) and $k_{SPP}$ is complex ($k_{SPP} = k'_{SPP} + i k''_{SPP}$). In order to have SPPs at their interfaces, the two media must fulfill the condition such that $\epsilon_D \epsilon_M(\omega)$ and $\epsilon_D + \epsilon_M(\omega)$ are both real and negative [62]. Usually, a dielectric medium presents a real and positive value and a metal a complex one with negative real part achieving the above condition.

Applying careful approximations i.e. $|\epsilon''_M| \ll |\epsilon'_M|$ and $|k''_{SPP}| \ll |k'_{SPP}|$ , useful pieces of information can be retrieved: the SPP wavelength $\lambda_{SPP}$, the propagation distance along the surface $L_{SPP}$ and the penetration depth (exponential decay) across the interface ($D_D$ for dielectric and $D_M$ for metal) [61, 62]:

$$\lambda_{SPP} = \frac{2\pi}{k'_{SPP}} \approx \sqrt{\frac{\epsilon'_M(\omega) + \epsilon_D}{\epsilon'_M(\omega)\epsilon_D}} \lambda_0 \tag{1.2}$$

$$L_{SPP} = \frac{1}{2k"_{SPP}} \approx \frac{\epsilon'_M(\omega)^2}{\epsilon"_M(\omega)} \left( \frac{\epsilon'_M(\omega) + \epsilon_D}{\epsilon'_M(\omega)\epsilon_D} \right)^{3/2} \frac{1}{k_0} \tag{1.3}$$

$$D_D = \frac{1}{|k_{z,D}|} = \left( \sqrt{\frac{-\epsilon_D^2}{\epsilon'_M(\omega) + \epsilon_D}} k_0 \right)^{-1} \tag{1.4}$$

$$D_M = \frac{1}{|k_{z,M}|} = \left( \sqrt{\frac{-\epsilon_M(\omega)^2}{\epsilon'_M(\omega) + \epsilon_D}} k_0 \right)^{-1} \tag{1.5}$$

For instance, at $\lambda_0 = 820$ nm and for a Au-air interface, $\lambda_{SPP} = 804$ nm, $L_{SPP} \simeq 50$ µm, $D_D \simeq 649$ nm, $D_M \simeq 25$ nm. , Fig. 1.5 represents the dispersion curve of a metal at the air and silica interface relative to the plasma frequency $\omega_P = \sqrt{\frac{ne^2}{\epsilon_0 m}}$ with $n$ the electron density, $e$ the elementary charge, $\epsilon_0$ the vacuum permittivity and $m$ the electron mass [61]. The dispersion curve of SPP is under the air light cone and thus cannot be excited directly by an incident beam (lack of momentum). To excite SPPs, one should find ways to give additional momentum to the impinging light. A first scheme is to use total internal reflection (TIR) within a prism: a) with a thin air space between the prism and the metal (Otto [63]) or b) with the metal sticked onto the prism (Kretchschmann [64]). For both techniques, the evanescent wave at the TIR excites SPPs at the metal air interface. Those two techniques permitted the developement of intensive studies of SPPs. A second way to generate SPPs is to use a diffraction grating [65]. The diffracted beam gives additional momentum to the incident $k_0$, achieving phase matching with the SPP. Moreover, this technique was the way Wood was exciting the "anomalous diffraction" (by smooth metallic grating i.e. not so deep grating compared to the incident wavelength). Third, SPPs can be excited by high angle incidence optical beam provided from an oil immersed high NA objective (NA > 1) [66]. In this way, the SPP momentum at the air/metal interface can be matched. Another way is to use scattering from a defect, a nanoparticle or a fluorescent molecule to locally excite SPPs [67]. Indeed, the scattering process yields locally large k vectors with one that matches the $k_{SPP}$. Other techniques exist using electron beams to

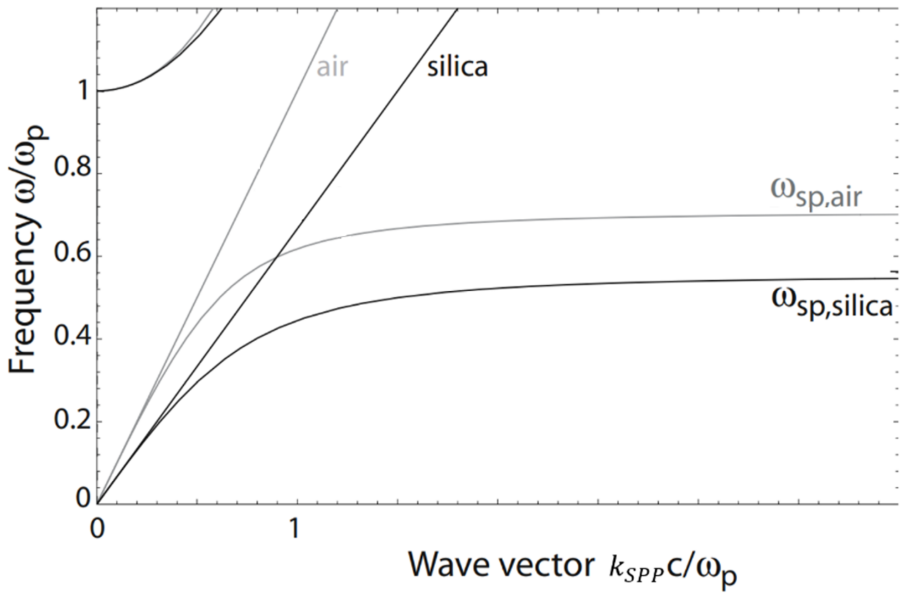


Figure 1.5: Dispersion curve of SPP at the interface: a) between air and metal and b) between silica and metal with their relative light for air and silica (modified from [61]).

excite SPP [68] or by leakage microscopy with a Scanning Nearfield Optical Microscope (SNOM) tip [69].

SPPs can be generated within different structure types. Thin metal films and smooth metallic gratings were the first strategies to excite SPPs. Another type are nanowaveguides or nanowires [70, 71]. A SPP is excited and propagates along the nanowaveguide and is confined within two dimensions. This scheme allows a stronger confinement and guides the light into subwavelength structures (superlocalization [72]). Other strategies are used to excite SPPs: V-grooves and gap SPPs [73], uniform and tapered plasmonic fibers (for nanofocusing) [74], to cite a few. Work has been done for achieving long range propagation of SPP (~ mm, ~ cm [75]) within nanowire with the purpose of plasmonic circuitry [56]. Moreover, some approaches permit the coupling between SPP modes. For example, a thin layer is sandwitched between two materials: a) metal-insulator-metal (MIM) [76] or b) insulator-metal-insulator (IMI) configurations [77]. An interesting phenomenon is obsereved when the nanowire is shorter than the propagation length $L_{SPP}$: backreflection occurs at the end of the wire. Then, a standing wave with interferences is observed all along the waveguide and resonances can be observed (nanoantenna) [70,71].

#### Localized Surface Plasmons (LSP)

Contrarily to propagative SPPs, some geometrical configurations of the metals confine the propagation of plasmons: producing so-called Localized Surface Plasmons (LSPs). LSPs are electromagnetic surface modes oscillating inside a metallic nanoparticle (NP) embedded in a dielectric media [61,78]. Those surface modes are resonantly oscillating at optical frequency. The LSP mode locally oscillates, unlike propagating SPP, and is tightly confined in 3 dimensions even more than SPP, highly improving light-matter interactions. Moreover, there is a strong electromagnetic field enhancement in the near field of NPs, yielding higher sensitivity to tiny refractive index variations. As a consequence, lot of applications emerge from LSPs: nano to molecular sensing [79], Surface Enhanced Raman Scattereing (SERS) spectroscopy [80], fluorescence enhancement [81], photovoltaics [82], chemical

reaction activation [83], photoemission [84], to cite a few.

A full analytical derivation of LSP can be done starting from the classical electromagnetic Mie theory [61]. The expressions are usually simplified under the quasi-static approximation by considering NPs much smaller than the incident wavelength. Under this approximation, the field is supposed to be uniform throughout the NP giving no dephasing time or spatial retardation effects. Part of the incident light is absorbed yielding hot electrons, heat or luminescence and the other part is scattered in all directions. Those phenomenons are expressed by the absorption and scattering cross sections. It is remarkable that a LSP at resonance will strongly enhance the absorption cross section to values even higher than its geometrical cross section [85]. Light-matter interaction is then increased below the diffraction limit by shaping the metal in a particular shape [86]. In the quasi-static approximation, the fundamental LSP mode yields scattered fields identical to an electrical dipole (also called dipolar approximation). The polarizability is the same as for the Clausius-Mossotti formula and the resonance is maximized under the Fröhlich condition: $\mathrm{Re}[\epsilon_M(\omega)] = -2\epsilon_D$ [61]. Under those approximations, the wavelength resonance depends only on the media refractive indices and the dimensions. Thus, a slight refractive index modification in the near-field will shift the resonance yielding plenty of applications in sensing [87]. An increase (resp. a decrease) of $\epsilon_D$ will red shift (resp. blue shift) the wavelength resonance. For a metallic nanosphere within a dielectric, the scattering and absorption cross sections under quasi-static approximation are expressed as [88, 89],

$$\sigma_{scatt}(\omega) = \frac{24\pi^3 a^6 \epsilon_D^2}{\lambda_0^4} \frac{(\epsilon'_M(\omega) - \epsilon_D)^2 + \epsilon"_M(\omega)^2}{(\epsilon'_M(\omega) + 2\epsilon_D)^2 + \epsilon"_M(\omega)^2} \propto \frac{a^6}{\lambda_0^4} \tag{1.6}$$

$$\sigma_{abs}(\omega) = \frac{18\pi a^3 \epsilon_D^{3/2}}{\lambda_0} \frac{\epsilon"_M(\omega)}{(\epsilon'_M(\omega) + 2\epsilon_D)^2 + \epsilon"_M(\omega)^2} \propto \frac{a^3}{\lambda_0} \tag{1.7}$$

with $a$ the nanosphere diameter. For small NPs (< 30 nm), the absorption is dominant while for bigger NPs (> 100 nm) scattering dominates. Fig. 1.6, extracted from Ref. 62, shows the full output calculation for the scattering cross section for different metals and dielectric media. If $\epsilon_D$ increases, the scattering cross section is enhanced and the resonance wavelength redshifts. Moreover, the metal absorption due to its complex dielectric function yields a LSP damping and a resonance broadening.

Beyond these approximations for increased NP size, one should use the full solution of the Mie theory for a nanosphere (expansion of the fields in spherical harmonics) [61, 88]. Within this calculation, retardation effects are taken into account. If the NP size increases, the resonance is red shifted and broadened due to much larger radiation losses. One could develop analytical solutions for other geometries than nanospheres: nanoellipsoids (known as Gans theory) and nanowires / nanogratings [88]. In order to overcome the limitations of analytical calculations, numerical simulations are typically used to compute LSP resonances: Finite Element Method (FEM), Finite Difference Time Domain (FDTD), Rigourous Coupled-Wave Analysis (RCWA) and Green Dyadic Method (GDM) are the most commonly used.

NPs exhibiting LSPs permit direct coupling with incident resonant wavelength. LSP can be easily observed by far field broadband excitation with dark-field scattering techniques or extinction microscopy [89]. The dark-field scattering technique consists in the excitation of a LSP structure at low (resp. large) incident angle and the collection of the scattered light only at large (resp. low) angles thanks to a dark field condenser [90]. Extinction microscopy directly excites the NP LSP resonances and yields the extinction spectra by careful normalization between the incident field and the specular

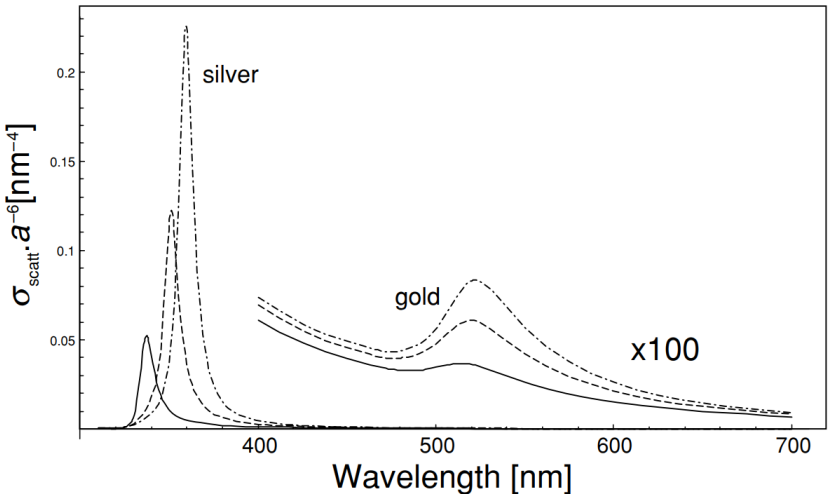


Figure 1.6: Scattering cross section for Au and Ag nanospheres with different dielectric media: solid line (vacuum, n=1), dashed line (water, n=1.33) and dashed-dotted line (glass, n=1.55) normalized by the size parameter $a^6$ [62].

reflection/transmission spectra [91]. Depending on the NP shape, size and orientation (e.g. nanoantenna), there is a dependance on the incident polarization and direction. Near-field optical spectroscopy has also been explored. In this scheme, a Scanning Near-field Optical Microscope (SNOM) probe excites or collects the near-field light in the near-field [92]. The dark-field scattering technique and the near-field optical spectroscopy allow one to investigate single particle LSP properties while extinction microscopy is more tricky because of a lower signal to noise ratio (lower contrast of specular reflection/transmission) [61]. Moreover, LSP can be generated within plenty of geometries [78,93] presenting their own properties: nanospheres [94], nanoantennas [95], long nanorods and gratings [96], nanocubes [97], bowtie nanoantennas [98] or even rough films [92], to cite a few. Au and Ag are the main materials used in plasmonics because they present resonances in the near IR and visible range while Al is advantageous for UV applications.

Approaching two or more LSP NPs (distance < 5 nm) can yield a near-field coupling between LSP modes with hybridizations (as in Linear Combination of Atomic Orbitals, LCAO). This more complex structures involve higher-order modes. If two LSP NPs are coupled, bonding and antibonding modes arise [99]. In this scheme, because NPs are very close to each other, within the gap they exhibit a high field enhancement (called Bonding Dimer Plasmon, BDP) [100]. Nanotructures presenting coupled LSPs can be dimers, nanoshells and nanovoids, or nanobowties. Furthermore, if broadband radiant modes couple with narrow subradiant modes, Fano resonances arise, as studied e.g. in nanodolmens [101]. Moreover, SPPs and LSPs can also be coupled [102], e.g. with nanodisks onto a thin metal film [103]. This strategy of coupling modes allows for more complex absorption and scattering spectra depending on the desired application.

Lastly, propagative SPPs and LSPs are strategies to enhance light-matter interactions in small volumes and are thus used to enhance low-efficiency processes. Surface plasmons increase the absorption and scattering cross sections permitting light harvesting applications. The NP shaping and careful material choice permit to control the high local field enhancement. Their resonant nature permits to selectively control processes such as Raman scattering and non linear processes [104]. Plasmonics also allows low scale components oscillating at optical frequency, thus, the advantage of ultrafast time characteristic (photonics) and at lower scale (electronics) [11], as already discussed.

### 1.2.2 Hot electrons physics and surface plasmons relaxation

As presented in the last section, propagative SPPs or LSPs confine strongly light within small volumes, enhancing light-matter interactions in favor of low efficiency processes. If a photon is impinging on a plasmonic metal structure: two absorption phenomena can arise. The first phenomenon is by direct photon absorption: the photon is absorbed and generates hot carriers. This process is usually very low in metal due to the short penetration length of the photons [105]. The second phenomenon occurs when light couples to SPs. Then, different scenarios can occur: a) SPs can either recouple to far-field and reemit a photon at the same wavelength (radiative decay), b) excite hot carriers by transferring SPs energy to electrons by Landau damping (non radiative decay) [106] or c) be dissipated via Joule heating and the production of phonons. "Hot" carriers refer to a non thermal energy distribution compared to a thermal energy distribution of carriers. If these hot carriers have energy sufficiently high compared to the work function of the metal, carriers are photoemitted (in the vacuum). But, if hot carriers have energy below the work function but sufficiently high compared to the Fermi level, they yield to plenty of applications in light harvesting (photovoltaic solar cell, photodetection), local heating or photocatalysis [10]. Moreover, hot electrons are very attractive because of their short lifetime (~ ps range) [107, 108].

To calculate the electromagnetic field within or surrounding a plasmonic structure, usually classical Maxwell's equation are sufficient. Then, to describe hot carriers behaviour, Time-dependent density functional theory (TD-DFT) in the jellium approximation (or free electron limit) are more appropriate [106]. A fully ab inito calculation with band structure can be used but will be limited by the plasmonic NP size (~ nm). Thus, the chosen model needs to be adapted to the studied structure i.e. a large structure (> 10 nm) will use classical electromagnetic wave model (so quantum effects cannot be predicted) and low dimension structures (~ nm) will use ab inito models.

In the next sections, I will present the behaviour of hot carriers, from their excitation to relaxation.

#### Generation of hot electrons by surface plasmons

In order to absorb light within a metal and create hot-carriers, one needs to find a way to increase the absorption. Indeed, by nature metal poorly absorbs light at optical frequencies, thus generating low amount of carriers. If a photon with an energy $h\nu$ is impinging onto a bulk metal with a photon energy below any interband transition, the photon will be largely reflected by the metal and only a small part will enter in the metal by skin effect. For a wavelength excitation $\lambda$, the entering field will be reduced by $1/e$ at the skin depth $\delta$, given by

$$\delta = \sqrt{\frac{\lambda}{\pi c \mu \sigma_c}} \tag{1.8}$$

where $c$ is the speed of light in vacuum, $\mu$ is the permeability ($\mu = \mu_r \mu_0$) and $\sigma_c$ is the conductivity of the material. For instance, Au with an excitation wavelength of 1.55 µm ($\sigma_c = 0.41 \times 10^8$ S/m) gives a skin depth $\delta_{Au} = 5.6$ nm and a small amount of hot carriers will be created because the absorption probability is low (no direct transition available).

Surface plasmons (SPs) are a strategy to enhance light absorption and hot carriers generation in metal. Of course, SPs involve collective oscillations of electrons in the conduction band and will excite other electrons in the metal conduction band not involved in the SPs. A direct photon absorption or a nonradiative decay gives an energy $E_e = h\nu$ to an

electron which passes from its fundamental state $E_0$ to an excited state $E_1$. This excitation creates also a hole i.e. also called hot hole. The excess of energy $E_r$ is the relative energy compare to the Fermi energy $E_F$: $E_r = E_1 - E_F$.

To go further, during hot carrier generation, there is a large mismatch between the low momentum of photons/surface plasmons and electrons in the metal. Hence, the direct photon absorption and the nonradiative decay of surface plasmon excite carriers with no momenta. Within the band diagram, if the incident photon energy is sufficiently high, a direct interband transition can be permitted by hot carriers. If not, the intraband transition can be permitted by an additional momentum given by phonon-assited decay (absorption or emission). But, in nanoscale structures, the additional momentum is given due to nanoscale size [109, 110]. Indeed, in nanostructures, electronic wave functions are more localized giving an uncertainty over the momentum. This is called geometry-assisted intraband transition [110]. There is then a non zero probability of transition below the interband energy threshold.

Moreover, it is usually tricky to dissociate hot carriers generated by the direct photon absorption or by the nonradiative decay of SPs (either by direct, phonon-assisted or geometry-assisted transition) because the probabillitiy of hot carriers generation depends on the sum of the electric field within the metal (photon and surface plasmon) [110]. To calcultate the allowed transitions, Sundararaman et al. [106] used from first principle DFT calculations to retreive the band diagram of metals (Fig. 1.7.a for Au). It turns out that in Au (Fig. 1.7.b) direct interband absorption exists at 2.6 eV (478 nm) due to d-band, producing mainly high hot holes and low energy hot electrons. Depending on the nanostructure size, material and shape, there is a competition between processes for the generation of hot carriers. Though, if an interband transition is feasible, almost only direct transition occurs [111]. The plasmon decay excites and generates a (hot) EHP in the metal. Higher number of hot electrons will be created from the s-p and d-band depending on the wavelength of excitation.

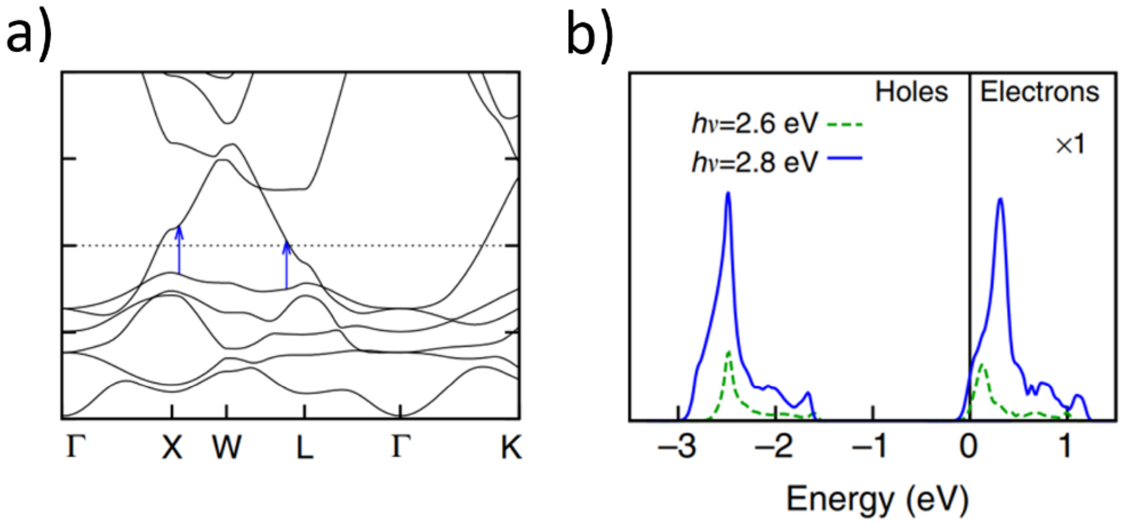


Figure 1.7: a) Band diagram by DFT calculation for Au with the two blue arrows representing the allowed interband transitions. b) Energy diagram population of excited carriers (electrons and holes) at 2.6 and 2.8 eV photon excitation [106].

The excitation probability of an electron by SPs is proportional to their intensity [112]. For instance, with a propagative SP, the probability of an electron to be excited at a posi-

tion x along the propagation is proportional to the intensity of the SPP

$$P_g(x) = \frac{1}{L_{SPP}} e^{-\frac{x}{L_{SPP}}} \tag{1.9}$$

In fact, the generation of hot carriers is higher close to the surface where the electric field is stronger.

Moreover, if the impinging light has high irradiance, Two Photon Absorption (TPA) in Au NPs can arise [113]. Indeed, with TPA, interband transitions to a real state happen with LSP NPs or nanoclusters. TPA is related to the third order nonlinear susceptibility of NPs and can be modified by the surrounding [114].

#### Transport of hot carriers within a metal

After hot carriers have been generated, they will be transported within the NPs and experience drift and diffusion. Predicting carrier transport is a challenge because carriers are far from equilibrium and their spatial distribution and temporal dynamics have to be known. Furthermore, in certain conditions, carriers can experience transport over a much longer distance than the NP's size, thus, reflection of carriers onto the boundaries have to be taken into account. To model such hot carrier transport, first principle calculations with TD-DFT or non-equilibrium Green functions can be used up to sizes of tens of nanometers and lead to highly demanding computation. Since plasmonic NPs are bigger (~ 100 nm), the semiclassical Boltzmann equation provides a complete model to out of equilibrium carrier transport [115] and is usually approximate to drift-diffusion equation [116]. Here, we will detailed some works on this topic but the thesis will not be focused on this specific behavior of hot carriers.

**a) Spatial transport** Carriers are created at a certain distance from the boundaries with an isotropic initial distribution of momenta. Along the transport towards an interface, carriers can experience scattering events: electron-electron (e-e), electron-phonon (e-p) scattering, impurities, defects and boundaries. The mean free path (or hot carrier attenuation length) $l_{MFP}$ is the average distance before a collision event occurs. Indeed, $l_{MFP}$ takes into consideration all scattering events that occur within the bulk metal. Through scattering events, carriers thermalize and get closer to the Fermi level. Hot carriers travel with two modes of transport [110]: ballistic, where carriers have low probability to scatter within the typical length of the nanostructure $l$ (high $l_{MFP}$), and diffusive, in which carriers have a high probability to scatter within a length $l$ (low $l_{MFP}$). Plasmonic nanostructures usually present both ballistic and diffusive transport ($l \approx l_{MFP}$), complexifying the models. If only inelastic collisions occur [112] with propagative SPP, the probabillity of an excited electron at a distance x from the interface to reach it (without experiencing a collision and thermalize) is

$$P_t(x) = e^{-\frac{x}{l_{MFP}}} \tag{1.10}$$

The transport behaviour depends on the hot carriers energy [117] and thus is linked to the excitation energy and the irradiance. Moreover, there is a $l_{MFP}$ discrepancy between electrons and holes [118].

For electrons, an ab initio model estimates the $l_{MFP}$ at 37.7 nm in Au with a 5.4 eV electron energy [119]. $l_{MFP}$ has been measured by photoelectric effect, to be 74 nm with a 0.81 eV electron energy [120], by point-contact emitter 52 nm with a 0.85 eV electron energy [121] while BEEM techniques gave a value between 10 to 20 nm with from 1 to 2 eV electron energy [122]. Those values are very interesting because they are of the order of

magnitude of LSP NPs and hot carriers could be used for applications at the NPs boundary. Thus, such parameters are important to be taken into account for the design of hot carrier devices

**b) Temporal dynamics** The hot carrier lifetime (or mean-free-time) is the average time for carriers to thermalize or recombine. The longer the hot carrier lifetime, the higher the probability to reach the NP interface. Then, hot carriers can be utilized for other processes. Though, if the carrier lifetime is too long, then the bandwidth of the photodetector will be reduced except if they are extracted faster than their lifetime. Carriers need to be extracted faster than their relaxation time decay. Hence, there is a balance between carriers lifetime and efficiency of carrier extraction.

Fig. 1.8 illustrates the order of magnitude of the processes occuring in metallic NPs (extracted from [10]). In plasmonic LSP Au nanostructures, after Landau damping, the generated non-thermal hot electron distribution experiences electron-electron scattering and equilibrates within 10 to 100 fs [123] yielding a Fermi-Dirac like distribution. After 100 fs, the hot electron distribution can be represented through the two temperature model (TTM) in which an effective temperature is associated to the lattice $T_l$ and to the electrons $T_e$ [124, 125]. Below 100 fs, $T_e$ is not well defined. From 100 fs to 1 ps, the hot electrons encounter electron-phonon scattering. From 100 ps to 10 ns, the electron distribution experiences heat dissipation and environment coupling [126]. Each electron-electron scattering results in a much higher energy loss for hot carriers than electron-phonon scattering [118]. Moreover, [127] showed that the higher the carrier energy, the lower their lifetime. The electron-phonon coupling is experimentally studied by pump-probe experiments in transient absorption scheme [128, 129]. On Au plasmonic NPs, ~ ps timescale are obtained for electron-phonon scattering [123].

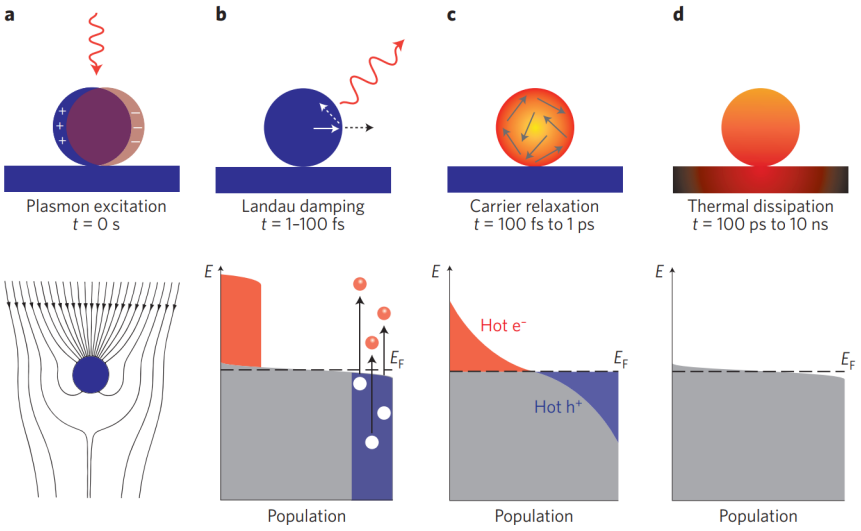


Figure 1.8: Steps of plasmon-enhanced hot electrons: a) their generation, b) Landau damping that excites hot electrons and radiative relaxation, c) hot carriers relaxation and d) thermal dissipation of hot carriers (extracted from [10]).

Thus, the *1st condition to be satisfied* to use hot carriers for applications is for carriers not to collide and thermalize before reaching the boundary. It has been shown that a small metal thickness compared to the mean free path leads to multiple reflections of hot carriers increasing the device efficiency [118]. However, a low metal thickness will

decrease the absorbance, leading to a small quantum efficiency. A trade-off has to be set between the metal thickness and a correct volume of absorbance.

### Photoluminescence (PL) of Au

In the following discussion, only Au will be considered. In fact, in other metals with visible and IR excitation, e.g. Ag, the d-band is at ~ 4 eV (310 nm) below the Fermi level, the interband transition from d to sp-band can be neglected and only intraband in the sp-band can be considered (yielding a more convenient predictible emission spectra). After being generated, hot carriers can recombine emitting photons with energies depending on the incident photons/plasmons energy and power. Indeed, two cases emerge depending on the incident photon/plasmon energy and whether interband transitions are available or not in a material. Moreover, if the incident power increases, other phenomenons can arise e.g. carrier energy redistribution followed by recombination and broadening of the emission spectrum. With incident photon energy below interband transitions, intraband absorption and TPA can occur yielding a PL with mixed underlying processes. To date, a debate in the community still exists about the underlying nonlinear PL physics. In Au LSP NPs and rough films, this broadband PL has been observed in many experiments [109, 130, 131]. This nonlinear PL is broadband and is composed both of wavelengths longer than the laser excitation (lower energy, called Stokes) and shorter than the laser (higher energy, called anti-Stokes).

Fig. 1.9 depicts four photoluminescence processes explaining the non linear photoluminescence (extracted from [131] and [132]) while Fig. 1.7 illustrates the excitation of hot carriers within the band diagram. Fig. 1.9 (i) is the interband luminescence i.e. the recombination from the sp-band to the d-band. Fig. 1.9 (ii) is the inelastic scattering based on Raman process. Fig. 1.9 (iii) is the intraband luminescence. Indeed, at nanoscale, the intraband transition are not forbidden because of selection rules (allowed by geometry-assisted, Sec. 1.2.2 [109, 110]). Fig. 1.9 (iv) is the Auger process due to hot holes in the d-band (Auger scattering) yielding hot electron in the sp-band followed by an intraband recombinantion in the sp-band.

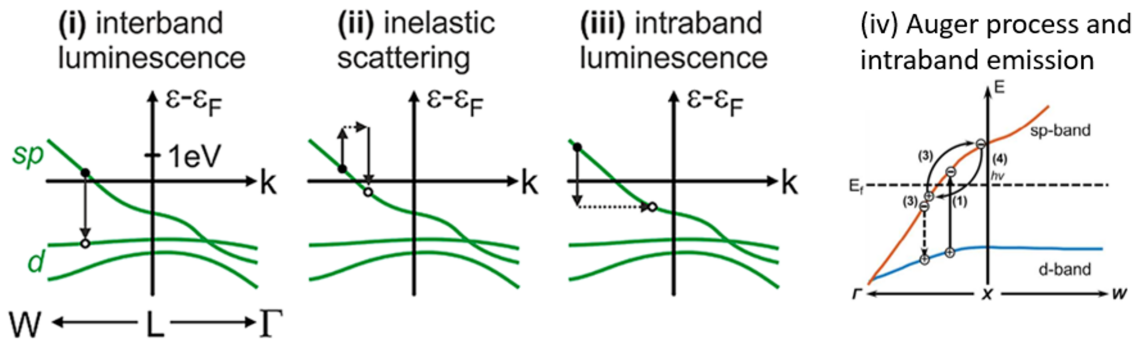


Figure 1.9: Schematic representation of the four processes explaining the origin of the broadband photoluminescence of Au : (i) interband PL, (ii) inelastic scattering, (iii) intraband PL and (iv) Auger process followed by intraband emission (extracted from [131] and [132]).

**a) Photon energy excitation above the interband transition** If the photon energy excitation is above ~ 1.8 eV (wavelength is below 690 nm) in Au NPs (with LSP energy res-

onance above the interband transition), the interband absorption from the d to the sp-band comes into play and the intraband absorption can be negleted (see Fig. 1.7). Once hot electrons have been excited, they are scattered by e-e and e-p interactions leading to an energy redistribution which is broadened and closer to the Fermi level. They then recombine from the sp (close to the Fermi level) to the d-band at lower energy either radiatively (Fig. 1.9 (i)) or non radiatively. The radiative recombination of hot electrons is possible only if there is a hole available in the sp or d-band [133] and its efficiency is proportional to the Photonic Density of States (PDoS) of the LSP [132].

The PL produced spans from the laser excitation to the lowest permitted interband recombination energy (~ 1.8 eV, ~ 690 nm). In bulk metals, the non radiative decay is much faster than the radiative decay leading to a low Quantum Yield[1] (QY) on the order of $10^{-10}$ [134]. A LSP provides another radiative decay channel and enhances the coupling to light, thus increasing the QY [135, 136]. Moreover in LSP, the direct interband radiative recombination is a very fast process (~ fs) [132, 137]. In 2000, Mohamed et al. [135] found a QY of $10^{-4}$ in nanoantennas of Au excited at the plasmonic resonance above the interband excitation.

The Stokes part of the PL was first observed by Mooradian [134] in 1969 on bulk Au. Such PL was considered as an undesired background in Surface Enhanced Raman Scattering (SERS) experiments, and known as SERS background [80, 138]. The Stokes PL part was first attributed to the interband recombination of carriers from the sp to the d-band because of its maximal intensity non dependence over the excitation wavelength [80, 134].

In order to study the radiative recombination path followed by carriers, Cai et al. [132] studied the excitations above the interband transition but with a LSP resonance below the interband transition. Indeed, the presence of a LSP enhances the PDoS at the LSP resonance wavelength (Purcell effect). After an interband excitation, part of the carriers directly radiatively recombine but another part radiatively relaxe by intraband transition. In fact, Cai et al. showed that non-radiative decay by Auger scattering can occur followed by intraband relaxation (Fig. 1.9 (iv)). The Auger process path is much longer than interband transitions (~ ps) [132]. In this regime the PL peak is dictated by the Au NP LSP resonance.

Lastly, when interband absorption is available, there is a consensus in the PL debate: interband absorption is major compared to other processes which can be neglected. Interband transition is followed by energy carriers redistribution and recombination explaining the yielded PL [136, 139]. If there is a LSP resonance, due to the PDoS enhancement, the electronic recombination will mainly follow Auger process and the PL maximal intensity will be at the LSP resonance wavelength.

**b) Photon energy excitation below the interband transition** If the photon energy excitation is below ~ 1.8 eV (wavelength is above 690 nm) in Au, the direct interband absorption of photons from the d to the sp-band is not permitted.

First, the photon absorption occurs via intraband absorption (also known as Free Carrier Absorption (FCA)) via geometry-assisted or phonon-assisted process. After their excitation, carriers relaxe via e-e and e-p scattering and their energy redistributes closer to the Fermi level. Then, hot electrons recombine via intraband transitions either radiatively (Fig. 1.9 (iii)) or non radiatively. This one-photon PL refers as the main component of the Stokes emission and is classicaly observed as an almost linear power response [109, 131].

[1] Quantum Yield: ratio between the number of photons emitted and the number of photon impinging onto the device, also called Photoluminescence Quantum Efficiency

Secondly, a direct two photon absorption (TPA) (single step) or an intraband followed by an interband absorption (two-step TPA) [140] can take place. Jiang et al. [141] showed that there are more arguments in favor of a TPA with a 2 steps process rather than a direct one also as demonstrated by auto-correlation measurements [108]. After they relax, hot electrons recombine via interband transition either radiatively producing Multiphoton Photoluminescence (MPL) or non radiatively. Hot electrons can also recombine with an intraband transition via Auger process. This MPL composes the anti-Stokes emission, usually observed as quadratic power response [109, 131], and is also part of the Stokes spectrum.

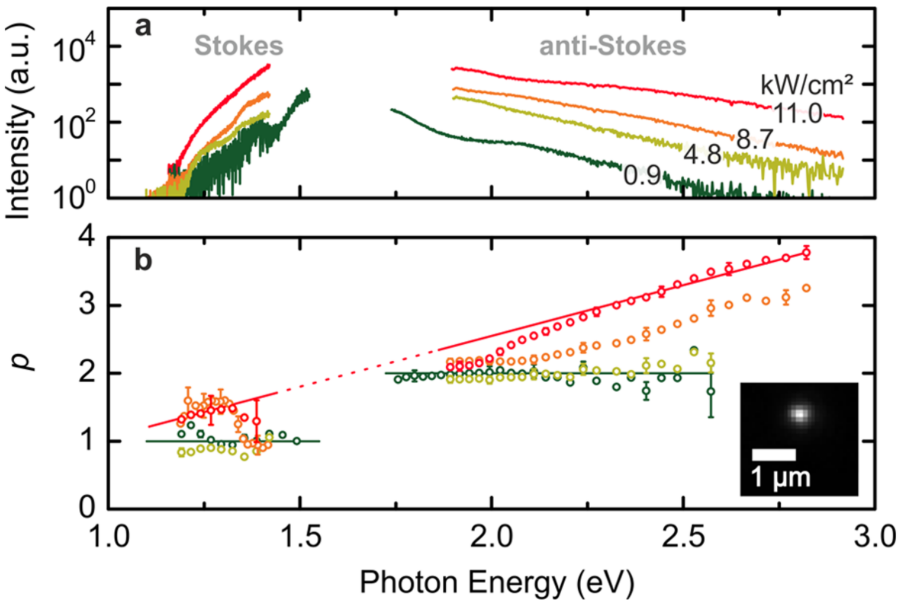


Figure 1.10: Broadband photoluminescence observed in Au NPs with the Stokes and anti-Stokes parts for several irradiance. a) Spectrums. b) The non linear order (here $p$) does not depend on the photon energy for 0.9 and 4.8 kW/cm$^2$ but, for 8.7 and 11 kW/cm$^2$, $p$ depends on the photon energy $h\nu$. Article of Roloff et al. [131]

The broadband PL is dependent on the irradiance which plays a key role. In Fig. 1.10, Roloff et al. [131] studied the non linear PL (intensity as a function of the photon energy, upper plot) and their non linear order as a function of the photon energy (lower plot). It turned out that passing an irradiance threshold (5 kW/cm$^2$) leads to different regime. In fact, below the threshold, the MPL is following linear PL of the Stokes part and second order non linear response of the Anti-Stokes part [109]. But, above the irradiance threshold, the non linear order becomes non integer and depends on the photon energy ($n(h\nu)$) which is a signature of absorption-induced heating of the conduction band electrons [130]. This regime is reached when the characteristic absorption rate is faster than the decay time of hot electrons (~ 1 ps) [132] yielding a hotter cloud of electrons. Thus, the laser excitation is heating the conduction band and leads to a blue shift of the PL compared to the scattered spectrum. Indeed, an effective electronic temperature $T_e$ is given to this cloud of hot electrons by fitting with the black-body radiation spectrum. The $T_e$ is therefore affecting the photon absorption. The emission within this regime can then be seen as an incandescent source of light [130].

Pulsed duration or c.w. laser excitation play also an important role on the PL. Cai et al. [142] showed that a c.w. excitation leads to lower non linearities than 2 and the

spectrum is less broad compared to pulsed excitation. Biagioni et al. [107] changed the non linear order PL, from TPL to Four-photon PL (FPL), by increasing the duration of the laser pulses from 100 fs to 700 fs. The shape of the nanoantennas also influences the PL. Indeed, Knittel et al. [143] shaped the MPL spectrum being produced by shaping the Au nanoantennas. Furthermmore, Sakat et al. [144] studied the lifetime of such PL and found ~ 1 ps time relaxation decay. Such lifetime measure, with many others [107,108,145], gives arguments to a hot electron origin of the MPL with real states being excited.

Another theory tries to explain the origin of NPs PL by inelastic light scattering (Raman process Fig. 1.9 (ii)) [146, 147]. However, many arguments are in favour of radiative recombination of hot carriers and incandescent theories. First, the phenomenon of PL does not depend on the laser line excitation [80]. Thus, if a Raman process occured the PL should be a wavelength-dependent process. In pulsed regime, anti-Stokes PL behaviour is explained but the model fails to explain the Stokes emission [147]. Moreover, the PL lifetime should be ~ fs (the order of pulsed laser excitation), not ps (as observed), in which e-p scattering takes place [148]. Though, measurements [149] show that a real state come into play and not a virtual state like it should be in Raman scattering (with an ultrashort lifetime). Furthermore, the blue shift of the PL compared to the scattering spectrum cannot be explained in Raman processes.

On the contrary, it is still unclear why the Stokes part is linear and the anti-Stokes part is non linear [131]. Indeed, the TPA generates hot electrons that could couples strongly to phonons yielding to a more than one non linear order in the Stokes part which is not clearly observed due to the linear absorption covering such process. Though, according to the incandescent black-body emission, there is no contradiction [130].

Finally, the broadband luminescence of Au NPs still intrigues and most probably further insights are needed to understand the underlying physics. The PL depends strongly on the irradiance, continous wave (c.w.) or pulsed laser excitation, the NPs' material and shape, and care must be taken to the substrate used (should be background free). The non linear PL sensitivity to all these parameters explains why such a number of experiments find disparate results explained by different models. This PL is the convolution of the allowed transitions permitted and the PDoS of the LSP. The emitted PL is then defined by the LSP resonance, not the excitation wavelength, with intraband and interband transitions and Auger process. Finally, hot carriers are efficiently enhanced by surface plasmons compared to bulk metal direct excitation. If one wants to use hot carriers to applications, one needs to extract them at their boundary before any relaxation path is being engaged by such hot carriers.

### 1.2.3 Extraction of hot electrons by a semiconductor

To build applications, there are several ways to extract hot carriers: either by adding a potential barrier to select a kind of carriers (the hot ones) or with a chemical reaction to be enhanced nearby the NPs surface [10]. In this study we will focus only on the potential barrier. By carefully choosing a metal and a semiconductor or an insulator (e.g. an oxide), a potential barrier is formed at their interface. Furthermore, when a photon, with an energy $h\nu$, is impinging on a metal-semiconductor junction, if the semiconductor has an energy bandgap $E_g > h\nu$ the photon will not be absorbed by the semiconductor. Since we only want the metal to absorb photons and not the semiconductor (or at least not by direct one photon absorption), the energy bandgap $E_g$ of the semiconductor has to be higher than the photon energy. However, once carriers have been generated within the metal and transported, they need to fulfill certain conditions to overcome the potential

barrier. In order to increase the capacities of the device, the probability for hot carriers to get over the barrier has to be maximized. This approach permits the integration in optoelectronic miniaturized devices.

### Schottky barrier

In order to design applications exploiting metallic plasmonic structures, those are brought nearby a semiconductor. A metal-semiconductor interface yields a Schottky barrier and I will present the main characteristics in this section.

The metal is characterized by its work function $W_m$ [150] and the semiconductor by its electron affinity $\chi_{sc}$ (Figure 1.11). When a metal and an n-type semiconductor are in contact, the Fermi levels equilibrate and a potential barrier is created, also called the Schottky barrier [133, 151]. If the semiconductor is a p-type semiconductor, an Ohmic contact is created (contact with a small resistance). At first order, for the case of $W_m > \chi_{sc}$ and $E_{F,m} < E_{F,sc}$, the height of the Schottky barrier is calculated by the Schottky-Mott rule

$$-e\phi_B = W_m - \chi_{sc}. \tag{1.11}$$

This model is referred to as the Schottky limit or the abrupt approximation. Within this model the barrier height does not depend on the applied voltage bias.

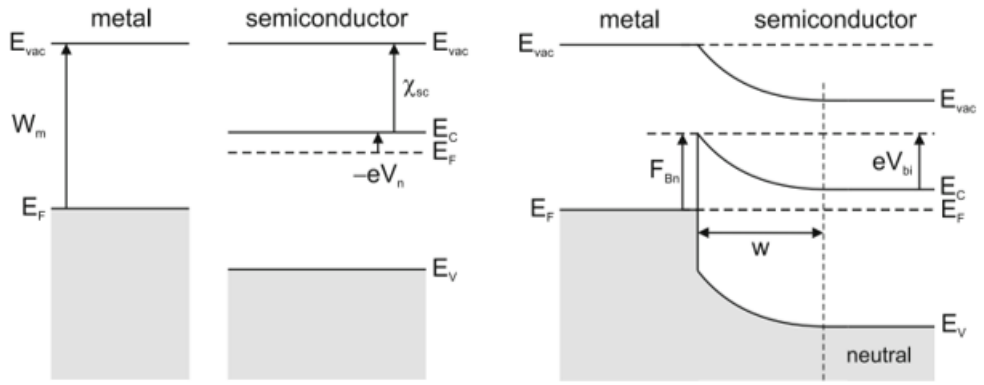


Figure 1.11: Energy band diagram of a metal-semiconductor junction. a) When the metal and the semiconductor are distant. b) When the metal and the semiconductor are brought together. Taken from [151].

However, if the semiconductor has a high density of surface state, the Fermi level can be pinned and a band bending is present even without the presence of a metal [152]. The semiconductor is then insensitive to the metal. This effect is called Fermi level pinning and modify the barrier height. Fermi level pinning can also arise via metal-induced gap states (MIGS) when the metal is in contact with the semiconductor [153, 154]. Moreover, the barrier height can be predicted more accuratly using a model based on interface dipoles [155]. This model is referred to as the Bardeen limit.

Another point to take into consideration is if an electron in the semiconductor is facing the metal. The equipotential metal surface acts as if there was a miror charge -q inside the metal. This effect is called the Shottky (or Image-force) effect and is lowering the Schottky barrier height [151, 156] by

$$e\delta\phi_B^{if} = e\sqrt{\frac{eE}{4\pi\epsilon_S}}, \tag{1.12}$$

where $e$ is elementary charge, E is the electric field and $\epsilon_S$ is the relative permittivity of the semiconductor. The barrier height depends then on the applied voltage bias.

There are mainly four techniques used to measure the Schottky barrier height [133]: current-voltage, activation-energy, capacitance-voltage, and photoelectric methods. According to a review [133], using these main techniques, the Schottky barrier height in a Au-Si junction is $\approx 0.83$ eV. The Ballistic-Electron-Emission microscopy (BEEM) technique is being used found a barrier height more accurately. Ref. 157 measured a value of $0.83 \pm 0.02$ eV using BEEM techniques in a Au-Si junction. All the measurements are specifying that the barrier height is strongly dependent on the pre and post surface treatment [158, 159].

The width $w$ of the depletion layer (or space-charge region) is solved from the Poisson equation considering a constant charge density within the depletion layer [133, 151]. In the Schottky-Mott model, the width of the depletion layer is

$$w = \sqrt{\frac{2\epsilon_S}{eN_D}(V_{bi} - V_{ext} - \beta^{-1})}, \tag{1.13}$$

where $N_D$ is the doping density, $V_{bi}$ is the built-in voltage, $V_{ext}$ is the external voltage bias applied and $\beta = e/k_B T$. Within the abrupt approximation, the width $w$ depends on the doping and voltage bias being applied.

By thoroughly choosing a metal and a semiconductor, one can tune the potential barrier depending on its application and wavelength. These pieces of information about Schottky barriers will be used to engineer a Schottky-based device later.

#### Emission over the Schottky barrier

When carriers reach the Schottky interface, only the ones with an excess of energy (*2nd condition to be satisfied*)

$$E_r > e\phi_B \tag{1.14}$$

have a probability to overcome the Schottky barrier (we neglect the tunnel effect across the barrier). The excess of energy $E_r$ will be framed between: $0 < E_r < h\nu$. If a high number of photons are impinging onto the metal, one can fairly assume that a uniform energy distribution $E_d$ of carriers is created.

Moreover, we assume that carriers are generated with an isotropic distibution of momenta. However, only the orthogonal component momenta of carriers with an associated kinetic energy higher than $\phi_B$ can get over the barrier [112, 118]. [118] argues that only the excess of energy $E_r$ is kinetic energy. The momentum $k_r$ of an electron corresponding to the excess of energy $E_r$ with a given angle of incidence $\alpha$ (Fig. 1.12.a) on the Schottky barrier wall have to fulfill (*3rd condition to be satisfied*)

$$\frac{(\hbar k_r \cos\alpha)^2}{2m} > \phi_B. \tag{1.15}$$

A sphere of radius $k_r$ (Fig. 1.12.b) represents all the possible momenta of hot electrons generated. Only carriers with a momentum greater than $k_{min} = \sqrt{2m\phi_B}/\hbar$, within the solid angle of an angle $\Omega$ can overcome the Schottky barrier (grey scaled in Fig. 1.12.b) and maximal momentum $k_\Omega$ with angle $\Omega$ . In the litterature, the condition of momentum is referred to as the escape cone (but should more be described as an escape cap as in Ref. [160]). The probability of emission of carriers towards the conduction band of

the semiconductor is then given by the ratio between the volume included with the solid angle $\Omega$ for $E_r > \phi_B$ and the volume of the k-space sphere $\Omega_k$ of all possible momenta

$$P_e(x) = \frac{\Omega_S(E_r > e\phi_B)}{\Omega_k}. \tag{1.16}$$

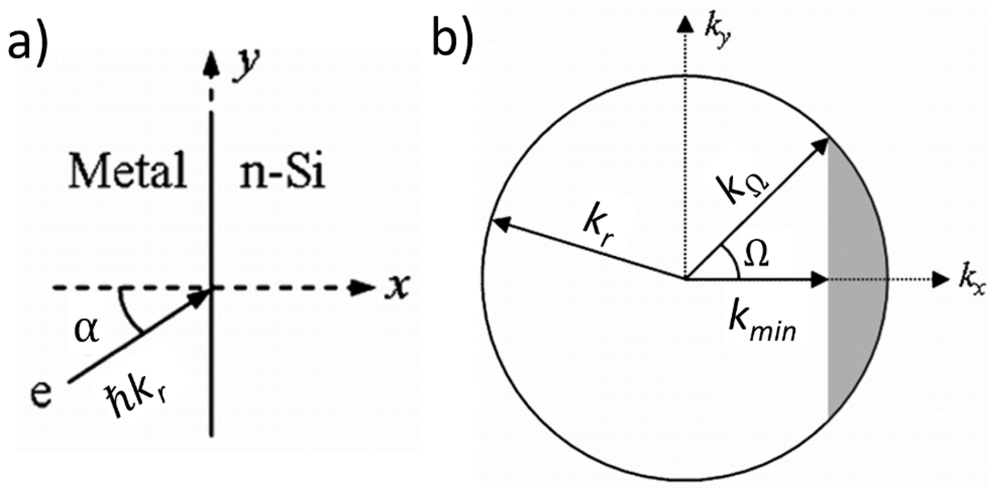


Figure 1.12: Momenta of generated hot electrons (extracted and modified from [118]). a) Angle α of the momentum compare to the Schottky barrier wall. b) K-space sphere of radius $k_r$.

This model allows one to know, for a plasmonic Schottky device, the probability of an electron in the metal to be emitted over the Schottky barrier. The external quantum efficiency (EQE)[1] of such a device can then be estimated depending on the geometry of metal (film, NPs, grating or waveguide) and taking into account the multiple reflections over the walls. The same process can be depicted with a p-type semiconductor with hot holes generation and emission towards the semiconductor. Care must be taken that the mean free path of hot holes can be different than for hot electrons.

**Transport of hot carriers within the semiconductor**

If a carrier have succeeded in overcoming the Schottky barrier and have reached the conduction band of the semiconductor, carriers will flow through the semiconductor to reach the contact electrode. By applying a voltage bias between metallic electrodes, an electric field is present within the semiconductor. The carriers will flow on a time $t_{drift}$ for a distance between electrodes $d_{elect.}$:

$$t_{drift} = \frac{d_{elect}}{\mu_c E}, \tag{1.17}$$

where $\mu_c$ ($cm^2/V/s$) is the mobility of the carrier (usually different between electrons and holes), which depends on the doping of the semiconductor and the temperature T, E (V/m) is the electric field applied. For example, for an electron travelling over a distance of 1 µm within a crystalline n-Si ($\mu_{Si,e}$ = 1400 $cm^2/V/s$) with a voltage bias of 1 V (i.e. $E = V/d_{elect.} = 10^6$ V/m), we obtain a $t_{drift}$ = 7.14 ps.

To sum up, three conditions must be fulfilled for carriers to overcome the Schottky barrier: a) carriers have not to experience any scattering during transport from where

[1]External Quantum Efficiency (EQE): ratio between the number of eletron extracted and the number of photon impinging on the photodetector

they are produced to the interface, b) carriers need to have sufficiently high energy to get over the barrier and c) carriers must not have too high angle of incidence or they will be reflected. The semiconductor material could be a drawback due to its low carrier mobility and reduce the device speed in Si. The criterions presented above will be discussed and taken into account for the design of our devices.

## 1.3 Photodetectors

Due to their sub-bandgap absorption and short lifetime properties, hot carriers devices are advantageous in photodetection technologies [10, 161]. Indeed, photodetectors are one of the key components in communication chains. Photodetectors convert an incident electromagnetic wave into a current. Nowadays, optical communications use mainly Near-Infrared (NIR) light from 1.3 to 1.65 µm. Hence, I will focus in this section onto high-speed photodetectors in the NIR. The ideal photodetector would have a high responsivity (~A/W), a fast response (>100 GHz), low noise (<nA), and small active area for integration purposes (~ µm). It would also be easy to fabricate at low cost, low power consumption, high reliability, CMOS-compatible and not bulky. Combining all these qualities in solely one photodetector is a real technological and scientific challenge. The best specifications depend on the application one wants to achieve.

The main challenge of nowadays photodetectors is to generate carriers wih high efficiency and keep a high speed, leading to a trade-off between quantum efficiency and bandwidth. Indeed, classical photodetectors present a bulky absorption part (enhancing their quantum efficiency) but drift-diffusion of carriers slows down the device. Therefore, reducing the absorption volume, e.g. in surface plasmon devices, is a very attractive strategy for speed enhancement. For such an aim, plenty of strategies are set: different materials, creative designs, multilayered effects just to mention a few. Rogalski in its infrared photodetector review [162] presents the Norton theorem [163]: "All physical phenomena in the range of about 0.1-1 eV (1.24-12.4 µm) will be proposed for IR detectors".

A classical way to compare photodetectors is by using the responsivity, i.e. the electrical current generated compared to the incident optical power. The Internal Quantum Efficiency (IQE) is the ratio between the quantity of generated electrons and the quantity of photons actually absorbed by the device whereas the External Quantum Efficiency (EQE) is normalized by the quantity of impinging photons. To compare the speed of photodetectors, the -3 dB cut-off frequency is the main used parameter, i.e. the frequency at which, for an amplitude modulated incident optical signal, the oscillating output current amplitude is divided by a factor of two.

Plasmon-enhanced hot electron metal components coupled with a Schottky barrier yield a valuable scheme to photodetectors and I will present the state of the art in the following. Later, I will compare such a strategy to commercially available photodetectors and current research approaches to push their speed further.

### 1.3.1 Plasmon-enhanced hot electrons Schottky photodetectors

Historically, the first idea to use hot carrier-based photodetectors was with a thin metallic film [164] in order to enhance the probability of carriers to overcome the Schottky barrier. Within the skin depth of the metallic film, photons are absorbed and hot carriers are created. The mean free path $l_{MFP}$ of generated hot electrons is much longer than the thickness $t$ of the film. A high number of reflections on the film interfaces increases the probability of an electron to be extracted by the semiconductor. [118]. These carriers are

usually treated as ballisitic with Monte-Carlo simulations [165]. This kind of device is referred to as a thin-film Schottky barrier detector. However, a thin layer also possesses poor absorption properties, limiting the number of generated carriers and the photodetector efficiency.

Surface plasmons are then a valuable approach to enhance the absorption in the metal. Plasmon-enhanced hot electrons Schottky photodetectors are composed of a plasmonic metallic junction close to a collection part (a semiconductor or an oxide/insulator). Following the previous explanations, I present here the most common one with a semiconductor. Fig. 1.13 depicts the photocurrent generation of a plasmon-enhanced hot electron device in a 3 steps process: 1) the generation of hot electrons, 2) their transport from the metal towards the Schottky interface and 3) their emission over the barrier. If the absorption is not enhanced by surface plasmon, the phenomenon is referred to as Internal Photon Emission (IPE). The modified Fowler theory [166] estimates the efficiency of such IPE process as [167, 168]

$$\eta \approx C\frac{(h\nu - e\phi_B)^2}{h\nu}, \tag{1.18}$$

where $h\nu$ is the incident photon energy, $\phi_B$ is the Schottky barrier height and C is the quantum emission coefficient (empirical parameter). The emission of carriers depends only on their photon energy compared to the Schottky barrier height. With a surface plasmon resonance, the output spectral response based on the Fowler theory is modulated by such a resonance. A fourth step is the carriers drift through the semiconductor towards the electrode of collection (Ohmic contact). For this electrode, the carriers are electrons. As presented in the last sections, when surface plasmons decay, hot carriers can be excited. If a Schottky barrier interface is not too far from the generated carriers (< 70 nm, see Sec. 1.2.2) and if they satisfy the conditions to overcome the barrier, carriers can be injected and collected by the semiconductor.

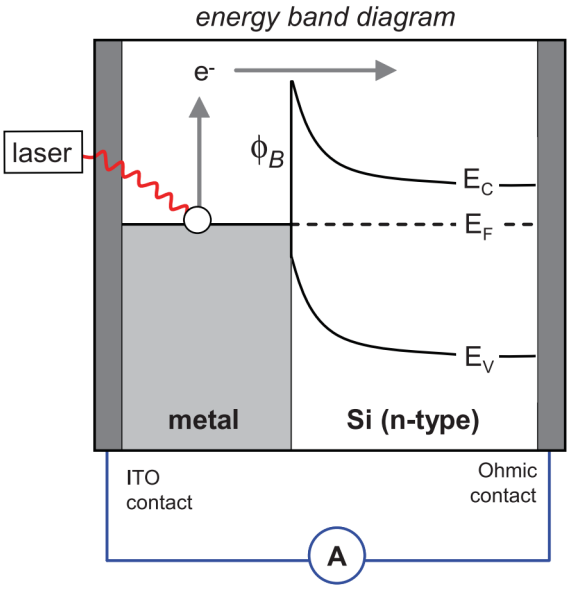


Figure 1.13: Principle of photocurrent generation by internal photon emission (IPE) with a Schottky barrier (extracted from [167]).

The main advantage of such a process is to permit sub-bandgap absorption and has been extensively studied. Indeed, in this kind of detector, the absorption wavelength is limited by the Schottky barrier height and not anymore by the semiconductor's bandgap.

Furthermore, the low absorption volume highly reduces the drift-diffusion of carriers allowing for high speed schemes. Such a process can also be applied to photovoltaic solar cells in order to enhance their photocurrent [82]. Plenty of strategies have been explored: different materials, geometries, wavelengths. I present here a classification based on the physical process involved: with propagative SPPs, LSPs, grating, metamaterials, tunnel-junctions and with graphene coupling.

**SPPs** In order to confine the incident light, a propagative SPP is used and excited carriers are collected by the nearby semiconductor. Early works by the end of the 1980s [169, 170] excited a SPP with a prism coupler on a thin metal film on GaAs. Selecting the angle of incidence under Otto configuration [63], at which SPPs were launched, Ref. 170 found a 10 to 20 times increased IPE.

A patent deposited in 2006 by Scales and Berini [171] describes the plasmonic Schottky barrier detector followed by an article in 2010 [172]. Scales and Berini developed a plasmonic $CoSi_2$ waveguide embedded into p-Si to support propagative SPP and enhance IPE (symmetric geometry). In 2010 in the same team, Akbari et al. developed a Au plasmonic waveguide on top of n-Si in order to confine light further and enhance light-matter interactions [173]. A responsivity $R_p$ = 1 mA/W at 1280 nm was obtained. A further improvement was made by Berini et al. [174] with Au plasmonic waveguides on p-type Si by using hot holes injection instead of hot electrons (Fig. 1.14.a). There are two Schottky barrier interfaces (because of embedding), increasing thus the emission probability of hot carriers above the barrier. These tips rise the responsivity to $R_p$ = 1 mA/W at 1550 nm for telecom applications.

Goykhman et al. [175] used a plasmonic Au waveguide with the Local-oxidation of silicon (LOCOS) technique on silicon on insulator (SOI) ($R_p$ = 0.25 mA/W at 1550 nm). This device has the strong advantage to be easily implemented in CMOS chains. They further improved their device by smoothing the rough surface at the Schottky barrier interface [176] reaching interesting responsivity of 12.5 mA/W at 1550 nm.

Finally, Muehlbrandt et al. used a plasmonic waveguide with Au and Ti with a 100 nm width nanostripe of Si in between [177]. This device yields a bandwidth > 40 GHz and $R_p$ = 0.12 A/W at 1550 nm, which is competitive compared to existing photodetectors.

**LSPs** For the purpose of increasing light-matter interactions, LSP resonances confine even more light than in SPP and Au nanoantennas have been an attractive approach. The absorption cross section is then increased above the geometrical cross section of nanoantennas. Furthermore, shaping the width, length and thickness of nanoantennas, one can tune the absorption resonance of LSPs. Nishijima et al. [178] have used Au nanoantennas on top of $TiO_2$ with reponsivity $R_p$ = 71 mA/W (at 1100 nm). Au nanoantennas on Si were studied by Knight et al. [167] (Fig. 1.14.c) and reached a $R_p$ = 3 µA/W (at 1550 nm). Other types of LSPs have been used like Au spherical NPs embedded into $TiO_2$ increasing the photoconductance ($R_p$ = 9 µA/W at 600 nm) [179], a plasmonic Au pyramidal shape [180] ($R_p$ = 30 mA/W at 1064 nm) or Au nanoislands on $TiO_2$ ($R_p$ = 10 mA/W at 600 nm) [168].

In order to increase the probability of hot carriers to overcome the Schottky barrier, Au nanostripes with a LSP resonance have been fully embedded into Si (increasing the extension of the Schottky barrier interface) [181]. 25 times higher responsivity has been observed compared to non-embedded nanostripes. Other improvements have been made by adding SPP, cavity enhancement and by increasing the area of the photodetector [182] ($R_p$ = 150 µA/W at 1550 nm).

To my knowledge, there is no bandwidth measure of hot electrons LSP Schottky photodetectors in the literature.

**Plasmonic gratings** A plasmonic grating is composed of nanostripes close together yielding a coupling between them. Indeed, by shaping the width and the periodicity, one can enhance the absorption resonance at a selected wavelength in Au by coupling LSPs and grating effects. Initial works in 1985 by Brueck et al. [183] developed a grating of Au on InP for enhancing the IPE process. Such a device, at resonant angle and wavelength, gives 30 times higher responsivity. Sobhani et al. [184] used a Au grating on top of n-Si in an Extraordinary Optical Transmission (EOT) scheme (deep high filling factor grating with vertical resonance [185]) strongly enhancing the responsivity ($R_p$ = 0.6 mA/W at 1500 nm) of a surface plasmon Schottky photodetector.

Further improvements with plasmonic metal-insulator-metal (MIM) gratings [186,187] provide better absorption in the metal compared to conventional gratings. Indeed, here a plasmonic grating is placed onto a thin layer of insulator giving a potential barrier (of $Al_2O_3$ or ZnO) for the extraction of hot carriers. [186] reached a high responsivity of $R_p$ = 6 A/W at 400 nm (Fig. 1.14.d). Other progresses have been made by integrating a metallic grating in between Si channels, increasing the probability of emitted carriers [188] and producing a responsivity of ~ 0.1 mA/W. In such a structure the grating is highly spectrally selecting compared to conventional gratings. Tanzid et al. [189] combined the enhancement of IPE due to the grating and Free Carrier Absorption (FCA). Such a device made of a Pd grating on p-Si yields a $R_p$ = 1 A/W at 1375 nm.

**Metamaterials** If plasmonic elements are sufficiently close with each other and interact together, such structures are referred to as metamaterials or metasurfaces. Metamaterials can reach perfect absorption (near unity EQE) and can be tuned to a selected wavelength. Li et al. [190] fabricated a metamaterial of 2D Au square resonators on n-Si (see Fig. 1.14.e). The advantage of this device is to be insensitive to polarization and yields $R_p$ = 1.8 mA/W from 1200 to 1500 nm. The same team has developed a plasmonic Schottky metamaterial capable to detect circularly polarized light [191].

**Tunnel junction** Hot carriers excited within a surface plasmon NP can be emitted through an insulator. Indeed, if the insulator is sufficiently thin, carriers can tunnel through it. Wang et al. [192] developed a Au-alumina-Au photodetector and demonstrated a power conversion efficiency 40 times higher compared to conventional MIM. This device was first demonstrated for photovoltaic solar cell applications and MIM has the advantage of being easy to fabricate. Using this process, Atar et al. [193] have fabricated a Au NP device for light harvesting on an insulator layer of $Al_2O_3$ and Au ($R_p$ = 8 µA/W at 800 nm).

**Plasmonic Graphene photodetector** Due to its high mobility carrier property, graphene is a very attractive area for ultrafast applications [194]. Fang et al. [195] combined the hot carrier emission from Au plasmonic nanoantennas to the conduction band of graphene and plasmon-enhanced excitation of intrinsic graphene electrons (see Fig. 1.14.b). The plasmon resonance is actually determined by a cluster of Au nanoantennas with a Fano resonance. Extracted hot carriers then take advantage of the high transport property of graphene. The device yields 800% enhancement of photocurrent compared to the device without nanoantennas and $R_p$ = 13 µA/W at 950 nm. Moreover, Shen et al. [196] used a metal-insulator-graphene structure. In this structure the IPE is enhanced by plasmonics and carriers jump over or tunnel the insulator layer towards graphene.

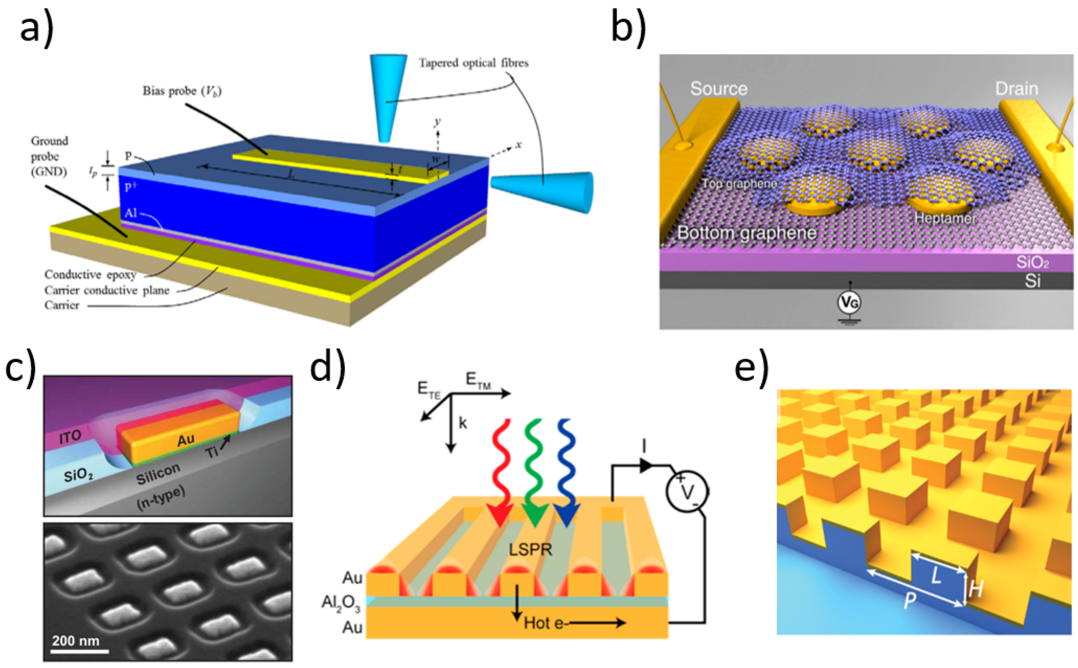


Figure 1.14: Plasmon-enhanced hot electrons Schottky photodetectors. a) Plasmonic waveguide on p-Si substrate excited by tapered optical fibers [174]. b) Plasmonic gold heptamer sandwiched between two monolayer graphene sheets [195]. c) Gold nanoantennas onto n-Si with scanning electron microscope image [167]. d) Grating metal-insulator-metal (MIM) photodetector [186]. e) Metamaterial of squared resonators perfect absorber [190].

### 1.3.2 Strategies to enhance the photodetector speed

In the last section, we have seen that plenty of approaches are exploiting the physical process of palsmon-enhanced hot carriers. However, drawbacks comes into play for the industrialization of such a process, since these devices present generally low quantum efficiency and they are using mainly metals which are expensive and difficult to introduce in semiconductor processes e.g. in chemical vapor deposition. To my knowledge, no such device is using in industry lines for photodetectors at the moment.

Since the discovery of infrared light by Herschel in 1800 [197], plenty of NIR detectors have been developed with very different physics. Indeed, different processes allow to detect IR light and convert photons towards electronic processing. The first known NIR detectors were based on thermal effects. Indeed, NIR light heats a structure (absorber) and a transducer measures the elevation of temperature, even very accurately. Seebeck's thermocouple (1821), Nobili-Melloni's thermopile (1833), Langley's thermistor bolometer (1880) and up to nowadays research, are long response time devices (µs to ms) [162, 198]. One of the main NIR photodetector issue is the low photon energy involved that can compete with thermal noise. Other NIR photodetectors were developed with different physics based on gas expansion (Golay cell) [199] or pyroelectric effect [200] but still are not able to reach the 100 GHz bandwidth. A very nice work on Superconducting Nanowire Single Photon photodetector (SNSPD) reached ~ ps response time [201]. Though, SNSPDs need to be cryogenically cooled with bulky systems and are very costly.

At present, the main commercially available high speed photodetectors are based on electron-hole pairs (EHP) generation in semiconductors [21]. In reasearch, there are other plasmonic strategies, compared to the hot carriers one, mainly by enhancing a nearby

physical process, usually the EHP generated in a close by semiconductor [202]. Other remarkable strategies use low-dimensional materials to confine the incident light or quantum dots [203]. This section will compare our approach with those strategies and will be divided into 3 parts: a) the classical strategy commercially available i.e. mainly semiconductors technology, b) the plasmonic strategy enhancing the processes and c) other approaches under reasearch to build ultrafast photodetectors.

**a) Semiconductor photodetectors**

Infrared (IR) semiconductor photodetectors classically operate by converting incident light wave into a current by the photoelectric effect i.e. the emission of an electron by the absorption of a photon. The first photoelectric effect was discovered in 1873 by Smith in selenium and the photoemission effect in 1887 by Hertz. Up to the end of the second world war, IR detectors have been strongly developed mainly for night vision applications: photocathodes of Cs-O-Ag in vacuum tube (in the US) and photoconductive thin films of PbS (in Germany) [162]. Later, in the 1950s, a lot of research was made on shaping the bandgap of semiconductor alloys (HgCdTe, InAsSb and PbSnTe) in order to detect IR light at the desired wavelength. Nowadays, at telecom wavelengths, semiconductor PIN and APD photodiodes are very much used commercially and studied in research. Indeed, they fulfill high speed detection requirements. I will present the PN/PIN and APD photodiodes before the MSM photodetectors. Later, intrinsic and sub-bandgap absorption will be depicted. Last, I will discuss the coherent detection used in telecommunication applications to enhance the bandwidth.

**PN and PIN photodiodes** PN and PIN photodiodes are based on the direct absorption of photons and are referred to as intrinsic photodetectors. A PN junction is built with a p-doped semiconductor brougth into contact with an n-doped semiconductor, creating a depletion layer in between with a doping dependent width [20]. The depletion layer is empty of free carriers and with a strong built-in electric field. The mechanism is an interband absorption within the depletion layer of the semiconductor creating an electron hole pair (EHP). Generated electrons drift to the n part (inversely to the p part for holes) due to the presence of the electric field [20].

The bandwidth of a PN photodiode is mainly limited by the carrier transit time $t_{\text{trans}}$, which is due to the drift of carriers from where they are created within the depletion layer and their diffusion through the undepleted region towards the electrode of collection. Indeed, under a large electric field, carriers drift at a certain speed $v_d$ depending on the electric field and can reach a saturation velocity $v_{sat}$.

$$t_{\text{trans}} = \frac{d_{\text{elect}}}{v_d} \tag{1.19}$$

with $d_{\text{elect}}$ the distance between electrodes. The diffusion of carriers generated by absorption of photons outside the depletion layer also limits the bandwidth. Carriers can then diffuse and be collected. Though, the diffusion is a very slow process and yields a long tail in the response time. Moreover, the carrier trapping effect reduces the bandwidth when the p and n doped parts are distinct semiconductors with a large bandgap difference i.e. an heterojunction. Carriers are then trapped at the heterojunction interface and are slowed down. Moreover, PN photodiodes have a RC time constant which also gives a bandwidth physical limit [21].

PIN photodiodes reduce the diffusion issue by diminishing the width of the p and n parts of a PN junction, and sandwiching an undoped semiconductor in between called

the i layer (for intrinsic). The depletion layer is then throughout the i layer with a high electric. If the i layer thickness is increased, the responsivity increases as well but the bandwidth diminishes. In fact, depending on the application pursued, a trade off has to be done between responsivity and bandwidth. The bandwidth limitations of PIN photodiodes are also due to the phenomemons presented above for PN photodiodes. For high-speed applications PIN photodiodes are prefered to PN junctions because of lower diffusion outside the depletion layer. In 1995, a PIN photodiode reached 110 GHz bandwidth with a GaInAs/InP double heterostructure [204]. To enhance the quantum efficiency, researchers used a Fabry-Perot cavity made of Bragg mirors over the GaAs PIN photodiode (QE $\approx$ 1) [205].

The main advantage of plasmon-enhanced hot carrier Schottky photodetectors compared to PN/PIN photodiodes is the absorption volume in the metal itself. Due to the small volume of NPs, the generated carriers are not limited by drift-diffusion. The bandwidth is highly enhanced while keeping a correct quantum efficiency.

To improve the photodiode capabilities the incident light has been coupled to an optical waveguide (by edge coupling) made of PIN layers (called waveguide photodiode, WGPD). Indeed, light is coupled within a small cross section, which reduces the RC constant while keeping a high quantum efficiency. A mushroom-mesa waveguide photodiode has reached 110 GHz bandwidth with $\tau_{RC} \approx 1$ ps for a 12 µm long waveguide [206]. In order to avoid impedance mismatch between the photodiode and the load, Travelling Wave (TW) photodiodes have been developed. Indeed, a TW photodiode is a WGPD in which the electrode is designed to match the external load, avoiding electrical reflection and reducing the RC constant. [207] reached 172 GHz bandwidth. Last but not least, in 1997 the uni travelling carrier (UTC) PIN photodiode has been developed in which only electrons are used for transport, not holes [208]. Electrons are generated in the absorption part (p-type) as minority carriers, and yield non-equilibriuum quasi balistic transport within the collection part. This strongly reduces the carrier transit time $t_{trans}$. 310 GHz bandwidth has been reached with UTC photodiodes [209]. Some works have also mixed UTC and TW photodiode concepts yielding 115 GHz bandwidth [210].

Due to their versatility and low fabrication cost processes, PN/PIN photodiodes are commonly used in laboratories. Progresses in PN/PIN photodiodes permit to reach above 100 GHz bandwidth and are very attractive in research, industry and telecommunications.

**Avalanche Photodiodes (APD)** In order to enhance the responsivity of PIN photodiodes, generated carriers are amplified through an additional part called multiplication layer placed between the i and n parts [20]. The primary EHPs are generated within the i layer and drift towards the multiplication layer (p type) where the secondary EHPs are generated. Moreover, in the multiplication layer, there is a high electic field. Primary carriers give their kinetic energy to carriers in the valence band, which creates many EHPs. This effect is called impact ionization and is represented by its impact-ionization coefficients: $\alpha_e$ for electrons and $\alpha_h$ for holes (1/cm).

The APD bandwidth is also submitted to the physical limitations of PIN photodiodes. Furthermore, generating secondary electrons leads to additional transit time, hence reducing the bandwidth. The multiplication factor M is usually used to express the increasing number of electrons: a high value of M then limits the bandwidth. Thus, a trade off has to be done between the multiplication factor M and the bandwidth. The APDs process of multiplication is fundamentally noisy. Indeed, secondary generated carriers participate to shot noise while the thermal noise is unchanged since it is due to the external circuit.

In some semiconductors, a tunneling breakdown occurs for an electric field below

the one for avalanche processes to occur. The tunneling breakdown is reduced by making a heterojunction between the i layer and the multiplication layer, which is referred to as separate absorption and multiplication (SAM) APDs. Though, if the band gap of the nearby heterojunction is too large, carrier trapping effects will slow down carriers, limiting the bandwidth. This effect is reduced by placing a graded layer [211] (100 GHz bandwidth) plus a charged layer [212].

In order to enhance the speed of APDs, a strategy to reduce the aborption layer and keep a high quantum efficiency is to use cavity enhancement (i.e. Fabry-Perot resonances). 290 GHz gain-bandwidth (GB) product was reached with a 60 nm thickness [213]. A second strategy is to use an optical waveguide [214], which reached 180 GHz GB product. The UTC principle, presented for PIN photodiodes (sec. 1.3.2), has also been applied to APDs [215] (GB product of 840 GHz). Due to their high sensitivity, APDs are used as single photon detectors.

The advantage of APDs compared to plasmonic Schottky photodetectors is their high sensitivity but the APD multiplication layer reduces inherently the speed of such devices. The UTC scheme in APDs allows then to highly improve their speed.

**Metal-Semiconductor-Metal (MSM) photodetectors** A MSM photodetector is composed of a semiconductor in between two metals, thus there are two Schottky barriers (see Sec. 1.2.3). A fundamental absorption of light takes place within the semiconductor and the generated EHPs drift towards the electrodes. Indeed, a bias voltage is usually applied in between the two metals. Wrapping two metals over a semiconductor is difficult but interdigitated metal devices are a convenient and usually preferred fabrication strategy.

The interdigitated MSM offers a low capacitance, thus a large bandwidth is expected. Large metal pads yield low reponsivity because of the reflectivity of metal in the NIR. To overcome this limitation, MSM photodetectors are back illuminated [216], when possible, or use transparent contacts made of ITO (indium tin oxide) or CTO (cadmium tin oxide) [217]. Large metal pads increase the capacitance, decreasing the bandwidth. Increase the space between metal pads increases the responsivity, by having a higher semiconductor area available, but also increases the transit time of carriers (decreasing the bandwidth). Hence, a trade off between responsivity and bandwidth needs to be done.

In order to reduce the dark current of MSMs, a strategy consists in adding a thin insulating layer, thus increasing the Schottky barrier height. This layer is called the Schottky enhancement layer (SEL). 4 GHz bandwidth was reached with a low dark current density of $5.6 \times 10^{-5}$ A/cm$^2$ [216]. A MSM photodetector reached 100 GHz bandwidth with Au interdigitated on GaAs [218]. The travelling waves TW scheme presented for PIN photodiodes has also been adapted for MSMs (called MSM-TW photodetector) and reached ultrahigh bandwidth of 570 GHz on GaAs [219].

In plasmonic Schottky barrier photodetectors, the absorption layer is the metal. On the contrary, in classical MSM photodetectors, the semiconductor is the absorption layer and the metal pads serve only as the collection electrodes. Due to their low RC constant, MSMs are very attractive for high speed photodetectors, reaching above 100 GHz bandwidth.

**Other types of intrinsic absorption** A lot of different geometries use fundamental absorption and drift of carrier towards a collection region. I present here the most important ones.

A Metal-Insulator-Semiconductor (MIS) detector consists of a thin insulator layer (usually an oxide) between a metal and a semiconductor [220]. EHPs generated in the semi-

conductor drift and tunnel through the insulator. If the layer is sufficiently thin, then an acceptable current is collected. An optical receiver made of MIS has reached 300 MHz bandwidth with a 2 nm thick silica layer on Ge [221]. MIS devices are promising with a thin layer of semiconductor, reducing the carrier transit time (like Ge-on-Insulator systems) [222].

A MISIM photodetector is made of Metal-Insulator-Semiconductor-Insulator-Metal layers and is fabricated by adding a thin layer of insulator between the metal and the semiconductor of an interdigitated MSM device. The main advatange of such a structure is to reduce the dark current of MSMs (which is usually high). Ref. 223 has reached 13 GHz bandwidth with a thin dielectric film on InGaAs.

**Semiconductor sub-bandgap absorption** In order to absorb light at an energy below the band gap of a semiconductor, defects can be implanted on purpose in the semiconductor [224]. Discrete levels are then created whithin the bandgap and allow mid-bandgap absorption (MBA) or defect-mediated absorption. A MBA photodetector at 1550 nm have reached 20 GHz made of Si+ implantation and annealing [225].

Another strategy for sub-bandgap absorption is to use surface or interface states [224]. Due to the abrupt end of the crystalline bulk structure, some of the electrons' wave function are bound with discrete energy out of the interface for $\sim$ 1 nm. These states can be used to absorb light in the NIR and the process is referred to as Surface-state absorption (SSA). To enhance the SSA, Ref. 226 optimized the optical mode of a waveguide at the surface. Up to now, as for MBAs, SSA is a promising strategy to enhance the speed of photodetectors.

Two photons can also be absorbed at the same time by an electron, the energy sum of the two photons corresponding to the absorbed energy (two-photon absorption, TPA). EHPs generated by TPA then diffuse towards the collection electrodes. The main drawback of such a strategy is its small efficiency, thus one needs to find a way to confine light and enhance light-matter interactions. Inherently, the EQE will be at maximum 0.5 because two absorbed photons yield one electron. Ref. 227 developed a TPA photodetector made with a photonic crystal (PhC) cavity and reached sub-GHz bandwidth. In order to amplify the generated carriers (because of the low efficiency of TPA), another strategy has been to employ an APD scheme [228]. A $\sim$ ps scale autocorrelation trace was measured on the TPA photodetector and is encouraging for GHz/THz photodetection.

**Coherent detection** A technique commonly used to reduce the thermal noise is the coherent detection. A local oscillator generates a stable optical frequency at $\omega_{LO}$ (a laser) and is combined (coherently) to the optical signal to detect on the photodetector at a frequency $\omega_s$. The signal optical power is amplified by the optical power of the local oscillator. The SNR of the receiver is then increased. Coherent detection permit also to recover the phase of the optical signal. It can be homodyne with $\omega_{LO} = \omega_s$, (SNR two times larger) or heterodyne with $\omega_{LO} \neq \omega_s$ (SNR four times larger). These techniques are used to decode the phase in optical communications and to improve the bandwidth. Some developed intergrated circuits contain the coherent detection thereon [20].

In conclusion, PN/PIN, APD and MSM are the main used semiconductor photodetectors. Other interesting physical processes permit attractive high-speed IR photodetectors such as MIS, MBA, SSA or TPA based photodetectors. But, to my knowledege, in bulk semiconductors: only PIN photodiodes, APDs and MSM photodetectors have reached 100 GHz bandwidth and above. Therefore, semiconductor photodetectors compete with plasmonic Schottky photodetectors in terms of responsivity and speed.

### b) Plasmonic photodetectors

Other types of plasmon-based photodetectors exist, since by their own properties, surface plasmons strongly localize the electromagnetic field and enhance nearby processes. Indeed, Fig. 1.15 sums up the different kinds of plasmonic photodetectors. The enhancement of hot carrier generation has been presented previously (right part). This section will focus on the semiconductor type (left part) and the different schemes in which surface plasmons can enhance photodetection. Such photodetector type produces more carriers within the absorber which can be a semiconductor waveguide, a graphene layers or quantum dots (QDs). The surface plasmons can be a LSP, a propagative SPP or a plasmonic grating. Plasmonic photodetectors are adaptable to a huge number of applications. Actually, one can tune the resonance of the surface plasmons to the desired wavelengths. This process is also very studied in photovoltaic area in order to obtain a better efficiency of solar cells [82].

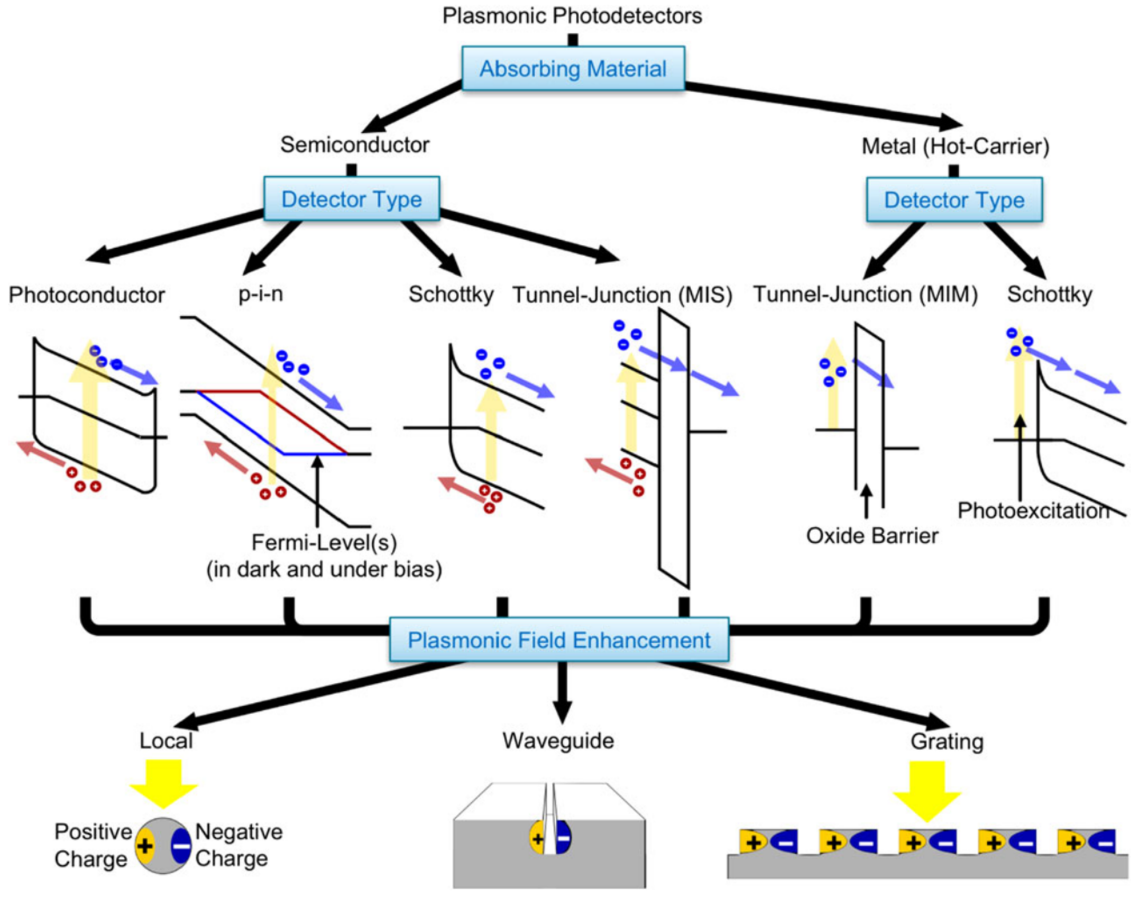


Figure 1.15: Plasmonic photodetector classification (extracted from Ref. 202)

The bandwidth of semiconductor photodetectors is mainly limited by the carrier transit time. Reducing the thickness of the depletion layer increases the bandwidth (but inherently reduces the responsivity). To overcome this limitation, Salamin et al. [229] have used a plasmonic waveguide made of two Au pads spaced by 160 nm in which there is a thin nanorod of Ge. Generated carriers come from interband transitions within Ge and the carrier transit time is strongly reduced (with a proper responsivity). This device has reached a high bandwidth of 100 GHz limited by their characterization set-up.

**c) Other approaches for photodetection**

Other promising technologies are used noawadays to push the boundaries of photodetector speed. Indeed, I have presented mainly photodetectors based on bulk semiconductor and surface plasmons metallic absorption. In order to enhance the capabilities of photodetectors, especially their speed, some approaches shrink the dimension of material yielding outstanding and emerging properties. Such photodetectors are made of 2D materials and quantum dots (QDs) and sometimes in combination with SPs to enhance their absorption.

2D materials are made of one or few atomic layers and thus usually cannot absorb enough light (for example graphene). Surface plasmons can enhance their absorption cross section allowing for 2D materials to have a better quantum efficiency and keep their outstanding properties. Ding et al. [230] have designed a metal-graphene-metal device enhanced by bowtie plasmonic antennas and reached 110 GHz bandwidth.

QD photodetectors are typically too thin to absorb light properly. On the other hand, a thin layer of QD is needed to keep a low dark current. Lee et al. [231] used a metalllic photonic crystal in which InAs QDs couple to SPP. This results in a 30 times higher sensitivity.

TPA is also a weak process, whose efficiency depends on the incident power. Indeed, a higher power leads to an increasing probability of TPA. Liang et al. [232] have developed a TPA photodetector for pulsed measurements. The main drawback is that the optical power input has to be high to work correctly.

Such plasmonics combination offers attractive concepts and permit to enhance low efficiency processes. Enhanced low dimension absorbing materials possess very low drift-diffusion time permitting to reach high bandwidth photodetection. Such devices offer a competing scheme with plasmon-enhanced hot carriers Schottky design.

To cite a few, low-dimentional material photodetectors without the combination of plasmonics are also very promising: graphene-based due to their high mobility carrier properties (128 GHz, [233]) and Transition Metal Dichalcogenides (TMD) for their tunability properties (300 GHz, [234]). Another strategy is to use superlattices made of type II (17 GHz [235]) and quantum wells for their low relaxation time (70 GHz [236]). Furthermore, strong light confinement occurs in photonic crystal-based (PhC) photodetectors and reached above 10 GHz bandwidth [237].

In conclusion, we have seen that ultrafast processing is a major issue in modern society. Ultrafast processes can be handled by surface plasmons and offer promisses for future applications in many areas. By proper design, hot carriers with their short lifetime are enhanced by surface plasmons. Such devices offer perspectives in photodetection schemes and are in competition with already existing approaches.

# Chapter 2

# Remote control of hot electron generation by propagative SPP in a Au waveguide

*" If the doors of perception were cleansed every thing would appear to man as it is, Infinite. "*

William Blake, The Marriage of Heaven and Hell, written 1790-1793

## Contents



This chapter will focus on hot electrons' generation after SPP propagation in a plasmonic device. Understanding and controlling the processes underlying hot electron production paves the way to develop efficient future hot electron devices. As presented in chapter 1, hot electrons are an out-of-equilibrium distribution of electrons with high kinetic energy. They can be efficiently generated by surface plasmons [145, 238]. The use of these carriers at the surface of nanoscale devices can improve the performance and lead to applications in many fields [10]: photovoltaics in solar cells [239], photodetection [167], photocatalytic hydrogen dissociation [83], and photosynthesis [240]. Up to now, the generation and relaxation of plasmon-enhanced hot electrons was mainly explored with localized surface plasmons (LSPs) [136]. In such nanoparticles exhibiting LSPs, hot electrons are produced and used at the same location where the optical excitation takes place. In contrast, to develop advanced hot electron devices, hot electrons

would need to be produced at a distance from the optical excitation, e.g. in nanocircuitry [241] or in remote chemical catalytic reactions [242]. The possibility to dissociate optical and electronic processes would for example limit the risk of damaging the elecronic part of the system by the strong optical flux. This chapter presents our work about the remote generation of hot electrons mediated by a propagative surface plasmons (SPP) with a plasmonic Au waveguide. We demonstrate that hot electrons can be produced at a distance of up to 12 µm from an optical excitation. If hot electrons are not extracted or do not take part into a chemical reaction, they relaxe in the metal. They can either relax by electron-phonon (e-p) interactions, which heat the device, or by emitting a photon by radiative recombination, giving indirectly precious informations about their own properties [136]. An advantage of using propagative SPPs is the possibility to dissociate the direct optically photoexcited carriers and the plasmonically generated carriers, which is difficult to do with LSP nanoantennas [105].

In order to excite efficiently the SPP along the waveguide, we designed a focusing grating coupler to couple the incident light to the SPP with Finite Element Method (FEM) simulations. Knowing the optimized parameters, the Au plasmonic waveguide has been fabricated using standard nanofabrication processes. To investigate the delocalized hot electron generation by the SPP along the waveguide, a far and near-field hyperspectral microscopy set-up was used, which provided new insights into the hot electron radiative relaxation process by nonlinear photoluminescence, a still controversial issue (see Sec. 1.2.2).

## 2.1 Propagative SPPs launched by grating couplers: principles and simulations

With the aim of increasing the number of hot carriers generated in metal, surface plasmons are interesting thanks to their ability to enhance light-matter interactions (see Sec.1.2.3). Until now, the processes underlying the generation and relaxation of hot carriers have been extensively studied with LSP resonant nanostructures: nanoantennas [109, 140], coupled nanoantennas [107], and metal-insulator-metal nanostructures [243]. However, only few works have investigated the remote hot electron generation via propagative surface plasmons exploiting e.g. nanotips (adiabatic focusing) [244–246], a nanoscale constriction [247], or nanowires [248, 249].

In this PhD thesis, we explore hot carrier production at a distance from the optical excitation via SPPs propagating on a plasmonic waveguide. To this aim, we use a Au waveguide with a length of 12 µm (Fig. 2.1). To efficiently generate electron-hole pairs, SPPs need to carry as much energy as possible. In order to couple incident light to the plasmons, we employ a focusing curved grating at one end of the waveguide (Fig. 2.1), which is illuminated by a collimated laser beam at oblique incidence. Since hot electrons are known to produce MPL [145], we follow indirectly their generation by analyzing the spatial behaviour of the MPL signal in such a device.

To achieve a high enough power propagating along the waveguide, we have used a femtosecond pulsed laser (Ti:Sapphire) with a wavelength of excitation centered at 820 nm. With the aim at increasing the probability of multiphoton (MP) absorption and then MP generation of hot electrons, a high optical peak-power is required. If the energy transported by the propagating SPP is sufficiently high, hot electrons generated by the SPP will recombine and emit MPL [108, 131, 141, 145, 149]. We then collect the MPL signal to probe the physical properties of such hot carriers. The MPL signal is collected spatially along

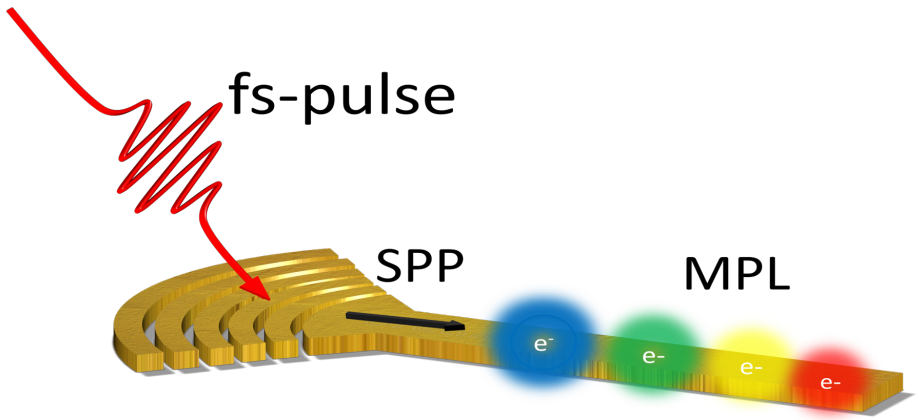


Figure 2.1: Schematic view of the remote generation of hot electrons within the plasmonic waveguide with its focusing curved grating

the waveguide by far-field and near-field hyperspectral microscopy techniques [250–252], which are detailed in Sec. 2.3.

The waveguide is made of Au because of its favourable plasmonic properties in the visible spectral range (see Sec.1.2.1) [61, 62] and its good stability compared to e.g. Ag or Al [253]. In such a waveguide, two SPP modes can propagate: one at the Au/air interface and one at the Au/silica interface [61]. Moveover, at such photon energy excitation (1.51 eV), there is no interband absorption from the d-band of Au (cut-off at ~ 690 nm, 1.8 eV, for Au [106]). Thus, a long SPP propagation length is expected with a low damping (by Joule heating).

We simulated the ratio between the power propagating along the waveguide compared to the incident optical power (called the coupling efficiency, CE). In order to maximize the CE, we designed a focusing curved grating coupler that allows for the efficient propagation of SPPs (see Fig. 2.1). For that, the grating diffracts light and the first order of diffraction matches the SPP wave vector. Modifying the angle of incidence will permit to change the first order of diffraction angle with the interface depending on the periodicity of the grating. Moreover, the grating coupler parameters has been optimized for 820 nm wavelength of excitation.

Furthermore, between the grating and the waveguide, there is a circular sector part (adiabatic taper). In other experiments the adiabatic taper's length is quite long (~ 100 µm in Si waveguide [254]) in order to smoothly focus the SPP towards the waveguide [255]. However, the longer the adiabatic taper, the higher the losses are. So, we decided to shorten the adiabatic taper to 1 µm because of damping of SPP at 820 nm to maximize the power fed into the waveguide. The focusing grating coupler allows for a compact footprint compared to linear grating couplers with adiabatic taper (eight times lower) but can suffer from reflections [256]. The grating coupler focuses the SPP into the waveguide's entrance to maximize the power carried by SPPs. In perspective, an apodized grating coupler (variation of the periodicity) could be another strategy to enhance the CE with less mode mismatch issues [254].

Connecting the focusing grating coupler with the waveguide permits to select the excitation of the desired SPP mode (at the Au/air or at the Au/silica interfaces) by selecting a specific angle of incidence (see Fig. 2.2.a). Indeed, taking the fundamental calculation

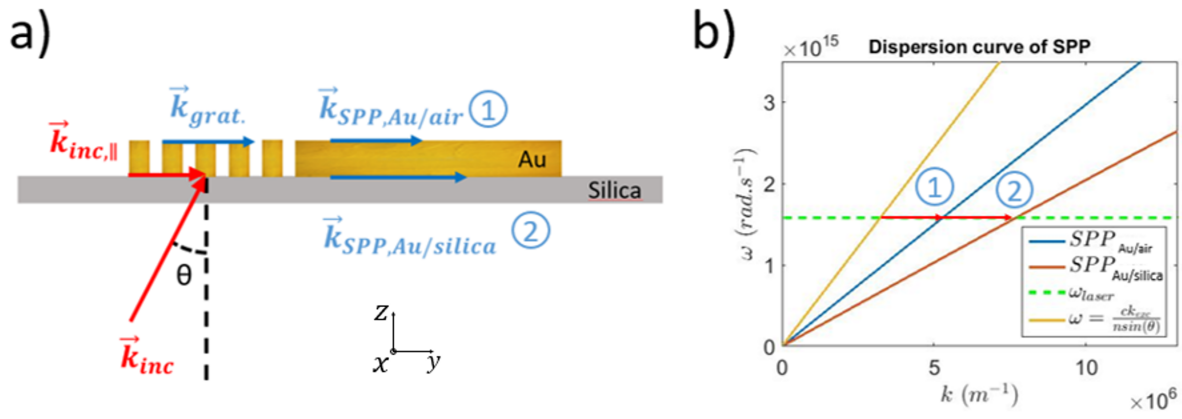


Figure 2.2: a) Schematic view of the angular control that permit the selective excitation of the SPP modes. b) Dispersion curve of SPP at the interface between Au/air (red) and Au/silica(blue) and the light cone (yellow). The horizontal dashed green line represents the laser excitation frequency

of SPPs propagating over an infinite interface between a dielectric (air or silica, $z < 0$) and Au ($z > 0$) [61] with an angle of incidence θ, the projection of the incident wavevector in a medium with a refractive index of n is $(2n\pi/\lambda)\sin(\theta)$. The grating coupler will diffract the incident light, adding a $\delta_k = \frac{2m\pi}{a}$ wavevector from the reciprocal lattice of the grating with a periodicity $a$ (with $m$ the order of diffraction, integer). Indeed, according to the dispersion relation plotted in Fig. 2.2.b, the selective excitation of the SPP by the grating coupler must satisfy the phase matching condition at the interface:

$$k_{\mathrm{SPP},i} = \frac{2n\pi}{\lambda}\sin(\theta) + \frac{2m\pi}{a} \tag{2.1}$$

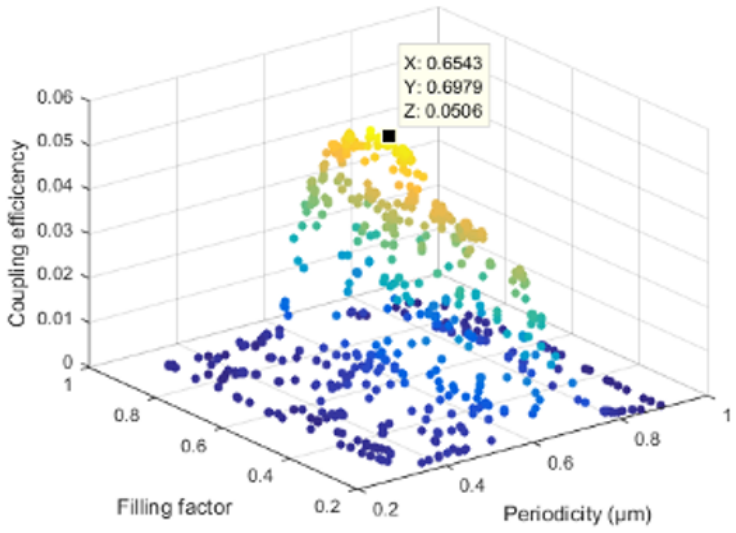


Figure 2.3: Simultation of the CE of Au/air SPP excitation as a function of the period (μm) and the filling factor.

For a given θ, by properly choosing the grating parameters, i.e. periodicity and filling factor, a SPP mode is selectively exciting at the Au/air or Au/silica interfaces. The grating design was determined using a Finite Element Method simulation (Comsol ®) with

an optimization algorithm (from Matlab® toolbox). For simulation convergence reasons and calculation time, a 2D model was used, which implies that waveguides and gratings are infinitely wide and the curved geometry is not taken into account. The device is excited by the optical plane wave on the grating from the silica region and the thickness of Au is 75 nm (grating and waveguide). The periodicity $a$ and the filling factor were set as free parameters to maximize the coupling efficiency (CE) between the incident optical wave in the silica and the Au/silica SPP mode (for an incidence angle of $\theta = 10°$). Fig. 2.3 represents the CE as a function of the periodicity and the filling factor. Within the simulation, the CE is evaluated by the ratio between the Poynting vector flux carried by the Au/silica SPP at the end of the waveguide and the incident optical Poynting vector flux. Each point represents a Comsol® simulation with CE as the output, for a given periodicity and filling factor. Then, a gradient optimization algorithm from Matlab® is used to probe the grating parameters and maximize the CE. CE reaches a maximum value of about 5% with a periodicity of 0.65 µm and a filling factor of 0.7.

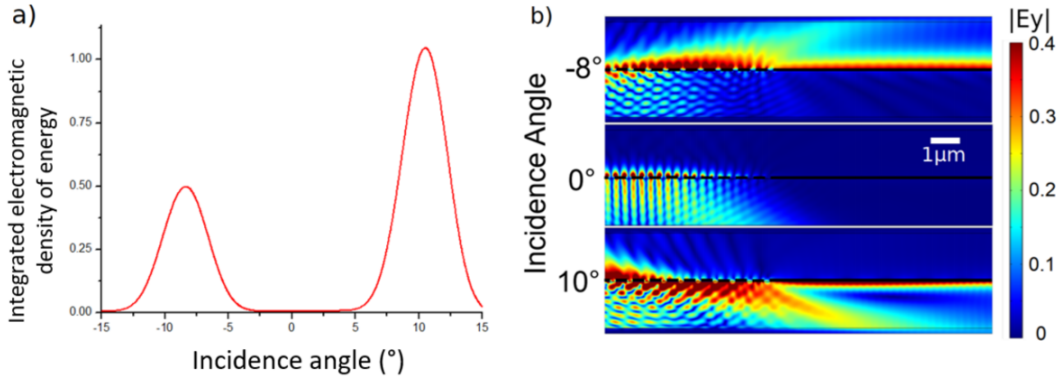


Figure 2.4: a) Integrated electromagnetic density of energy as a function of the incidence angle θ after 12 µm of propagation along the waveguide. b) Electric field ($|E_y|$) distribution for -8° (top), 0° (middle), and 10° (bottom).

Then, utilizing the optimized grating parameters which are $a$ = 650 nm and ff = 0.63, the angle of incidence θ is scanned to verify the angle that maximizes the Au/air SPP excitation. The electromagnetic density of energy carried inside the waveguide is represented Fig. 2.4.a after a propagation of 12 µm as a function of the excitation angle. According to this procedure with the optimized parameters, the Au/silica SPP is most efficiently excited for an angle of 10° while the Au/air SPP requires an angle of -8°. The electric field distribution ($|E_y|$) corresponding to both excitation angles is displayed in Fig. 2.4.b (upper and lower images), together with the field distribution resulting for normal incidence that shows no coupling to any SPP. Fig. 2.4 depicts a clear selective angle-controlled of the SPPs excitation. Thus, the upper plasmon (i.e. Au/air SPP mode) carries inside the waveguide half of the energy than the lower plasmon (i.e. Au/silica SPP mode) after a propagation of 12 µm. The Au/silica SPP has then a larger probability to efficiently excite hot carriers also because its field is more confined at the interface.

In order to observe where hot carriers have more probability to be excited, Fig. 2.5 represents the spatial distribution of the electric field norm inside the waveguide. The horizontal axis represents the thickness of the waveguide: 0 is the silica/Au interface and 75 nm is the Au/air interface. The blue curve (resp. green) corresponds to the Au/air SPP (resp. Au/silica SPP). Therefore, hot electrons have maximal probability to be produced where the energy of SPP is maximal at interfaces. The penetration depths of both SPP are

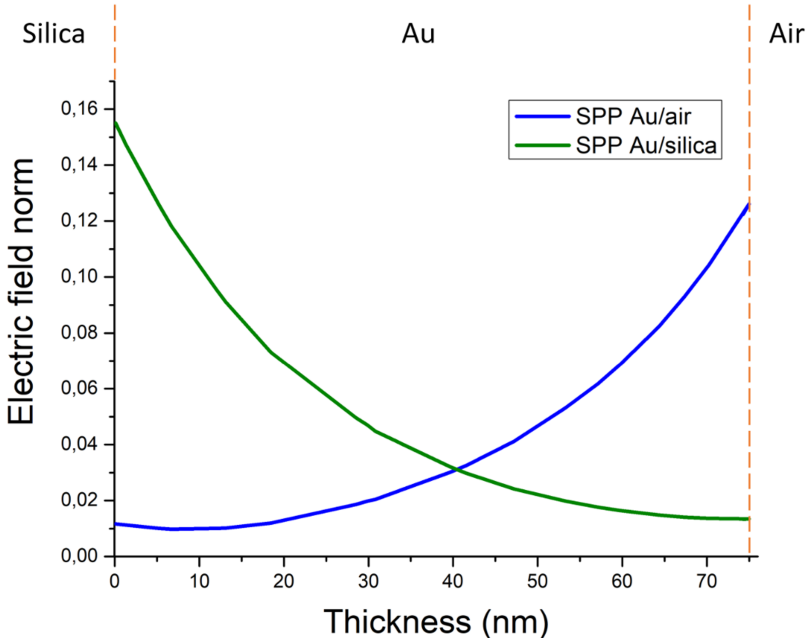


Figure 2.5: Electric field norm inside the waveguide after 12 µm of propagation when the Au/air SPP (blue) or Au/silica (green) SPP is excited

comparable and Fig. 2.5 emphasizes that the two interfaces of the waveguide are mostly uncoupled, implying that hot electrons produced by a given plasmon will be mostly generated at interfaces rather than in the volume. Furthermore, using an unfocused beam onto the grating coupler will permit to use higher optical power without the risk of damaging the structures.

In conclusion, we investigated the grating periodicity that maximizes the power transmitted along the waveguide by SPP. The SPP Au/air or Au/silica can be selected by controlling the angle of incidence. The probability to produce hot carriers is maximal at the interfaces due to the enhanced electromagnetic field.

## 2.2 Nanofabrication of a plasmonic Au waveguide

After having determined the grating parameters that optimize the CE, the Au plasmonic waveguide was fabricated at the ARCEN-CARNOT platform of the ICB laboratory in Dijon. I have implemented the plasmonic waveguide geometry into the RAITH software to obtain a GDS file with the periodicity and filling factor parameters found by simulations. Since the spatial confinement of the waveguide is not taken into account in the simulations presented Sec.2.1. I empirically tried four different lateral widths for the waveguides: 0.5, 1.2, 1.8 and 2.5 µm to maximize the focusing efficiency of the grating coupler. Morever, in order to focus with a small length adiabatic taper, I arbitrarily chose a radius of 2.6 µm for the circular section.

The substrate used was a silica glass coverslip cleaned by piranha etching (sulfuric acid and hydrogen peroxide) in order to remove possible contaminants for the next steps. Two layers of PMMA (first 50 molecular weight of K and second 200 molecular weight of K) were spincoated on the coverslip (160 µL for ≈ 300 nm thickness, speed ramped from 100 to 3000 rpm) followed by a baking step (180 s at 150 °C). The molecular weight of the first layer is lower than the second one because, when the sample will be irradiated

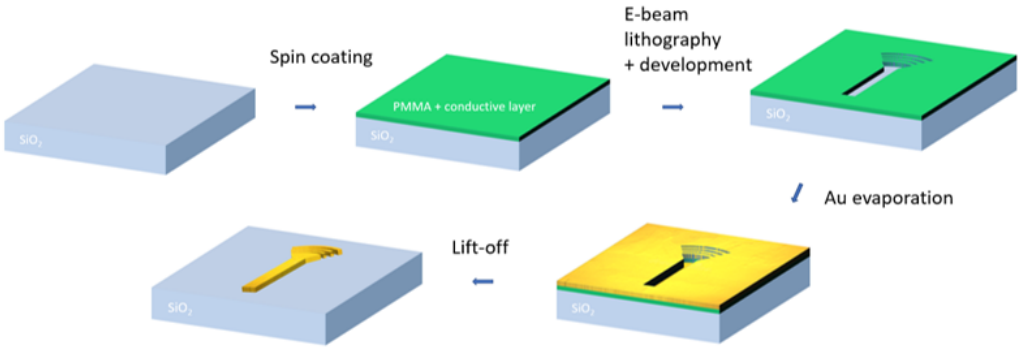


Figure 2.6: Nanofabrication steps of the Au plasmonic waveguide with the focusing grating coupler

by electrons, the edges will be sharper. With this precaution, the evaporated material forming the nanostructures has lower probability to be riped off at the lift-off step. I then added a conductive layer of Electra 92 (200 µL) by spin coating followed by a baking step (180 s at 90 °C) because the substrate is not conductive. This layer permit to visualize the sample by Scanning Electron Microscope (SEM).

Loading the prepared GDS file, the electron-beam lithography (EBL) was applied onto the sample by the Pioneer (Raith ®). The EBL parameters used were ≈ 40 pA current with a dose of 200 µC/cm$^2$ and an electron gun voltage of 20 kV. The parts of PMMA imprinted by the lithography were removed by a developer (Methyl Isobutyl Ketone (MIBK) and acetone, for 50 s) followed by a stopper (acetone, for 50 s) (development step). Before the next steps, I checked that the structures were present with dark field optical microscopy (allowing for better contrast compared to bright field).

Then, evaporation was performed by e-beam techniques (MEB 400, Plassys ®). This evaporation is made under very low pressure with a cryo pump (∼ $10^{-7}$ mbar). A thin layer of Ti (5 nm) was evaporated onto the sample to improve Au adhesion onto the coverslip. Thereafter, a 75 nm thickness of Au was evaporated. The excess of Au was removed by lift-off with aceton in a baker (≈ 1 hour), leaving only the nanostructures onto the glass.

I have then checked the general shape of the 12 µm Au waveguides with the focusing grating couplers by dark field optical microscopy (Fig. 2.7.a) and more accurately measured the waveguide's parameters by Scanning Electron Microscopy (SEM) (see Fig. 2.7.b). I thus confirmed the good agreement between the measured and the desired parameters for the waveguide (width and length) and the grating coupler (periodicity and filling factor).

In conclusion, the simulated plasmonic waveguides were fabricated following standard e-beam lithography procedure. The nanostructures were then characterized confirming the desired grating and waveguide dimensions.

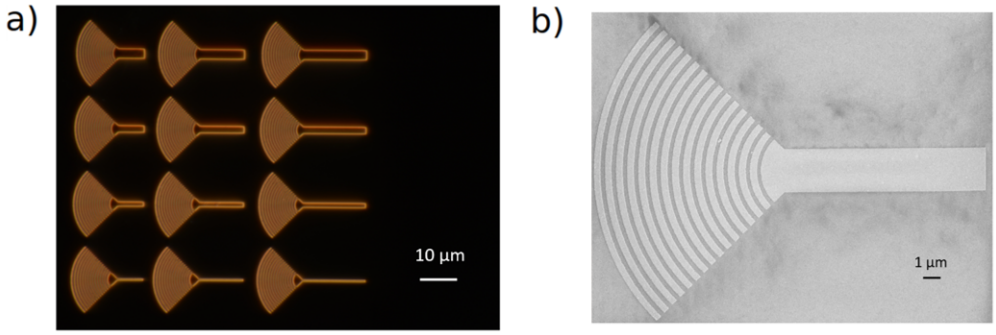


Figure 2.7: a) Dark field optical microscope image with three different lengths (7, 12 and 17 µm, columns) and four different waveguide widths (0.5, 1.2, 1.8 and 2.5 µm, lines). b) SEM image of a 12 µm length Au plasmonic waveguide.

## 2.3 Remote excitation of hot electrons by a propagative SPP

### 2.3.1 Hyperspectral imaging with angular control excitation experimental set-up

After the Au plasmonic waveguides were fabricated, the first step was to validate that SPPs can be launched with angle controlled excitation. I have investigated the remote excitation of hot electrons with this device at ICB in Dijon. For that, I took in charge the hyperspectral imaging experimental set-up with angular control excitation illustrated Fig. 2.8. In order to maximize the energy propagated by the SPP and enhance the probability of producing hot electrons, a Ti:Sapphire femtosecond laser was used with a high intensity per pulse (wavelength of 820 nm, pulse duration ~100 fs, 80 MHz repetition rate, average optical power of 28 mW).

To selectively control the angle of incidence (see Sec. 2.1), we have used a high-numerical aperture (NA) immersive oil objective (x60, NA=1.49) under episcopic (reflected) illumination with an inverted microscope (Nikon Ti Eclipse). This high-NA objective allows to reach a small spot and to collect high angle emitted wavevectors from the sample. This scheme allows one to excite selectively either the Au/air SPP or the Au/silica SPP. The laser is focused at the back focal plane (BFP) of the microscope objective, i.e. the Fourier plane (π-Fourier in Fig 2.8). In this scheme, the laser beam is collimated thereon the sample keeping a small spot diameter (~ 10-20 µm) with an illumination angle controlled by moving a miror in front of the focusing lens [257]. Controlling the position where the beam is focused in the Fourier plan (with a motor stage), the BFP illumination permits to select the desired angle of incidence on the sample.

Along the propagation of the laser pulses from the laser output to the sample, group velocity dispersion occurs due to all the optical elements on the optical path and the pulses are stretched on the sample. This dispersion is corrected by a home made dispersion compensation module [145]. A first grating (optimized at 820 nm) diffracts light, which is then sent onto two cylindrical mirrors. All the spectral components are then recombined by a second grating. Displacing the end grating along the optical axis allows one to introduce a quadratic chirp that compensates for the one introduced by the optics. This allows for a temporally compressed pulse which is Fourier transform limited in the focal plane of the microscope objective. In order to confirm this pulse compression, we maximized the SHG signal by autocorrelation from a sample in the objective plane as a function of the introduced chirp.

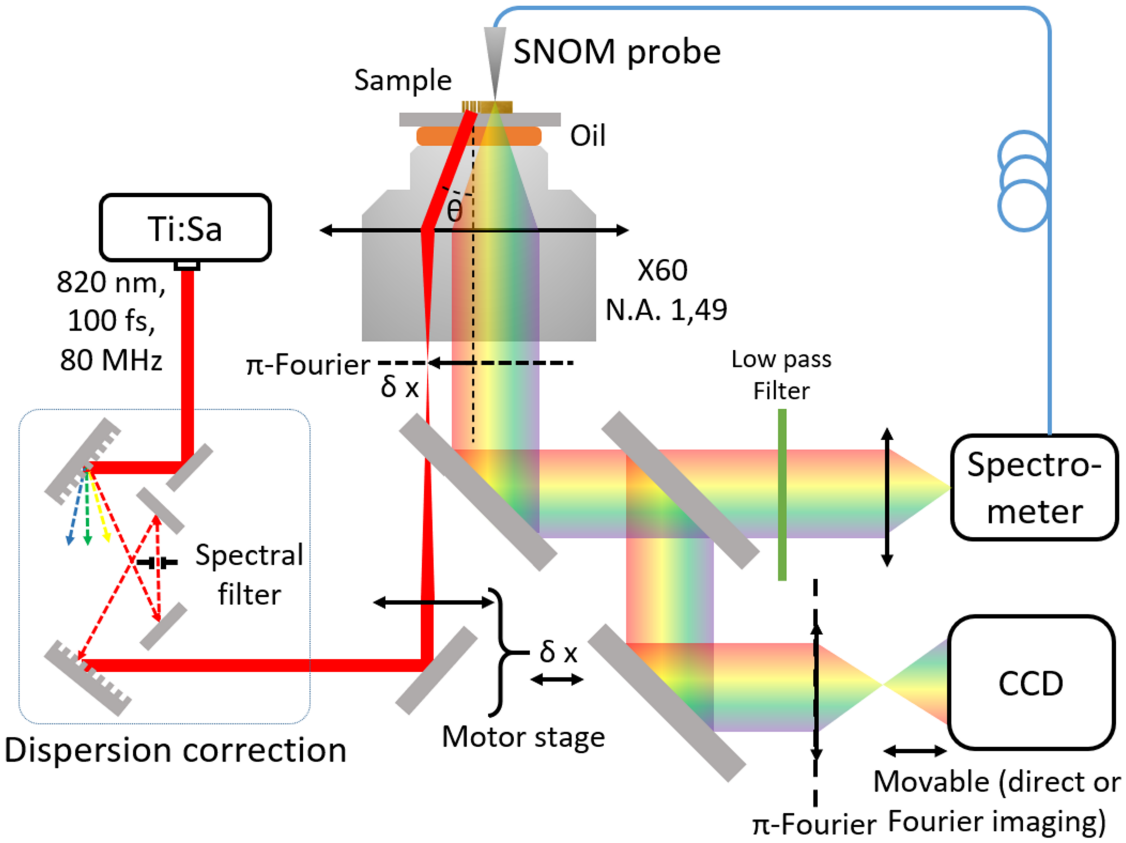


Figure 2.8: Hyperspectral imaging in the near-field and far-field set-up with a k-space control of excitation.

We then probe the signal emitted by the plasmonic waveguide by hyperspectral near-field and far-field techniques. The near-field technique allowed us to get spatially-resolved spectra emitted by the waveguide i.e. a hyperspectral imaging.

We image the Fourier plane on the CCD camera. Fig. 2.9.a illustrates this concept: the inner circle is the air-silica critical angle ($\theta_c$) while the outer circle is the maximal angle of k-vectors that can be collected. For normal incidence excitation, the brighter spot is the specular reflection and the two lateral spots are the two first orders of diffraction introduced by the grating (m=±1). Fig. 2.9.b is the CCD image of the waveguide under white light illumination. All other images are recorded at the excitation wavelength of 820 nm. Fig. 2.9.c shows the Fourier plan image of the laser reflection onto the grating with a normal incidence excitation, with the central spot and the two first orders of diffraction. Fig. 2.9.d and Fig. 2.9.f are images towards the silica substrate [258] of the propagation of the Au/air and the Au/silica SPPs along the plasmonic waveguide when the angle of incidence of the laser beam is set to efficiently excite these SPPs. Indeed, the angle of incidence of the laser onto the grating is varied so that the +1 order of diffraction of the grating matches the Au/air or Au/silica SPP wavevectors. Thus, the wavevector $k_{//}+\delta_{k,grat.}$ of excitation and grating is matching $k_{SPP,Au/air}$ or $k_{SPP,Au/silica}$ depending on the angle of incidence. Fig. 2.9.d shows the image of the leaky mode SPP propagating at Au/air with shining edges due to scattering by edge defects. The spatial modulation along the waveguide is represented in the Fourier plan by the vertical line modulation (parallel to the $k_y$ axis). Fig. 2.9.f represents the propagating Au/silica SPP with a low signal resulting from a wavevector out of the microscope numerical aperture. Fig. 2.9.e and Fig. 2.9.g show the

Fourier images of the leakage of the Au/air SPP and the Au/silica SPP respectively. In far-field onto the CCD camera, the Au/silica SPP is not observed because it does not radiate towards the substrate.

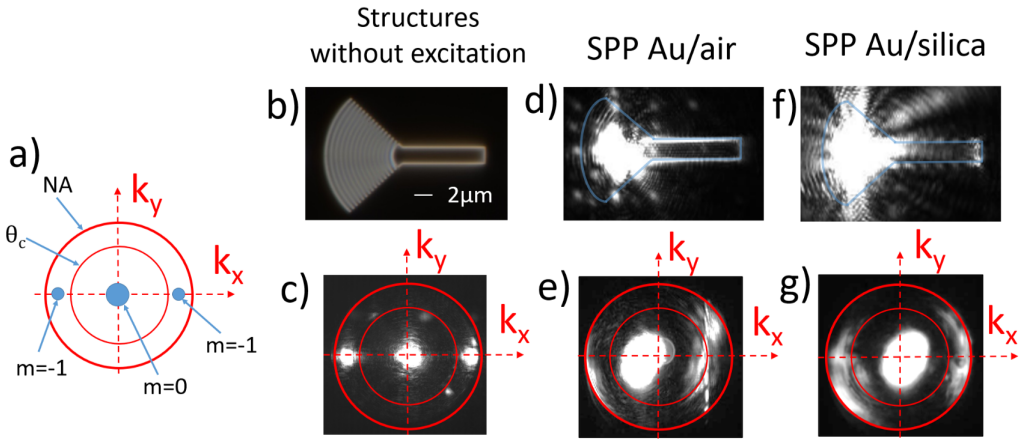


Figure 2.9: a) Schematic view of a typical Fourier plane images. b) Direct brigth image of the waveguide. c) Fourier plane with normal incidence excitation. d) Direct image with the excitation of the Au/air SPP (resp. f) Au/silica SPP). e) Fourier plane with the excitation of the Au/air SPP (resp. g) Au/silica SPP).

The images of Fig.2.9 validate that the implemented setup is able to: a) lauch SPPs on the plasmonic waveguide by means of angle-resolved excitation and a grating coupler, b) control the wavevector k of excitation in order to select the launched surface plasmon (the Au/air SPP or the Au/silica SPP ) and c) spatially collect the signal radiating from the plasmonic waveguide to the far-field at the same time. This also validates the parameter choices for the periodicity and filling factor.

In the next two parts we will focus on the Au/air SPP mode because this mode is more efficiently coupled to the far-field readily compared to the Au/silica one and it is more likely that MPL generated by the relaxation of hot electrons would also radiates. In the following, to demonstrate the remote excitation of hot electrons by SPPs, we will study the hyperspectral distribution of the emitted MPL along the plasmonic waveguide excited by the Au/air plasmon. The upper interface is also more attractive for applications that enhances physicochemical reactions.

### 2.3.2 Hyperspectral far field imaging

In order to demonstrate the delocalized hot electron generation, we investigated the MPL produced along the plasmonic waveguide by far-field hyperspectral imaging techniques.

We first select the -8° angle of incidence that excites the Au/air SPP mode. Fig. 2.10.a shows the waveguide image on the spectrometer under white light illumination. Actually, the signal emitted by the waveguide is sent in free-space to the spectrometer which enables to follow the spectral distribution along the waveguide (Fig. 2.10.b). The far-field hyperspectral detection collects the MPL via the high-NA microscope objective. A short-pass filter at 730 nm is used to cut the laser line and we measure only the short wavelength contribution of the MPL (compared to the laser line). Furthermore, in the dispersion correction part (see set-up Fig. 2.8), after separating the different spectral components of the pulse, the beam is spectrally filtered with abrupt edges in order to control the laser

linewidth (see figure next section, Fig. 2.15). Thus, the collected light outside the spectrum laser line only originates from the sample. For these experiments, we used a 12 µm long waveguide. In Fig. 2.10.b, we observe that light is produced at the entrance of the waveguide (0 µm), around 5 µm and at the extremity (12 µm). A hypothesis is that these scattering points might enhance the MPL diffusion, also the MPL produced at the Air/Au interface is unlikely to efficiently radiates across the waveguide. The end of the waveguide is a natural scatterer and we assume a defect at the 5 µm position that scatters light efficiently. These spectra, acquired only when SPPs are propagating, are similar to the typical MPL obtained with nanoantennas [142]. Thus, this first figure suggests a relationship between the SPP propagating and the collected spectrum.

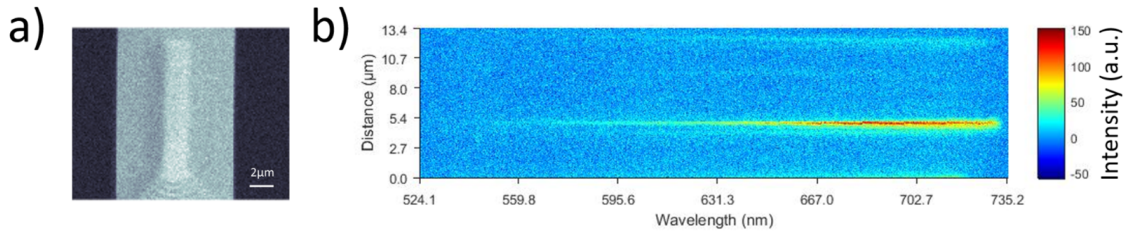


Figure 2.10: a) Image of the waveguide onto the spectrometer. b) Spectra obtained at different distances along the waveguide.

Fig. 2.11 represents the MPL emitted at the input, at 5 µm and at the end of the waveguide (12 µm). The blue line at the entrance represents the MPL emitted at the grating/entrance of the waveguide ranging from 410 nm to 730 nm (filter cut-off). Only when the angle of excitation is -8°, we observed MPL being emitted at 5 µm and at the waveguide extremity (12 µm). These MPL spectra show a redshift or a narrowing of the peak along the propagation axis. The high-energy part of the spectrum is red shifted of ≈ 80 nm at 5 µm, and of at least ≈ 175 nm at 12 µm, where the spectrum is strongly cut by the filter that rejects the laser line. Indeed, along the SPP propagation, since the SPP intensity is decaying less electron-hole pairs are produced locally and as a consequence the electron density and temperature is lowered. MPL spectra are an indication of hot electrons cloud temperature and density and a less heated hot electron cloud distribution leads to a redshifted spectrum [130]. At this point of the interpretation, the cloud of hot electrons, excited by SPP, is less energetic than at the entrance producing a narrower MPL radiation. Moreover, we observed second harmonic generation (SHG) as a sharp peak at 410 nm. The SHG peak intensity is decreasing very rapidly along the propagation axis. Such SHG phenomenon is explained by the tight focusing at the entrance of the waveguide. The SPP loosing its energy along propagation yields less SHG [259].

Then, we explored the influence of the angle of excitation on the MPL intensity. For this, we changed the angle of incidence θ and we collected the MPL spectrum radiated along the plasmonic waveguide in the far-field. Fig. 2.12 illustates the maximal intensity of the MPL spectrum as a function of the angle of incidence taken at the entrance of the waveguide (grey dashed line) and after 5 µm (blue dashed line). At the entrance of the waveguide close to the grating, the MPL is produced for any angle since it is the result of direct laser excitation (grey points in Fig. 2.12). On the contrary, after 5 µm of the SPP propagation, the integrated MPL intensity is strongly increased only for an angle of incidence of -8° corresponding to the Au/air SPP angle of excitation. This gives an argument that the MPL is being produced mainly from the local generation by the upper SPP (Au/air) and does not result from a MPL produced at the grating which would prop-

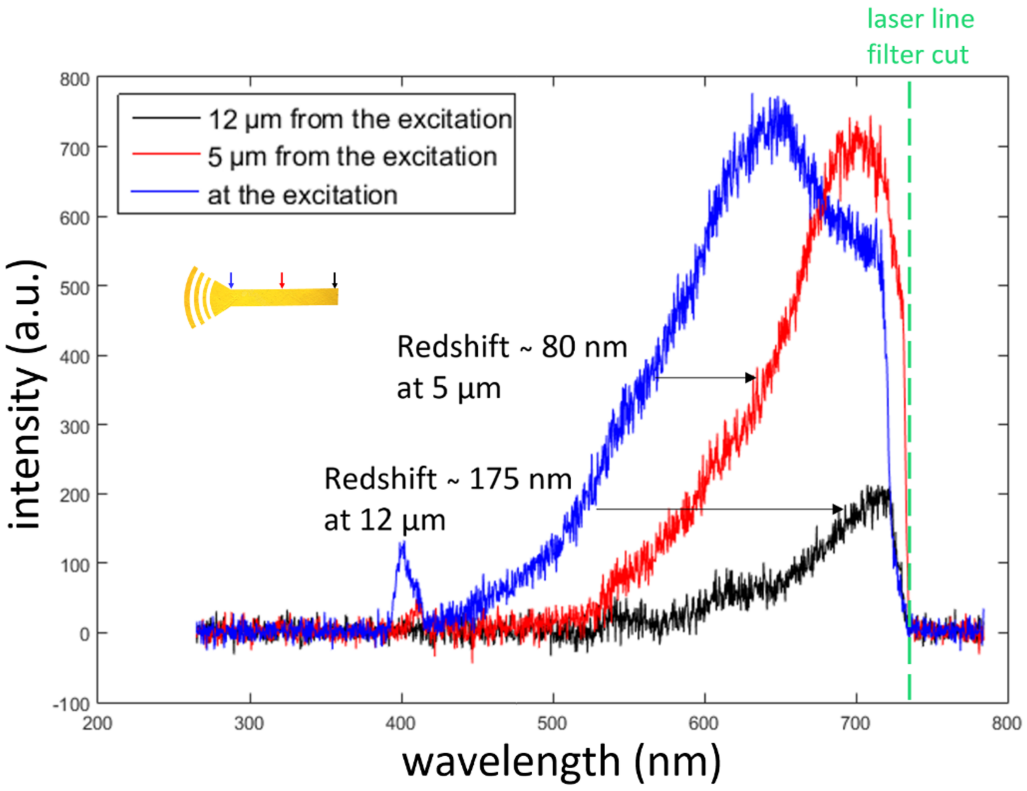


Figure 2.11: Far field spetrum along the propagation: at the entrance of the waveguide (blue), at 5 µm along propagation (red) and at the end of the waveguide (12 µm, black)

agate along the waveguide. Indeed, in this latter case, scattered MPL would follow the behaviour of MPL at the entrance.

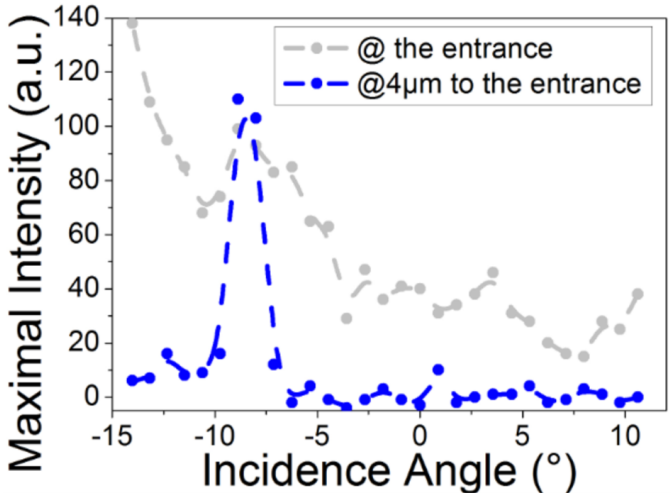


Figure 2.12: Maximal intensity of MPL as a function of the incidence angle of excitation taken at the entrance of the waveguide (grey) and at 4 µm (blue)

These experiments show the possibility of producing hot electrons at a distance from their optical excitation by propagating SPPs. The hot electron energy distribution (temperature) is then determined by the local SPP intensity along its propagation. In the following, we will investigate more deeply such an energy distribution.

### 2.3.3 Hyperspectral near field imaging

In order to investigate the spatial behaviour of the hot electron energy distribution, we focus on probing the plasmonic waveguide by near-field hyperspectral imaging with k-space excitation control. In these experiments, we still focus on the Au/air SPP (see Fig. 2.9.d) since the near-field probe cannot access the Au/silica interface.

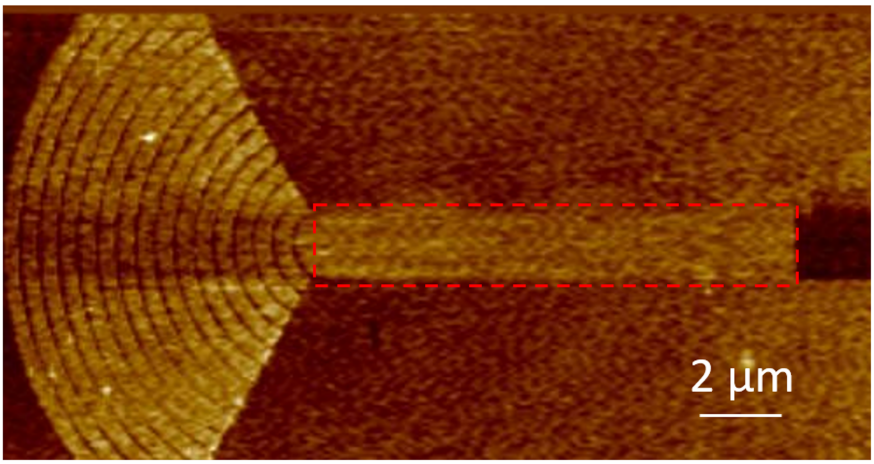


Figure 2.13: Near-field topography of a 12 µm plasmonic waveguide. The red dashed line is the region of interest presented Fig. 2.14.

The near-field hyperspectral set-up collects the MPL by a scanning near-field optical microscope (SNOM) on top of the sample [260]. The SNOM is composed of a near-field probe (thin tapered optical fiber with a 50 nm aperture at the apex) scaning the surface at a few nanometers distance. The probe is connected to a piezoelectric head and is oscillating at a frequency slightly shifted from the resonance peak. When approaching the surface, due to shear-forces, the resonance frequency shifts. The feedback loop then controls the vertical position of the head yielding the topography map (Fig. 2.13). The SNOM technique allows one to reach a spatial resolution of ~5 nm vertically and 20 nm laterally. Simultaneously, the optical fiber collects the optical near-field and allows it to be analyzed spectrally by the use of a spectrometer with a mounted intensified cooled camera [251]. The near-field spectra are recorded synchronously with the scan, i.e. for each point of the scanned area, a spectrum is collected.

We have employed the hyperspectral near-field imaging technique to map the MPL emitted by the plasmonic waveguide along the SPP propagation. Fig. 2.14 represents spatial near-field images recorded at specific wavelengths. For a 12 µm long waveguide with no defects on it, the spatial intensity distribution of the propagating SPP (at 825 nm near the laser wavelength excitation) is mapped as well as the spatial intensity distribution emitted at 700 nm and 854 nm on both sides of the filtered laser line. We observe that, no matter the emitted wavelength, the intensities decay along the waveguide. Moreover, a periodic spatial modulation is observed along the plasmonic waveguide for all wavelengths. This modulation refers to a standing wave which could result from an interference pattern due to the back reflection at the end of the waveguide. This phenomenon has been observed in other experiments with plasmonic nanowires but only at the wavelength of excitation (here 820 nm) [70, 71].

Furthermore, the collected intensity is higher at the end of the waveguide regardless the wavelength. This enhancement of the field has been reported in previous experiments

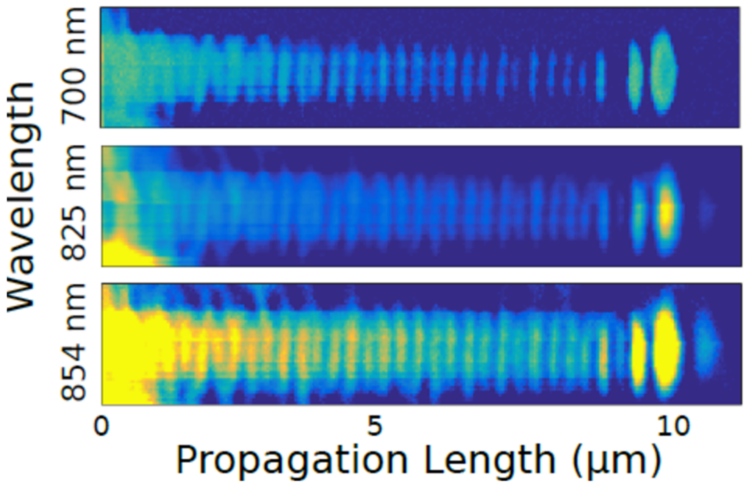


Figure 2.14: Optical near-field images for wavelengths: at near the laser line (825 nm), and at 700 and 854 nm (for a 12 μm waveguide).

in plasmonic waveguides [70, 71, 248] and is attibuted to the enhancement of scattering of the SPP induced at the extremity [244–246] allowing for a better near-field coupling of the emitted light.

At this point, the interference patterns for all wavelengths seem to share the same periodicity which is of the SPP wavelength. If so, that would suggest that the MPL is being locally produced where hot electrons are being produced by the SPP.

Let's turn to the full spectrum emitted at different positions along the waveguide. Fig. 2.15 shows the typical MPL spectra (in linear and log scale) by near-field measurements above the waveguide at two different positions: the entrance and after 8 μm. Note that these spectra are normalized at 860 nm for clarity. We can distinguish two contributions apart from the laser line: one with wavelengths longer than the laser wavelength (lower energy, also called Stokes photoluminescence) and one with wavelengths shorter than the laser wavelength (higher energy, also called Anti-Stokes photoluminescence). The long wavelength part does not vary significantly after 8 μm of SPP propagation but the short wavelength part is strongly attenuated.

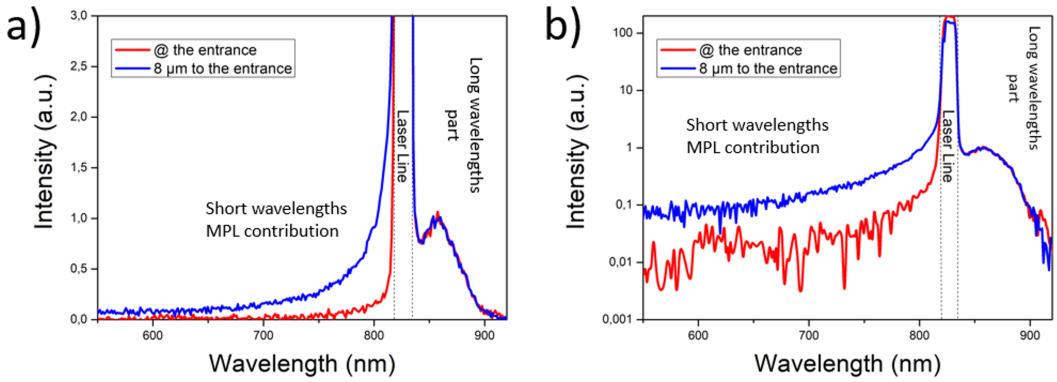


Figure 2.15: Typical near-field MPL spectrum taken at two position along the waveguide: at the entrance (blue) and at 8 μm along propagation (red). a) In linear scale. b) In log scale.

Then, the underlying physics of the short and long wavelength part seems to be different because of different attennuation processes observed. The efficiency of MPL gen-

eration is wavelength dependent and these spectra are measured along SPP propagation, thus the SPP intensity decay along propagation influences the process. These results suggest a link between the MPL being emitted and the propagating SPP. Moreover, the two vertical lines in Fig. 2.15 represent the abrupt edges of the filtered laser line. Thus, the collected light with spectrum outside the spectrum laser line originates only from the sample.

To go further, Fig. 2.16 represents the spectral evolution of the near-field MPL spectrum along the plasmonic waveguide, the vertical axis corresponds to the spectra at the position of propagation indicated in abscissa. At the entrance of the waveguide, the near-field spectrum emitted is broad, ranging from 400 to 900 nm. At the laser line (820 nm), the intensity saturates due to the higher radiation of the linear plasmonic propagation. The spatial modulation in Fig. 2.16 is the same since we observe vertical lines in this map for every wavelength with a periodicity of 286 nm. These shared spatial periodicity indicates that the SPP damping and interference pattern due to the back reflected SPP are dictating the MPL being generating (identical interference pattern at 700 and 854 nm than at 825 nm radiated wavelength). This gives a strong argument in favour of the MPL being produced locally by hot electrons due to SPP propagation rather than MPL propagation coming from the grating in Fig. 2.16.

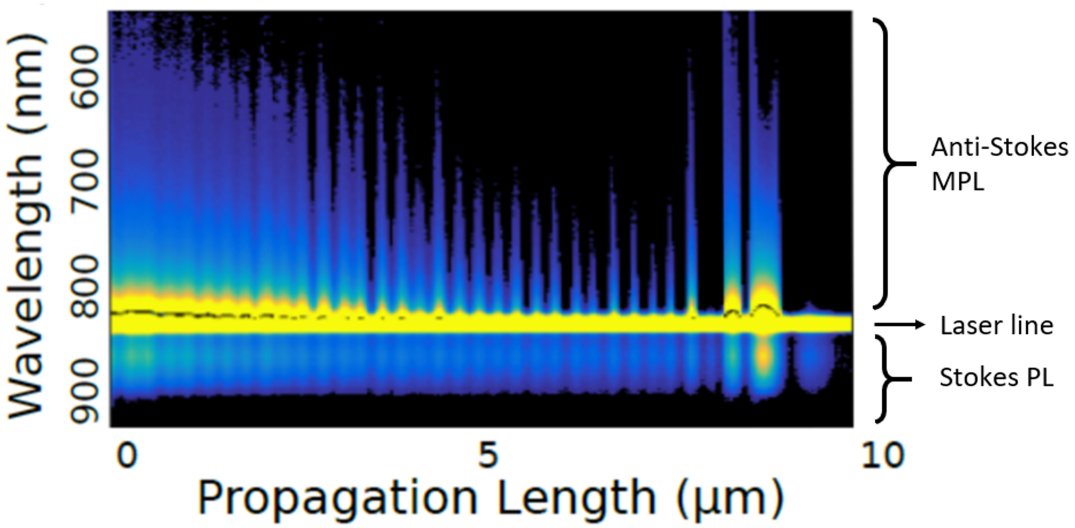


Figure 2.16: Spectral distribution of the MPL along the SPP propagation (brut spectra).

Indeed, if the MPL was propagating along the plasmonic waveguide, due to dispersion, the spatial periodicity of the standing wave should be wavelength-dependent. Another counter-argument could be that the MPL is being produced by plenty of SPP propagating at their wavelength. Since light scattering at the entrance of the waveguide could excite broadband SPPs propagation [261]. However, in this case the spatial modulation should also depend on the wavelength. Moreover, if other angles of excitation are selected, no MPL is observed along the plasmonic waveguide emphasizing the crucial role of SPP excitation.

Hot electrons diffuse and relaxe at a distance quite shorter than the surface plasmon standing wave periodicity (286 nm). Indeed, if hot electrons would diffuse longer than the interference pattern periodicity, a blurring of the fringes would appear. For a lifetime of hot electrons that is ≈ 0.5 ps in gold [141], if the diffusion length is no longer than the period (286 nm), this yields to a carrier velocity ≈ 0.1-0.2 µm/ps, which stays below

the commonly admitted Fermi speed value in gold of 1.4 µm/ps [262]. Thus, this means that the scattering rate of hot electrons is low. As a consequence, the SPP distibution is directly a map of the hot electron spatial distribution. Hence, the management of the SPP intensity distribution allows one to control both the spatial generation of hot electrons and the energy distribution. Furthermore, those observations suggest that the lifetime of hot carriers is shorter than their diffusion time or they would highly diffuse longer than the location of their production.

Furthermore, Fig. 2.17 represents the intensity as a function of the propagation distance for three wavelengths: 700 nm, 825 nm and 850 nm. The damping along the propagation is strongly wavelength dependent. The long wavelength contribution is slowly damped along SPP propagation compared to the short wavelengths. We modeled this behaviour by an exponential decay with a damping coeffient α and a non linear order $n$ related to the non linear absorption. The intensity of MPL $I_{MPL}(\lambda, y)$ is basically related to intensity of the damped SPP $I_{SPP}(y)$ by

$$I_{MPL}(\lambda, y) \propto I_{SPP}(y)^n(\lambda) \propto e^{(-n(\lambda)\,\alpha\, y)} \tag{2.2}$$

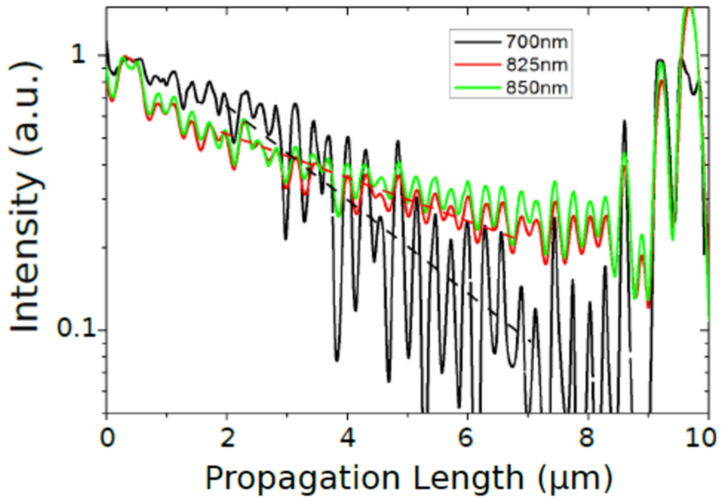


Figure 2.17: Intensity decay along the propagation is plotted for the three wavelengths (700, 825, and 850 nm). Dashed lines are guide eye of the decay along the propagation. Normalized by the optical power at the waveguide input for given wavelengths.

In Fig. 2.17, the long wavelength contribution nearly overlaps to the SPP decay. This points out that this part of the spectrum relates to a linear process. In contrast, at 700 nm, the high energy contribution of the MPL decays faster than SPP damping, suggesting a nonlinear absorption process. From this figure, the different damping constants are estimated by focusing on the 2-7 µm region of the waveguide (depicted by dashed lines) where the contributions of the scattering at the waveguide's input and at the waveguide end are minimized. We find a damping length $l$ (= 1/α) close to 14 µm for the SPP (and for the long wavelength contribution), while the damping length at 700 nm is close to 6.7 µm. There is a factor of about 2 between $l$ at the SPP wavelength and at 700 nm, which indicates a second order non linear process for the high energy contribution of the spectrum. Therefore, since the MPL spectrum is driven by the hot electron energy distribution [108, 145], we show here that the SPP propagation also drives their energy distribution along the propagation. This result could give new insights in controlling remotely chemical reactions by the energy distribution of hot electrons [242].

In order to go further in the understanding on nonlinearities, we took the intensity of the SPP $I_{SPP}$ and the corresponding intensity of MPL $I_{MPL}(\lambda)$ for the long and short wavelength parts. In Fig. 2.18, plotting $I_{MPL}(\lambda)$ as a function of $I_{SPP}$ represents the power transfer function from the SPP to the MPL. Each point represents the intensity of the normalized SPP as a function of the corresponding normalized intensity of MPL. In Fig. 2.18, each color is for a specific wavelength in the MPL. For $\lambda$ = 850 nm, the long wavelength part of MPL depends linearly on the SPP intensity. This observation is correlated to the previous Fig. 2.17 and is suggesting that, for long wavelength contributions, hot electrons are produced by a linear absorption process and a recombination of hot electrons whithin the sp-bands (radiative intraband recombination). The intraband transitions are available because of additional k-vectors given by the nanogeometry or by electron-phonon interactions (c.f. intraband geometry-assisted and phonon-assisted transitions in Sec.1.2.2).

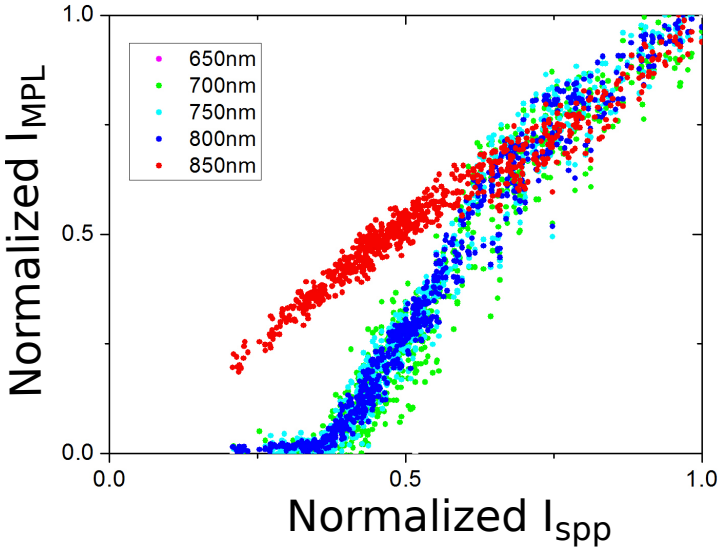


Figure 2.18: Normalized intensity emitted at several wavelengths as a function of the local SPP intensity. Each point represents a pixel on the hyperspectral image : the intensity at the SPP wavelength and at the desired wavelength. The $I_{SPP}$ is normalized by the highest SPP intensity and the $I_{MPL}$ is normalized by the highest intensity of MPL signal.

On the other hand, for $\lambda$ = 650, 700, 750 and 800 nm, the high energy part depends nonlinearly on the SPP intensity (higher slope). A non linear order of 2 is noted, which is in good agreement with the previous discussion. The interpretation is that a two plasmon absorption process comes into play from the d-band to the sp-band, in a single step process (interband absorption [107]) or a two steps process (sp intraband followed by d to sp interband [140, 149]) leaving hot holes behind. Hot electrons experience multiple e-e and e-p scattering events which redistribute the electron energy in a broad distribution (Fermi smearing) once the equilibrium is reached. Hot electrons then recombine from the sp-band to the hot holes within the d-band emitting photons (radiative interband recombination). This interband recombination of hot electrons finally produces a broad spectral emission.

Also, the power transfer is saturating when the local SPP intensity is high ($I_{SPP}(z) \approx 1$), probably related to Au saturable absorption [263]. An interpretation is that the SPP is carrying enough energy and locally saturates the two plasmon absorption from the d-band to the sp-band. Indeed, the spectral range of the MPL is induced by the local variation of the SPP intensity. The spectral width is maximal where the SPP intensity is maximal produc-

ing a high local density of the hot electrons cloud. In fact, the highest the SPP intensity, the strongest the nonlinear absorption is.

In conclusion, along with a SPP propagation, we have observed a MPL luminescence with upper and lower wavelength components and each one of them have its own underlying physical process.

## 2.4 Discussion on the MPL origin

As presented in Sec. 1.2.2, the underlying physics of the MPL is still under debate in the community. Our MPL study observed along a Au plasmonic waveguide is giving additional clues in the discussion.

In our experiment, the excitation wavelength (1.51 eV, 820 nm) was below the interband transition, thus, there is no possible direct interband absorption. We have observed the Stokes and anti-Stokes parts of the nonlinear PL (see Fig. 2.15). Our Stokes part is linear and anti-Stokes part is non linear with a non linear order of 2. Indeed, Beversluis et al. [109] also observed such PL behaviour on gold rough film excited at 780 nm wavelength and collecting the nonlinear PL in the far-field. According to Roloff et al. [131], above a certain irradiance threshold, the non linear order depends on the photon energy (see Sec. 1.2.2 [130, 131]). We have not observed such a photon enegy dependence. This could fairly be explained by the fact that the power transported by the SPP is not enough to overcome the threshold.

To my knowledge, in the literature, all nonlinear photoluminescence experiments were done on NPs apart from [248,249]. Our experiments showed that a stronger MPL is yielded where the field is higher. Thus, if one wants to engineer hot electrons generation, one should manage the field and enhanced it as much as possible. The surface plasmons are controlling the spatial generation of hot electrons and their energy distribution. Furthermore, there is also a threshold for the intensity of SPP to the anti-Stokes side (see Fig. 2.18) of the spectrum and a saturation of incident absorption.

In conclusion, we demonstrated that hot electrons can be generated at a distance from their optical excitation. Propagative SPPs within a waveguide connected to a focusing grating coupler remotely and efficiently generated hot carriers. The local SPP intensity is mapping the hot electrons spatial and energy distribution. By engineering the plasmonic intensity, this work opens perspectives of new applications to remotely set off chemical reactions. This study gives new insight into the debate on Au nanoparticles photoluminescence. We showed that, at higher energy, the interband radiative recombination is dominant but at lower energy, the intraband process is dominant. This opens the way to innovative devices where the engineering of the SPPs propagation gives the opportunity to fully master together the spatial and energetic distributions of hot carriers generated in a remote fashion.

# Chapter 3

# Surface plasmon optimization of hot electron generation in gold grating

*" Now that you know that the answer to the Ultimate question of Life, the Universe, and Everything is forty-two, all you need to do now is find out what the Ultimate Question is. "*

Douglas Adams, The Hitchhiker's Guide to the Galaxy, 1979

## Contents



We have seen in the last chapter how to efficiently excite a propagative SPP and remotely generate hot electrons. In order to build a photodetector, chapter 3 will present hot electron generation using LSP and grating resonances followed by their extraction thanks to a Schottky barrier. This chapter will present the principles, modelisation and nanofabrication of such a device.

## 3.1 Plasmon-enhanced hot electron photodetection

Incident photons can be absorbed by the metal in a Schottky barrier (see Sec. 1.2.3) generating electron-hole pairs (EHPs). If hot carriers have enough energy, they can overcome the Schottky barrier and be separated by the junction thus generating a current. This process has naturally a poor efficiency due to weak metal-light interactions and can

be enhanced by surface plasmons [10]. Thus, the photodetector is based on plasmon-enhanced hot electrons, namely enhanced Internal Photon Emission (IPE) processes (depicted in Sec. 1.2.3).

The plasmon-enhanced IPE process was first mainly studied for its sub-bandgap property [167, 169, 170, 172, 173, 178, 183]. Indeed, in plasmon-enhanced hot electron metal-semiconductor devices, the photon energy absorption cut-off depends on the barrier height and not on the semiconductor bandgap $E_g$. The barrier height can then be readily tuned (e.g. by adding an oxyde layer) depending on the desired application. Furthermore, the plasmonic properties rely only upon the metal shape and its environment. Thus, such process is a convenient way to fabricate a sub-bandgap photodetector. Such photodetectors are of particular interest in many applications sush as: Si-based solar cells (to improve their efficiency by harvesting IR region [82]), silicon photonics (for optical interconnects [264]), in optical telecommunication (for integrated optical circuits [265]), and biological and chemical sensing [266].

As reported in Sec. 1.2.2, the hot electron lifetime is short (in the ps range, [145, 149]). Therefore, harvesting them faster than their relaxation decay rate could allow for ultrafast photodetectors at THz speed. To my knowledge, only few works have measured or estimated the speed of such a device, in a non resonant structure, to values larger than the GHz bandwidth [224, 267, 268]. In this work, we study the feasability of such a detector involving sub-bandgap absorption in a plasmonic metal-semiconductor-metal (MSM) photodetector.

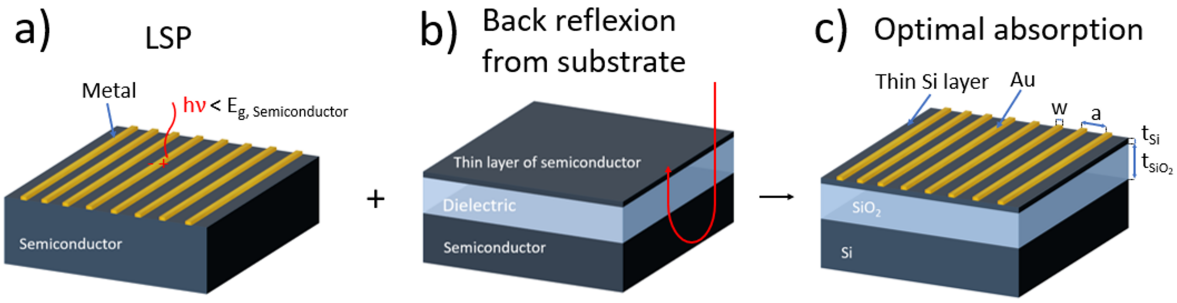


Figure 3.1: a) Metallic grating on a semiconductor substrate (with a bandgap $E_g$ greater than the photon energy). b) Multilayer stack with a thin layer of semiconductor and a layer a dielectric. c) Au grating (with a width $w$ and period $a$) on top of the Silicon On Insulator (SOI ) (with a Silicon thickness $t_{Si}$ and a Silica thickness $t_{SiO_2}$) substrate.

Fig. 3.1 resumes the strategies used to optimize the absorption within Au. In Fig. 3.1.a, to efficiently generate hot carriers, we have used a plasmonic resonant Au grating. If a grating is illuminated by light, the electromagnetic field distribution depends on the periodicity compared to the wavelength, the filling factor ff, the height and the material, the substrate and the angle of incidence of the impinging light. We focus on an excitation wavelength at 1550 nm for possible applications in telecommunication. If the polarization is orthogonal to the grating, nanoantenna-like LSPs enhance the absorption cross section. Thus, the geometrical parameters (periodicity, width and height) have to be optimized in order to match the LSP and the grating resonance. If the polarization is parallel to the grating, the absorption cross section is the geometrical cross section, hence, a small amount of light is absorbed (by skin effect) and the incident light is mainly reflected by specular reflection. The thickness of Au is set to 50 nm in order for hot carriers not to diffuse further since their mean free path is around 50 nm (see Sec. 1.2.2).

In Fig. 3.1.b, a thin layer is introduced to reduce the carrier diffusion and target the highest photodetection speed possible. The semiconductor was chosen to be non absorbant at 1550 nm (0.8 eV < $E_{g,Si}$ = 1.12 eV). In order to increase the absorption within the Au grating, we have used a multilayer stack to obtain a constructive interference in Au (their thickness are defined next section) by back reflection from the substrate. Our idea turned to a silicon-on-insulator (SOI) substrate in which the Si and $SiO_2$ thicknesses can be well controlled and Si is non absorbant above 1100 nm excitation wavelength. SOI wafers are usually built commercially under very controlled fabrication processes.

Fig. 3.1.c depicts the device principles combining: a) the LSP resonance, b) semiconductor energy bandgap higher than 1550 nm, c) thin layer of semiconductor and d) the SOI substrate. Still, stripes need to be connected in order to control the voltage applied between them i.e. the electric field. Fig. 3.2.a shows the grating stripes placed in an interdigitated scheme leading to a Metal-Semicondutor-Metal (MSM) device. For that, two pads are placed to contact the electrical bonds allowing for the interdigitated MSM scheme. The device is excited from the top at normal incidence. Compared to NPs, such interdigitated grating is more convenient to control the applied voltage. Actually, nanoparticles, such as nanoantennas [167], tipically need to be electrically connected by transparent electrodes usually made of indium tin oxide (ITO) and the applied voltage is more difficult to control.

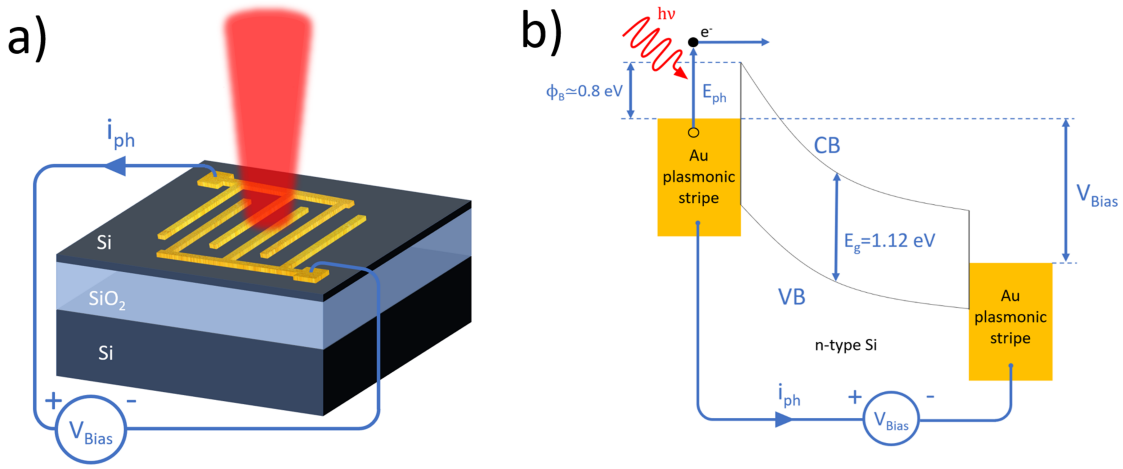


Figure 3.2: a) Schematic view of the plasmonic MSM photodetector. b) Energy band diagram of the Au stripe absorbing in a double Schottky barrier MSM structure.

Fig. 3.2.b shows the principle of the MSM design which is physically a double Schottky barrier structure. If a sufficiently high potential bias is applied to the left stripe presented on Fig. 3.2.b, the flat band voltage is reached, namely an electric field is present in the same direction all along in the Si [269]. The Schottky barrier height between Au and n-type Si is around 0.8 eV [133] enabling hot electrons to overcome the barrier. Actually, the barrier height is slightly lower than 0.8 eV because a thin layer of Ti is sandwiched between Au and Si to help Au adhesion onto Si during the fabrication process ($e\phi_{B,Ti-Si} \simeq 0.6$eV [133]). The hot carriers drift towards the right stripe thanks to the voltage bias applied between the stripes. Hot electrons have enough energy to be harvested by the right interface between Si and Au. If light hits the right stripes, hot electrons will be generated and will overcome the Schottky barrier but they will face an electric field that won't allow them to reach the left stripes. Thus, the application of a voltage breaks the symmetry of the system and there is a flow of current in one direction only (from left to right here). If light hits the

Si region, there is no absorption because the photon energy is below the bandgap of Si. Only if the incident power is large enough, two photon absorption (TPA) in Si could occur and generate carriers. The undesired TPA process is thus superimposed to the direct absorption in gold.

Simulations and plasmonic modes analysis will be performed in order to find the correct grating parameters. The grating must fullfil some specifications for photodetection applications: a) be feasible to fabricate ($\approx$ 0.5 filling factor), b) be practical to use (normal incidence excitation resonance), c) have a very confined mode (more hot electrons per unit cross section area), d) have the electromagnetic field very close to the interface (increasing the probability for carriers to overcome the Schottky barrier), and e) have the shortest periodicity possible to reduce the transit time of carriers.

The main advantage of such a plasmonic photodetector compared to classical semiconductor photodetectors is that it requires a very thin semiconductor layer, minimizing carriers scattering time and maximizing the photodetector bandwidth. The main drawback is the low efficiency of the IPE process which might lead to a low signal to noise ratio.

## 3.2 Electromagnetic modelisation of the Au grating absorption

The ultimate goal of this study would be to obtain perfect absorption inside gold i.e. all the incident field is absorbed within the grating and as close as possible to the Schottky barrier.

The history of perfect absorbers started with the first observations of Wood in 1902 [4] on metallic grating. He observed a drop in the reflection spectra for certain wavelengths, certain angles and only for TM polarization (transverse magnetic, polarization orthogonal to the grating). After Rayleigh's first attempt with the diffraction theory in 1907 [50] to explain this "singular anomalies", Ugo Fano in 1941 [270] and Hessel and Oliner in 1965 [52] showed that it was linked to a suface plasmon excitation. Plasmonic perfect absorbers were first predicted [271] and showed experimentally [272] in shallow metallic grating exciting delocalized SPPs in the 1970s. Perfect absorbers were also demonstrated with deep rectangular metallic grating with sub-wavelength width grooves (deep narrow channel) [273]. A groove acts as a Fabry-Perot-like cavity with eigenmodes and its height is of the order of magnitude of the wavelength [274]. These modes can be excited either by TE (transverse electric, polarization orthogonal to the grating) or TM polarization and are waveguide-like modes strongly confined within the groove (vertical standing waves) [273, 275]. Metamaterials are encouraging for future perfect broadband absorbers particularly interesting for photovoltaic cells [276] and can be an inspiring approach as well.

During light matter interaction, the imaginary part of the dielectric constant of a material yields the losses i.e. the electromagnetic energy dissipation [61]. For electromagnetic confinement in NPs, where the field inside the metal is the strongest is where the losses are maximal. In order to model and optimize the Au grating absorption, I modeled the optical absorption by such electromagnetic losses. For that, I used the Rigorous coupled-wave analysis (RCWA) method and the finite element method (FEM). The convention that will be used in the following is: $z$ is the normal axis, $x$ (resp. $y$) is orthogonal (resp. parallel) to the grating. Thus, TM is p-polarized light and its electric field is orthogonal to the grating.

The RCWA method is a frequency-domain modal method to solve the Maxwell equa-

tions in periodic structures. RCWA is based on expressing the fields by the Rayleigh expansion thanks to the Floquet theorem. I used the Matlab© code developed by the team of Dr. Philippe Lalanne (Reticolo v.8) [277]. It uses an eigenmode solver in which the eigenmodes are computed in all the layers in a Fourier basis [278, 279]. It solves the diffraction problem in periodic media taking into account a number of Fourier harmonics (user-defined parameter in the software). Each layer of the grating is defined by its refractive index which is a complex number if the material has losses. Reticolo calculates the diffracted electromagnetic waves within the periodic cell and finds the absorption losses L within a certain surface $s$ (in 2D simulations) by

$$L = \frac{\pi}{\lambda} \int_S \mathrm{Im}(\epsilon) |E(x,y)|^2 \mathrm{d}s. \tag{3.1}$$

All the RCWA simulations are done with an absolute error $(1 - T - R - A)$ below $10^{-4}$. The RCWA method is fast and handily adapted to 1D gratings onto multilayers.

The FEM simulation finds an approximate solution of problems managed by Partial Differential Equations (PDE) (here the Maxwell equations) [280]. The space of the problem is discretized by meshing it to triangles (2D) or tetragons (3D) or higher-order mesh structures. We define certain boundary conditions e.g. here periodic Floquet conditions. For each element, the PDE is linearized, i.e. the PDE is replaced by a system of linear equations, which can be expressed by a matrix. The matrix of each element are then combined into a global matrix solved by the software. The Maxwell equations are then solved on certain nodes of the mesh. The field a each point of the defined space can then be found by interpolation. I used Comsol Multiphysics© with the wave optics module (Electromagnetic Waves, Frequency Domain, ewfd). The absorption losses in the grating are then computed by the electromagnetic power loss density (in $W/m^3$). Indeed, Comsol solves in 3D and the depth is by default 1 m so $W/m^3$ can be used in such 2D simulations. The FEM requires a larger computation time than the RCWA method but gives more accurate maps of the field distribution within the grating structure. Thus, both methods are complementary in view of optimizing our device and understanding the way light is absorbed.

### 3.2.1 Au grating on Si

I first studied a Au grating on a Si substrate to isolate the grating effect from any multilayer stack effect. In order to find the grating parameters that maximize the Au absorption, I swept the periodicity $a$ (from 50 nm to 2000 nm with 20 nm of increment) and the filling factor ff (from 0.01 to 0.99 with 0.02 of increment). I used a RCWA method which is faster than FEM method to sweep those parameters. For each parameters $a$ and ff, the structure is excited from the top by a 1550 nm electromagnetic plane wave. The cell is represented in the (x,z) plane as a section of the stripe. I used 50 nm for the Au grating thickness on top of a Si substrate. The material properties are represented by their refractive index. For 1550 nm wavelength excitation, I used refractive indexes of 0.47 + 11.0i for Au [281] and 3.48 for Si [282]. Fig. 3.3.a depicts the cell used with the real part of the refractive indexes and Fig. 3.3.b the x component of the electric field exciting the structure.

For normal incidence excitation, the RCWA results are represented in Fig. 3.4, which plots the relative Au absorption as a function of the filling factor and the periodicity. Thus, if the relative Au absorption reaches 1, all the electromagnetic field is absorbed in the metal. In Fig. 3.4.a, the grating is excited with TM polarization, orthogonal to the grating, while in Fig. 3.4.b the grating is excited with TE polarization, parallel to the grating.

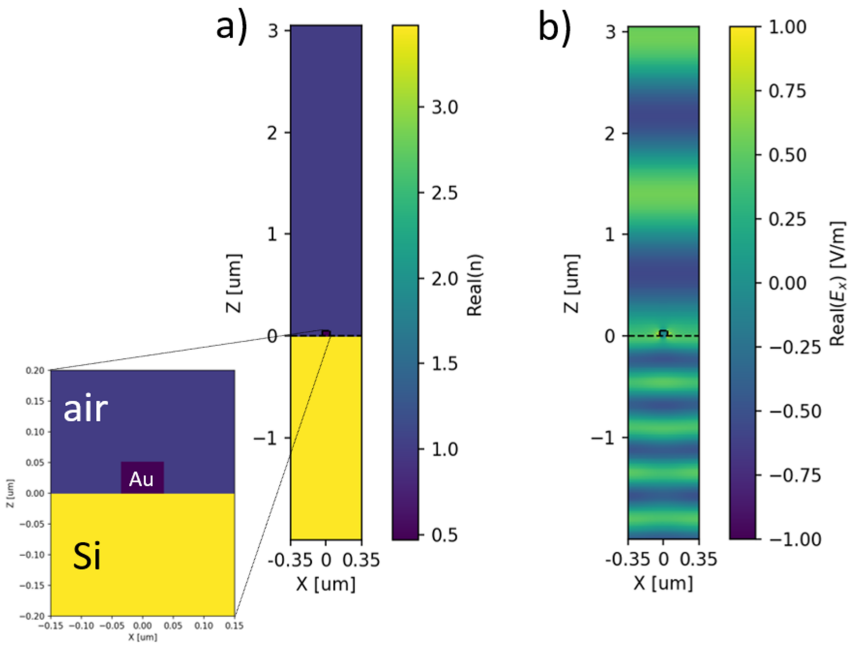


Figure 3.3: RCWA simulation cell for the Au grating on Si substrate. a) Real part of the refractive indexes. b) X component of the electric field in RCWA method (TM polarization, orthogonal to the grating).

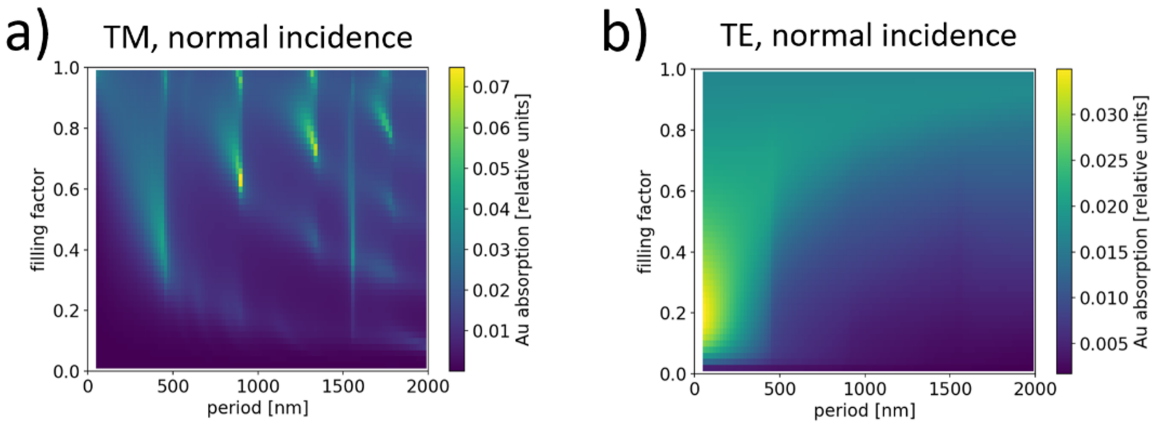


Figure 3.4: Au grating absorption on Si substrate as a function of the period $a$ and the filling factor ff (RCWA method simulation) for normal incidence: a) TM polarization, orthogonal to the grating and b) TE polarization, parallel to the grating.

Fig. 3.4.a exibits eight modes and a vertical line for a 1550 nm period (corresponding to the excitation wavelength). The four first rows of Tab. 3.1 report the moderate filling factor modes with their grating parameters and their percentage of absorption. Instead, the four last rows of Tab. 3.1 are the high filling factor modes (close to 1). These resonances absorb from 3.6 to 7.5 % of the incident light. Until now, we can assume that these resonances are the LSPs nanoantenna-like modes of the Au nanostripes excited by the orthogonal polarization. However, the resonances show a dependance on the periodicities meaning that there is most probably a coupling with the grating. Those resonances can be associated only the odd modes (mode K=1, 3, 5, ...) because even modes cannot be

excited [283] at normal incidence excitation. Such modes couple readily to the incident field but also easily radiate i.e. there are more losses. Moreover, the underlying physics of the high filling factors should be different than the moderate filling factors. High filling factor modes have very small grooves and the stripes are very close to each other. This is suggesting a coupling between the LSP of the stripe and the SPP propagating at the Au/air interface. Furthermore, the vertical line at 1550 nm is suggesting the presence of a guided mode of the grating because it is appearing at the excitation wavelength.

Fig. 3.4.b, for TE polarization, shows a lower absorption around 2 to 3.5 % and an increase of Au absorption when the periodicity decreases. In fact, the absorption is increased only in the thin film regime i.e. for slits very close to each other. The higher the gold coverage is, the higher is the absorption. In the bottom left part of the plot, there is a slight increasing of the absorption to 3.5 % (a = 50 nm, ff = 0.19, w = 9.5 nm). The absorption is low and the physics underlying such a process should be different than the LSP one. Deeper exploration has to be done to understand more such a case.

| n° | periodicity (nm) | ff | width (nm) | Au absorption (%) |
|---|---|---|---|---|
| 1 | 430 | 0.43 | 184.9 | 4.3 |
| 2 | 890 | 0.63 | 560.7 | 7.5 |
| 3 | 1330 | 0.71 | 944.1 | 6.9 |
| 4 | 1750 | 0.79 | 1382.5 | 5.0 |
| 5 | 430 | 0.95 | 427.5 | 4.0 |
| 6 | 890 | 0.95 | 845.5 | 5.7 |
| 7 | 1310 | 0.97 | 1270.7 | 5.8 |
| 8 | 1730 | 0.97 | 1678.1 | 3.6 |

Table 3.1: Resonances from Fig. 3.4.a. The four first rows are the resonances with moderate filling factors and the four last rows represent their associated high filling factor resonances.

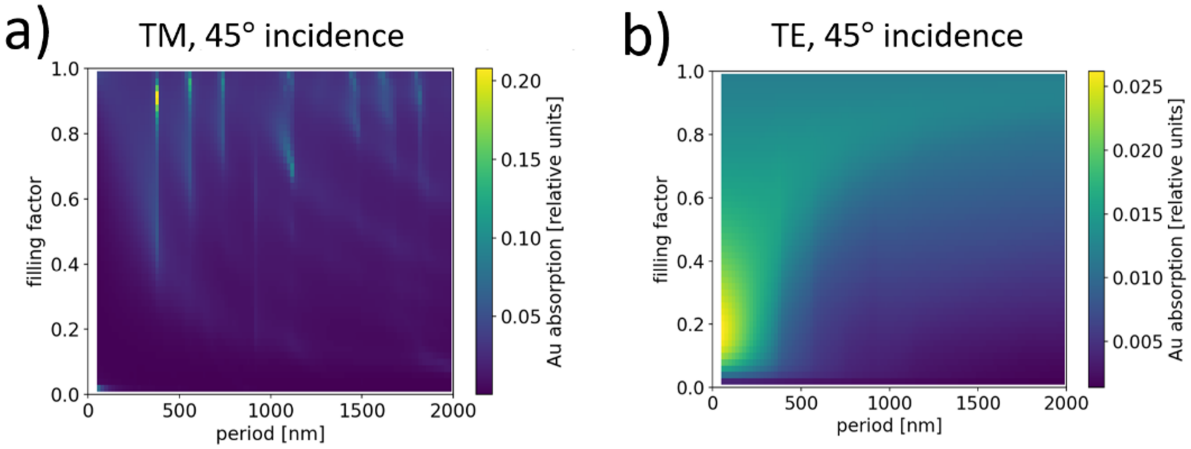


Figure 3.5: Au grating absorption on Si substrate as a function of the period $a$ and the filling factor ff (RCWA method simulation) for 45° angle of incidence: a) TM polarization, orthogonal to the grating, and b) TE polarization, parallel to the grating.

| n° | periodicity (nm) | ff | width (nm) | Au absorption (%) |
|---|---|---|---|---|
| 1 | 370 | 0.49 | 181.3 | 5.7 |
| 2 | 550 | 0.69 | 379.5 | 5.4 |
| 3 | 730 | 0.81 | 591.3 | 5.6 |
| 4 | 1110 | 0.69 | 765.9 | 9.3 |
| 5 | 1450 | 0.85 | 1232.5 | 5.2 |
| 6 | 1610 | 0.91 | 1465.1 | 5.1 |
| 7 | 1810 | 0.91 | 1647.1 | 6.8 |
| 8 | 370 | 0.91 | 336.7 | 20.7 |
| 9 | 550 | 0.95 | 522.5 | 13.7 |
| 10 | 730 | 0.95 | 693.5 | 9.5 |
| 11 | 1190 | 0.97 | 1154.3 | 6.9 |
| 12 | 1450 | 0.95 | 1377.5 | 6.5 |
| 13 | 1610 | 0.97 | 1561.7 | 6.3 |
| 14 | 1790 | 0.97 | 1736.3 | 6.0 |

Table 3.2: Resonances from Fig. 3.5.a. The seven first rows are the resonances with moderate filling factor and the seven last rows represent their associated high filling factor resonances.

In Fig. 3.5, the grating is excited with 45° of incidence in order to separate the collective oscillation resonances from the localized ones with the same sweep of the periodicity and the filling factor as for Fig. 3.4. Fig. 3.5.a, for TM polarization, shows fourteen modes and a vertical line at 910 nm. All those resonances are listed on Tab. 3.2 with moderate filling factor and high filling factor modes. For moderate filling factor modes, the Au absorption ranges from 5 to 9%, whereas for high filling factor modes, it ranges from 6 to 21%. New resonances appear compared to normal incidence excitation and they are attributed to the even modes. Those high filling factor resonances absorb more efficiently than for normal incidence excitation. Indeed, with an angle of incidence, the SPP excitation is most probably enhanced and can couple to LSP resonances more readily. Furthermore, excited even modes can poorly couple and radiate i.e. modes are more confined and absorption is increased compared to moderate filling factor modes. Moreover, the vertical line at 910 nm suggests again a guided mode of the grating. Fig. 3.5.b, for TE polarization, yields almost the same plot as for normal incidence.

In order to understand the modes implied, from Fig. 3.4.a and 3.5.a, I plotted, for the periodicity 1970 nm, the Au absorption as a function of the Au stripe width in Fig. 3.6, for normal incidence excitation (red curve) and 45° (blue curve). Both curves show an increasing trend with the width. Indeed, the larger the width, the higher the absorption because we have more absorbant medium. For normal incidence excitation, the peaks correspond to the values of the odd modes of the nanoantenna-like LSP resonances. They correspond to the results of the 4 first rows in Tab. 3.1. The blue curve represents 45° excitation, the peaks represent the odd and even modes. The peak values correspond to the width of the 7th first rows of Tab. 3.2. In the RCWA simulation Fig. 3.5.a, for a given periodicity (here 1970 nm), the filling factor is swept, and the widths match with geometries which exhibit nanoantenna-like LSP resonances. Some modes are more absorbing, compared to normal incidence excitation, as the ones in Tab. 3.2 because of, most likely, a coupling with grating modes.

To go further, I computed with FEM simulations the modes listed in Tab. 3.1 and Tab. 3.2. For all these 2d simulations, I used an incident E-field of 1 V/m. From the Comsol© solution, I extracted the electromagnetic power loss density $Q_e$ (W/m$^3$) in the cross section of a Au stripe on Si (xz plane). This quantity represents where the field is absorbed in

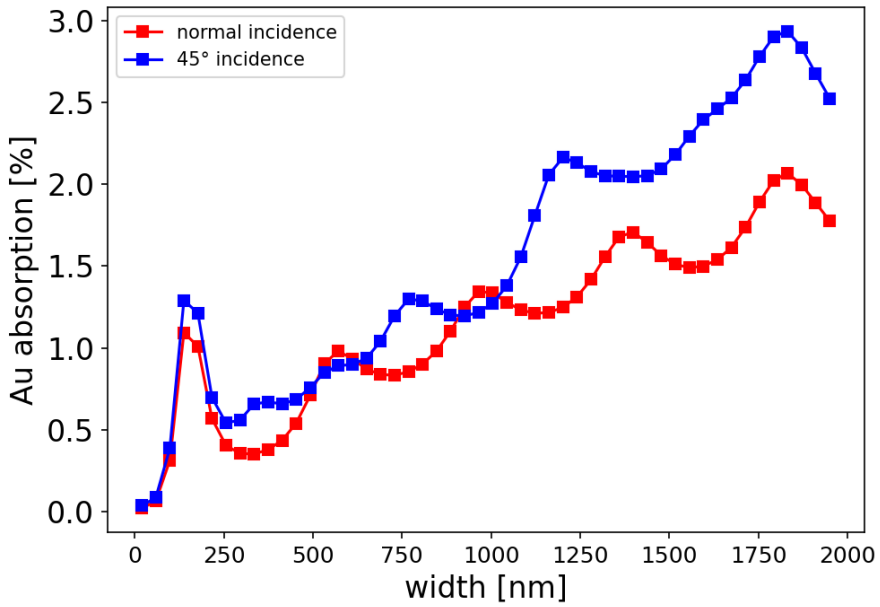


Figure 3.6: For a constant periodicity 1970 nm in Fig. 3.4.a and Fig. 3.5.a, Au absorption as a function of the width (converted filling factor) for normal and 45° excitation. It represents the odd modes (red) and the odd and even modes (blue).

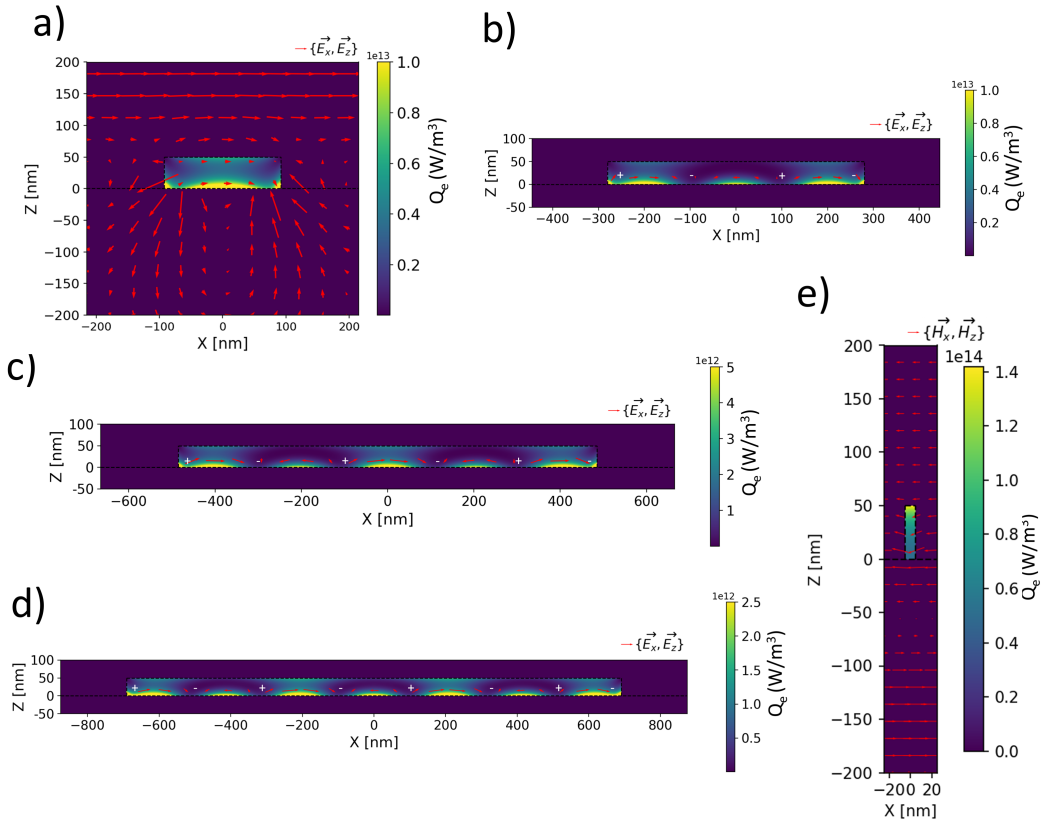


Figure 3.7: Odd resonances for the Au grating on Si. For TM polarization (orthogonal to the grating), the four moderate filling factor resonances are represented: a) n°1, b) n°2, c) n°3 and d) n°4 (from Tab. 3.1). For TE polarization (parallel to the grating) the mode is represented by e).

Au. For Fig. 3.7 a), b), c) and d) the E-field is represented by red arrows whereas for Fig. 3.7.e the arrows represent the H-field. For clarity reasons, I did not plot the E-field and H-field red arrows over the whole 2d cross section maps (as in Fig. 3.7.a) but I kept a few arrows and +/- polarity signs which represent the electrical dipole/multipole configuration.

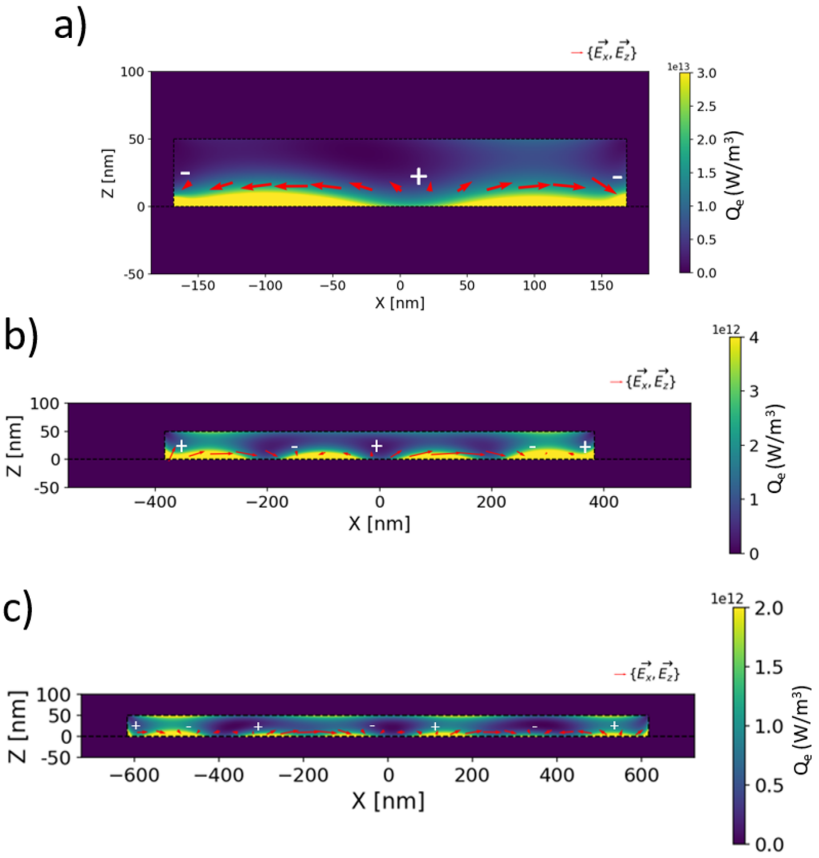


Figure 3.8: Even resonances for the Au grating on Si under 45° angle of incidence excitation. For TM polarization (orthogonal to the grating), the 3 resonances: a) n°8, b) n°4 and c) n°6 (of Tab. 3.2).

Fig. 3.7 a), b), c) and d) are the four moderate filling factor resonances in TM polarization at normal incidence excitation (four first rows in Tab. 3.1). As expected, those four resonances are the odd modes, the even ones being forbidden [284]. Observing the electric field orientation, we deduce the dipole/multipole orientation. In Fig. 3.7.a, the first resonance is a dipole and the second one, Fig. 3.7.b, is a linear quadrupole, and so on for c) and d). Thus, with a Au grating on Si, the local fields maxima (bellies) give arguments to a nanoantenna-like resonance i.e. without coupling to a propagating mode. Moreover, those modes are interesting because absorption is higher, close to the Au/Si interface. Propagative SPP Air/Au or Si/Au modes could be observe only if the separation is less than the extension of the near-field outside the stripes. As seen in Sec. 1.2.2, where the field is enhanced, the probability to generate carriers increases as well. Thus, the higher the number of carriers generated nearby the interface, the higher the probability to transfer them to Si is. I do not observe vertical cavity modes as in Ref. 273 because 50 nm Au thickness is too thin to observe any.

In Fig. 3.7.e, the large resonance in Fig. 3.4.b presents a mode with its maximal losses at the upper part of gold. For practical representation, the H-field is represented because

the excitation is for TE polarization. Thus, such resonance is less interesting for Schottky barrier applications.

The even modes can be excited only if symmetry is broken e.g. excitation with an angle of incidence. I studied with Comsol© the modes excited with a 45° angle of incidence. Fig. 3.8.a shows the even resonance n°8 in Tab. 3.2. It is an even mode with its two bellies. In Tab. 3.2, Fig. 3.8.b represents the mode n°4 and Fig. 3.8.c represents the mode n°6. Those figures also outline mirror symmetry under the (y,z) plane. This model can be optimized by finding the angle that maximizes the excitation of grating modes and the coupling with the LSP.

### 3.2.2 Au grating on Silicon on Insulator (SOI)

In order to enhance the Au absorption, the idea was to use a multistack effect to yield constructive interferences within the Au stripes. There were three SOI wafers available in our laboratory with different thicknesses: a) $t_{Si}$ = 1 µm and $t_{SiO_2}$ = 2 µm, b) $t_{Si}$ = 0.145 µm and $t_{SiO_2}$ = 1 µm and c) $t_{Si}$ = 0.5 µm and $t_{SiO_2}$ = 1.5 µm. Three RCWA simulations were done with 50 nm thickness Au grating on SOI, for each wafer parameter, at normal incidence and for orthogonal polarization excitation. The cell used for this simulation is similar to Fig. 3.3 by adding Si and $SiO_2$ layers with specific thicknesses and refractive indexes. The refractive index of $SiO_2$ was 1.466 [285]. I obtained the Au absorption as a function of the periodicity and the filling factor (as for Fig. 3.4 but on SOI). The wafer b) ($t_{Si}$ = 0.145 µm and $t_{SiO_2}$ = 1 µm) yielded the highest value of 29% absorption peak and was chosen for fabrication. Indeed, the other wafers yielded no more than 5% of Au absorption.

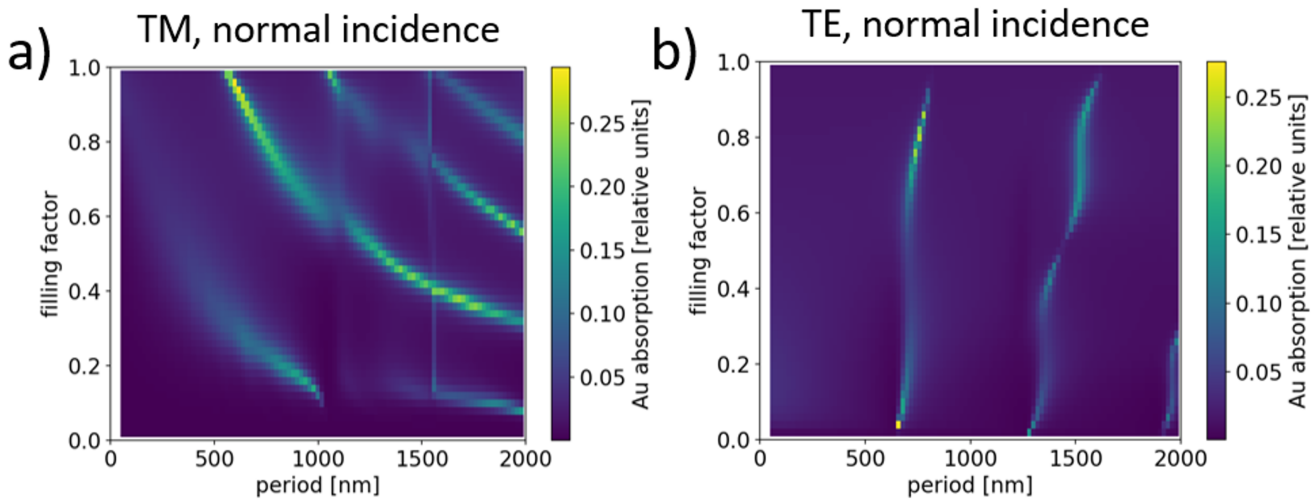


Figure 3.9: Au grating absorption on SOI substrate as a function of the period *a* and the filling factor ff (RCWA method simulation) for normal incidence: a) TM polarization, orthogonal to the grating, and b) TE polarization, parallel to the grating.

In Fig. 3.9, the grating is excited at normal incidence. For TM polarization, orthogonal to the grating, Fig. 3.9.a presents 5 main resonances (and 2 which begin and finish out of the map) and a vertical line at 1550 nm. The values of those resonances are reported Tab. 3.3 and are the odd ones (because of normal incidence excitation [283]). As for Au on Si substrate, I retrieve resonances with moderate and high filling factor. In Tab. 3.3, the resonance n°4 gives the highiest absorption (29.4%) but its filling factor is very high i.e.

the two stripes will be very close from each other (spaced by only 29.5 nm) which would induce nanofabrication difficulties. The resonance n°1 has a lower absorption compared to n°4 but its filling factor of 0.13 is easier to process. The space between stripes is lower for resonance n°4 (970-126.1 = 843.9 nm) than for resonance n°2 (1670 - 617.9 = 1052.1 nm) reducing the carrier transit time. Furthermore, the stripe surface area with the grating parameters of resonance n°4 is the lowest ($\sigma_{geom.}$ = 6305 nm$^2$). Thus, the mode is more confined in this tiny section and the density of hot electrons generated is the highest for this configuration (number of hot electrons per unit surface area).

Surprisingly, Fig. 3.9.b, for the TE polarization (parallel to the grating), gives sharp resonances up to 27%. Those resonances are not very dependent on the filling factor but are mainly dependent on the periodicity. The physics underlying this absorption process should be linked to a coupling with the periodicity and is very different compared to the LSP nanoantenna-like absorption.

| n° | periodicity (nm) | ff | width (nm) | Au absorption (%) |
|---|---|---|---|---|
| 1 | 970 | 0.13 | 126.1 | 18.1 |
| 2 | 1670 | 0.37 | 617.9 | 24.9 |
| 3 | 1930 | 0.57 | 1100.1 | 23.6 |
| 4 | 590 | 0.95 | 560.5 | 29.4 |
| 5 | 1050 | 0.97 | 1018.5 | 22.7 |

Table 3.3: Resonances from Fig. 3.9.a. The three first rows are the resonances with moderate filling factor and the two last rows represent the high filling factor resonances.

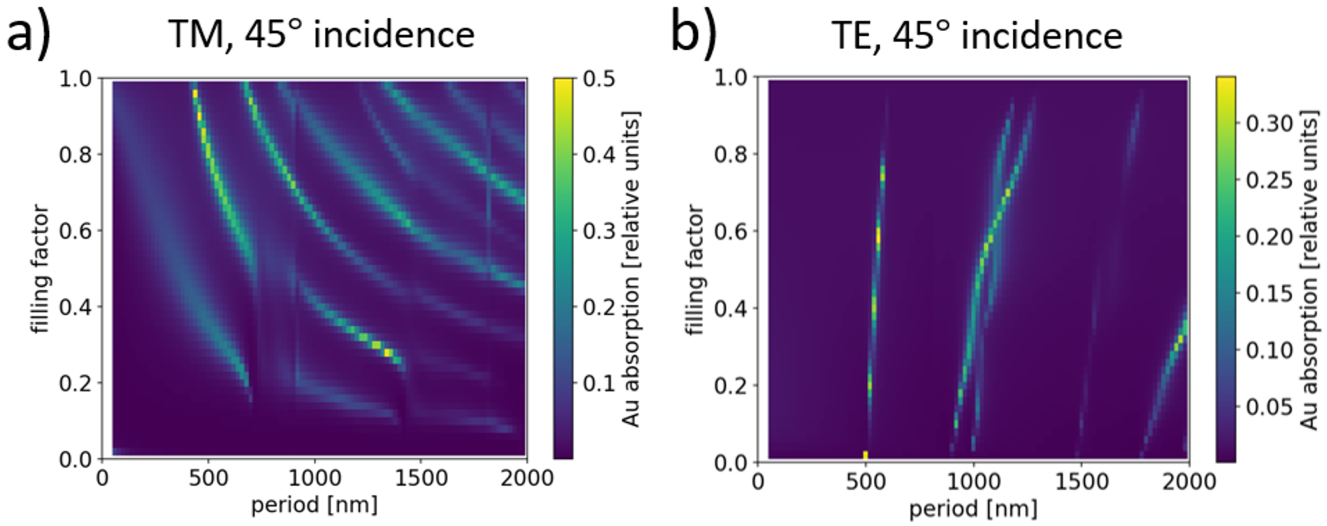


Figure 3.10: Au grating absorption on SOI substrate as a function of the period $a$ and the filling factor ff (RCWA method simulation) for 45° angle of incidence: a) TM polarization, orthogonal to the grating, and b) TE polarization, parallel to the grating.

To better understand the modes in these nanostripes, Fig. 3.10 illustrates the same geometry for 45° incidence excitation. In Fig. 3.10.a, the excitation is for TM polarization, orthogonal to the grating and the resonances are listed Tab. 3.4. The 45° excitation breaks the symmetry and allows one to excite the even modes. For instance in Tab. 3.4, resonances n°2 and n°3 are new compared to Fig. 3.9.a. The resonances n°1 of Tab. 3.3 and

n°1 of Tab. 3.4 have close parameters and could then correspond to the same plasmonic mode (only the electromagnetic 2D maps can answer this next). The resonance n°5 has the highest absorption (50%) followed by resonance n°2 (48.8%). Indeed, such modes are difficult to excite and to couple radiatively. Thus, they might be less lossy and absorb more with a higher quality factor. But, we did not choose these grating parameters for the final device because a normal incidence excitation is preferred for a device.

| n° | periodicity (nm) | ff | width (nm) | Au absorption (%) |
|---|---|---|---|---|
| 1 | 650 | 0.23 | 149.5 | 25.0 |
| 2 | 1330 | 0.27 | 359.1 | 48.8 |
| 3 | 1430 | 0.61 | 872.3 | 31.9 |
| 4 | 1870 | 0.71 | 1327.7 | 29.7 |
| 5 | 450 | 0.89 | 400.5 | 50.0 |
| 6 | 690 | 0.93 | 641.7 | 42.2 |
| 7 | 830 | 0.97 | 805.1 | 15.8 |
| 8 | 1370 | 0.95 | 1301.5 | 25.9 |
| 9 | 1650 | 0.95 | 1567.5 | 13.0 |

Table 3.4: Resonances of Fig. 3.10.a. The four first rows are the resonances with moderate filling factor and the five last rows represent the high filling factor resonances.

For TE polarization, parallel to the grating, Fig. 3.10.b, exibits other resonances and 34% absorption is reached. As for Fig. 3.9.b, those resonances depend especially on the periodicity. The resonances around 500 nm periodicity is most likely a coupling between resonant cavity modes (enhancement for 4 filling factors) and the periodicity of the grating.

To better understand the origin of those resonances found with the RCWA method, I performed FEM simulations with Comsol©. I used the same procedure as for the Au grating on Si but with the layered substrate (SOI). I first simulated the electromagnetic field with the grating parameters given in Tab. 3.3. I confirmed that the three first lines of Tab. 3.3 correspond to the three first odd modes (K=1, 3, 5) in FEM simulations (by studying the bellies and nodes) while the two last lines give the modes K=3 and K=5. Thus, similar field are acquired within the grating as in Fig. 3.7 for Si. Actually, the width parameters of Tab. 3.3 are very close to the ones found for Si (see Tab. 3.1). This suggests the resonances found with the SOI substrate are nanoantenna-like LSPs enhanced by the multilayer effect. And, in Tab. 3.3 resonances 2/4 and 3/5 yield close width parameters (617.8/560.5 nm and 1100.1/1018.5 nm) suggesting that similar nanoantenna-like resonances are excited. Moreover, those modes present electromagnetic fields very close to the interface which is a good argument to increase the probability for hot carriers to overcome the Schottky barrier.

I also simulated the electromagnetic field with grating parameters given in Tab. 3.4. Both odd and even modes were obtained as in Fig. 3.8. Those modes present mirror symmetry compares to the (y,z) plane. Their electromagnetic field is nearby the Schottky barrier interface which is very interesting for photodetection applications. Again, for normal or 45° incidence, there is no vertical cavity mode which would occur only with deep and narrow slit [185].

It is worth noticing the unexpected resonances for TE polarization. Fig. 3.11 represents the 4 main resonances of Fig. 3.9.b: a) periodicity = 650 nm, ff = 0.03, width = 19.5 nm, absorption = 28%, b) periodicity 750 nm, ff = 0.79, width = 592.5 nm, absorption =

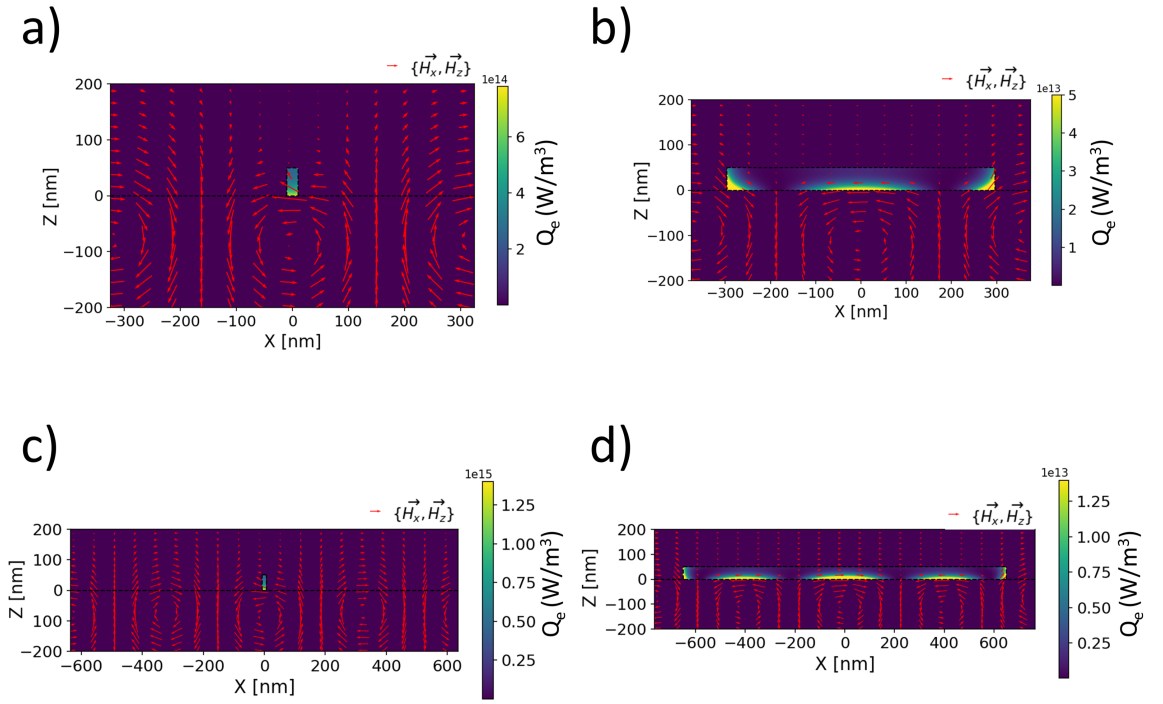


Figure 3.11: Resonances for the Au grating on SOI under normal incidence excitation. For TE polarization (parallel to the grating), a), b), c), and d) represent the four main resonances in Fig. 3.9.b.

24%, c) periodicity = 1270 nm, ff = 0.01, width = 12.7 nm, absorption = 14%, and d) periodicity = 1530 nm, ff = 0.85, width = 1300.5 nm, absorption = 16%. The absorption rates are high and also sharp, in a sense that a slight modification of the grating parameters would lead to no absorption (not robust to fabrication). The red arrows represent the magnetic field $\vec{H}$. For the resonances, the magnetic field distribution shows vortices rotating around the y-axis at 100 nm below the stripe. Three vortices are in Fig. 3.11.a) and b) and four in Fig. 3.11.c) and d). Those resonances could be explained by the stripe width and the multistack effect allowing the rotation of the magnetic field for those particular parameters.

After having studied the resonances occuring within a 50 nm thickness Au grating on SOI substrate of 145 nm/1000 nm, we chose to fabricate the grating with a periodicity of 970 nm, filling factor 0.13 and width of 126.1 nm, yielding 18.1% of absorption (n°1 in Tab. 3.4). Such a grating fullfils the grating specifications presented Sec. 3.1. Even if this mode has not the highest absorption rate, it yields the best trade off to enhance the absorption and obtain a high speed device.

### 3.2.3 Simulation of the spectral behaviour of the selected grating

In order to characterize the device with the selected grating parameters, I studied the absorption, reflection and transmission spectra with RCWA simulations taking into account chromatic dispersion of the materials. Fig. 3.12 represents the efficiencies of absorption, reflection and transmission, as a function of the wavelengths for TM and TE polarization. In Fig. 3.12.a, there is an enhancement of absorption at 1550 nm. The reflection (resp. transmission) is strongly enhanced (resp. inhibited) at the resonance close to 1550 nm. Except for the variation of the reflection and transmission, the absorption is enhanced up

to 20% at the resonance showing that the resonance localizes the field inside the metallic structure. For TE polarization, Fig. 3.12.b presents no absorption at 1550 nm but a peak at 1910 nm. This resonance may have the same physical origin as for Fig. 3.11.

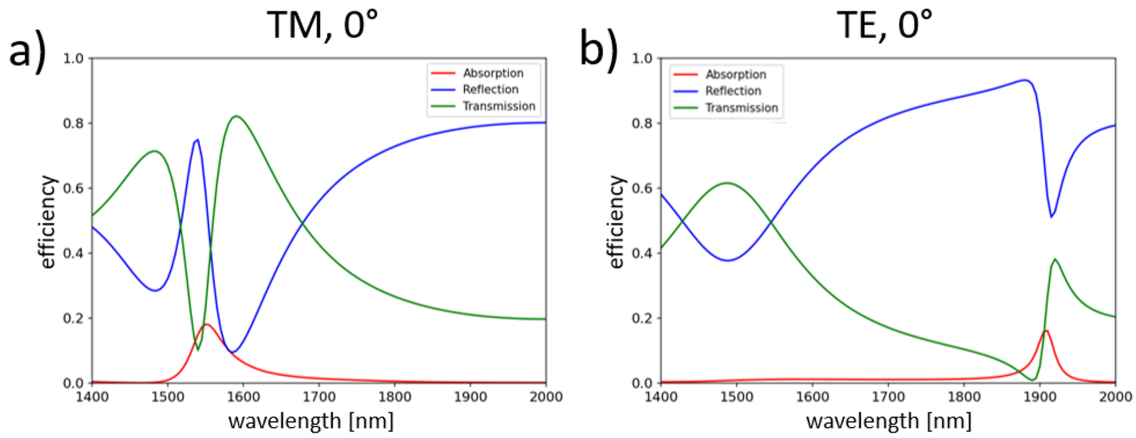


Figure 3.12: Absorption, Reflection and Transmission efficiencies spectra for: a) TM polarization (orthogonal to the grating) and b) for TE polarization (parallel to the grating).

To test the robustness of the device, I simulated the grating absorption spectra for several stripe widths. In fact, during the fabrication process, the filling factor can be slightly higher/lower because of the applied dose during the e-beam lithography step (see Sec. 3.3). This results in a modification of the stripe width which shifts the resonant wavelength. For longer widths, we expect a longer wavelength resonance (c.f. Sec. 1.2.1). In order to study how the absorption spectra changes if the filling factor is modified, Fig. 3.13.a represents the Au absorption as a function of the filling factor and the wavelengths (for a constant periodicity of 970 nm). For a constant wavelength, Fig. 3.13.a shows two resonances: one with a low filling factor and one with a high one. The resonance wavelength and the filling factor evolve linearly with a positive slope.

The resonance we chose (width = 126 nm) is within the lower section of Fig. 3.13.a. Fig. 3.13.b depicts the wavelength of maximal absorption (blue) and its absorption (red) as a function of the stripe width. If the width increases from 50 nm to 300 nm, the wavelength resonance red-shifts from 1500 nm to 1950 nm. This behaviour is expected for LSP nanoantenna-like resonance (see Sec. 1.2.1). If the width is modified, from 100 nm to 180 nm, the Au absorption varies from 15 to 25%. Thus, during the fabrication process, if the width is unintentionally varied, the resonance will be tuned to red but the absorption will remain high yielding a proper robustness for the proof of principle of the grating.

To promote the adhesion of Au on Si, a thin layer of Ti is deposited (between 5 and 8 nm) between Si and Au. This thin layer could somehow affect the resonance. However, curiously, the refractive index of Ti is not well defined in the literature, with large discrepancies between studies, at 1550 nm: 3.5983 + i4.0483 (Mash and Motulevich, 1973 [286]), 3.6845 + i4.6088 (Johnson and Christy, 1974 [287]), 4.0263 + i3.8136 (Ordal et al., 1988 [288]), 0.6850 + i12.970 (Werner et al., 2009 [289]), and 3.4323 + i3.1162 (Palm et al., 2018 [290]). Care must be taken on the study of Werner et al. which has very large difference compare to other studies.

In order to take this effect into account, I simulated absorption spectra for each Ti refractive index value (RCWA simulations) with the selected grating parameters (periodicity = 970 nm, ff = 0.13 and width = 126.1 nm). For each of these values, Fig. 3.14.a depicts the maximal Au absorption rate and Fig. 3.14.b the wavelength of maximal absorption

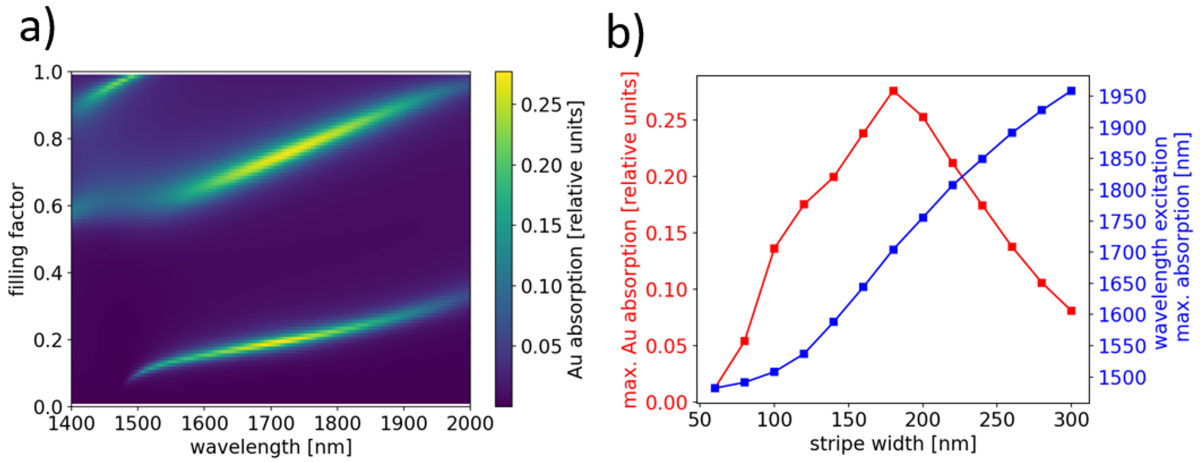


Figure 3.13: a) Au grating absorption on SOI substrate as a function of the filling factor ff and the excitation wavelength (RCWA method simulation) with a constant period (950 nm). b) Representation of the absorption spectra (maximal absorption and resonant wavelength) as a function of the stripe width.

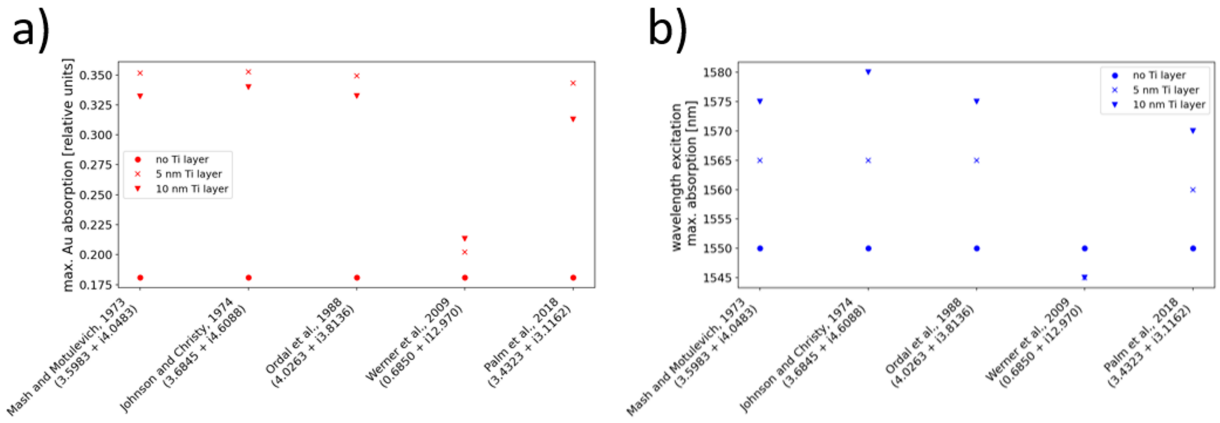


Figure 3.14: a) Maximal Au absorption (resp. b) wavelength of maximal absorption) within a RCWA simulation Au absorption spectra as a function of five values of Ti in the literature.

as a function of the different values given in the literature for Ti (for 5 nm, 10 nm or no Ti layer). The trend is to increase the absorption under the presence of Ti (50%) and to slightly red-shift the resonance wavelength by less than ≈2% (except for the Werner et al. values). Thus, the effect of the Ti layer is to increase the absorption of the incident light and redshifting the resonant wavelength. Furthermore, at the Ti-Si interface the Schottky barrier height is 0.6 eV [133]. Hence, the presence of Ti sligthly reduces the Schottky barrier between Au-Si (which is 0.8 eV), increasing the probability of carriers to be emitted over the barrier. This emphasizes on the importance to consider carefully the role of this intermediate layer.

### 3.2.4 Free optimization of the device parameters

In order to further optimize the device parameters maximizing the Au absorption without the constraints given by the available SOI wafers, I finally used optimization algorithms

within two approaches: a fixed Au thickness of 50 nm or a variable thickness. I used the Matlab© Global optimization toolbox to find the global optimum of RCWA models. The model is made of a vector containing the parameters to be optimized: here the grating periodicity and filling factor, the Si and $SiO_2$ thicknesses of the SOI (plus the Au grating thickness). The optimization criterion is the Au absorption given by the RCWA model. I used the solver fmincon which is applied for non linear constraint problems with the algorithm Sequential Quadratic Programming close to the Newton method i.e. an algorithm to find the root of continous functions. The constraints of this problem are the lower and higher boundaries (e.g. for the Si thickness, the problem will explore values between minimal and maximal Si thicknesses). At every iteration, the solver changes the vector's values exploring the parameters space depending on the gradient. Indeed, the gradient is estimated by finite differences and function evaluations around the previous iteration point. The iterations stop when the solver: a) tries a step size smaller than a relative bound (TolX) with condition $|(x_i - x_{i+1})| < \text{TolX}(1 + |x_i|)$, b) finds a value of the objective function below a relative bound (TolFun) with condition $|(f(x_i) - f(x_{i+1}))| < \text{TolFun}(1 + |f(x_i)|)$, or c) finds a value of the first-order optimality smaller than a relative bound (OptimalityTolerance). For my simulations I kept the relative bounds TolX, TolFun and OptimalityTolerance at $10^{-6}$. Running several initial vectors (with the MultiStart option), the algorithm explores the space parameters, finds local minima and may find the global maximum of the problem. As every start, the initial vector is defined randomly by MultiStart to maximize the space exploration. After the algorithm finds minima, we still have to understand the physical interpretation of those outputs.

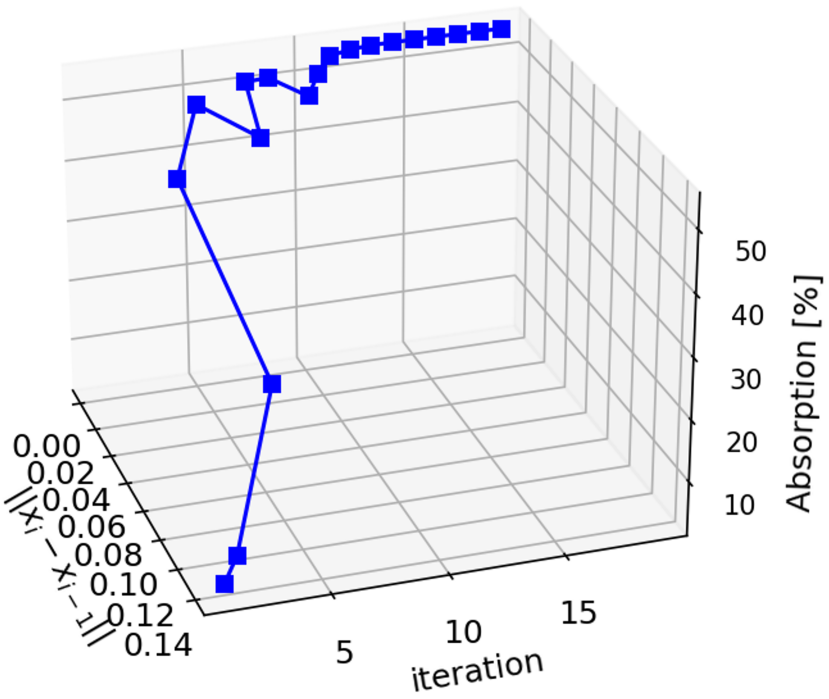


Figure 3.15: Optimization algorithm convergence for the step size stopping criteria.

For the step size stopping criteria, Fig. 3.15 presents how the algorithm convergence path evolves from a step size $\approx 0.12$ at iteration 1 with 2% absorption (bottom left) to below $10^{-6}$ at iteration 19 with more than 50% absorption (up right).

**Au thickness as a constant parameter** In a first approach, I used four parameters: the grating periodicity a and filling factor ff, the thickness of Si $t_{Si}$ and silica $t_{SiO_2}$ (thus vector x to be optimized has dimension four), keeping 50 nm Au thickness. The question to answer is: what would be the SOI wafer and the grating parameters that maximize the Au absorption within 50 nm thickness of Au? The lower and upper boundaries are a = 50 to 2000 nm, ff = 0.01 to 0.99, $t_{Si}$ = 50 to 2000 nm, and $t_{SiO_2}$ = 50 to 2000 nm.

With 200 multistarts, keeping a Au thickness of 50 nm and without the Ti layer, solutions reach maximal Au absorption of 65%. Fig. 3.16 gives the parameter distribution for solutions with absorption larger than 30%. Fig. 3.16.a presents the solutions as a function of their length, so I can retreive if there are recurrent solutions (for example, which Si thickness gives converging solutions). The width solutions converge around three lengths: a) 131 nm, b) 542 nm, and c) 895 nm (means of those values, represented by horizontal black solid lines on Fig. 3.16.a). It is very interesting to notice that those widths correspond to the stripe width exibiting LSP modes for the Au grating on Si discussed earlier (see Fig. 3.6). So, the algorithm found that the solutions absorbing the most (between 30 to 65 %) are modes linked to the LSP nano-antenna like resonances. Fig. 3.16.b shows the histograms of the solutions after convergence. The values are represented as histograms and the vertical black solid lines are the means of values if some of them are grouped together.

On Fig. 3.16.a and .b, the periodicity seems to have no specific influence on the absorption. Previous work in Sec. 3.2.2 showed that there is a small coupling with the periodicity, thus here there might not be enough convergent solutions to obtain a clear statistical evidence of the physical behaviour.

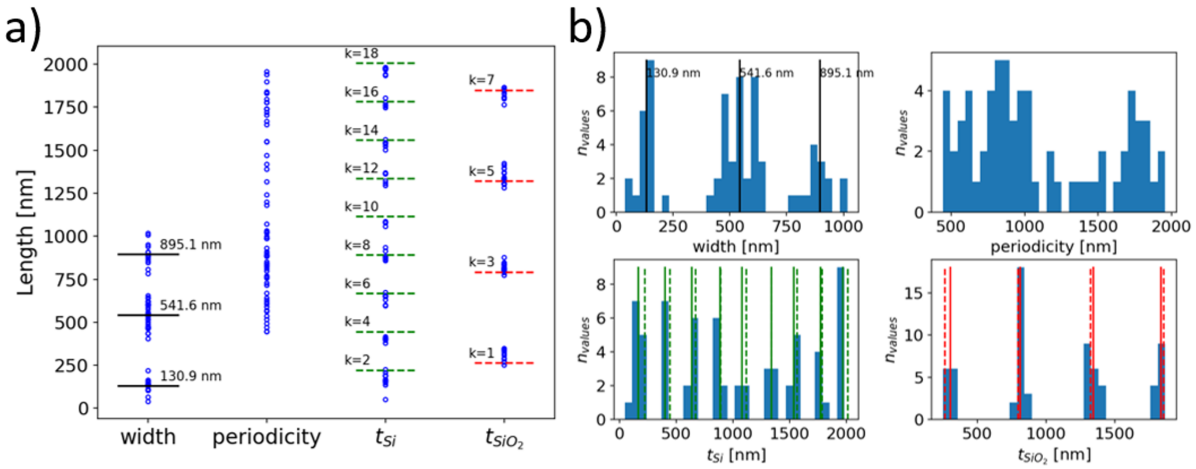


Figure 3.16: Representation of the converging solutions for absorption between 30 to 65% (maximal value) for the grating periodicity and width and for the Si and $SiO_2$ thicknesses. The Au grating thickness is constant: 50 nm. The black solid lines are the means of clumped values of the width. The green (resp. red) dashed line is the even (resp. odd) values of the Bragg condition ($\lambda_{Bragg}/4n$). a) Vertical representation as a function of the length of each parameter and b) histogram representations.

On the contrary, in Fig. 3.16.a, the Si and silica thicknesses are clumped to multiples. I found that the Si thicknesses of convergent solutions are the even multiples of $\frac{\lambda_0}{4n_{Si}}$ (represented by horizontal green dashed lines). While $SiO_2$ thicknesses are the odd multiples of $\frac{\lambda_0}{4n_{SiO_2}}$ (represented by horizontal red dashed lines). This simply means that the optimal stack of layers is that of a Bragg mirror reflecting light thanks to constructive interferences.

However, in usual Bragg mirors, the first layer has a refractive index lower than the second one so that the thickness $t_i = \frac{\lambda_{Bragg}}{4n_i}$ (with $i$ the considered medium) gives a phase shift of $\pi/2$ in each layer. This does not apply here, because the first layer has a higher refractive index ($n_{Si}$) than the second one ($n_{SiO_2}$) and the phase shift has to change. In fact, Fig. 3.17 represents two cases to obtain constructive intereferences for reflections at the second and third interfaces. In the first case, if the incident wave is arriving on the second interface (i.e. from Si to $SiO_2$), there is no additional $\pi$ phase shift as in the classical Bragg mirror (because $n_{SiO_2} < n_{Si}$). Thus, the propagation through the first layer should give a $\pi$ phase shift instead of $\pi/2$ phase shift. The thickness of the first layer is then $t_{Si} = 2k\frac{\lambda_{Bragg}}{4n_{Si}}$ (with $k \in \mathbb{N}^*$). In the second case, if the wave is impinging on the third layer (i.e. from $SiO_2$ to Si), the reflected field will gain an additional $\pi$ phase shift. Therefore, the thickness of the second layer should just give a $\pi/2$ phase shift and its thickness is $t_{SiO_2} = (2k+1)\frac{\lambda_{Bragg}}{4n_{SiO_2}}$ (with $k \in \mathbb{N}^*$). We are not looking for constructive interferences exactly at the first interface (between air and Si) to obtain a perfect reflector. Here, the constructive interferences occur within the 50 nm thinckness of Au in order to confine as much energy density as possible within the grating.

Combining the LSP nano-antenna like behaviour and the multistack effect constructive interferences leads to a maximal absorption of 65% within only 50 nm of Au.

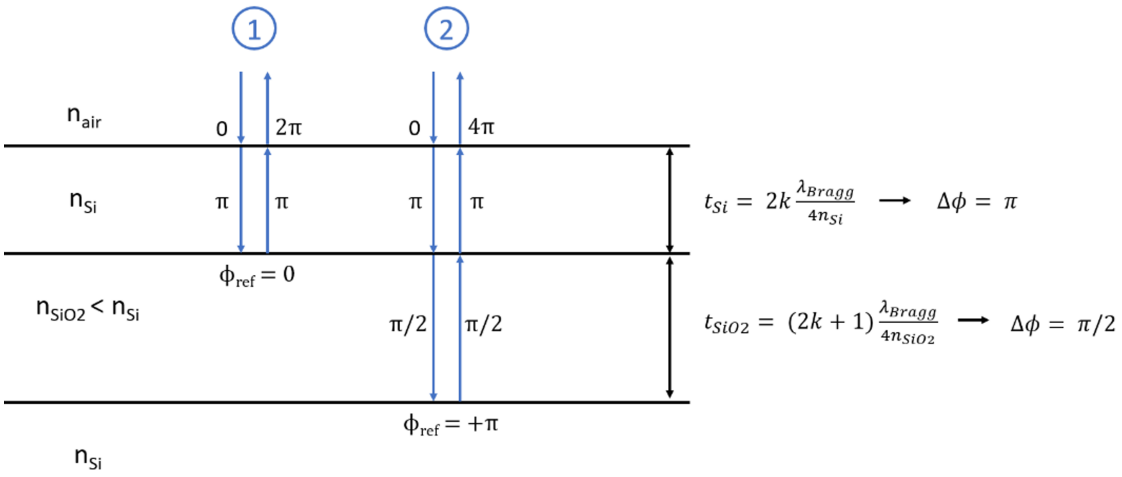


Figure 3.17: Bragg mirror with the first layer higher refractive index factor ($n_{Si}$).

**Au thickness as a free parameter** With the second approach, I used five parameters to optimize the Au absorption: the four parameters used for the first approach plus the Au grating thickness as a free parameter. The question was: is it possible to obtain a perfect absorber varying all the geometrical device parameters? Thus, the vector x to be optimized is 5D. The lower and upper boundaries are a = 50 to 2000 nm, ff = 0.01 to 0.99, $t_{Au}$ = 10 to 2000 nm, $t_{Si}$ = 50 to 2200 nm, and $t_{SiO_2}$ = 50 to 2200 nm.

Since it is not possible to plot a 5D graph we reported the possibility to have perfect absorption with more than 99% absorption. A major result is that the algorithm reaches perfect absorption within Au. The solver converges to more than 99% aborption for Au thickness larger than 50 nm (that was used in the previous approach).

Fig. 3.18.a shows the geometries which present perfect absorption for the grating thickness of Au: a) 208.7 nm, b) 786.4 nm, c) 1396.3 nm, and d) 1917.5 nm. Those modes

are most likely vertical cavity modes within deep and narrow slits [185]. The histogram Fig. 3.18.b shows clear evidence of those vertical modes.

In Fig. 3.18.a, the periodicity, width and the thicknesses of Si and $SiO_2$ give less clear evidence of multiple values than for the first approach (more spread). It seems that the vertical modes are so absorbing that they need less the multistack effect to have constructive interferences within the Au grating. Observing the row data of the converged solutions, I found that there are resonances with high filling factor (close to 1) and with moderate filling factor ($\approx 0.7$). This is a strong suggestion of several physics underlying those phenomenons (at least two). Another argument for this is in Fig. 3.18.b, where the slit width (the distance between two stripes) gives a mean around 50 nm but there are also values between 100 to 150 nm rendering vertical modes impossible.

In order to complete this work, I translated the conditions for perfect absorber resonances into Comsol simulations. I selected four resonances represented in Fig. 3.19: the two upper ones are high filling factor resonances whereas the two bottom ones are the moderate filling factor resonances . We can clearly see different physics related to those resonances.

In Fig. 3.19, I represent the high filling factor resonances: a) a = 421 nm, ff = 0.973, w = 897 nm, $t_{Au}$ = 190.1) and b) a = 925.4 nm, ff = 0.969, w = 897 nm, $t_{Au}$ = 248 nm. These resonances have lateral vertical resonance coupled to the nearby stripes and the electromagnetic field is localized on the lateral edges as well. This gives a clear argument in favour of vertical narrow and deep slit modes. Moreover, a mode close to the interface with Si is also present suggesting a coupling between the vertical and horizontal SP modes.

The moderate filling factor resonances are presented Fig. 3.19: c) a = 874.5 nm, ff = 0.746, w = 652.4 nm, $t_{Au}$ = 289 nm and d) a = 1459.9 nm, ff = 0.758, w = 1106.3 nm, $t_{Au}$ = 167.2 nm. They have no vertical resonances and present only absorption modes close to the Schottky barrier. These device parameters present all the characteristics to be a perfect absorber adapted to photodetection since the electromagntic field is localized nearby the Schottky barrier.

In conclusion, most of the resonances have high filling factor (close to one) because vertical modes are more absorbing. But there exist modes without vertical character still being perfect absorbers.

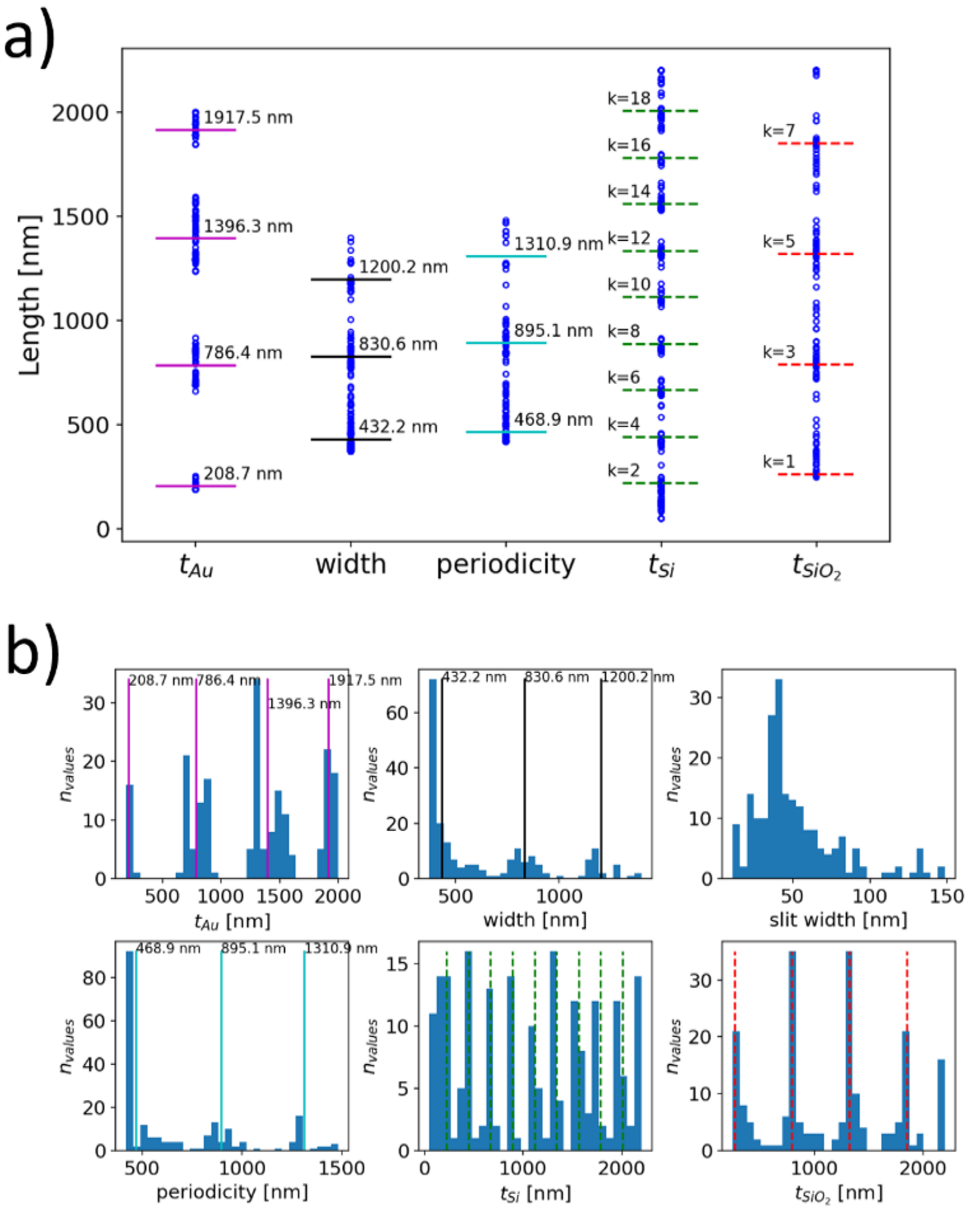


Figure 3.18: Representation of the converging solutions for absorption between 99 to 100% (maximal value) for the grating thickness, periodicity and width, and for the Si and $SiO_2$ thicknesses layers. The black, purple and green solid lines are the means of the clumped values. The green (resp. red) dashed line is the even (resp. odd) values of the Bragg condition ($\lambda/4n$). a) Vertical representation as a function of the length of each parameter and b) histogram representations.

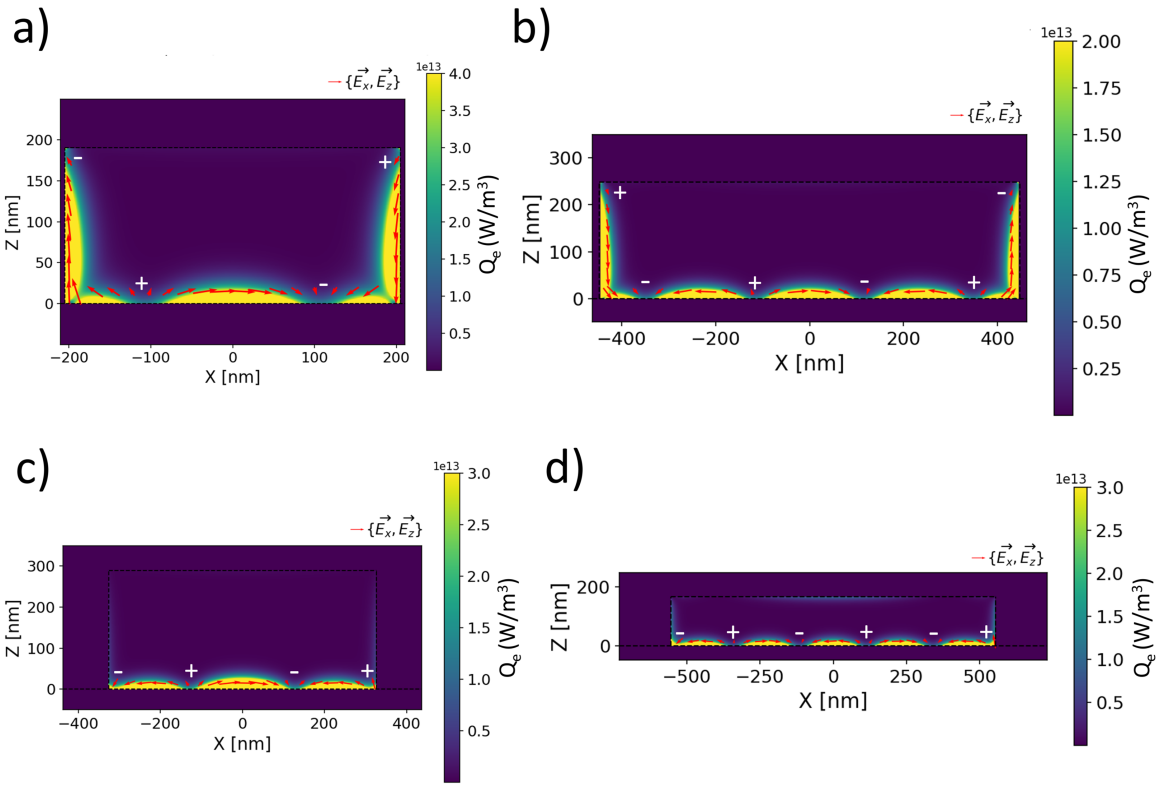


Figure 3.19: Optimized to perfect absorption resonances for the Au grating on SOI under normal incidence excitation. a) and b) are for the high filling factor resonances, c) and d) are for the lower filling factor resonances.

## 3.3 Nanofabrication

The interdigitated MSM plasmonic photodetector was fabricated with the chosen parameters at the L-NESS laboratory of Politecnico di Milano in Como (Italy). I took part in the fabrication under the supervision of Dr. Monica Bollani.

I used the Raith software to design the Au structure to be fabricated (Fig. 3.20). There are two large pads of 200 × 300 $\mu m^2$ in order to connect the wires (bonding step) and the structure is in the middle of the fabricated sample (3.20.a). The pads cannot be reduced because it would be too difficult then to bond any wire. We decided to make a square MSM detector of 50 × 50 $\mu m^2$ because (Fig 3.20.b) a) the scanning stage for optical testing has a range of 100 × 100 $\mu m^2$ and b) larger devices give larger photocurrent but also slow down the bandwidth (by increasing the RC constant) and increases the dark current. The stripes are connected to the electrodes and we added a trianglular taper in order to facilitate the development and lift-off steps. The Raith software output is a .gds file that is used by the e-beam lithography apparatus.

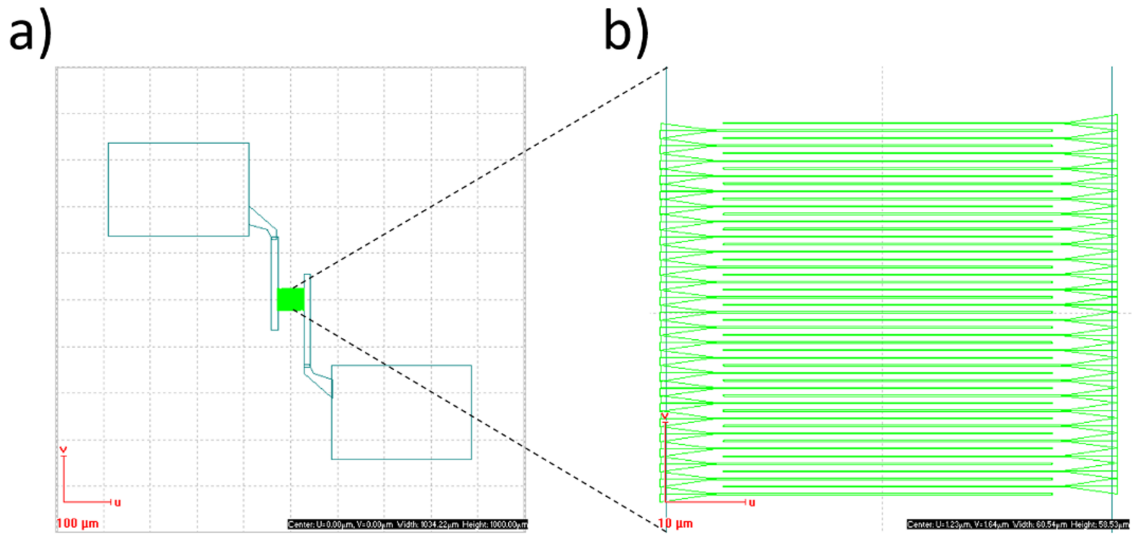


Figure 3.20: MSM design using Raith software. a) The whole structure with the pads. b) Zoom onto the detector area.

All the fabrication steps are summurized in Fig. 3.21 and the parameters are described in Tab. 3.5. We used a Silicon on Insulator (SOI) wafer (145 nm of Si and 1000 nm of $SiO_2$) and I cut a square sample of 2 × 2 $cm^2$ from it. Then, I cleaned the sample with ultrasounds (US) in acetone followed by an IsoPropyl Alcohol (IPA) bath and air dry. By spin coating, I added two layers of PolyMethylMethAcrylate (PMMA) with different molecular weight followed by baking steps. We used two different weights in order not to have rectangular edges at the e-beam lithography step but slightly bended edges and thus facilitate the development step. The sample is then exposed by e-beam lithography. PMMA is a positive resist meaning that the exposed regions will be removed after development. Several tests were done to optimize the dose and get the correct stripe width. The dose to be applied depends on the stripe width, connection to electrodes design and the PMMA solution. We used a smaller writing field (WF) for the stripes (more accurate but slower) than for the pads (less accurate but faster). The sample was developed with Methyl Isobutyl Ketone (MIBK) and acetone followed by a bath of acetone. After this step, we controlled the result with an optical microscope in dark field. Then, we evaporated 5 nm of Ti and 50 nm

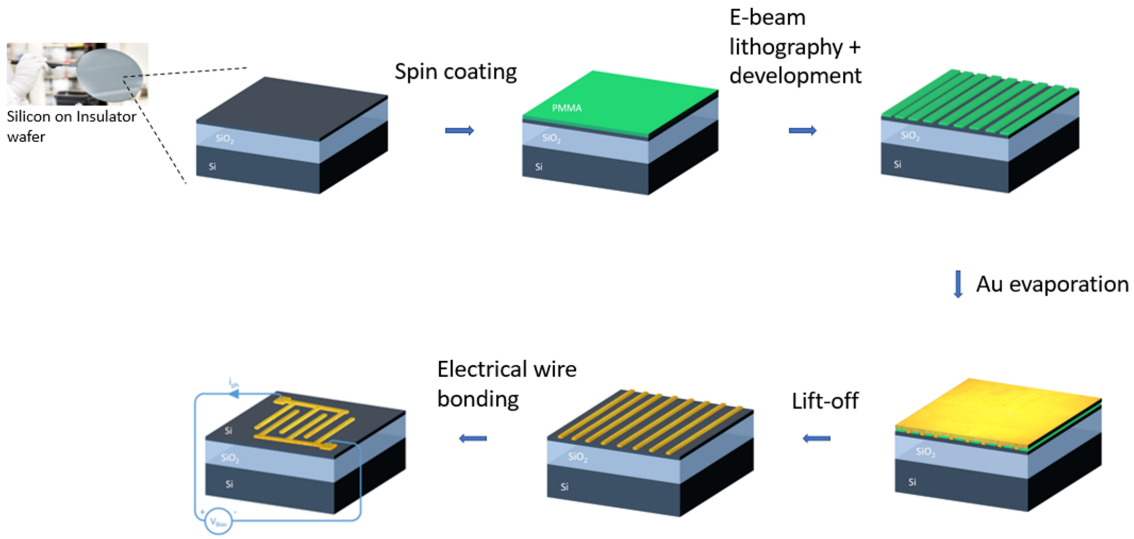


Figure 3.21: Nanofabrication steps used for the MSM plasmonic photodetector.

of Au. The last step of fabrication was the lift-off which consists in removing the PMMA and Au. The final result is shown in Fig. 3.22 by Scanning Electron Microscopy (SEM).

The measured periodicity of the grating is close to the one expected (950 nm) but, the stripe width is higher (180 nm) than the one expected but remains in the range of good absorption according to simulations (see Fig. 3.13). With such grating parameters, a RCWA absorption spectra simulation, as in Fig. 3.12, yields a resonance around 1650 nm and 20% of incident light Au absorption.

Fig. 3.22.c shows the amplitude image of Atomic Force Microscope (AFM). Fig. 3.22.d is the AFM amplitude signal along the red line. The height $h$ is between 50 to 60 nm which is of the order of what we were expected to find ($\approx$ 55 nm). Moreover, the space between stripes yields 984 nm (measured with Gwyddion software) which is in good aggreement with what was found with SEM measure.

After the device has been characterized by SEM and AFM, the bonding step consists on connecting the pads to a chip board (Fig. 3.23). The wire used is a thin Ag wire of 100 µm diameter. Fig. 3.23, represents how looks like the device fully fabricated. The sample presents on its surface 13 structures to be characterized. Then, by changing the connection wires (yellow and black on the image), we can get the photocurrent output from the desired structure.

In conclusion, the interdigitated MSM plasmonic photodetector has been modeled to enhance the Au absorption and the bandwidth. After considering the different trade-offs concerning the grating and sample parameters, we fabricated the optimized device. The next chapter will focus on the experimental characterization of the physics underlying this photodetector.

| n° | Step | Parameters |
|---|---|---|
| 1 | Cut | Square of 2 x 2 cm in SOI wafer |
| 2 | Cleaning | 5’ acetone with US<br>30" IPA bath<br>air dry |
| 3 | Spin coating | 1st layer 200 nm PMMA 200 (1’, 200 rpm)<br>then baking 90° for 1’30"<br>2nd layer(to be checked) 200 nm PMMA 50 (1’, 200 rpm)<br>then baking 90° for 1’30" (to be checked) |
| 4 | e-beam lithography | area dose ~ 200 $\mu C/cm^2$<br>dose factor 1.5 |
| 5 | Development | MIBK and acetone (1:3, 1’30")<br>acetone (1’) |
| 6 | Evaporation | 1st: Ti (5 nm)<br>2nd: Au (50 nm) |
| 7 | Lift-off | acetone (24 h)<br>and N-Ethyl-Pentedrone (NEP) |

Table 3.5: Nanofabrication step parameters for the MSM plasmonic photodetector.

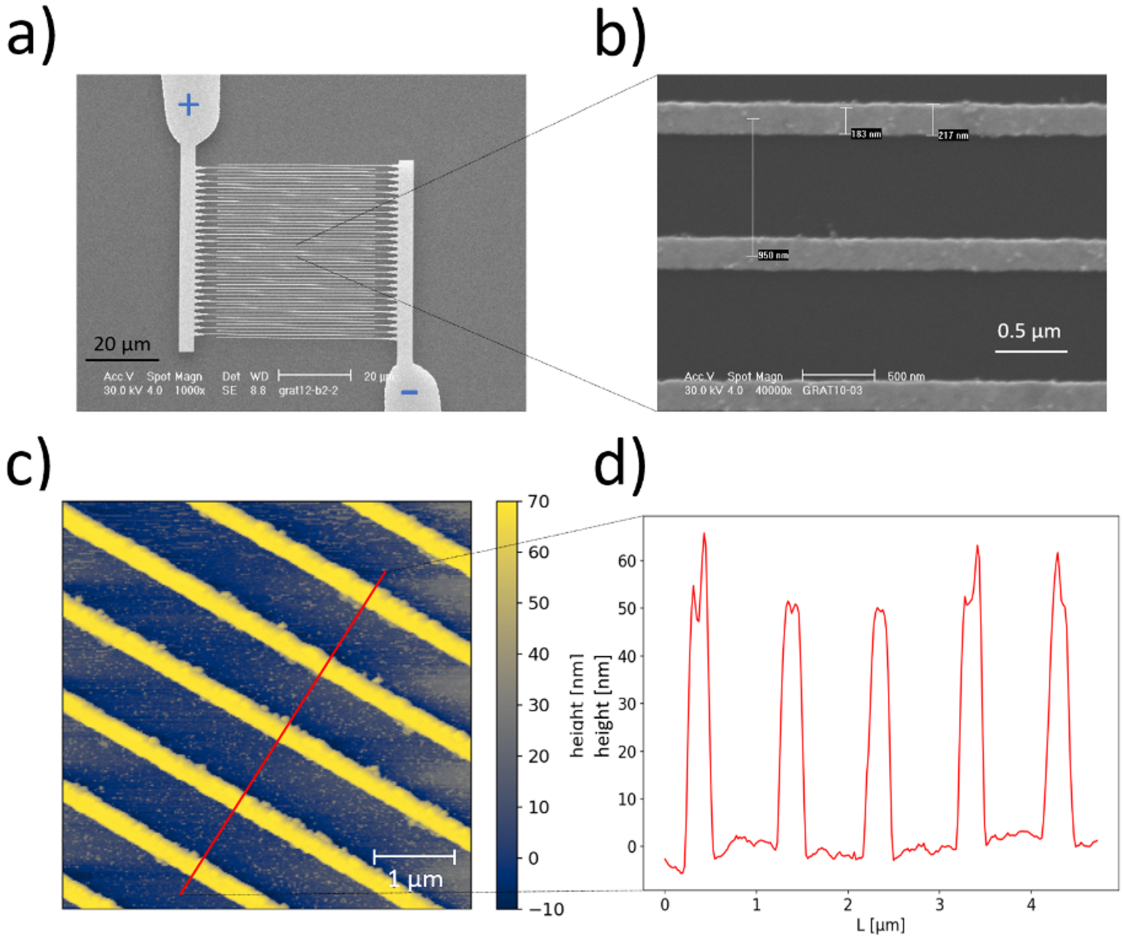


Figure 3.22: SEM image of the nanostructure. a) Stripes and electrodes. b) Zoom on the stripes. AFM image of the nanostructure. c) False-colour image of the amplitude signal (stripes). d) Amplitude signal (height) along the red line.

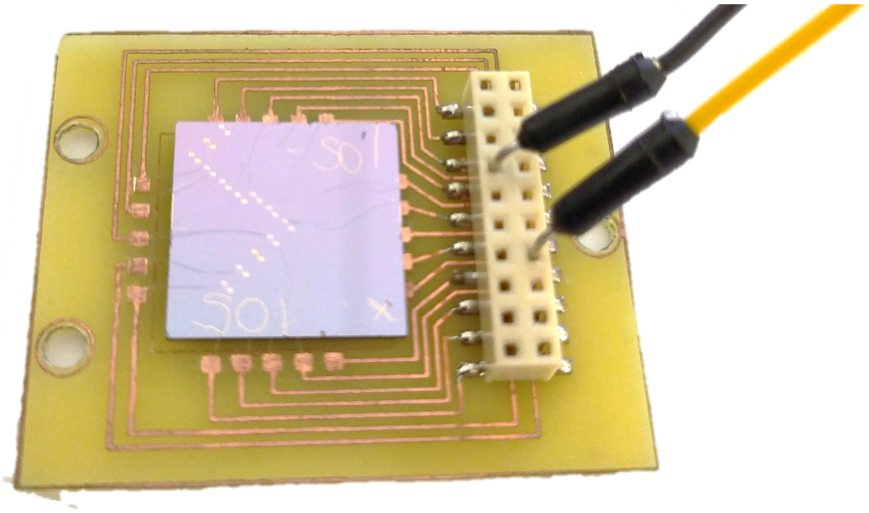


Figure 3.23: Sample fully fabricated. The SOI substrate with the 13 nanostructures on it connected by thin Ag wires to the board chip.

# Chapter 4

# Characterization of MSM plasmonic detectors

*" Nature hides its secret because of its essential loftiness, but not by means of ruse. "*

Albert Einstein, 1930

## Contents



The previous chapter has described the design and the fabrication of an interdigitated MSM plamonic photodetector. All the parameters were set to find a fair trade-off between responsivity and bandwidth. We have first studied a former Ge photodetector to take in charge photocurrent experiments. Then, after basics studies on the MSM photodetector on SOI, I have explored the photodetector non linearities in order to understand more the underlying physics related to the measured photocurrent. This work opens perspectives to bandwidth characterization and gives new methodologies to build more efficient photodetectors.

## 4.1 Ge-based plasmonic MSM photodetector

In the framework of the collaboration between Politecnico di Milano and the ICB laboratory, and at the early stage of the PhD thesis, I started to explore MSM photodetector configurations based on Ge. This device was fabricated by Dr. Monica Bollani and Dr. Mario Lodari for optoelectronic and sensing applications in the NIR [291]. It allowed us to initiate photocurrent experiments and take in charge the optical experiments. Indeed, we were looking for photocurrent and bandwidth measurements. In this sample, the absorption occurs in Ge and is promoted by the grating LSP resonance at 1.55 µm. The underlying physics are different than for the SOI substrate in which Au is the active layer. The Au stripes design with the pads (see Fig. 3.20) is comparable to the one discussed earlier for the SOI device but the geometric parameters are different. In this device, the substrate is composed of 1 µm thick Ge grown onto Si. Thus, the responsivity of this device is supposed to be high and adapted for sensing but is not optimized for high speed applications. Moreover, those photodetectors are large (150 × 100 µm$^2$) increasing the RC constant and the dark current but yielding higher photocurrent. After the experimental set-up presentation, I will describe two sets of experiments: a) the responsivity/reflection measurements and b) the bandwidth measurements.

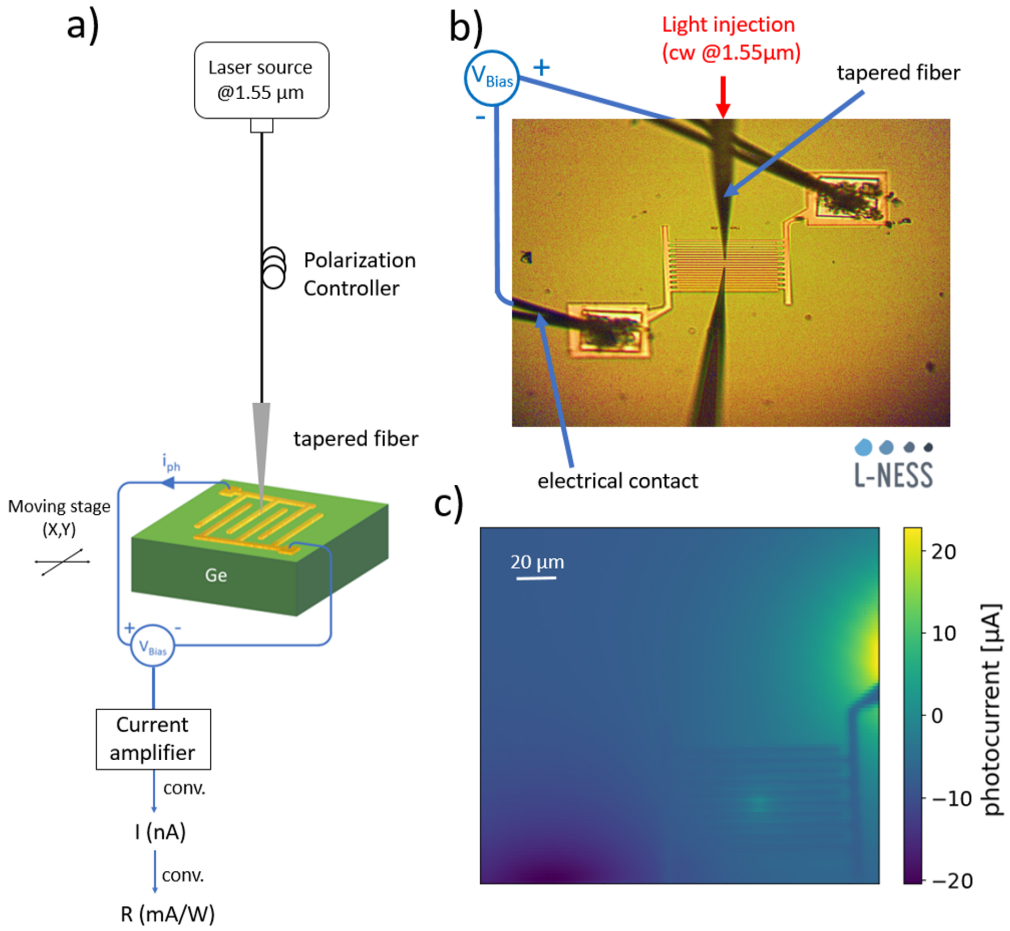


Figure 4.1: a) Experimental set-up for the tapered fiber. The output signals is the photocurrent. b) Interdigitated MSM picture of the two connection pads and the tapered fiber (with its reflection). c)Photocurrent map, the device is on the bottom right in order to observe the carriers diffusion.

In order to collect a photocurrent and an enhancement due to the grating, we used

the experimental set-up presented in Fig. 4.1.a. The device was raster scanned with a 1.55 µm c.w. laser (Tunics) through a near-field tapered fiber. The collected photocurrent was then amplified by a current amplifier (Keithley 428) with a gain of $10^5$ V/A. The current amplifier is also used to apply a voltage bias $V_{bias}$ between the stripes.

Fig. 4.1.b is an image of the device with the two lateral pads connected to thin Ag wires. The tapered fiber is visible in the upper part of the image while the bottom one is the reflection by the substrate.

In Fig. 4.1.c, the tapered fiber is approached close to the sample (few nm), and the stage on which the sample is hold is scanned over 200 by 200 µm: a photocurrent map is thus collected. The device is placed on the bottom right in order to observe the carrier diffusion towards electrodes. Indeed, lateral photocurrent (photocurrent generated outside the stripes) due to diffusion of locally generated electron-hole pairs was observed around the sample. In Fig. 4.1.c, the laser spot is small compared to the stripe width (i.e. below 10 µm), so the spatial resolution is high. Moreover, the polarization output of a tapered fiber is not well controlled. The localized SPP of the grating depends strongly on the polarization, thus, no plasmonic enhancement can be demonstrated with this scheme.

To observe where the carriers are being produced, the near-field optical fiber was approached at few nm to the surface to the sample surface as in near-field experiments (see Sec. 2.3.1). We were able to get the topography on the surface as well as the photocurrent. Fig. 4.2.a and .c show the topography. There is whether a shift due to scanning or the thickness is actually higher. Fig. 4.2.b and .d illustrate the collected photocurrent. The highest yielded photocurrent is obtained on Ge to 0.5 V, with a gain of $10^5$ V/A, it gives ≈ 5 µA. With 1 mW incident optical power (measured at the fiber output), the responsivity is ≈ 5 mA/W. Indeed, the active medium is Ge i.e. where the EHPs are produced. When the tip is above the metal stripes, Ge is shadowed by the 200 nm thickness of Au, lowering the photocurrent yield. This experiment was done onto an off resonant device (called device A).

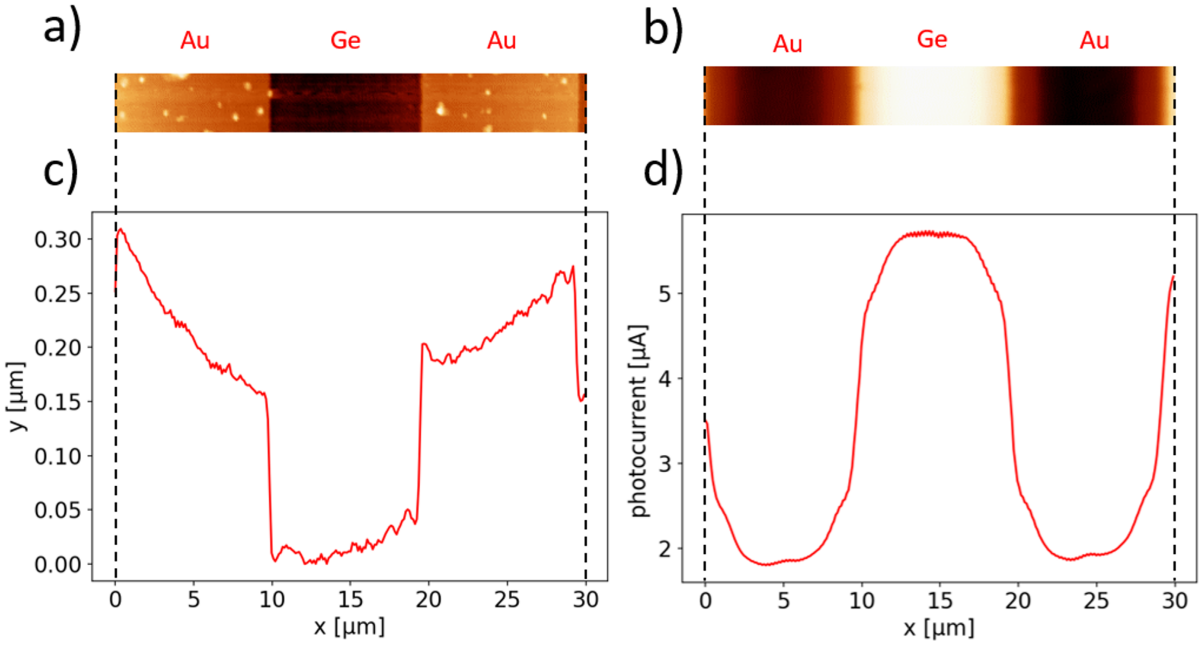


Figure 4.2: Off resonant large stripes, with tapered fiber excitation on SNOM head (with feedback loop). a) Topography and c) a slice in it. b) Photocurrent and d) a slice in it.

Under this first approach, no resonance was found due to a lack of polarization state control on the off resonant device. In a second experiment, the wavelength was swept from 1440 nm to 1640 nm using a cut fiber to inject light and another cut fiber to collect the reflected light (Fig. 4.3.a and .b). In this case, the laser spot is larger than with a tapered fiber (including several stripes) and the polarization is well tuned by a 3-paddle polarization controllers with bent fibers. Sweeping the cw laser wavelength while illuminating the plasmonic grating, an enhancement of the photocurrent due to localized SPP was observed for a certain wavelength. Fig. 4.3.c shows a photocurrent (blue line) relative enhancement of more than a factor of 2 at the wavelength of the localized SPP resonance (1.55 µm). A drop in the reflected spectra is also observed at the same wavelength of the enhanced photocurrent (red line). The incident optical power is the same for all the wavelengths. The reflectance was obtained by normalizing the reflected beam by the reflection on the Au pads.

In order to characterize the Ge photodetector speed, we performed bandwidth measurements. After the c.w. laser source, the optical fiber is passing through an electro-optic modulator (EOM) before being injected through a cut fiber (as in Fig. 4.3.a). Thus, the cw laser was modulated in amplitude at the EOM frequency. The $f_{-3dB}$ is given when the photocurrent oscillating amplitude is devided by 2. The $f_{-3dB}$ is $\approx$ 130 kHz. The current amplifier could in principle allow bandwidth up to MHz and is then not at the origin of this low bandwidth.

We have discussed here the first experiments performed onto an already existing sample exploiting Ge as the active medium for photodetection. Photocurrent map experiments were developed in order to study the lateral photocurrent. Near-field experiments gave additional informations on the local generation of EHPs and the device topography. The Ge-based plasmonic MSM photodetector presents a LSP resonance at 1.55 µm but has a low bandwidth (time response $\sim$ 10 µs). These first experiments allowed us to gain experience on photocurrent measurements and mapping as well as bandwidth characterization for the work on SOI plasmonic photodetectors.

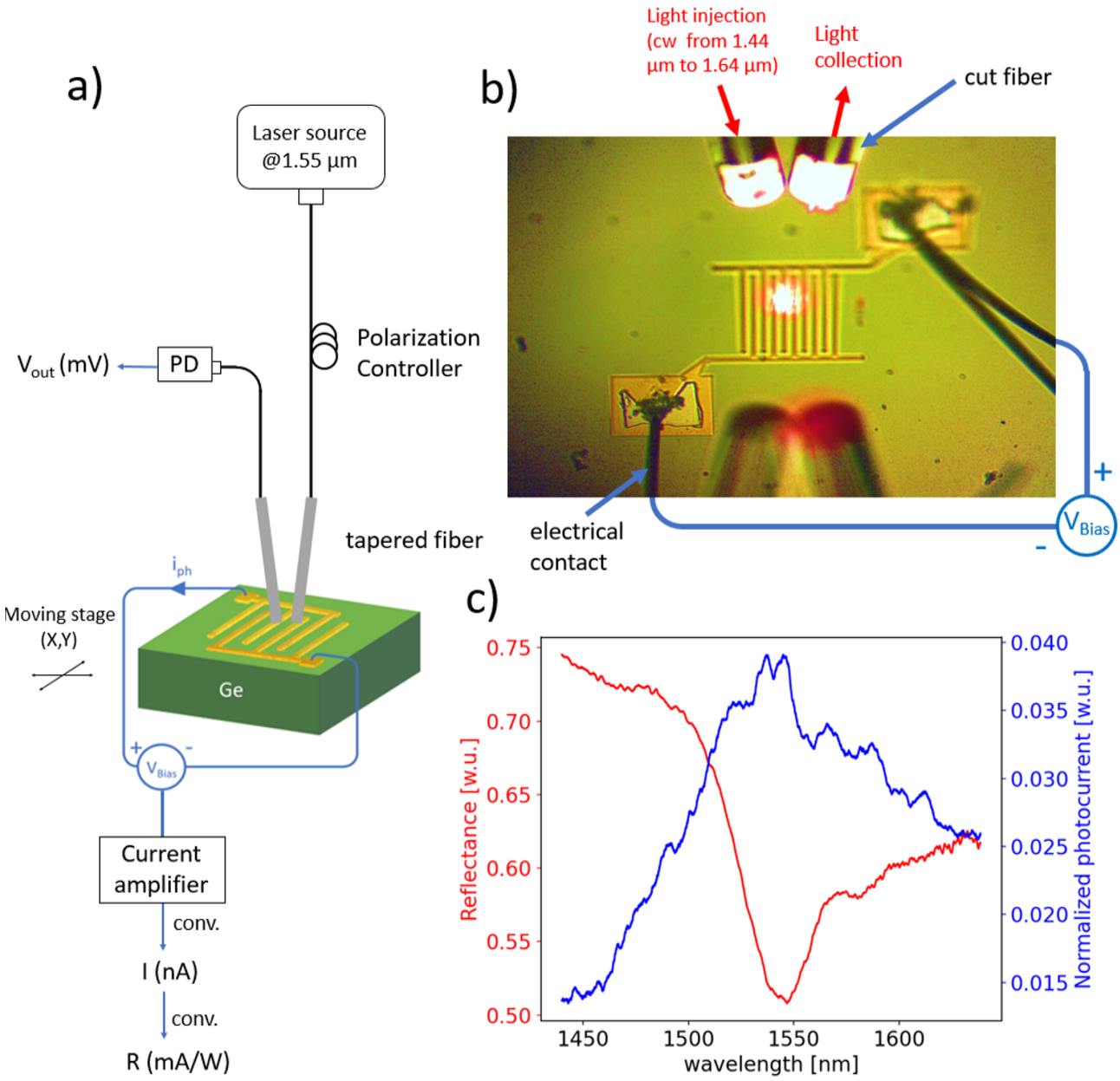


Figure 4.3: a) Experimental set-up with two cut fibers (10° tilt). The output signals are the photocurrent and reflection. b) Interdigitated MSM picture with the two connection pads and the two cut fibers (with their reflections). c)Reflectance and normalized photocurrent spectrum.

## 4.2 SOI-based plasmonic MSM photodetector

After the simulations discussed in the previous chapter to optimize the photodetector (responsivity and bandwidth) and its fabrication, the plasmonic MSM photodetector with SOI substrate was first characterized in Milano and then in Dijon allowing for different investigations. In Milano, we first studied the current-voltage characteristics, the spatial and spectral properties of the produced photocurrent under cw illumination. Then, in Dijon, we focused on the underlying physics by pulsed illuminations. More precisely, we investigated the nonlinearity of the devices and their bandwidth properties.

### 4.2.1 Current-voltage characteristics

In order to check that the general device behaviour was symmetric, as a first characterization, I acquired I-V curves with and without illumination. Indeed, the symmetrical behaviour is a critical parameter to validate such MSM device fabrication. If not, the device might be seriously damage or has suffered from strong fabrication process errors. The wavelength used in this experiment was 790 nm (1.6 eV) allowing for one photon absorption by Si without resonant contribution. The laser was collimated and its spot was sufficiently high to encompass the whole structure (>0.33 $mm^2$). Varying the voltage $V_{bias}$ applied, the current was collected by an ampere meter.

Fig. 4.4 shows the I-V curves on a structure without illumination and under illumination up to 6 mW. The current-voltage characteristic shows a nearly symmetric behaviour. If we invert the potential applied, it yields the same behaviour. With 1 V applied and an incident power of 6 mW yields 64.4 µA, thus, a responsivity of 10.7 mA/W.

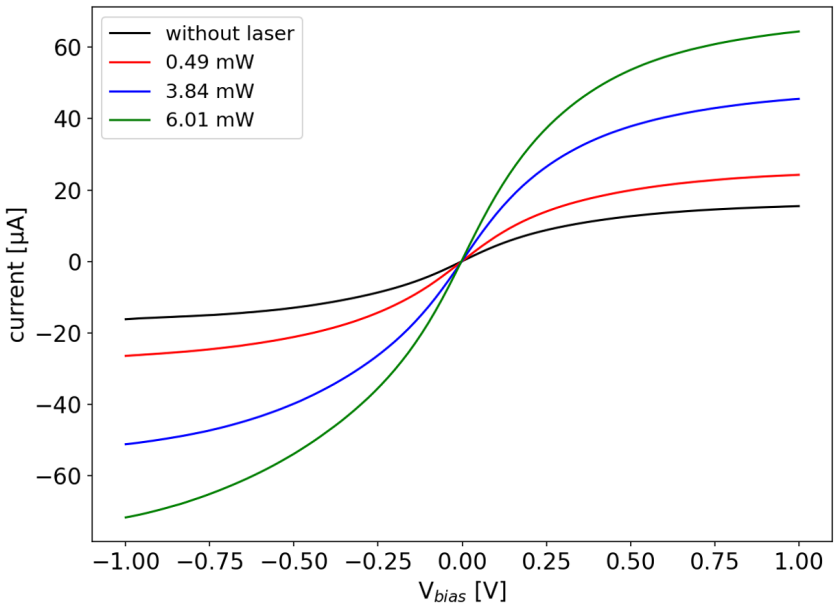


Figure 4.4: I-V curves under several incident powers at 790 nm wavelength onto the SOI plasmonic MSM photodetector.

In conclusion, we observed the fairly symmetric behaviour of the I-V curves with and without illumination for one photon absorption, thus validating the MSM geometry.

### 4.2.2 Photocurrent maps

In order to observe and ensure a proper laser alignment onto the structures, I used a confocal microscope in a scheme that also permits to collect the yielded photocurrent and the reflected beam onto the sample (Fig. 4.5). Such an experiment is also essential to observe where the photocurrent is being produced i.e. where the incident field is absorbed. The laser source was a supercontinuum (NKT Photonics SuperK EXTREME EXZ-12) spectrally filtered by a monochromator. According to the supercontinuum datasheets, the laser pulses are > 5 ns long and yield a spectrum ranging from 400 nm to 2 µm. We used a monochromator in order to select the incident wavelength. This is done by a Pellin-Broca prism on a rotation stage, which allows to select a wavelength by rotating it. The

selected wavelength was then sent through an optical fiber (acting as the exit slit of the monochromator) towards the confocal microscope. A lens collimates the beam which then passes through a half waveplate to control the polarization onto the sample. Two objectives were used depending on the purpose. One is for the near infrared part of the spectrum with high NA 0.7 (Nikon ELWD S plan Fluor 60x/0.70), thus producing smaller spot and higher resolution than the other one, which is for the visible range with 0.4 NA (Nikon LWD 20x/0.40), produces larger laser spots. The collected photocurrent was then amplified by a Keithley 428. The photocurrent yield is low, thus I had to implement a chopper ($f_0$ = 372 Hz) with a lock-in amplifier. Indeed, the lock-in integration time (between 30 and 300 ms) was much higher than the time constant of the chopper (2.7 ms). Thus, the collected voltage output of the lock-in $V_{outputlock-in}$ is:

$$V_{outputlock-in} = \frac{V_{signal} V_{ref}}{2} \cos\theta \tag{4.1}$$

where $V_{signal}$ is the output of the current amplifier, $V_{ref}$ is the reference of the chopper, and $\theta$ is the phase between the signal and the reference. With the $V_{ref}$ being of the order of the volt and without phase, the photocurrent pc is estimated by:

$$pc = \frac{V_{outputlock-in} \times sens}{max_{lock-in\ output}} \frac{1}{G} \tag{4.2}$$

with sens the lock-in sensitivity, $max_{lock-in\ output}$ is the maximal output value of the lock-in (10 V) and G is the gain (in V/A). The reflected beam was collected with a 90/10 beam splitter and then focused by a lens onto an InGaAs photodetector.

The procedure to acquire maps is as follow: to first take a reflection map, then, we move the stage to place the laser spot onto the Au pad and optimize the height untill the higher value of reflection is reached. This allows to to position the grating into the waist and to check that the spot is well focused (by changing the height). Then, we acquire the photocurrent map.

For 0.5 V applied between the stripes, Fig. 4.6 presents the typical maps acquired at 790 nm excitation: a) for the reflection and b) for the photocurrent. For the reflection map, a higher (resp. a lower) signal is obtained as the laser spot is on the metallic pads (resp. on the Si), wheras it is intermediate onto the photodetector's stripes. For the photocurrent map the higher photocurrent is obtained onto the photodetectors stripes. The lower signal is acquired onto the pads where the metal is shadowing the Si limiting direct absorption. The intermediate signal is yielded onto the SOI substrate. At the upper and lower edges, there is an enhancement of the yielded photocurrent observed for all the structures. This phenomenon could be explained as a breaking of the structure periodicity enhancing locally the field. Further investigations should be done at other wavelengths in order to understand more this process which could be related to surface modes in the periodic structure [292]. I present here a photocurrent map with 790 nm excitation because at 1550 nm the map was very noisy (low photocurrent) and needs a long integration time (chopper and lock-in amplifier).

In order to characterize the quality of the laser focus, as first approximation, on Fig. 4.6 we can nearly see the stripes, meaning that the laser spot size might be of the order of the µm. Another way is to assume that the beam profile is Gaussian and consider a sharpe edge (known as the knife or edge-scan technique [257]). Then, the method is about to scan from the substrate to the metal pad and acquiring the reflection beam intensity. The intensity along an $x$ scan is suppose to follow [257]:

$$I(x) = \frac{I_0}{2}\left(1 + \mathrm{erf}\left(\frac{\sqrt{2}(x_0 - x)}{w(Z)}\right)\right) \tag{4.3}$$

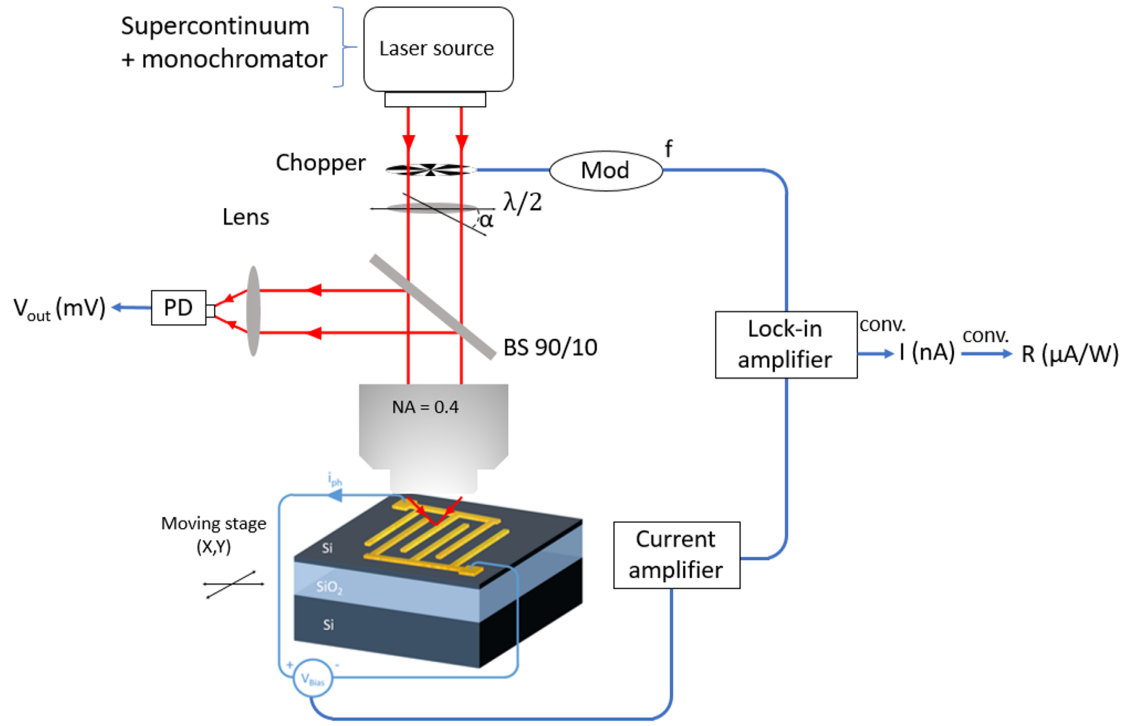


Figure 4.5: Confocal microscope set-up with photocurrent and reflection outputs.

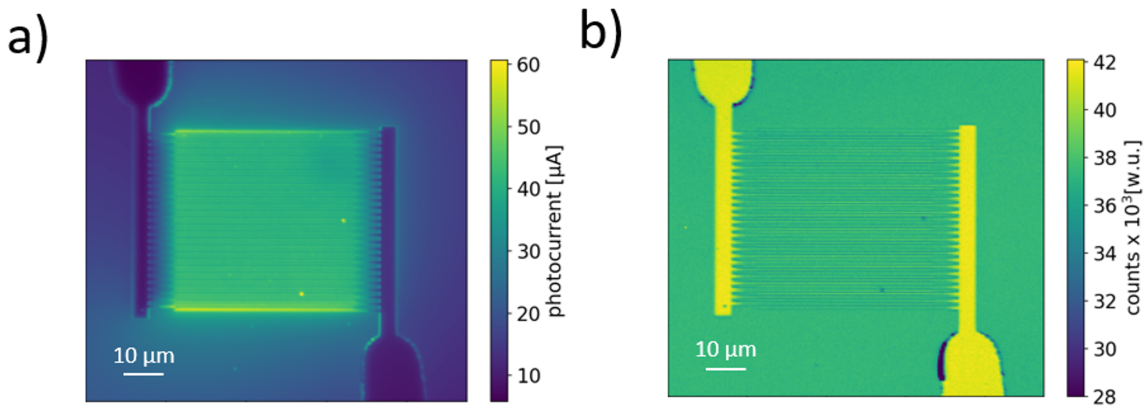


Figure 4.6: Typical maps obtained. a) Photocurrent map. b) Reflection map.

with $I_0$ the maximal instensity, $x_0$ the edge position and $w(Z)$ the waist radius for constant Z. Fitting the obtained measure allows to estimate the laser waist radius, thus the spot diameter. Fig. 4.7 is an edge-scan measure on the bottom right pad of the reflection map in Fig. 4.6.b. The fit parameter yields a waist radius of 0.55 µm, thus a a beam diameter of $\approx$ 1.1 µm.

### 4.2.3 Photocurrent spectrum and polarization dependence

In order to prove that the process involded in the device is a hot electron-based plasmonic one (see Sec. 1.2), we have to: a) sweep wavelengths to find a resonance and b) check that

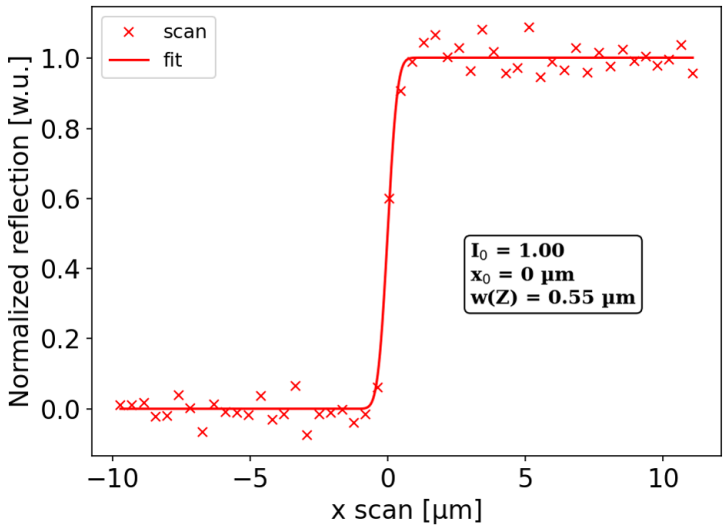


Figure 4.7: Spot analysis by edge-scan technique on the bottom right pad in the reflection map Fig. 4.6.b normalizing to 1 in the caption.

the polarization affects the resonance. Those two arguments are robust to demonstrate the plasmonic-based device.

The procedure to get a photocurrent spectrum was as follows. I first started with the alignement and a reflection map (see last section). After, I placed the laser spot onto one of the metal pads, I then optimized the height (i.e. the focus) to maximize the reflection and ensure a proper focusing of the laser beam. Then, I moved the stage to place the laser spot in the middle of the grating. The wavelength was swept from 1100 to 1800 nm by automatically rotating the Pellin-Broca prism with a LAbVIEW program. Several attempts have shown that higher efficiency with the 0.4 NA objective is obtained. Indeed, a larger spot with identical irradiance yields to a higher photocurrent encompassing more stripes.

Fig. 4.8.a shows the photocurrent spectrum acquired with the plasmonic MSM device. The applied $V_{bias}$ voltage is 200 mV. For polarization orthogonal to the grating, a resonance is observed at 1670 nm closeby where it is expected to be (at 1680 nm). At 1300 and 1450 nm, there are out of resonance bulges. For parallel polarization, above 1300 nm, no photocurrent enhancement is observed. For both polarizations, below 1200 nm, the photocurrent increases due to Si absorption (close to the indirect bandgap of Si). These spectra demonstrate the expected plasmonic enhancement of the photoresponse.

In order to access the responsivity of the photodetector, the photocurrent should be normalized by the illumination spectrum of the semiconductor. For that, the power spectrum output must be calibrated. I placed a Thorlabs infrared photodetector just after the objective and collected the power spectrum. Fig. 4.8.b shows for both polarizations the power spectrum of light impinging onto the device. The parallel polarization between 1100 to 1400 nm presents oscillations which, afterwards, were discovered to be due to a beam splitter used in the confocal microscope. Further normalization was thus used to remove these artefacts.

Dividing the photocurrent by the power calibration yields the responsivity spectrum (Fig. 4.9). The resonance at 1680 nm is observed. At the resonance the maximal responsivity is

$$R_p = \frac{I_p}{P_{in}} \approx 15\ \mu A/W. \tag{4.4}$$

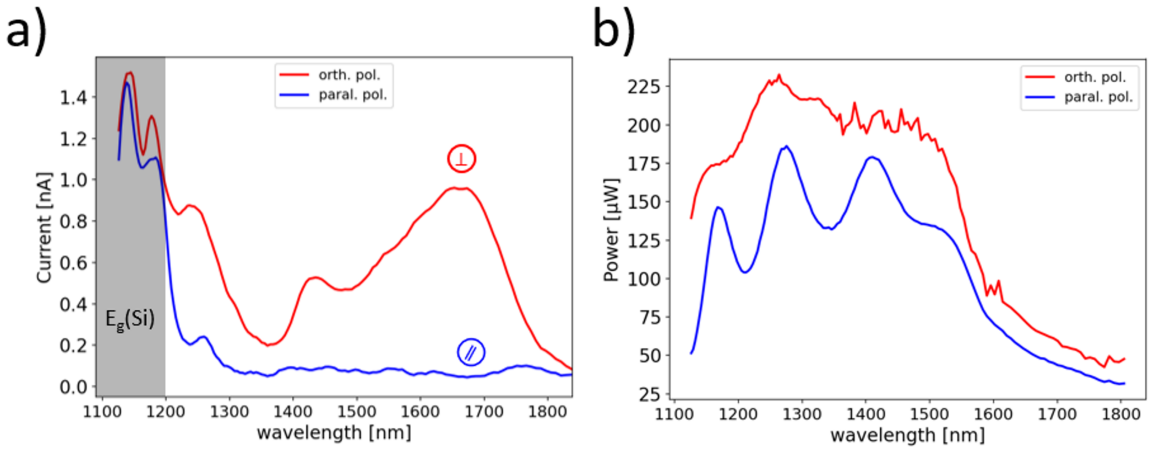


Figure 4.8: For orthogonal and parallel to the grating polarization: a) Photocurrent spectrum. b) Optical power calibration spectrum.

with $I_p$ the current generated by the photodetector (A) and $P_{in}$ the incident optical power (W). From this value, the External Quantum Efficiency (EQE) can be retreived:

$$\mathrm{EQE} = \frac{hc\mathrm{R_p}}{\lambda e} \approx 0.001\% \tag{4.5}$$

Considering A = 18 % of absorption from simulations, the Internal Quantum Efficiency (IQE) can be calculated as:

$$\mathrm{IQE} = \frac{\mathrm{EQE}}{\mathrm{A}} \approx 0.006\% \tag{4.6}$$

The IQE is of the same order of magnitude as the ones in the literature for devices based on close principles: Knight [167] 0.01 %, Goykhman [175] 0.02 % or the best one achieved by Sobhani [184] 0.2 %. Below 1200 nm, the EHP generated by direct absorption in Si increases the responsivity as expected.

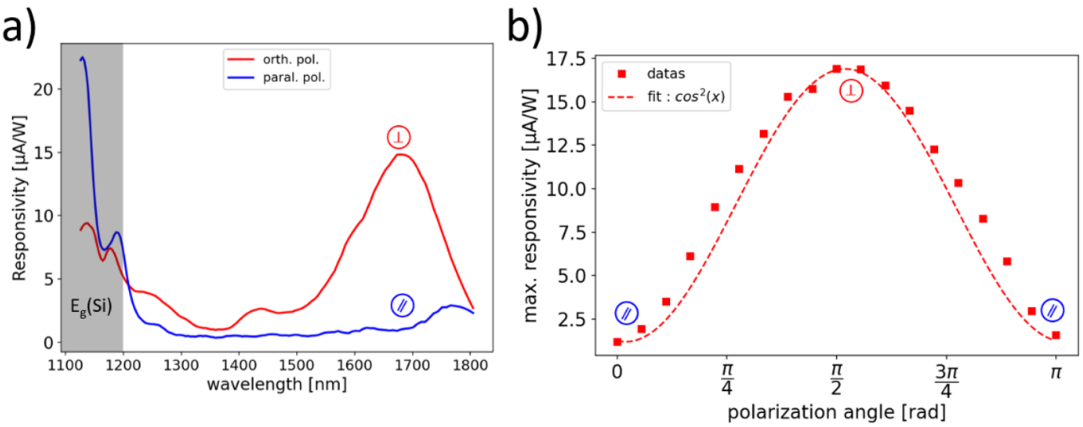


Figure 4.9: a) For both polarization, spectral responsivity. b) At the resonance, polarization dependence with a square cosine fit function.

Three arguments allows to confirm that this photocurrent is based on EHPs produced by within the Au stripes by plasmonic resonances. First, the wavelength at which they are

produced is below the Si bandgap, then photon cannot be absorbed linearly (two photon absorption could still occur). Then, the resonance observed and its polarization dependence are argument to confirm a plamonic assisted EHP generation. Thus, in order to definitively confirme the plasmonic resonance assisted absorption, we repeated this measurement four times onto the grid and onto the Si where no resonace is observed. Responsivity spectra onto the pad and on Si give no such resonant spectra. Spectra on other devices on this sample yields all the same lineshape and the same resonance at the same wavelength (they all present the same stripe width). The responsivity slightly varies ($\approx$ 15-20 %) which could come from differences between the ohmic contacts due to the wire bonding step.

Fig. 4.9.b represents the polarization dependence of the resonance. At 0 and $\pi$ the polarization is parallel to the grating stripes while at $\pi/2$ it is orthogonal. Each point represents a responsivity spectrum and the peak value at resonance is reported. We observe the maximal responsivity for $\pi/2$ polarization and an almost vanishing signal when the polarization is parallel to the grating. The polarization angle dependence of the responsivity matches with a square cosine function as expected in the Malus law. The fit function used is:

$$f_{\text{fit}}(x, \text{phase}) = \text{A}\cos^2(\pi x + \text{phase}) + \text{val}_{\text{min}} \tag{4.7}$$

where A is the measured maximal value minus the minimal value and $\text{val}_{\text{min}}$ is the minimal value measured. The fit algorithm changes the phase to minimize the distance between the measured values and the fit, yielding Fig. 4.9.b.

Finally, in order to study the influence of the bias, Fig. 4.10 shows the responsivity at the resonance versus the applied voltage. The behaviour is nearly symmetric i.e. -200 mV yields below 12 µA/W wheras is 15 µA/W for +200 mV. This slight asymmetry can be explained by the Ag contact pads which may be slightly different from each other.

Moreover, the level of noise comming from the device is hard to determined due to the use of a lock-in amplifier and a current amplifer device.

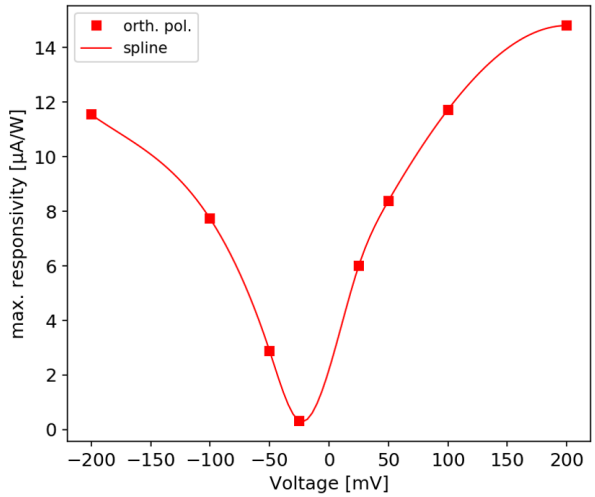


Figure 4.10: At the resonance excitation, voltage dependance under orthogonal polarization.

In the end, a plasmonic resonance was found at 1680 nm and depends strongly on the polarization. At the resonance excitation, I-V curve shows a nearly symmetric behaviour validating the MSM geometry. Actually, the SP resonance could enhance the two photon absorption (TPA) of Si and also yield a photocurrent. So, further investigation has to be

done to discriminate between the two processes and are presented in the following paragraph.

### 4.2.4 Photocurrent power dependence

The last section has shown arguments that a nanoantenna-like plasmonic resonance is involved in the measured photocurrent. However, the underlying physics may also be a LSP resonance that enhances the TPA of Si or the local heat generated by the stripe LSP. To distinguish between those phenomena, we have conducted different photocurrent power dependence experiments under various conditions.

#### Supercontinuum source

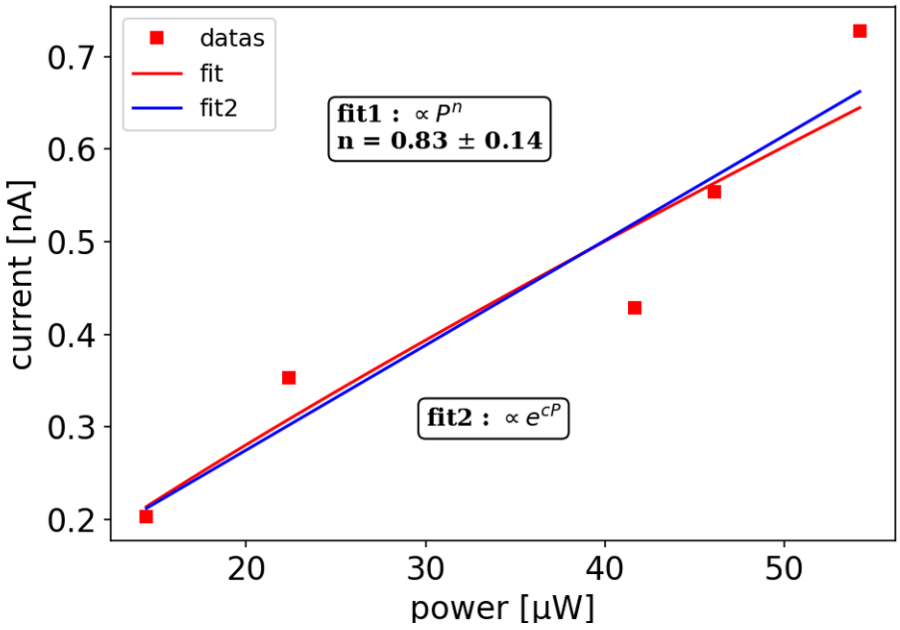


Figure 4.11: Current power curve at 1680 nm excitation with non linear order curve fitting (fit 1) and exponential curve fitting (fit 2).

As a first experiment, we excited the structure at the resonant wavelength (using the set-up presented Fig. 4.5), while the incident power was modified with density filters. Fig. 4.11 presents the photocurrent acquired as a function of the incident power onto the device. In order to obtain the order of non linearity, I fitted the data by $y = ax^n$ (fit1, red line, linear regression on the logarithm). Because the current is very low (~ 0.5 nA), the parameter $a$ used in the fit has a large uncertainty. The order of non linearity $n$ is close to 1. With LSP resonance at low power excitation, we are expecting a linear photon absorption process. According to [293], a linear dependence would suggest a one photon absorption (linear) while an exponential dependence would be a signature of a photothermal effect. Indeed, reactions dependant on thermal effect follow Arrhenius-type equation in which the rate is exponentially temperature dependant [293]. The "fit2" (blue line) used an exponential fit in order to distinguish the two phenomena. Because the photocurrent and the impinging optical power onto the device are low, the tendency seems to be linear but further insight has to be acquired to characterize the linearity or exponential

characteristics. Indeed, in Fig. 4.11 both fit curves could work. Moreover, to separate such phenomena, one should change the incident power by orders of magnitude [293]. Acquiring the photocurrent on such a small power range does not allow to discriminate between the two phenomena. On the other hand, if the power is too high, then other effects get involved (non linear absorption or damaged structures), making it more difficult to disentangle those effects. In any case, in this experiment, the supercontinuum does not allow for more irradiance onto the sample.

Rather than changing the incident optical power, another idea [293] was to place an iris just before the objective, thus the diameter of the beam incident onto the sample can be changed. This experimental condition is called constant irradiance, when the beam surface is reduced (by the iris), the optical power is reduced but onto the sample the excitation surface is enlarged. Under these conditions, the efficiency of one photon absorption is proportional to the square of the iris radius $R^2$ while photothermal process go as $R^3$ [293]. Fig. 4.12.a presents the photocurrent as a function of the iris radius. The two last points are not taken into account because there is a plateau effect where the iris has a diameter larger than the beam diameter. The non linear order gives $n \approx 1.45$ and seems to be closer to a one photon behaviour than a photothermal process. With more power and in 4-f configuration, this experiment may give a more accurate result but the tendency of this phenomenon looks closer to $R^2$ (hot electrons process) than to $R^3$ (photothermal process). Fig. 4.12.b is complementary to the power curve presented before (Fig. 4.11). The impinging power is modified by the iris diameter and also yields close to 1 non linear order. Further investigations are done next to complete those observations.

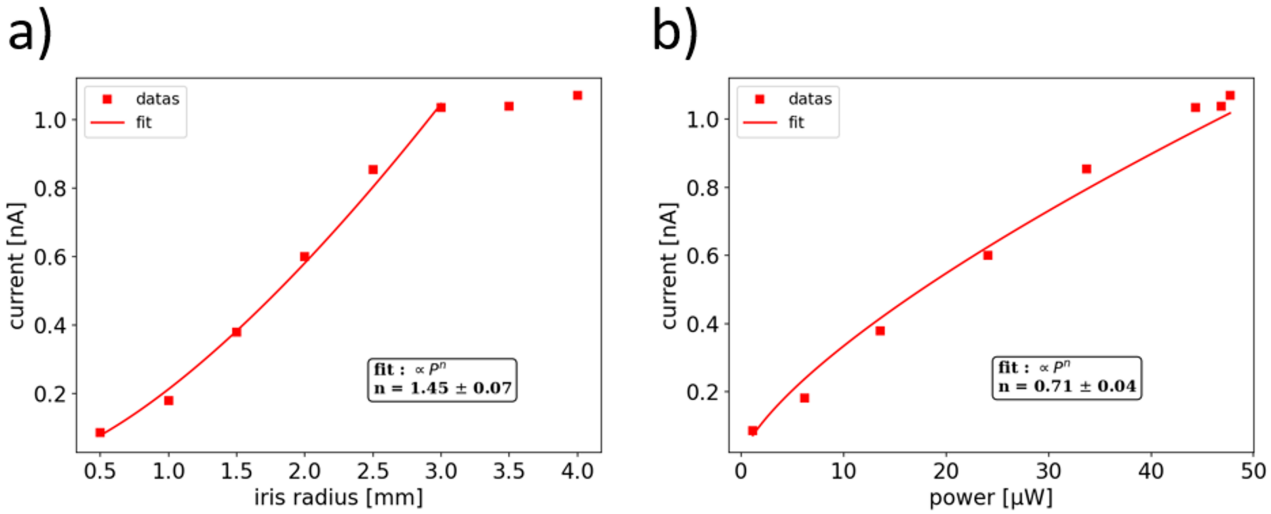


Figure 4.12: a) Current collected when varying the diameter of an iris placed before the objective. b) Current power curve obtained by varying the laser beam diameter.

### 1.55 µm femtosecond source

A femtosecond source is used to obtain higher optical average power without damaging the sample. The available source in Milan was at 1.55 µm (0.8 eV, Onefive Origami-15) which is close to the resonance (1680 nm, 0.74 eV). Indeed, since the responsivity in Fig. 4.9.a shows a broad resonance (FWHM ≈ 180 nm), we can consider the involved mechanisms will remain the same. Thus, the femtosecond source replaced the supercontinuum

source in the experiment presented in Fig. 4.5. Measurements were taken in the middle of the structure.

I studied first the polarization dependence to understand the behaviour of the photodetector under pulsed excitation. Fig. 4.13 shows the responsivity as a function of the polarization angle. Indeed, rotating the half-wave plate permits to control the polarization onto the sample. The optical power is 7.5 mW. When the polarization is parallel, there is still a responsivity of ≈ 2 µA/W, compared to Fig. 4.9.b, where the responsivity was reaching almost 0 (dark current level). Thus, for higher excitation power, another effect is occuring for parallel polarization. The maximal responsivity is divided by 3 compared to Fig. 4.9.b because the excitation wavelength is slightly off-resonance.

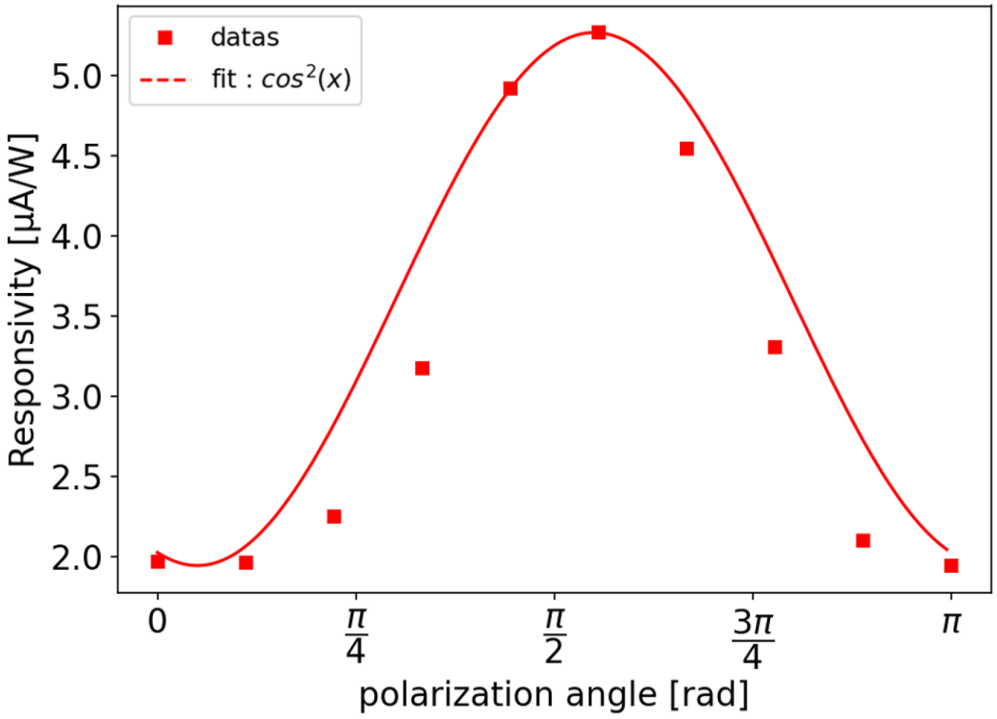


Figure 4.13: For 1.55 µm wavelength femtosecond excitation, polarization dependence with a square cosine function fit (as expected in the Malus law).

In order to go further, Fig. 4.14 shows the power dependence of the photocurrent in a log-log scale. The slope of the curves corresponds then to the nonlinearity and should allow to identify the mecanism involved. The optical power was changed with density filters and calibrated with a Ge detector. The orthogonal polarization is generating a higher photocurrent than the parallel polarization. The non linear orders are very close (≈ 1.5). That was unexpected because the one photon absorption should be linear (red curve expects n ≈ 1) and the blue curve should be due to TPA of Si (n ≈ 2). One explanation could be that, for orthogonal polarization, there is a competition between the plasmonic linear absorption and the enhanced TPA yielding intermediate non linear order (n ≈ 1.5). For parallel polarization, the TPA of Si could be reduced by the presence of the grating (for example propagative SPP).

The spot diameter is estimated to be 2-3 µm and is perhaps too small, a larger one, with the same irradiance, would allow including more stripes, yielding higher photocurrent. However, such investigation needs higher power laser output in order to observe clearer power dependence behaviour.

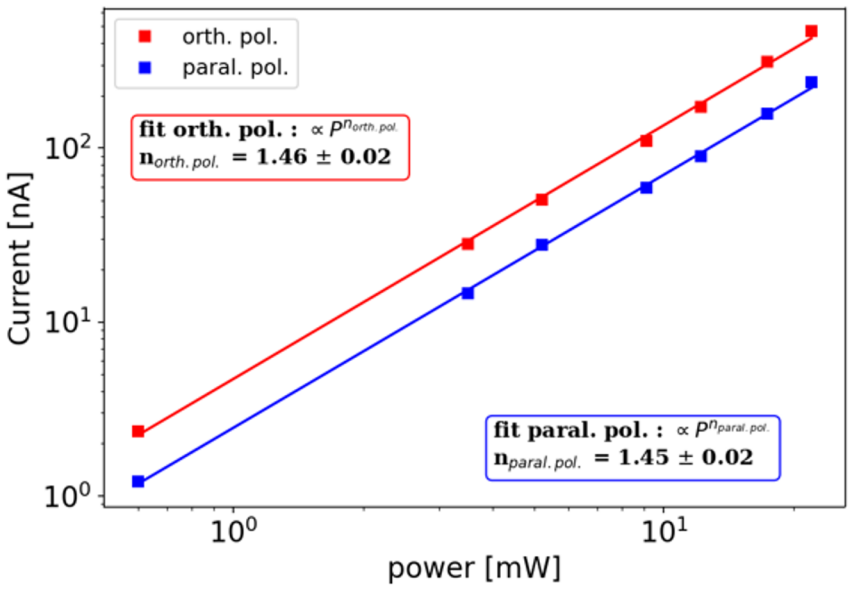


Figure 4.14: Current power curve at 1.55 µm femtosecond excitation with non linear order curve fitting for orthogonal polarization (red curves) and parallel (blue curves) in log-log scale.

Those experiments were done in Milan and had provided a first set of promising datas.

#### Ti:Sa oscillator and Optical Parametric Oscillator (OPO)

The following experiments were finally carried out in Dijon. The underlying idea was to separate plasmonic hot-electron, TPA or photothermal phenomena by means of power-dependent studies.

The experimental set-up used in Dijon is similar to the one of Fig. 4.5 but the source is a Ti:Sa laser (Mai Tai, Spectra Physics) followed by an Optical Parametric Oscillator (OPO, Spectra Physics). Under phase matching condition, rotating the OPO non linear crystal permits to cover wavelengths from 340 to 2500 nm theoretically. In the infrared, the conversion is less efficient and gives less optical power output. I implemented a half-wave plate on a motor stage followed by a polarizer (placed after the chopper in Fig. 4.5). The motor stage was then remotely controlled by LabVIEW to control the optical power onto the device. The Nachet objective used in the experiment was optimized in the infrared with a slightly higher NA of 0.6.

Due to the long laser path, a sligth alignement modification could severely displace the beam and change the power onto the device. For those reasons, we only worked at the resonance wavelength and we configured the OPO at the 1680nm wavelength. First, the OPO wavelength (1680 nm) must be selected and its optical power optimized (cavity mirrors) and then never touched for the rest of the experiment. Then, the normal incidence of the beam on the microscope objective is monitored and adjusted by Fourier lens and Fourier back focal plane observations. Care must be taken to accurately calibrate the power before every power curve measurement. A Ge powermeter was placed just before the objective to control accurately the power and the half-wave plate was rotating automatically, then a corrective factor (obtained from the objective calibration) was applied to get the power onto the device. Such a calibration curve is represented Fig. 4.15. For parallel polarization the highest value reached is slightly lower than for orthogonal polarization. This turns out to be due to the polarization change (with a half waveplate) from

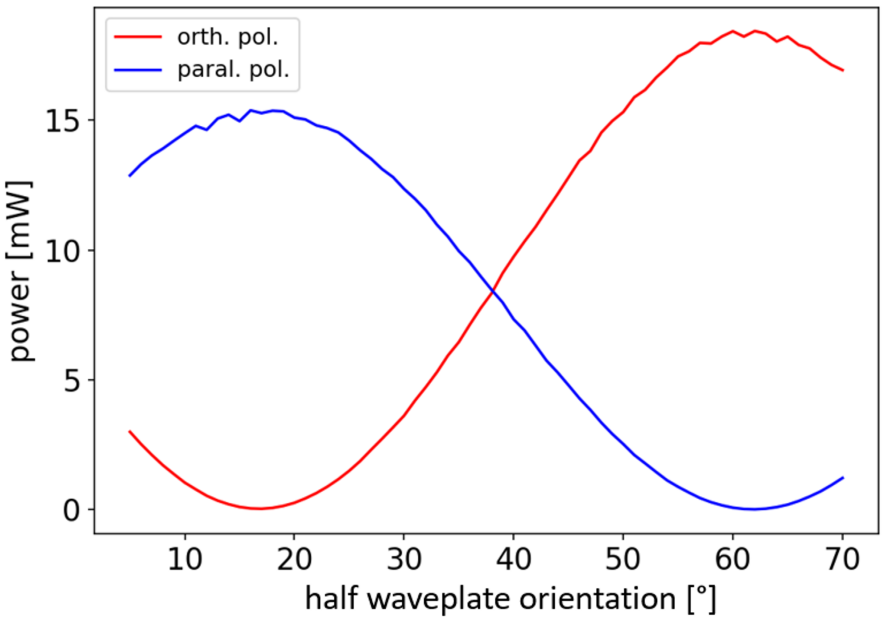


Figure 4.15: Power calibration rotating the λ/2 for orthogonal and parallel polarization compared to the grating.

orthogonal to parallel. This slight modification changes the optical path and impinge on a slightly different position onto the beam splitter placed before the objective.

The last step of the procedure was to record a reflection map. Then, the motor stage was moved to place the laser beam onto a large metal pad. In such a condition, the focus/z-position was optimized to get the highest reflectivity and ensure that the laser is always focused onto the device in the same way.

Fig. 4.16 represents three power curves in three different condition: a) on the stripes (in the middle on the strucure) with orthogonal polarization (red line), b) with parallel polarization (blue line) and c) on Si outside the structure (≈ 10 µm away, green line). The obtained data are then fitted by linear regression in log-log representation of datas. On the stripes with orthogonal polarization, a non linear order close to 1.5 is acquired (accordingly to what was observed with the set-up in Milan, Fig. 4.14). This is another argument for the presence of two processes: plasmonic one photon processes and the TPA from Si. On Si a non lineartity of 2 is measured demonstrating the TPA whatever the polarization. However, on the stripes, depending on the polarization, the nonlinear order varies from 1.5 to ~1.8 for perpendicular or parallel polarization. Indeed, on stripes the competition between TPA and gold absortion occurs, for nonresonant condition (parallel), the TPA dominates and gives a nonlinear order slightly below 2, while for resonant condition, the linear absorption in gold increases, lowering the nonlinear order to 1.5.

Changing the z-focus, with the same optical power, will change the laser spot area onto the device together with the irradiance. This condition is called constant-power condition (opposite to previously presented constant-irradiance condition, see Sec. 4.2.4) [293]. Fig. 4.17 shows non linear orders obtained by changing the focus from -20 to +20 µm around the z focus position on the sample. Each point represents the non linear order extracted from data taken in the middle of the structure. The zero position is the position found under the alignment procedure presented just before. Then, the z position were selected using the fine focus knob of the inverted Nikon eclipse Ti-U microscope. For orthogonal polarization, when the the z-focus is between -20 to -10 and +10 to +20, the non linear

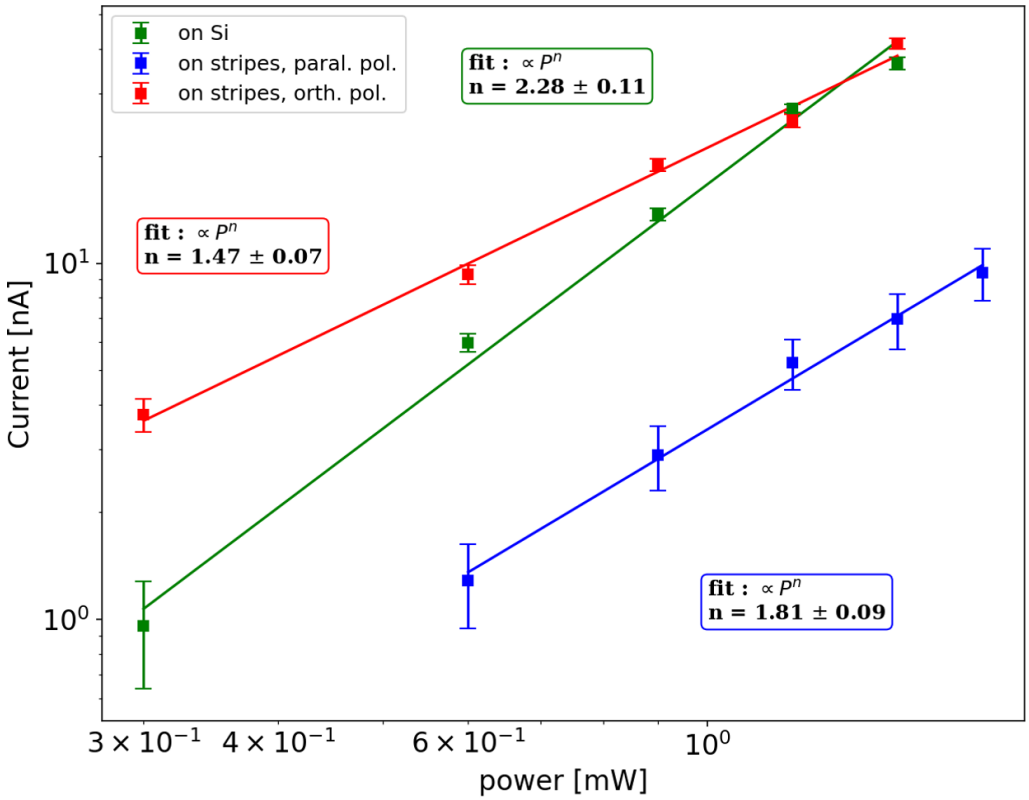


Figure 4.16: Current power curve under OPO excitation (1.68 µm): on the stripes (orthogonal and parallel polarization) and on the Si substrate. In the fit boxes, P is the power and n the nonlinear order. The error bar is obtained by recording the photocurrent for 20 s and obtain the standard deviation σ.

order is between 1 to 1.2. But, when the focus is reaching its highest value, the non linear order reaches almost 1.5 (in agreement with what was found previously Fig. 4.16). Thus, there is an enhancement of the nonlinear order at the zero position in agreement with the increase of efficiency of nonlinear mecanism when irradinace increases. When the beam is less focused, only one photon absorption processes are taking place within the gold stripes. On the contrary, if the beam is focused, a higher non linear order is obtained. There is a threshold of irradiance above which both processes get involved. For parallel polarization, the non linear order is going from 1.8 to 2.2 because EHP generation in gold is quite inneficient if not assisted by plasmon resonances.

Moreover, an important observation is that the standard deviation of orthogonal polarization is lower than for parallel polarization. There are two explanations for that: a) the signal is lower for parallele polarization and b) there is a slight oscillation in the signal for parallel polarization following two times the periodicity (not present for orthogonal polarization). Indeed, for orthogonal polarization, the scattering cross section is higher than the stripes (plasmonic resonance, see Sec. 1.2.1). Thus, when the position in the middle of the structure is changed the current signal stays the same. While for parallel polarization, the scattering cross section is lower meaning that the beam can have more Si or more Au and will strongly depends on its position. This observation gives an explanation of why parallel polarization non linear order gives variable values between 1.8 to 2.2, in Fig. 4.17, while orthogonal polarization yields stable values around 1.5.

The non linearity orders have been studied in three different schemes in order to distinguish the processes that come into play and the competition between them. It turns

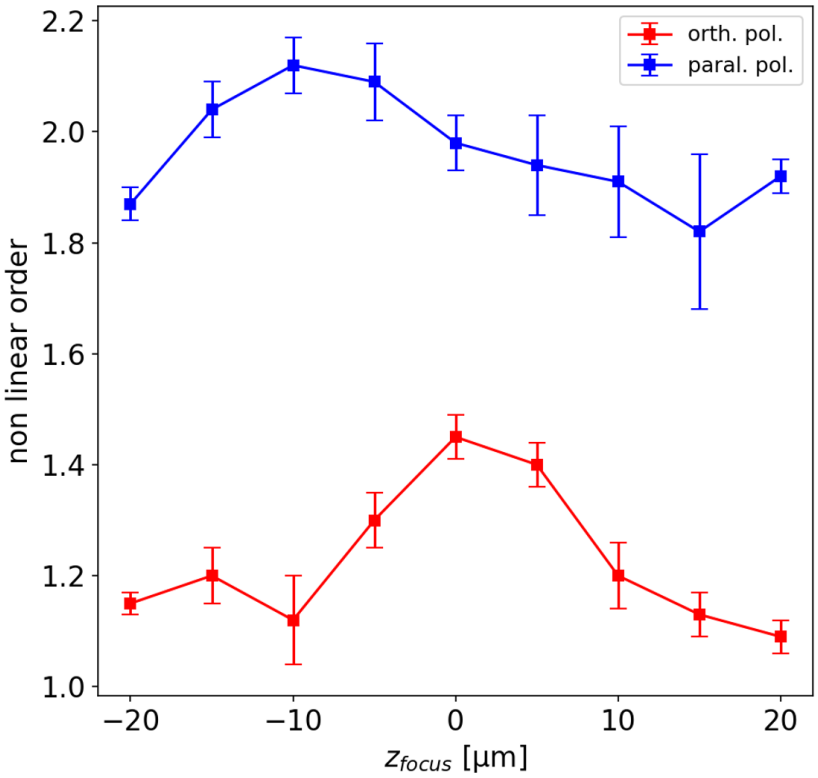


Figure 4.17: z-focus dependence under constant-power condition for orthogonal and parallel polarization. The error bar represents standard deviation of the non linear order calculation (by linear regression).

out that, at low irradiance with orthogonal polarization, plasmonic one photon absorption is the process involved. While above a certain irradiance threshold the TPA of Si enhanced by LSP participates to the photocurrent. More arguments are going towards plasmonic and TPA rather than photothermal effects. Indeed, the only way to remove photothermal effect is to do autocorrelation measurements because thermal effects are known to be slow processes (~ µs range).

### 4.2.5 Autocorrelation for speed and power characterizations

Another way to study the underlying physics is by investigating the process time scale. Autocorrelation is a common technique to explore time dependencies: separating pulses with a beam splitter, recombining them and delaying one arm with respect to the other. If the process has a longer timescale than the pulse width: two tails, called intensity autocorrelation, are present at the sides of the interference of the pulses. This tail gives the characteristic time of the process. Moreover, the process involved has to be non linear or there will be just interference and no tail. The ratio between the highest interference with the background allows one to retreive the non linear order. Since the plasmonic hot electron process is a linear one photon process, this experiment will investigate if there is a tail in the autocorrelation due to the TPA of Si.

Fig. 4.18 shows the experimental set-up. I used the Ti:Sa followed by the OPO, getting in the interferometer composed of a beam splitter with two mirrors. The beam splitter was optimized in the infrared by optical alignements to keep a high optical power to excite the device. One mirror is mounted onto a motorized stage to control remotely via

LabVIEW the delay $\delta x$ introduced between the two replicas. The rest of the experiment is the same as presented in Sec. 4.2.4.

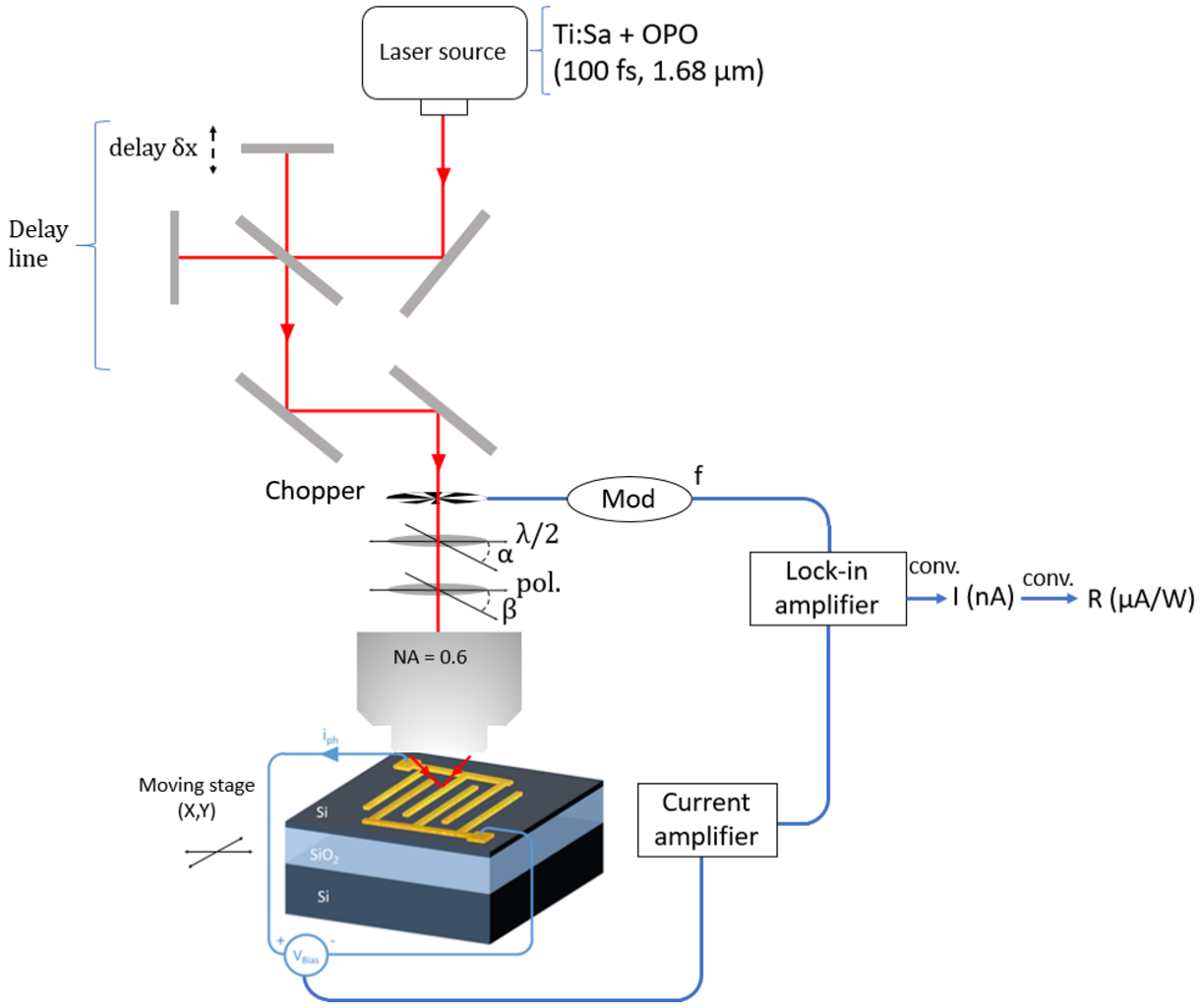


Figure 4.18: Confocal microscope set-up with the collected photocurrent and with the delay line. The reflection is collected with a photodiode but not represented on the diagram for practical reason.

In order to keep the same z-focus position for all experiments, the same alignement procedure presented before was applied here. Then, once a stable photocurrent map was acquired, I moved the stage towards the center of the device and outside on Si (≈ 10 µm away). Fig. 4.19 shows autocorrelation measurements in three different schemes: a) on stripes with orthogonal polarization, b) with parallel polarization and c) on Si. The interference fringes are well distinguished and the production of photocurrent follows the optical interference from the two delayed pulses. Moreover, under TPA autocorrelation experiments [108], an intensity tail is observed and gives the dynamics of the involved process. Here, no such observation is done. A hypothesis is that the process involved is faster than our pulse resolution (~ 100 fs).

From these interferences, one could extract the nonlinear order of the processus involved in the production of photocurrent. Indeed, the autocorrelation ratio, beetween the highest interference and the signal background when pulses are temporally separated, to

recover the non linear order n is:

$$\text{Ratio} = \frac{|2\text{E}|^{2n}}{2|\text{E}|^{2n}} = 2^{2n-1} \tag{4.8}$$

with E the electric field. Fig. 4.19.a is yielding a ratio of 4.7 which is approximately a non linear order of 1.5 when the spot is on the stripes and for orthogonal polarization. This non linear order is in good agreement with what was observed previously under the 1.55 µm femtosecond pulse and 1.68 µm OPO. Moreover, for parallel polarization, the ratio is giving 6.6 thus a non linear order of 1.8. The non linear order is lowered from 2 as observed and explained in the last section. On Si (for both polarizations) a ratio of 8.3 is obtained, so a non linear order of about 2. This is also in good agreement to what was observed in the last section.

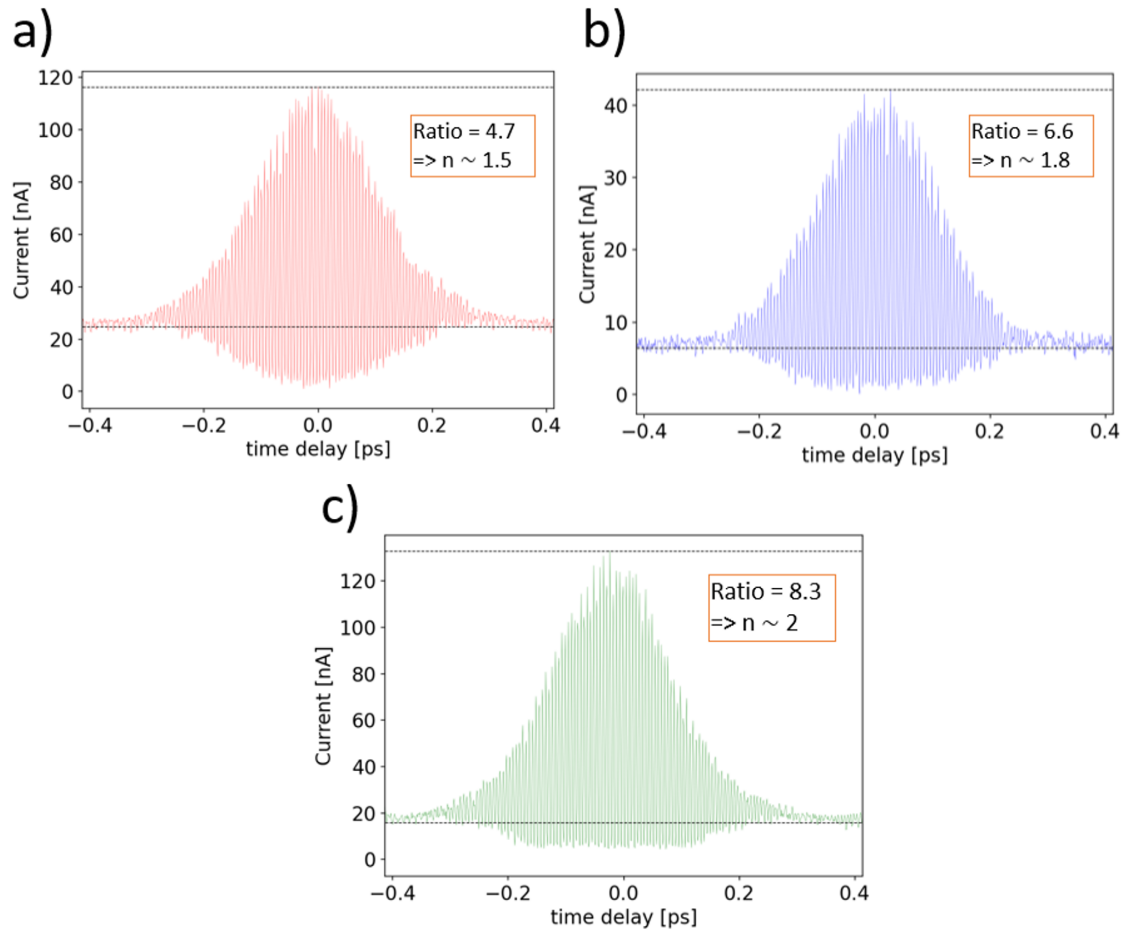


Figure 4.19: Autocorrelation measures: a) on stripes for orthogonal polarization, b) on stripes for parallel polarization and c) on Si substrate.

Therefore, the autocorrelation measurement was used to measure time scales. Actually, this experiment regained previous non linear orders found in power-dependent experiments, validating the results.

## 4.3 Discussion: expected photodetector specifications

After the nonlinear measurements that allowed to decouple the different processes involved, I describe in the following the performance that we can expect from the nanos-

tructure, in terms of bandwidth, dark current and noise.

### 4.3.1 Bandwidth limitations

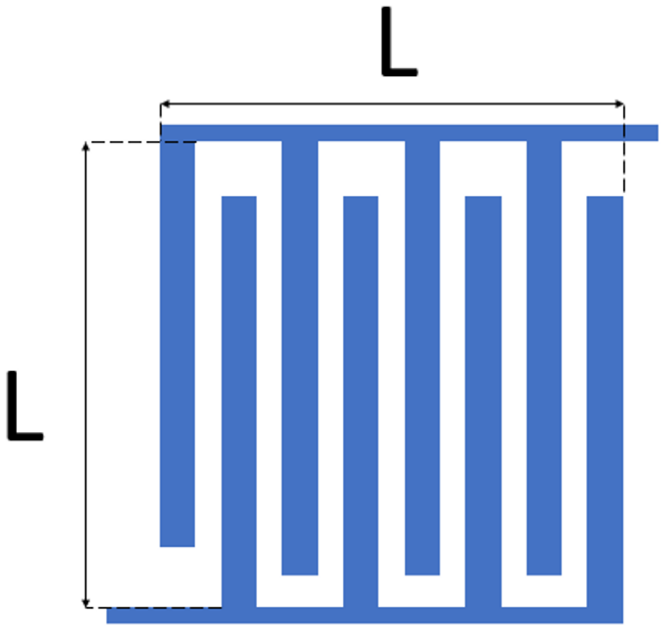


Figure 4.20: Sketch of the MSM photodetector with length L equal to the MSM width (square shape).

At first order approximation to estimate the plasmonic MSM photodetector bandwidth, the RC constant and the carrier transit time are the two main limiting factors. Every photodetector has a certain RC constant, thus a time constant $\tau_{RC}$, that intrisically limits the bandwidth [20]. MSM photodetectors can be approximated by an equivalent circuit, see Fig. 4.21, with: a) an ideal current source $I_S$(the generated carriers), b) a parallel junction capacitance $C_J$(due to the stripes), c) an internal series resistance $R_S$(due to the ohmic contacts and bulk resistances), and d) a parallel load impedance $Z_L$(to be connected to an external circuit) [294]. The RC constant is affected by the photodetector's geometry and active area. By itself, the geometrical design of an MSM photodetector has a low capacitance compared to PIN and APD photodetectors since the distance between the edges of the stripes of the order of few hundreds of nm is quite short compared to APD and PIN thicknesses of several µm. Moreover, the metal stripes are the active area of the plasmonic MSM photodetector. The capacitance of a square-shape interdigitated MSM photodetector can be estimated by conformal mapping techniques [295] or readily by empirical values from numerical evaluations (assuming that the stripe length is larger than the periodicity and is equal to the MSM width, see Fig. 4.20) [296, 297]:

$$C = 0.266 N L \epsilon_0 (\epsilon_{Si} + 1)(6.5 ff^2 + 1.08 ff + 2.37) \tag{4.9}$$

with N = L/2$a$ the number of finger pairs, L the length of a stripe (and the MSM width), $a$ the periodicity, ff = $w/a$ the filling factor, $\epsilon_{Si}$ = 12.8 the relative permittivity of Si and

$\epsilon_0$ the vacuum permittivity. With the device parameters extracted from previous sections (periodicity of $a$=970 nm, width $w$=126 nm, stripe length L=45 µm), the capacitance C yields 75.5 nF. With a typical resistance R of 50 Ω (taken here as a hypothesis for all the calculations), the RC constant $\tau_{RC}$ gives 3.8 ps, $f_{3dB,RC} = \frac{1}{2\pi\tau_{RC}}$ = 42 GHz and rise time[1] $T_{r,RC} = 2.2\tau_{RC}$ gives 8.3 ps. Reducing the length of a stripe (i.e. the MSM width) will reduce the capacitance but there will be less carriers generated (less active area, here Au) and it will be more difficult to focus a beam on the structure. Moreover, reducing the number of finger pairs is possible by increasing the width $w$ but it will shift the plasmonic resonance and become non absorbant structure. Here, the worst case is considered, if the laser spot is including all the stripes, generated carriers will face the capacitor $C_J$, $R_S$ and $Z_L$ used above (without considering the pads electrodes connections). But, if the laser spot is small (2-3 µm), generated carriers will face only the capacitance where the laser spot is. Thus, with a small laser spot, the bandwidth of the photodetector should be increased, however, the signal-to-noise ratio will be reduced.

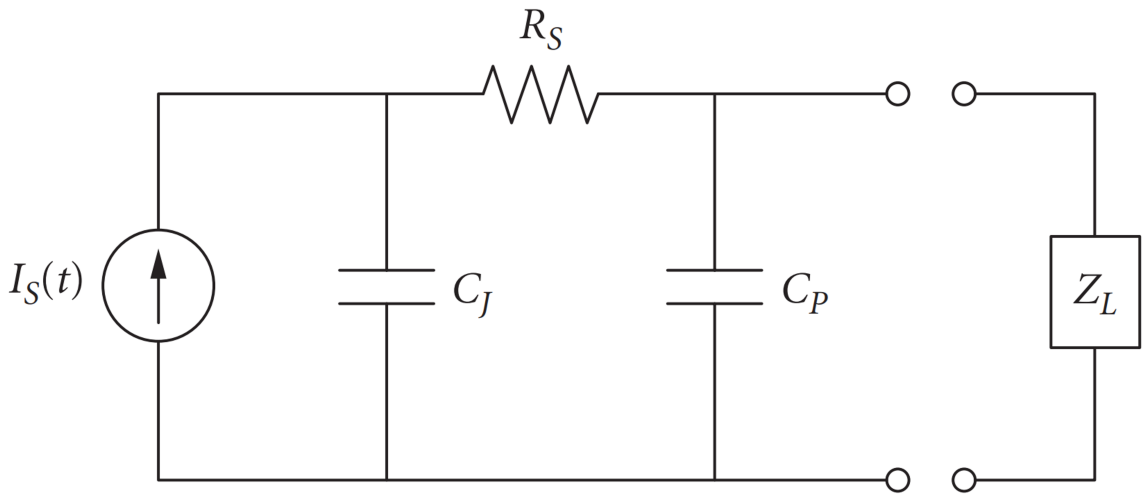


Figure 4.21: Equivalent circuit a of photodetector (extracted from [294]).

In this device, the carrier transit time represents the time for carriers to go from one electrode to the other one passing through the Si substrate. We neglect the time of travel from where the carrier is generated to the Schottky barrier (see Sec. 1.2.2). We also neglect the travel time within the BNC cable which should be at the order of the speed of light. Assuming that the electric field is sufficiently high to permit a drift velocity at or close to the saturation velocity, the transit time $t_{trans}$ is given by

$$t_{trans} = \frac{g}{v_s}\eta \tag{4.10}$$

with $g$ the gap between stripes, $v_s = v_{s,e} = v_{s,h} = 10^5$ m/s the saturation velocity[2] of carriers in Si and $\eta = 1$ the carrier drift distance corrective coefficient [297]. With the device parameter, $t_{trans}$ yields 8.4 ps and a bandwidth $f_{3dB,trans} = \frac{1}{2\pi\tau_{trans}}$ = 19 GHz. Hot carriers are expected to have a large velocity in Au, but once they overcome the Schottky barrier, hot carrier transport through Si is much lower. The transit time is therefore the limiting factor of the bandwidth.

[1] Rise time $T_r$: time taken by a photodetector to go from 10% to 90% of the final output current with an optical Heaviside step excitation.

[1] Saturation velocity: highest velocity carriers can reach in a semiconductor.

Considering the RC constant $\tau_{RC}$ and the transit time of carriers $t_{trans}$, we apply the definition of the -3 dB frequency cut-off frequency i.e. the bandwidth

$$f_{-3dB} = \frac{1}{2\pi(t_{trans} + \tau_{RC})} \tag{4.11}$$

yielding for the MSM photodetector $f_{-3dB}$ = 17 GHz and a rise time $T_r$ = 26.8 ps. Therefore, the bandwidth will be limited by the geometric parameters of the device. In usual photodetectors, namely PIN or APD photodetectors, to estimate the bandwidth limitation, there are other parameters to be considered: a) the time diffusion of carriers in the undepleted region (but we assume here that there is only drift because the electric field is present all along between stripes) and b) the carriers traping effect in heterojunction geometries (which is not the case here) [294].

### 4.3.2 Dark current and noise

In order to assess the reliability of the MSM device, we need also an estimation of the dark current, shot noise and thermal noise. The dark current is the current yielded by the photodetector without any incident light [298]. In this device, we can fairly neglect the dark current coming from the semiconductor and from tunneling [133], since for Schottky photodetectors, thermionic emission of carriers (electrons and holes) from the metal parts is the main source of dark current [151, 269]. We estimate the dark current in the regime where a high $V_{bias}$ is applied, larger than $V_{FB}$ (the flat band voltage), defined (for symmetric Schottky barriers) as:

$$V_{FB} = \frac{eN_D d^2}{2\epsilon_{Si}} \tag{4.12}$$

with $d$ = 844 nm the gap between two stripes, $N_D = 10^{15}$ cm$^{-3}$ the intrinsic doping of Si and $\epsilon_{Si} = 12.8\epsilon_0$ the permittivity of Si. With those parameters, $V_{FB}$ yields 0.5 V. In this discussion, as shown in Fig. 3.2.b, the left stripes are considered as the positive electrodes (1) while the right stripes are the negative ones (2). Thus, we consider only the reverse direction (i.e. electrons comming from $\phi_{B,n1}$ and holes from $\phi_{B,p2}$) and we neglect the forward direction (i.e. electrons comming from $\phi_{B,n2}$ and holes from $\phi_{B,p1}$).

In this approximation, the thermionic emission of electrons from the left stripe (1, positive) can be written as [151, 269]:

$$J_{1,n} = J_{1,n,sat} e^{\beta e \Delta\phi_{B,n1}} \tag{4.13}$$

with $\beta = 1/k_B T$ and T the temperature. $\Delta\phi_{B,n1}$ is the Schottky barrier lowering for electrons due to image force effect (see Sec. 1.2.3)

$$\Delta\phi_{B,n1} = \left( \frac{e\sqrt{2eN_D(V_1 + V_{1,built-in}/\epsilon_s)}}{4\pi\epsilon_s} \right)^{1/2} \tag{4.14}$$

with

$$V_1 + V_{1,built-in} = \frac{(V_{bias} + V_{FB})^2}{4V_{FB}} \tag{4.15}$$

with $V_1$ the potential on the left stripe (1), $V_{1,built-in}$ the built-in potential at the left Schottky barrier (1). If the voltage bias is increased, the Schottky barrier is lowered by $\Delta\phi_{B,n1}$, increasing the thermionic emission and thus the dark current. With those parameters, for

$V_{bias}$ of 1 V applied between the stripes, the barrier lowering is equal to 14 meV. $J_{1,n,sat}$ is the electron saturation current density

$$J_{1,n,sat} = A^*_{n,Si} T^2 e^{-\beta \phi_{Bn1}} \tag{4.16}$$

with $A^*_{n,Si}$ = 2.1 × 120 = 252 A/$cm^2$/$K^2$ the Richardson constant for electrons in Si [299] and $\phi_{Bn}$ = 0.8 eV is the Schottky barrier height for electrons (without the lowering due to image force effect). Thus, $J_{1,n,sat} = J_{1,n,sat}(V_{bias})$ and with $V_{bias}$ = 1 V, $J_{1,n,sat}$ gives $8.2\times10^{-7}$ A/cm$^2$, yielding $J_{1,n}$ the current density of electrons of $1.4\times10^{-6}$ A/cm$^2$.

The same demonstration can be done for the thermionic emission of holes from the right stripes (2, negative) evaluation:

$$J_{1,p} = J_{1,p,sat} e^{\beta e \Delta \phi_{B,p2}} \tag{4.17}$$

$\Delta\phi_{B,p2}$ has a slightly different expression for the Schottby barrier lowering for holes at the left stripes (2):

$$\Delta \phi_{B,p2} = \sqrt{\frac{e(V_{bias} - V_{FB})}{4\pi\epsilon_s d}} \tag{4.18}$$

With a $V_{bias}$ = 1 V, $\Delta\phi_{B,p2}$ gives 8 meV and $J_{1,p,sat}$ is the holes saturation current density

$$J_{1,p,sat} = A^*_{p,Si} T^2 e^{-\beta \phi_{Bp}} \tag{4.19}$$

with $A^*_{p,Si}$ = 0.66 × 120 = 79 A/cm$^2$/K$^2$ the Richardson constant for holes in Si [299] and $\phi_{Bp} \approx 1.12 - 0.8 = 0.32$ eV is the Schottky barrier height for holes at the right interface (without the lowering due to image force effect). With $V_{bias}$ = 1 V, $J_{1,p,sat}$ gives 30 A/cm$^2$ and $J_{1,p}$ the current density of holes of 41 A/cm$^2$. Meaning that, in the regime of $V_{bias} > V_{FB}$, the dark current is mainly due to holes by several orders of magnitude compared with electrons (strong holes injection [151]).

The total current density is then yielded by

$$J_{tot} = J_{1,n} + J_{1,p} \tag{4.20}$$

Here, for $V_{bias}$ = 1 V, we get $J_{tot} \approx J_{1,p}$ = 41 A/cm$^2$. The dark current estimation is given by $I_d = J_{tot} S$. S the metal surface area: 53 interdigitated stripes of length L = 45 µm and a width $w$ = 0.126 µm. The estimation of $I_d$ yields 0.12 mA for 1 V bias applied.

Shot noise and thermal noise are current fluctuations with a constant incident optical power $P_{in}$ applied [20]. These noises are fundamental, they can be reduced and optimized but cannot be avoided. The shot noise (or quantum noise) is due to the fluctuation of the dc current collected and is related to the quantum nature of current. Indeed, discrete electrons generation and collection are following a Poisson statistics. The dark current also participates to this noise. The root mean square of the shot noise (i.e. the standard deviation of the ac current) is given by

$$\sigma_S = \sqrt{\langle i_S^2(t) \rangle} = \sqrt{2e(\overline{I_p} + I_d) f_{3dB}} \tag{4.21}$$

Using the bandwidth found in the last section $f_{3dB}$ = 17 GHz, an estimated dark current at $I_d$ = 0.12 mA and a hypothetic yielded photocurrent of 1 A, $\sigma_S$ gives 0.074 mA.

The thermal noise (or Johnson-Nyquist noise) is due to thermal fluctuations and dissipation within the load resistance $R_L$ [20]. In fact, electrons are randomly moving and

induce a fluctuation of the current output. In the photodetector, the thermal noise is produced within the load resistance $R_L$:

$$\sigma_t = \sqrt{\frac{4k_B T}{R_L} f_{3dB}} \tag{4.22}$$

For T = 300 K, $R_L$ = 50 Ω and $f_{3dB}$ = 17 GHz, $\sigma_t$ gives 0.002 mA.

The Flicker noise (pink noise or 1/f-noise) has different origins depending on the device [298]. This type of noise is related to low frequencies and can be neglected for high bandwidth photodetectors.

For ± 1 V, the dark current measured (≈ 15 µA, black line on Fig. 4.4) is 1 order of magnitude lower than the dark current calculation done for 1 $V_{bias}$ (≈ 0.12 mA). Maybe the calculation is overestimating the dark current because in the experiment with 1 V applied is not already in the flat band condition [269]. Moreover, the dark current is estimated and measured between 10 to 100 µA while the collected photocurrent signal is between 10 to 100 nA. This is in good agreement with the use of a lock-in amplifier.

In conclusion, the main bandwidth limitation is the low carrier mobility in Si i.e. the space between stripes. To enhance the bandwidth of such a photodetector, strategies are to: a) reduce the space between stripes to reduce the space for carriers to travel, b) use another semiconductor (e.g. Transition Metal Dichalcogenides, TMD), c) use thin 2D materials (e.g. graphene) that both have higher carrier mobility and/or d) use a highly doped semiconductor that reduces the resistance thus lowering the RC constant. Moreover, the dark current is estimated to a tenth of mA. The thermal noise and 1/f noise can be neglected compared to the shot noise. In order to be detected with a good SNR, the photocurrent should be at mA order of magnitude or other techniques have to be used to detect current below their dark current and noise i.e. a lock-in amplifier. Moreover, the use of such an amplifier will reduce the bandwidth and the measurement will be limited by the set-up itself, not by the device.

## 4.4 Perspective: measure the dynamic of the plasmonic hot electrons process

Our main issue to measure the photodetector's speed was its low current value. Indeed, the photodetector needed a current amplifier stage (Keithley 428). But, for a gain of $10^6$ V/A the bandwidth was strongly attenuated to 100 kHz (10 µs rise time in the datasheets). To overcome this limitation, two options are possible to enhance the photocurrent generated: a) build a new device with another geometry that yields higher photocurrent or b) use a higher power laser in order to have a larger spot on the sample (keeping the same irradiance) and illuminate the whole structure yielding higher photocurrent. Those two options are to avoid using an amplification stage thus improving the bandwidth. Moreover, if the laser spot includes the whole structure, it might slow down the bandwidth due large photocurrent generated in all stripes.

Once the current amplification issue is overcome, there are several classical techniques to measure the bandwidth. The first one is by using a laser pulsed onto the photodetector and characterize the rise time and fall time (with a high speed oscilloscope) [300]. This technique is called the impulse response. Knowing the rise time and fall time, the bandwidth can be easily retreived. However it is challenging in the THz range due to the lack of fast enough detectors. A second option is to use an electro-optic modulator (EOM) with a CW laser. When the EOM frequency increases, the amplitude of the output

current will diminish thus providing an indication of the bandwidth. A third solution is to use a frequency comb as a source to excite the photodetector [229]. With a spectrum analyzer, the cut-off frequency is directly measured. A fourth solution is to use the two laser beating mode technique [229]. Two lasers are slightly frequency offset and then recombined yielding a beating. Controlling the offset allows to reach 100 GHz bandwidth measures.

Moreover, to avoid bandwidth limitations due to electrical wires or BNC cables, high frequency currents are usually collected by microwave or RF probes. Indeed, classical BNC cables work untill 4 GHz and will strongly limit the bandwidth. To reach 100 GHz special RF cables are needed and above 100 GHz expensive cable and RF connectors are needed. The shorter this RF cable is, the less the current is attenuated. Therefore, the photodetector has to be as close as possible to the highspeed oscilloscope or the spectrum analyzer.

Another solution would have been using the autocorrelation measurements but since the plasmonic process is linear, no bandwidth evaluation is possible in this scheme. In 2019, Shan et al. [243] proposed a pump probe experiment to measure directly the hot electron process plasmonic grating onto a semiconductor device. The pump is exciting hot electrons in the Au resonant stripe while the probe is exciting EHPs in the semiconductor. Delaying the pump and the probe permits to explore the dynamic range of the process. It turns out that the process is $\sim$ 40 fs, giving high hopes for future investigations in such devices. To my knowledge, only this experiment measured the speed transfer of hot electrons from the metal to the semiconductor, so far in the literature.

In conclusion, a first Ge-based sample allowed us to take in charge photocurrent measures. The SOI-based plasmonic MSM photodetector has exibited plasmon mediated process. Depending on the optical excitation, experiments are strongly suggesting a coexistance between a Au plamonic one photon absorption and a TPA of Si. Autocorrelation measurements gave nearby values of non linearities and confirmed previous power transfer functions measures. Further insight should be done to develop a set-up that fullfil the requirements needed to measure high bandwidth photocurrent to the THz regime.

# Conclusion and perspectives

*“ ... en s’installant à Retz, il [François Racine de Monville] utilisa une colonne brisée pour représenter l’oeuvre humaine, imparfaite et à jamais inachevée. ”*

Pierre Berloquin, Codes, 2013

In conclusion, in this manuscript I have presented the work done on the hot carriers remote generation and the plasmon-assisted hot carriers photodetection. This work has been done thanks to both expertize of the Politecnico di Milano physics department and the ICB laboratory in Dijon.

We have demonstrated the possibility to generate remotely hot carriers at up to 12 µm from the optical excitation. For that, the SPP propagation along a plasmonic waveguide has been simulated by FEM simulation. To maximize the coupling between the incident light and the SPPs, a grating is joined to the plasmonic waveguide. The grating coupler parameters have been optimized to maximize the energy transmitted by the SPPs. With the identified parameters, the plasmonic gold waveguide has been fabricated following a standard e-beam lithography procedure. A femtosecond laser source with Fourier control excitation set-up has been used to properly excite SPPs with enough energy. Simultaneously, hyperspectral near-field imaging technique has been used to probe the nonlinear PL emitted along the waveguide. We found that the SPP intensity spatial distribution is mapping the hot carriers spatial and energy distribution. Furthermore, we demonstrated that hot carriers relaxe where they are produced and do not diffuse further. Moreover, for long wavelength nonlinear PL, linear relaxation by intraband transition is dominant whereas, for short wavelength nonlinear PL, interband transition dominates. This is suggesting a linear intraband absorption, a TPA and Auger process getting involved. Such observations are in good agreement with previous experiments on nonlinear PL under different schemes, mainly with LSPs resonances [109]. However, some observations, made by Roloff et al. [131], exhibit an irradiance threshold above which the nonlinear order depends on the photon energy. Such results is characteristic of a heated cloud of hot electrons and further insight should be done to explore such physics.

These delocalized hot carriers open the way to complex hot carrier circuitry in which the active area is prevented from direct illumination which avoid any damage. We think such a work allows for new architectures in adsorbing or functionalizing molecules on the plasmonic waveguide and could be used to set off many chemical reactions (see Ref. 242). In photochemistry, hot carriers can be used directly by an acceptor or by generating heat. Ref. 301 shown that hot electrons transfer to an acceptor occur before thermalization in very short timescale i.e. this process is not driven by heat. Thus, hot carriers can be used in photocatalysis: to oxidize or reduce compounds, to excite electronic or vibrational

molecule adsorbed on metallic NPs. To cite a few, plasmon-enhanced hot carriers could be used for the photodissociation of $H_2$, to set off such unefficient reaction, or the water splitting, for alternative fuel production of hydrogen. More generally, plasmonic circuits generating locally hot carriers could be used for local detection of molecules or drive locally chemical reactions onto microchip. Furthermore, thanks to SPs and/or hot carriers coupling to phonons, such hot carriers enhanced by SPs process provides great potential in terms of energy efficiency by controlling local heating by not heating the whole environment. Furthermore, the nonlinear PL yielded along the plasmonic waveguide could be used as an on-chip spectrum analyzer.

Then, we have demonstrated the photodetection in a plasmonic device employing hot carriers for future applications in ultrafast photodetection. To efficiently absorb light and generate hot carriers, I used a gold grating on top of SOI. The gold grating is combining LSP resonances and grating effects in order to maximize light absorption within the gold structure. The multi-layer stack, with thicknesses determined by numerical simulations, presents constructive interferences in gold. Combining those effects, the grating parameters were calculated by RCWA method simulations to maximize the gold grating absorption on top of SOI. For normal incidence excitation, the plasmonic gold grating is absorbing around 30 % of the incident light, while at oblique incidence, 50 % of incident light was absorbed, which is significant in such a small thickness of 50 nm of gold. Furthermore, at normal incidence excitation, only the odd LSP modes can be excited and, at oblique incidence, odd and even LSP modes were present confirming nanoantenna-like behaviour resonances. FEM simulations were done to investigate where the electric field was located within the stripes. The LSP modes present electric field localized near to the interface with SOI which is interesting for generating carriers as close as possible to the Schottky barrier. Moreover, I did simulations to analyse the robustness of the device during the nanofabrication process in terms of spectral absorption and adhesion layer presence. Varying the width stripe still keeps on an appropriate gold absorption with wavelength resonance shift. The presence of an adhesion layer of Ti reduces the Schottky barrier height and improves the gold absorption keeping a good photodetection performance.

I performed numerical investigations that showed the opportunity to get perfect absorption with adequate parameters. However, in this work, due to materials constraints, we could not explore these parameters, and I think there is a great opportunity to improve the photodetection efficiency of devices by using such parameters. It could theoretically allow for sensitivity up to 100 µA/W. Such procedure could be used to engineer more complex devices with perfect absorption.

We built the gold grating in an interdigitated scheme yielding a metal-semiconductor-metal device. Depending on the SOI wafers available yielding maximal gold absorption, we used standard e-beam lithography. Ag boundings on a microchip were used to connect the nanostructures and the electronic processing. The nanostrucutre dimensions were then characterized by SEM and AFM.

Thanks to photocurrent mapping, we obtained a photocurrent enhancement onto the photodetector for a polarization orthogonal to the stripes. More precisely, the spectral responsivity presented an enhancement at the LSP wavelength resonance. Thus, such observations illustrate hot carrier plasmon-mediated photodetection and the absorption is maximized thanks to a plasmonic resonance coupled to grating effects. At the resonance, the numerical optimization of the device parameters yielded efficiency up to a responsivity of 15 µA/W with the same order of magnitude compared to devices based on similar process [167, 175].

To explore the underlying physics with the power transfer function of the MSM photodetector, we demonstrated that both absorption process appears in our devices: a competition occurs between the linear plasmon-assisted hot electron production and the non-linear absorption by the Si. The relative efficiency of both parameters is then governed by illumination conditions (flux, polarization, focalisation). Furthermore, to explore the time scale of the photodetection, autocorrelation measurements were done but we did not succeed to get any information on the device temporal dynamics.

The intrinsic dynamic of the plasmonic hot carrier photodetector is supposed to be in the THz but still needs to be measured. In order to measure such high speed photocurrent, one has to implement radiofrequency probes under e.g. the two lasers beating mode technique. Pump-probe experiment is also a solution to be considered with a pump at photon energy above the interband transition and a probe below. The delay between the pump and the probe could permit to reach the dynamic of such a process. Another possibility is to couple the plasmonic structure to a THz antenna. The yielded THz current then radiates THz wave and would be collected by a THz detector. Moreover, bandwidth calculations yielded that the expected 19 GHz is mainly limited by the low carrier mobility in Si. According to their high carrier mobility properties, 2D materials, such as graphene and Transition Metal Dichalcogenides (TMDs), could strongly be considered to raise the photodetector speed. Simulations yielded perfect absorption with our device and the fabrication of such a device, with the SOI wafer with the found thicnkesses, could provide higher responsivity. This would eliminate the use of a current amplifier that is strongly limiting the measurements. To sum up, in the future, coupling interdigited plasmonic array to a conducting 2D layer and a SOI stacking authorizing perfect absorption in gold, would allow to maximize the absorption efficiency together with optimal dynamic properties.

Such device could also be improved by adding, close to the grating, an electron-donor solution or with hole transporting material either organic or inorganic. This approach permits to enhance the collected photocurrent by rapidly transfer hot carriers before hot carriers thermalize [239, 302]. A very attractive strategy would be to use emergent plasmonic materials e.g. conductive oxides (indium tin oxide ITO, aluminum doped zinc oxide AZO) [303], transition-metal nitrides (TiN, ZrN, HfN, TaN) [304, 305], alloys of noble metals and transition-metals (Au-Cd) [306] and semiconductors (Ge) [307]. Indeed, noble metals permit sharp resonances and such new materials for plasmonics present broadband absorption resonance due to additional optical losses that could be used to detect multiple wavelengths close to 1.55 µm. However, White and Catchpole [308] presented the limitation of such hot carriers plasmonic Schottky device to 8% EQE. Such limitation is mainly due to the fact that carriers are excited close to the Fermi level. Thus, by modifying the DOS closer to the Fermi level, they found that such process can reach above 20% EQE. Engeneering the DOS to improve plasmonic NPs absorption is an outstanding strategy to be considered.

The future of photodetectors appears to be on-chip with many elements carrying out functions for processing. Each element combines the advantages of different approaches : electronics, for its down sizing, photonics for its speed and plasmonics for both. This kind of integration could improve on-chip plasmonic photodetectors e.g. adding on-chip amplifiers. Due to their high speed underlying physics, hot carrier plasmonics device could be directly used for on-chip all-optical processing and is a very attractive future approach.

In addition, SPs combined with superconductors [309] has great potential by reducing the losses due to cooling down reducing the losses. Combining such approach with

hot carrier devices could improve strongly their efficiency in terms of carrier extraction and dynamics. Plasmonic hot carrier process could be used as a component in plenty of devices fully integrated.

In order to build a versatile and ultrafast plasmonic hot carriers photodetector one has to handle materials, size and shape of plasmonic NPs but also on electron-donor, nearby semiconductor bandgap and Fermi level alignement. Moreover, to commercialize such photodetectors one has to take into account for the fabrication processes and the materials to be cost effective and as environmental friendly as possible.

# List of Figures

# List of publications and conference contributions

**Publications**

- Romain Hernandez, Renato Juliano Martins, Adrian Agreda, Marlene Petit, Jean-Claude Weeber, Alexandre Bouhelier, Benoit Cluzel, and Olivier Demichel. Delocalized hot-electrons generation controled by propagative SPP. ACS Photonics 2019 6 (6), 1500-1505. doi : 10.1021/acsphotonics.9b00245
- Adrian Agreda, Deepak K. Sharma, Sviatlana Viarbitskaya, Romain Hernandez, Benoît Cluzel, Olivier Demichel, Jean-Claude Weeber, Gerard Colas des Francs, G.V. Pavan Kumar, and Alexandre Bouhelier. Spatial Distribution of the Nonlinear Photoluminescence in Au Nanowires. ACS Photonics 2019, 6 (5), 1240-1247. doi : 10.1021/acsphotonics.9b00181
- D. Halpaap, M. Marconi, R. Hernandez, A. M. Yacomotti, J. Tiana-Alsina, and C. Masoller. Experimental study of speckle patterns generated by low-coherence semiconductor laser light. Chaos 2020, 30, 063147. doi : 10.1063/5.0006007

**Talks**

- Cleo Europe Munich, Virtual Conference 2021 : « Plasmon-induced hot-electrons for ultrafast photodetection ».
- CNano, in Dijon 2019 : « Investigating hot electrons remote excitation and their harvest with a semiconductor ».
- Photonics day, in Besançon 2019 : « Investigating hot electrons remote excitation and their harvest with a semiconductor ».
- Plasmonica 2019, in Naples, Italy : « Remotely Generated Hot-electron using Propagative Surface Plasmon Polaritons ».
- Summer school Plasmonica 2018, in Cetraro, Italy : « Hot-carrier generation along SPP propagation ».

**Posters**

- Optique Dijon SFO 2021 : « Investigating hot-electrons with metal-semiconductor-metal slit arrays ».
- Plasmonica 2019, in Naples, Italy : «Investigating hot-electrons with metal-semiconductor-metal slit arrays » .

- Faraday discussion 2019, London, United Kingdom : « Hot-carriers generation and dynamics along SPP propagation ».
- SPIE Photonics, in Strasbourg 2018, France : « Delocalized hot carrier generation by propagating SPP ».
- GDR Ondes, in Nice Sophia Antipolis 2017, France : attendance

# References


[1] James Clerk Maxwell. A dynamical theory of the electromagnetic field. *Philosophical Transactions of the Royal Society*, 155:459–512, 1865. 1

[2] Heinrich Hertz. Ueber einen einfluss des ultravioletten lichtes auf die electrische entladung. *Annalen der Physik*, 267(8):983–1000, 1887. 1

[3] Albert Einstein. Uber einen die erzeugung und verwandlung des lichtes betreffenden heuristischen gesichtspunkt (on a heuristic point of view about the creation and conversion of light). *Annalen der Physik*, 17(6):132–148, 1905. 1

[4] R.W. Wood. On a remarkable case of uneven distribution of light in a diffraction grating spectrum. *Phil. Mag.*, 4(6):396–402, 1902. 1, 9, 58

[5] O. M. Lord Rayleigh. Note on the remarkable case of diffraction spectra described by prof. wood. *Philos. Mag.*, 14:60–65, 1907. 1

[6] David Pines and David Bohm. A collective description of electron interactions: Ii. collective vs individual particle aspects of the interactions. *Physical Review*, 85(2):338–353, 1952. 1

[7] U. Fano. Atomic theory of electromagnetic interactions in dense materials. *Phys. Rev.*, 103(5):1202–1218, 1956. 1, 9

[8] R. H. Ritchie. Plasma losses by fast electrons in thin films. *Phys. Rev.*, 106(5):874–881, 1957. 1, 9

[9] Daniel Maystre. *Plasmonics - From Basics to Advanced Topics - In Chapter 2 : Theory of Wood's Anomalies*. Springer, stefan enoch, nicolas bonod edition, 2012. 1, 9

[10] Mark L. Brongersma, Naomi J. Halas, and Peter Nordlander. Plasmon-induced hot carrier science and technology. *Nature Nanotechnology*, 10:25–34, 2015. 1, 14, 17, 21, 25, 37, 56, 111

[11] Rashid Zia, Jon A. Schuller, Anu Chandran, and Mark L. Brongersma. Plasmonics: the next chip-scale technology. *materialstoday*, 9(7-8):20–27, 2006. 1, 7, 8, 13

[12] David Reinsel, John Gantz, and John Rydning. The digitization of the world - from edge to core, 2018. 4

[13] David Reinsel and John Rydning. Global datasphere, 2020. 4

[14] InternetLive Stats. Internet usage and social media statistics, 2020. 4

[15] Cisco. Cisco annual internet report (2018–2023), Updated in March 2020. 4

[16] Knud Lasse Lueth. State of the iot 2018: Number of iot devices now at 7b – market accelerating, 2018. 4

[17] Cisco. Cisco visual networking index: Forecast and trends,2017–2022, 2018. 4, 111

[18] Peter J. Winzer, David T. Neilson, and Andrew R. Chraplyvy. Fiber-optic transmission and networking: the previous 20 and the next 20 years [invited]. *Optics Express*, 26(18):24190–24239, 2018. 4, 5

[19] Yasuharu Suematsu and Shigehisa Arai. Single-mode semiconductor lasers for long-wavelength optical fiber communications and dynamics of semiconductor lasers. *IEEE Journal of Selected Topics in Quantum Electronics*, 6(6):1436–1449, 2000. 4, 5

[20] Govind P. Agrawal. *Fiber-Optic Communication Systems*. John Wiley and Sons Inc., Hoboken, New Jersey, 4th edition edition, 2010. 4, 30, 31, 33, 101, 104

[21] Zeping Zhao, Jianguo Liu, Yu Liu, and Ninghua Zhu. High-speed photodetectors in optical communication system. *Journal of Semiconductors*, 38(7):121001, 2017. 4, 5, 29, 30

[22] T. Miya, Y. Terunuma, T. Hosaka, and T. Miyashita. Ultimate low-loss single-mode fibre at 1.55 um. *Electronics Letters*, 15(4):106–108, 1979. 4

[23] L.G. Cohen, Chinlon Lin, and W.G. French. Tailoring zero chromatic dispersion into the 1.5–1.6 um low-loss spectral region of single-mode fibres. *Electronics Letters*, 15(12):334, 1979. 5

[24] Steven Cherry. Edholm's law of bandwidth. *IEEE Spectrum*, 41(7):58–60, 2004. 5, 111

[25] Thomas Kurner and Sebastian Priebe. Towards thz communications - status in research, standardization and regulation. *Journal of Infrared, Millimeter, and Terahertz Waves*, 35:53–62, 2014. 5, 111

[26] C.E. Shannon. A mathematical theory of communication. *The Bell System Technical Journal*, 27(3):379–423, 1948. 5

[27] Rene-Jean Essiambre, Gerhard Kramer, Peter J. Winzer, Gerard J. Foschini, and Bernhard Goebel. Capacity limits of optical fiber networks. *Journal of Lightwave Technology*, 28(4):662–701, 2010. 5

[28] Mohammad D. Al-Amri, Mohamed M. El-Gomati, and M. Suhail Zubairy. *Optics in Our Time*, chapter 8 : Optical Communication: Its History and Recent Progress, pages 177–199. Springer, 2016. 5

[29] T. Morioka, H. Takara, S. Kawanishi, O. Kamatani, K. Takiguchi, K. Uchiyama, M. Saruwatari, H. Takahashi, M. Yamada, T. Kanamori, and H. Ono. 1 tbit/s (100 gbit/s/spl times/10 channel) otdm/wdm transmission using a single supercontinuum wdm source. *Electronics Letters*, 32(10):906–907, 1996. 5

[30] Xiang Zhou, Jianjun Yu, Ming-Fang Huang, Yin Shao, Ting Wang, Lynn Nelson, Peter Magill, Martin Birk, Peter I. Borel, David W. Peckham, Robert Jr. Lingle, and Benyuan Zhu. 64-tb/s, 8 b/s/hz, pdm-36qam transmission over 320 km using both

pre- and post-transmission digital signal processing. *Journal of Lightwave Technology*, 29(4):571–577, 2011. 5

[31] D. J. Richardson, J. M. Fini, and L. E. Nelson. Space-division multiplexing in optical fibres. *Nature Photonics*, 7:354–362, 2013. 6

[32] NICT. World record transmission of 172 terabit/s over 2,040 km distance coupled-3-core multi-core fiber, 2020. 6

[33] Peter J. Winzer. Energy-efficient optical transport capacity scaling through spatial multiplexing. *IEEE Photonics Technology Letters*, 23(13):851–853, 2011. 6

[34] Tom Bawden. Global warming: Data centres to consume three times as much energy in next decade, experts warn, 2016. 6

[35] Hai-Feng Liu. Integrated silicon photonics links for high bandwidth data transportation. *OFC 2014*, 2014. 6, 7, 111

[36] Keren Bergman, Luca P. Carloni, and Jeffrey Kash. On-chip photonic communication for high-performance multi-core processors. *HPEC workshop*, 2007. 6, 7, 111

[37] Winnie N. Ye and Yule Xiong. Review of silicon photonics: history and recent advances. *Journal of Modern Optics*, 60(16):1299–1320, 2013. 6

[38] Ashish Dhiman. Silicon photonics: A review. *IOSR-JAP*, 3(5):67–79, 2013. 6

[39] M. Fukuda, Y. Tonooka, T. Inoue, and M. Ota. Feasibility of plasmonic circuits for on-chip interconnects. *Solid-State Electronics*, 156:33–40, 2019. 7

[40] J.A. Conway, S. Sahni, and T. Szkopek. Plasmonic interconnects versus conventional interconnects: a comparison of latency, crosstalk and energy costs. *Opt. Express*, 15(8):4474–4484, 2007. 7

[41] C. Koos, P. Vorreau, T. Vallaitis, P. Dumon, W. Bogaerts, R. Baets, B. Esembeson, I. Biaggio, T. Michinobu, F. Diederich, W. Freude, and J. Leuthold. All-optical high-speed signal processing with silicon–organic hybrid slot waveguides. *Nature Photon*, 3:216–219, 2009. 7

[42] Xin Tu, Chaolong Song, Tianye Huang, Zhenmin Chen, and Hongyan Fu. State of the art and perspectives on siliconphotonic switches. *Micromachines*, 10(51), 2019. 7

[43] R. Dekker, N. Usechak, M. Forst, and A. Driessen. Ultrafast nonlinear all-optical processes in siliconon-insulator waveguides. *J. Phys. D: Appl. Phys.*, 40(14):R249–R271, 2007. 7

[44] J. P. Guillet, B. Recur, L. Frederique, B. Bousquet, L. Canioni, I. Manek-Hönninger, P. Desbarats, and P. Mounaix. Review of terahertz tomography techniques. *J Infrared Milli Terahz Waves*, 35:382–411, 2014. 7

[45] R.A. Lewis. A review of terahertz sources. *J. Phys. D: Appl. Phys.*, 47(37):374001, 2014. 7

[46] S.-H. Yang, R. Watts, X. Li, N. Wang, V. Cojocaru, J. O'Gorman, L. P. Barry, and M. Jarrahi. Tunable terahertz wave generation through a bimodal laser diode and plasmonic photomixer. *Opt. Express*, 23(24):31206–31215, 2015. 8, 111

[47] S. Koenig, D. Lopez-Diaz, J. Antes, F. Boes, R. Henneberger, A. Leuther, A. Tessmann, R. Schmogrow, D. Hillerkuss, R. Palmer, T. Zwick, W. Koos, C. andFreude, O. Ambacher, J. Leuthold, and I. Kallfass. Wireless sub-thz communication system with high data rate. *Nature Phot*, 7:977–981, 2013. 8

[48] Science Mission Directorate Technology Highlights Report NASA. Advancing local terahertz oscillators to enable cosmic observations, 2017. 8

[49] Kevin F. MacDonald, Zsolt L. Samson, Mark I. Stockman, and Nikolay I. Zheludev. Ultrafast active plasmonics. *Nature Photon*, 3:55–58, 2008. 9

[50] O. M. Lord Rayleigh. On the dynamical theory of gratings. *Proc. R. Soc. Lond.*, 79:399–416, 1907. 9, 58

[51] U. Fano. The theory of anomalous diffraction gratings and of quasi-stationary waves on metallic surfaces (sommerfeld's waves). *J. Opt. Soc. Am.*, 31(3):213–222, 1941. 9

[52] A. Hessel and A. A. Oliner. A new theory of wood's anomalies on optical gratings. *Appl. Opt.*, 4(10):1275–1297, 1965. 9, 58

[53] Jiri Homola, Sinclair S. Yee, and Gunter Gauglitz. Surface plasmon resonance sensors: review. *Sensors and Actuators B*, 54(1-2):3–15, 1999. 9

[54] S. L. Cunningham, A. A. Maradudin, and R. F. Wallis. Effect of a charge layer on the surface-plasmon-polariton dispersion curve. *Phys. Rev. B*, 10(8):3342, 1974. 9

[55] Mark L. Brongersma, John W. Hartman, and Harry H. Atwater. Plasmonics: Electromagnetic energy transfer and switching in nanoparticle chain-arrays below the diffraction limit. *Mater. Res. Soc. Symp. Proc.*, 502:H10.5, 1999. 9

[56] Thomas W. Ebbesen, Cyriaque Genet, and Sergey I. Bozhevolnyi. Surface-plasmon circuitry. *Phys. Today*, 61(5):44, 2008. 9, 11

[57] Kristjan Leosson. Optical amplification of surface plasmon polaritons: review. *J. of Nanophotonics*, 6(1):061801, 2012. 9

[58] A. L. Lereu, A. Passian, J-P. Goudonnet, T. Thundat, and T. L. Ferrell. Optical modulation processes in thin films based on thermal effects of surface plasmons. *Appl. Phys. Lett.*, 86:154101, 2005. 9

[59] Domenico Pacifici, Henri J. Lezec, and Harry A. Atwater. All-optical modulation by plasmonic excitation of cdse quantum dots. *Nature Photon*, 1(7):402–406, 2007. 9

[60] Dmitry Yu. Fedyanin and Aleksey V. Arsenin. Semiconductor surface plasmon amplifier based on a schottky barrier diode. *AIP Conference Proceedings*, 1291:112, 2010. 9

[61] Stefan Alexander Maier. *Plasmonics - Fundamentals and Applications*. Springer, 2007. 9, 10, 11, 12, 13, 39, 40, 58, 111

[62] L. Novotny and B. Hecht. *Principles of Nano-Optics*, chapter Chapter 12 : Surface plasmons. Cambridge University Press, 2006. 9, 10, 12, 13, 39, 111

[63] A. Otto. Excitation of surface plasma waves in silver by the method of frustrated total reflection. *Z. Physik*, 216:398–410, 1968. 10, 27

[64] E. Kretschmann and H. Raether. Radiative decay of non-radiative surface plasmons excited by light. *Z. Naturforsch.*, 23(12):2135–2136, 1968. 10

[65] I. R. Hooper and J. R. Sambles. Dispersion of surface plasmon polaritons on short-pitch metal gratings. *Phys. Rev. B*, 65(16):165432, 2002. 10

[66] A. Bouhelier and G. P. Wiederrecht. Excitation of broadband surface plasmon polaritons: Plasmonic continuum spectroscopy. *Phys. Rev. B*, 71(19):195406, 2005. 10

[67] H. Ditlbacher, J. R. Krenn, N. Felidj, B. Lamprecht, G. Schider, M. Salerno, A. Leitner, and F. R. Aussenegg. Fluorescence imaging of surface plasmon fields. *Appl. Phys. Lett.*, 80(3):404, 2002. 10

[68] J. T. van Wijngaarden, E. Verhagen, A. Polman, C. E. Ross, H. J. Lezec, and H. A. Atwater. Direct imaging of propagation and damping of near-resonance surface plasmon polaritons using cathodoluminescence spectroscopy. *Appl. Phys. Lett.*, 88:221111, 2006. 11

[69] B. Hecht, H. Bielefeldt, L. Novotny, Y. Inouye, and D. W. Pohl. Local excitation, scattering, and interference of surface plasmons. *Phys. Rev. Lett.*, 77(9):1889–1892, 1996. 11

[70] Harald Ditlbacher, Andreas Hohenau, Dieter Wagner, Uwe Kreibig, Michael Rogers, Ferdinand Hofer, Franz R. Aussenegg, and Joachim R. Krenn. Silver nanowires as surface plasmon resonators. *Physical Review Letters*, 95(25):257403, 2005. 11, 49, 50

[71] J.-C. Weeber, J. R. Krenn, A. Dereux, B. Lamprecht, Y. Lacroute, and J. P. Goudonnet. Near-field observation of surface plasmon polariton propagation on thin metal stripes. *Physical Review B*, 64(4):045411, 2001. 11, 49, 50

[72] Sergey I. Bozhevolnyi. *Plasmonic - Nanoguides and Circuits*. Pan Stanford Publishing, 2009. 11

[73] C. L. C. Smith, N. Stenger, A. Kristensen, N. A. Mortensen, and S. I. Bozhevolnyi. Gap and channeled plasmons in tapered grooves:a review. *Nanoscale*, 7:9355–9386, 2015. 11

[74] Michael W. Vogel and Dmitri K. Gramotnev. Adiabatic nano-focusing of plasmons by metallic tapered rods in the presence of dissipation. *Physics Letters A*, 363:507–511, 2007. 11

[75] Pierre Berini. Long-range surface plasmon polaritons. *Adv. Opt. Photon.*, 1(3):484–588, 2009. 11

[76] Stephane Collin, Fabrice Pardo, and Jean-Luc Pelouard. Waveguiding in nanoscale metallic apertures. *Opt. Express*, 15(7):4310, 2007. 11

[77] Pierre Berini. Plasmon-polariton waves guided by thin lossy metal films of finite width: Bound modes of symmetric structures. *Phys. Rev. B*, 61(15):10484, 2000. 11

[78] Javier Aizpurua and Rainer Hillenbrand. *Plasmonics - From Basics to Advanced Topics - In Chapter 6 : Localized Surface Plasmons: Basics and Applications in Field-Enhanced Spectroscopy*. Springer, stefan enoch, nicolas bonod edition, 2012. 11, 13

[79] Surbhi Lal, Stephan Link, and Naomi J. Halas. Nano-optics from sensing to waveguiding. *Nature Photon*, 1:641–648, 2007. 11

[80] Tamitake Itoh, Vasudevanpillai Biju, and Mitsuru Ishikawa. Surface-enhanced resonance raman scattering and background light emission coupled with plasmon of single ag nanoaggregates. *The Journal of Chemical Physics*, 124:134708, 2006. 11, 19, 21

[81] Pascal Anger, Palash Bharadwaj, and Lukas Novotny. Enhancement and quenching of single-molecule fluorescence. *Phys. Rev. Lett.*, 96(11):113002, 2006. 11

[82] S. Pillai, K. R. Catchpole, T. Trupke, and M. A. Green. Surface plasmon enhanced silicon solar cells. *J. Appl. Phys.*, 101(9):093105, 2007. 11, 27, 34, 56

[83] Shaunak Mukherjee, Florian Libisch, Nicolas Large, Oara Neumann, Lisa V. Brown, Jin Cheng, J. Britt Lassiter, Emily A. Carter, Peter Nordlander, and Naomi J. Halas. Hot electrons do the impossible: Plasmon-induced dissociation of h2 on au. *Nano Letters*, 13(1):240–247, 2013. 12, 37

[84] Phillip M. Nagel, Joseph S. Robinson, Bruce D. Harteneck, Thomas Pfeifer, Mark J. Abel, James S. Prell, Daniel M. Neumark, Robert A. Kaindl, and Stephen R. Leone. Surface plasmon assisted electron acceleration in photoemission from gold nanopillars. *Chemical Physics*, 414(12):106–111, 2013. 12

[85] Craig F. Bohren. How can a particle absorb more than the light incident on it? *American Journal of Physics*, 51:323, 1983. 12

[86] William L. Barnes, Alain Dereux, and Thomas W. Ebbesen. Surface plasmon subwavelength optics. *Nature*, 424:824–830, 2003. 12

[87] Yong Chen and Hai Ming. Review of surface plasmon resonance and localized surface plasmon resonance sensor. *Photonic Sensors*, 2(1):37–49, 2012. 12

[88] Craig F. Bohren and Donald R. Huffman. *Absorption and Scattering of Light by Small Particles*. Wiley Professional, 1983. 12

[89] Jana Olson, Sergio Dominguez-Medina, Anneli Hoggard, Lin-Yung Wang, Wei-Shun Chang, and Stephan Link. Optical characterization of single plasmonic nanoparticles. *Chem. Soc. Rev.*, 44(40):40–57, 2015. 12

[90] Sheldon Schultz, David R. Smith, Jack J. Mock, and David A. Schultz. Single-target molecule detection with nonbleaching multicolor optical immunolabels. *PNAS*, 97(3):996–1001, 2000. 12

[91] K. Lindfors, T. Kalkbrenner, P. Stoller, and V. Sandoghdar. Detection and spectroscopy of gold nanoparticles using supercontinuum white light confocal microscopy. *Phys. Rev. Lett.*, 93(3):037401, 2004. 13

[92] V. A. Markel, V. M. Shalaev, P. Zhang, W. Huynh, L. Tay, T. L. Haslett, and M. Moskovits. Near-field optical spectroscopy of individual surface-plasmon modes in colloid clusters. *Phys. Rev. B*, 59(16):10903, 1999. 13

[93] Huakang Yu, Yusi Peng, Yong Yang, and Zhi-Yuan Li. Plasmon-enhanced light–matter interactions and applications. *npj Computational Materials*, 5(45), 2019. 13

[94] O. L. Muskens, N. Del Fatti, F. Vallée, J. R. Huntzinger, P. Billaud, and M. Broyer. Single metal nanoparticle absorption spectroscopy and optical characterization. *Appl. Phys. Lett.*, 88:063109, 2006. 13

[95] Paolo Biagioni, Jer-Shing Huang, and Bert Hecht. Nanoantennas for visible and infrared radiation. *Rep. Prog. Phys.*, 75(2):024402, 2012. 13

[96] C. Sonnichsen, T. Franzl, T. Wilk, G. von Plessen, J. Feldmann, O. Wilson, and P. Mulvaney. Drastic reduction of plasmon damping in gold nanorods. *Phys. Rev. Lett.*, 88(7):077402, 2002. 13

[97] Leif J. Sherry, Shih-Hui Chang, George C. Schatz, Richard P. Van Duyne, Benjamin J. Wiley, and Younan Xia. Localized surface plasmon resonance spectroscopy of single silver nanocubes. *Nano. Lett.*, 5(10):2034–2038, 2005. 13

[98] P. J. Schuck, D. P. Fromm, A. Sundaramurthy, G. S. Kino, and W. E. Moerner. Improving the mismatch between light and nanoscale objects with gold bowtie nanoantennas. *Phys. Rev. Lett.*, 94:017402, 2005. 13

[99] E. Prodan, C. Radloff, N. J. Halas, and P. Nordlander. A hybridization model for the plasmon response of complex nanostructures. *Science*, 302:419, 2003. 13

[100] O. Perez-Gonzalez, N. Zabala, and J. Aizpurua. Optical characterization of charge transfer and bonding dimer plasmons in linked interparticle gaps. *New J. Phys.*, 13:083013, 2011. 13

[101] Jianjun Chen, Fengyuan Gan, Yujia Wang, and Guozhou Li. Plasmonic sensing and modulation based on fano resonances. *Adv. Optical Mater.*, 6:1701152, 2018. 13

[102] Thomas Maurer, Pierre-Michel Adam, and Gaetan Leveque. Coupling between plasmonic films and nanostructures: from basics to applications. 4:363–382. 13

[103] Jean Cesario, Maria Ujue Gonzalez, Stephanie Cheylan, William. L. Barnes, Stefan Enoch, and Romain Quidant. Coupling localized and extended plasmons to improve the light extraction through metal films. *Opt. Express*, 15(17):10533–9, 2007. 13

[104] Martti Kauranen and Anatoly V. Zayats. Nonlinear plasmonics. *Nature Photon*, 6(11):737–748, 2012. 13

[105] Bob Y. Zheng, Hangqi Zhao, Alejandro Manjavacas, Michael McClain, Peter Nordlander, and Naomi J. Halas. Distinguishing between plasmon-induced and photoexcited carriers in a device geometry. *Nature Communications*, 6:7797, 2015. 14, 38

[106] Ravishankar Sundararaman, Prineha Narang, Adam S. Jermyn, William A. Goddard III, and Harry A. Atwater. Theoretical predictions for hot-carrier generation from surface plasmon decay. *Nature Communications*, 5(5788), 2014. 14, 15, 39, 111

[107] Paolo Biagioni, Daniele Brida, Jer-Shing Huang, Johannes Kern, Lamberto Duò, Bert Hecht, Marco Finazzi, and Giulio Cerullo. Dynamics of four-photon photoluminescence in gold nanoantennas. *Nano Letters*, 12(6):2941–2947, 2012. 14, 21, 38, 53

[108] Regis Mejard, Anthonin Verdy, Marlene Petit, Alexandre Bouhelier, Benoit Cluzel, and Olivier Demichel. Energy-resolved hot-carrier relaxation dynamics in monocrystalline plasmonic nanoantennas. *ACS Photonics*, 3(8):1482–1488, 2016. 14, 20, 21, 38, 52, 99

[109] Michael R. Beversluis, Alexandre Bouhelier, and Lukas Novotny. Continuum generation from single gold nanostructures through near-field mediated intraband transitions. *Phys. Rev. B*, 68(11):115433, 2003. 15, 18, 19, 20, 38, 54, 107

[110] Prineha Narang, Ravishankar Sundararaman, and Harry A. Atwater. Plasmonic hot carrier dynamics in solid-state and chemical systems for energy conversion. *Nanophotonics*, 5(1):96–111, 2016. 15, 16, 18

[111] Ana M. Brown, Ravishankar Sundararaman, Prineha Narang, William A. Goddard, and Harry A. Atwater. Nonradiative plasmon decay and hot carrier dynamics: Effects of phonons, surfaces, and geometry. *ACS Nano*, 10:957–966, 2016. 15

[112] Ilya Goykhman, Boris Desiatov, Joseph Shappir, Jacob B. Khurgin, and Uriel Levy. Model for quantum efficiency of guided mode plasmonic enhanced silicon schottky detectors. *arXiv*, 2014. 15, 16, 23

[113] Joanna Olesiak-Banska, Magdalena Waszkielewicz, Patryk Obstarczyk, and Marek Samoc. Two-photon absorption and photoluminescence of colloidal gold nanoparticles and nanoclusters. *Chem. Soc. Rev.*, 48(15):4087–4117, 2019. 16

[114] M. Trejo-Valdez, R. Torres-Martinez, N. Perea-Lopez, P. Santiago-Jacinto, and C. Torres-Torres. Contribution of the two-photon absorption to the third order nonlinearity of au nanoparticles embedded in tio2 films and in ethanol suspension. *J. Phys. Chem. C*, 114(22):10108–10113, 2010. 16

[115] Adam S. Jermyn, Giulia Tagliabue, Harry A. Atwater, William A. Goddard III, Prineha Narang, and Ravishankar Sundararaman. Transport of hot carriers in plasmonic nanostructures. *Phys. Rev. Materials*, 3(7):075201, 2019. 16

[116] B. R. Nag. Diffusion equation for hot electrons. *Phys. Rev. B*, 11(8):3031, 1975. 16

[117] John J. Quinn. Range of excited electrons in metals*. *Phys. Rev.*, 126(4):1453, 1962. 16

[118] Christine Scales and Pierre Berini. Thin-film schottky barrier photodetector models. *IEEE Journal of Quantum Electronics*, 46(5):633–643, 2010. 16, 17, 23, 24, 25, 111

[119] Daniel Gall. Electron mean free path in elemental metals. *Journal of Applied Physics*, 119:085101, 2016. 16

[120] C. R. Crowell, W. G. Spitzer, L. E. Howarth, and E. E. LaBate. Attenuation length measurements of hot electrons in metal films. *Physical Review*, 127:2006, 1962. 16

[121] C. R. Crowell and S. M. Sze. Ballistic mean free path measurements of hot electrons in au films. *Physical Review Letters*, 15:659, 1965. 16

[122] C. Girardin, R. Coratger, R. Pechou, F. Ajustron, and J. Beauvillain. Study of the electron mean free path by ballistic electron emission microscopy. *Journal de Physique III, EDP Sciences*, 6(5):661–669, 1996. 16

[123] Gregory V. Hartland. Optical studies of dynamics in noble metal nanostructures. *Chem. Rev.*, 111(6):3858–3887, 2011. 17

[124] M. Bauer, A. Marienfeld, and M. Aeschlimann. Hot electron lifetimes in metals probed by time-resolved two-photon photoemission. *Progress in Surface Science*, 90:319–376, 2015. 17

[125] N. Del Fatti, C. Voisin, M. Achermann, S. Tzortzakis, D. Christofilos, and F. Vallee. Nonequilibrium electron dynamics in noble metals. *Phys. Rev. B*, 61(24):16956, 2000. 17

[126] Guillaume Baffou and Herve Rigneault. Femtosecond-pulsed optical heating of gold nanoparticles. *Phys. Rev. B*, 84(3):035415, 2011. 17

[127] Florian Ladstadter, Ulrich Hohenester, Peter Puschnig, and Claudia Ambrosch-Draxl. First-principles calculation of hot-electron scattering in metals. *Phys. Rev. B*, 70(23):235125, 2004. 17

[128] Ilya Razdolski, Alexander L. Chekhov, Alexander I. Stognij, and Andrzej Stupakiewicz. Ultrafast transport and relaxation of hot plasmonic electrons in metal-dielectric heterostructures. *Phys. Rev. B*, 100(4):045412, 2019. 17

[129] A. Block, M. Liebel, R. Yu, M. Spector, Y. Sivan, F. J. Garcia de Abajo, and N.F. van Hulst. Tracking ultrafast hot-electron diffusion in space and time by ultrafast thermo-modulation microscopy. *Sciences Advances*, 5(5), 2019. 17

[130] Tobias Haug, Philippe Klemm, Sebastian Bange, and John M. Lupton. Hot-electron intraband luminescence from single hot spots in noble-metal nanoparticle films. *Phys. Rev. Lett.*, 115(6):067403, 2015. 18, 20, 21, 47, 54

[131] Lukas Roloff, Philippe Klemm, Imke Gronwald, Rupert Huber, John M. Lupton, and Sebastian Bange. Light emission from gold nanoparticles under ultrafast near-infrared excitation: Thermal radiation, inelastic light scattering, or multiphoton luminescence? *Nano Letters*, 17(12):7914–7919, 2017. 18, 19, 20, 21, 38, 54, 107, 111

[132] Yiyu Cai, Jun G. Liu, Lawrence J. Tauzin, Da Huang, Eric Sung, Hui Zhang, Anneli Joplin, Wei-Shun Chang, Peter Nordlander, and Stephan Link. Photoluminescence of gold nanorods: Purcell effect enhanced emission from hot carriers. *ACS Nano*, 12(2):976–985, 2018. 18, 19, 20, 111

[133] S. M. Sze and Kwok K. Ng. *Physics of Semiconductor Devices*. Wiley, 3rd edition edition, 2007. 19, 22, 23, 57, 70, 103

[134] A. Mooradian. Photoluminescence of metals. *Physical Review Letters*, 22(5):185–187, 1969. 19

[135] Mona B. Mohamed, Victor Volkov, Stephan Link, and Mostafa A. El-Sayed. The 'lightning' gold nanorods: fluorescence enhancement of over a million compared to the gold metal. *Chemical Physics Letters*, 317(6):517–523, 2000. 19

[136] Tingting Yin, Liyong Jiang, and Zexiang Shen. Recent progress on photoluminescence from plasmonic nanostructures: Phenomenon, mechanism, and application. *Chin. Phys. B*, 27:097803, 2018. 19, 37, 38

[137] O. P. Varnavski, T. Goodson III, M. B. Mohamed, and M. A. El-Sayed. Femtosecond excitation dynamics in gold nanospheres and nanorods. *Physical Review B*, 72(23):235405, 2005. 19

[138] A. Otto. Surface enhanced raman scattering (sers), what do we know? *Applications of Surface Science*, 6(3-4):309–355, 1980. 19

[139] H.A. Alluhaybia, S.K. Ghoshala, B.O. Alsobhib, and W.N. Wan Shamsuri. Visible photoluminescence from gold nanoparticles: A basic insight. *Optik - International Journal for Light and Electron Optics*, 192:162936, 2019. 19

[140] Kohei Imura, Tetsuhiko Nagahara, and Hiromi Okamoto. Near-field two-photon-induced photoluminescence from single gold nanorods and imaging of plasmon modes. *The Journal of Physical Chemistry B*, 109(27):13214–13220, 2005. 20, 38, 53

[141] Xiao-Fang Jiang, Yanlin Pan, Cuifeng Jiang, Tingting Zhao, Peiyan Yuan, T. Venkatesan, and Qing-Hua Xu. Excitation nature of two-photon photoluminescence of gold nanorods and coupled gold nanoparticles studied by two-pulse emission modulation spectroscopy. *The Journal of Physical Chemistry Letters*, 4:1634–1638, 2013. 20, 38, 51

[142] Yi-Yu Cai, Eric Sung, Runmin Zhang, Lawrence J. Tauzin, Jun G. Liu, Behnaz Ostovar, Yue Zhang, Wei-Shun Chang, Peter Nordlander, and Stephan Link. Anti-stokes emission from hot carriers in gold nanorods. *Nano Letters*, 19(2):1067–1073, 2019. 20, 47

[143] Vanessa Knittel, Marco P. Fischer, Tjaard de Roo, Stefan Mecking, Alfred Leitenstorfer, and Daniele Brida. Nonlinear photoluminescence spectrum of single gold nanostructures. *ACS Nano*, 9(1):894–900, 2015. 21

[144] Emilie Sakat, Ilaria Bargigia, Michele Celebrano, Andrea Cattoni, Stephane Collin, Daniele Brida, Marco Finazzi, Cosimo D'Andrea, and Paolo Biagioni. Time-resolved photoluminescence in gold nanoantennas. *ACS Photonics*, 3:1489–1493, 2016. 21

[145] Olivier Demichel, Marlene Petit, Sviatlana Viarbitskaya, Regis Mejard, Frederique de Fornel, Edouard Hertz, Franck Billard, Alexandre Bouhelier, and Benoit Cluzel. Dynamics, efficiency, and energy distribution of nonlinear plasmon-assisted generation of hot carriers. *ACS Photonics*, 3(5):791–795, 2016. 21, 37, 38, 44, 52, 56

[146] Jan Mertens, Marie-Elena Kleemann, Rohit Chikkaraddy, Prineha Narang, and Jeremy J. Baumberg. How light is emitted by plasmonic metals. *Nano Letters*, 17(4):2568–2574, 2017. 21

[147] James T. Hugall and Jeremy J. Baumberg. Demonstrating photoluminescence from au is electronic inelastic light scattering of a plasmonic metal: The origin of sers backgrounds. *Nano Letters*, 15(4):2600–2604, 2015. 21

[148] J.P. Heritage, J.G. Bergman, A. Pinczuk, and J.M. Worlock. Surface picosecond raman gain spectroscopy of a cyanide monolayer on silver. *Chemical Physics Letters*, 67(2-3):229–232, 1979. 21

[149] P. Biagioni, M. Celebrano, M. Savoini, G. Grancini, D. Brida, S. Mátéfi-Tempfli, M. Mátéfi-Tempfli, L. Duò, B. Hecht, G. Cerullo, and M. Finazzi. Dependence of the two-photon photoluminescence yield of gold nanostructures on the laser pulse duration. *Phys. Rev. B*, 80(4):045411, 2009. 21, 38, 53, 56

[150] Gregory N. Derry, Megan E. Kern, and Eli H. Worth. Recommended values of clean metal surface work functions. *J. Vac. Sci. Technol. A*, 33:060801, 2015. 22

[151] Marius Grundmann. *The Physics of Semiconductors - An Introduction Including Nanophysics and Applications*. Springer, 3rd edition edition, 2016. 22, 23, 103, 104, 111

[152] John Bardeen. Surface states and rectification at a metal semi-conductor contact. *Physical Review*, 71(10):717–727, 1947. 22

[153] Volker Heine. Theory of surface states. *Physical Review*, 138(6A):1689, 1965. 22

[154] W. Monch. 125 years of metal-semiconductor contacts: Where do we stand? *Advances in Solid State Physics*, 39:13–24, 1999. 22

[155] Raymond T. Tung. Formation of an electric dipole at metal-semiconductor interfaces. *Physical Review B*, 64:205310, 2001. 22

[156] Walter E. Meyerhof. Contact potential difference in silicon crystal rectifiers. *Physical Review*, 71(10):727–735, 1947. 22

[157] Robert Balsano, Akitomo Matsubayashi, and Vincent P. LaBella. Schottky barrier height measurements of cu/si(001), ag/si(001), and au/si(001) interfaces utilizing ballistic electron emission microscopy and ballistic hole emission microscopy. *AIP Advances*, 3:112110, 2013. 23

[158] J. L. Saltich and L. E. Terry. Effects of pre- and post-annealing treatments on silicon schottky barrier diodes. *PROCEEDINGS OF THE IEEE*, pages 492–494, 1970. 23

[159] Raymond T. Tung. Schottky barrier height-do we really understand what we measure? *Journal of Vacuum Science and Technology B*, 1993. 23

[160] C. Daboo, M.J. Baird, H.P. Hughes, N. Apsley, and M.T. Emeny. Improved surface plasmon enhanced photodetection at an au-gaas schottky junction using a novel molecular beam epitaxy grown otto coupling structure. *Thin Solid Fims*, 20(1):9–27, 1991. 23

[161] Wei Li and Jason G. Valentine. Harvesting the loss: surface plasmon-based hot electron photodetection. *Nanophotonics*, 6(1):177–191, 2017. 25

[162] Antoni Rogalski. History of infrared detectors. *Opto-Electronics Review*, 20(3):279–308, 2012. 25, 29, 30

[163] Paul R. Norton. Infrared detectors in the next millennium. *Proc. SPIE, Infrared Technology and Applications XXV*, 3698, 1999. 25

[164] Chenson K. Chen, Bettina Nechay, and Bor-Yeu Tsaur. Ultraviolet, visible, and infrared response of ptsi schottky-barrier detectors operated in the front-illuminated mode. *IEEE Transactions on Electron Devices*, 38(5):1094–1103, 1991. 25

[165] R. Stuart, F. Wooten, and W. E. Spicer. Monte carlo calculations pertaining to the transport of hot electrons in metals. *Physical Review*, 135:A495, 1964. 26

[166] R. H. Fowler. The analysis of photoelectric sensitivity curves for clean metals at various temperatures. *Phys. Rev.*, 38(1):45, 1931. 26

[167] Mark W. Knight, Heidar Sobhani, Peter Nordlander, and Naomi J. Halas. Photodetection with active optical antennas. *Science*, 332(6030):702–704, 2011. 26, 27, 29, 37, 56, 57, 90, 108, 111, 112

[168] Young Keun Lee, Chan Ho Jung, Jonghyurk Park, Hyungtak Seo, Gabor A. Somorjai, and Jeong Young Park. Surface plasmon-driven hot electron flow probed with metal-semiconductor nanodiodes. *Nano Letters*, 11(10):4251–4255, 2011. 26, 27

[169] K. M. Torosian, A. S. Karakashian, and Y. Y. Teng. Surface plasma-enhanced internal photoemission in gallium arsenide schottky diodes. *Appl. Opt.*, 26(13):2650–2652, 1987. 27, 56

[170] C. Daboo, M.J. Baird, H.P. Hughes, N. Apsley, and M.T. Emeny. Improved surface plasmon enhanced photodetection at an au-gaas schottky junction using a novel molecular beam epitaxy grown otto coupling structure. *Thin Solid Films*, 201(1):9–27, 1991. 27, 56

[171] Christine Scales and Pierre Berini. Schottky barrier photodetectors. *U.S. Patent 7 026 701*, 2006. 27

[172] Christine Scales, Ian Breukelaar, and Pierre Berini. Surface-plasmon schottky contact detector based on a symmetric metal stripe in silicon. *Optics Letters*, 35(4):529–531, 2010. 27, 56

[173] Ali Akbari, R. Niall Tait, and Pierre Berini. Surface plasmon waveguide schottky detector. *Opt. Express*, 18(8):8505–8514, 2010. 27, 56

[174] Pierre Berini, Anthony Olivieri, and Chengkun Chen. Thin au surface plasmon waveguide schottky detectors on p-si. *Nanotechnology*, 23:444011, 2012. 27, 29, 112

[175] Ilya Goykhman, Boris Desiatov, Jacob Khurgin, Joseph Shappir, and Uriel Levy. Locally oxidized silicon surface-plasmon schottky detector for telecom regime. *Nano Letters*, 11(6):2219–2224, 2011. 27, 90, 108

[176] Ilya Goykhman, Boris Desiatov, Jacob Khurgin, Joseph Shappir, and Uriel Levy. Waveguide based compact silicon schottky photodetector with enhanced responsivity in the telecom spectral band. *Opt. Express*, 20(27):28594–28602, 2012. 27

[177] S. Muehlbrandt, A. Melikyan, T. Harter, K. Kohnle, A. Muslija, P. Vincze, S. Wolf, P. Jakobs, Y. Fedoryshyn, W. Freude, J. Leuthold, C. Koos, and M. Kohl. Silicon-plasmonic internal-photoemission detector for 40 gbit/s data reception. *Optica*, 3(7):741–747, 2016. 27

[178] Yoshiaki Nishijima, Kosei Ueno, Yukie Yokota, Kei Murakoshi, and Hiroaki Misawa. Plasmon-assisted photocurrent generation from visible to near-infrared wavelength using a au-nanorods/tio2 electrode. *The Journal of Physycal Chemistry Letters*, 1(13):2031–2036, 2010. 27, 56

[179] Syed Mubeen, Gerardo Hernandez-Sosa, Daniel Moses, Joun Lee, and Martin Moskovits. Plasmonic photosensitization of a wide band gap semiconductor: Converting plasmons to charge carriers. *Nano Letters*, 11:5548–5552, 2011. 27

[180] Boris Desiatov, Ilya Goykhman, Noa Mazurski, Joseph Shappir, Jacob B. Khurgin, and Uriel Levy. Plasmonic enhanced silicon pyramids for internal photoemission schottky detectors in the near-infrared regime. *Optica*, 2(4):335–338, 2015. 27

[181] Mark W. Knight, Yumin Wang, Alexander S. Urban, Ali Sobhani, Bob Y. Zheng, Peter Nordlander, and Naomi J. Halas. Embedding plasmonic nanostructure diodes enhances hot electron emission. *Nano Letters*, 13(4):1687–1692, 2013. 27

[182] Keng-Te Lin, Hsuen-Li Chen, Yu-Sheng Lai, and Chen-Chieh Yu. Silicon-based broadband antenna for high responsivity and polarization-insensitive photodetection at telecommunication wavelengths. *Nature Communications*, 5:3288, 2014. 27

[183] S. R. J. Brueck, V. Diadiuk, T. Jones, and W. Lenth. Enhanced quantum efficiency internal photoemission detectors by grating coupling to surface plasma waves. *Appl. Phys. Lett.*, 46(10):915, 1985. 28, 56

[184] Ali Sobhani, Mark W. Knight, Yumin Wang, Bob Zheng, Nicholas S. King, Lisa V. Brown, Zheyu Fang, Peter Nordlander, and Naomi J. Halas. Narrowband photodetection in the near-infrared with a plasmon-induced hot electron device. *Nature Communications*, 4(1643), 2013. 28, 90

[185] T. W. Ebbesen, H. J. Lezec, H. F. Ghaemi, T. Thio, and P. A Wolff. Extraordinary optical transmission through sub-wavelength hole arrays. *Nature*, 391:pages 667–669, 1998. 28, 67, 74

[186] Hamidreza Chalabi, David Schoen, and Mark L. Brongersma. Hot-electron photodetection with a plasmonic nanostripe antenna. *Nano Letters*, 14(3):1374–1380, 2014. 28, 29, 112

[187] Kai Wu, Yaohui Zhan, Cheng Zhang, Shaolong Wu, and Xiaofeng Li. Strong and highly asymmetrical optical absorption in conformal metal-semiconductor-metal grating system for plasmonic hot-electron photodetection application. *Scientific Reports*, 5:14304, 2015. 28

[188] Hongbin Xiao, Shu-Cheng Lo, Yi-Hsin Tai, J. Kenji Clark, Ya-Lun Ho, Chih-Zong Deng, Pei-Kuen Wei, and Jean-Jacques Delaunay. Hot electron photodetection with spectral selectivity in the c-band using a silicon channel-separated gold grating structure. *Nano Ex.*, 1(1):010015, 2020. 28

[189] Mehbuba Tanzid, Arash Ahmadivand, Runmin Zhang, Ben Cerjan, Ali Sobhani, Sadegh Yazdi, Peter Nordlander, and Naomi J. Halas. Combining plasmonic hot carrier generation with free carrier absorption for high-performance near-infrared silicon-based photodetection. *ACS Photonics*, 5(9):3472–3477, 2018. 28

[190] Wei Li and Jason Valentine. Metamaterial perfect absorber based hot electron photodetection. *Nano Letters*, 14(6):3510–3514, 2014. 28, 29, 112

[191] Wei Li, Zachary J. Coppens, Lucas V. Besteiro, Wenyi Wang, Alexander O. Govorov, and Jason and Valentine. Circularly polarized light detection with hot electrons in chiral plasmonic metamaterials. *Nature Communications*, 6(8379), 2015. 28

[192] Fuming Wang and Nicholas A. Melosh. Plasmonic energy collection through hot carrier extraction. *Nano Lett.*, 11:5426–5430, 2011. 28

[193] Fatih B. Atar, Enes Battal, Levent E. Aygun, Bihter Daglar, Mehmet Bayindir, and Ali K. Okyay. Plasmonically enhanced hot electron based photovoltaic device. *Opt. Express*, 21(6):7196–7201, 2013. 28

[194] Thomas Mueller, Fengnian Xia, and Phaedon Avouris. Graphene photodetectors for high-speed optical communications. *Nature Photon*, 4:297–301, 2010. 28

[195] Zheyu Fang, Zheng Liu, Yumin Wang, Pulickel M. Ajayan, Peter Nordlander, and Naomi J. Halas. Graphene-antenna sandwich photodetector. *Nano Letters*, 12(7):3808–3813, 2012. 28, 29, 112

[196] Lang Shen, Nirakar Poudel, George N. Gibson, Bingya Hou, Jihan Chen, Haotian Shi, Ernest Guignon, William D. Page, Arturo Pilar, and Stephen B. Cronin. Plasmon resonant amplification of a hot electron-driven photodiode. *Nano Research*, 11(4):2310–2314, 2018. 28

[197] William Herschel. Xiv. experiments on the refrangibility of the invisible rays of the sun. *Phil. Trans. R. Soc.*, 90:284–292, 1800. 29

[198] A. Graf, M. Arndt, M. Sauer, and G. Gerlach. Review of micromachined thermopiles for infrared detection. *Meas. Sci. Technol.*, 18:R59–R75, 2007. 29

[199] Kaoru Yamashita, Akishi Murata, and Masanori Okuyama. Miniaturized infrared sensor using silicon diaphragm based on golay cell. *Sensors and Actuators A: Physical*, 66(1-3):29–32, 1998. 29

[200] Jon W. Stewart, Jarrett H. Vella, Wei Li, Shanhui Fan, and Maiken H. Mikkelsen. Ultrafast pyroelectric photodetection with on-chip spectral filters. *Nat. Mater.*, 19(2):158–162, 2020. 29

[201] Boris Korzh, Qing-Yuan Zhao, Jason P. Allmaras, Simone Frasca, Travis M. Autry, Eric A. Bersin, Andrew D. Beyer, Ryan M. Briggs, Bruce Bumble, Marco Colangelo, Garrison M. Crouch, Andrew E. Dane, Thomas Gerrits, Adriana E. Lita, Francesco

Marsili, Galan Moody, Cristian Pena, Edward Ramirez, Jake D. Rezac, Neil Sinclair, Martin J. Stevens, Angel E. Velasco, Varun B. Verma, Emma E. Wollman, Si Xie, Di Zhu, Paul D. Hale, Maria Spiropulu, Kevin L. Silverman, Richard P. Mirin, Sae Woo Nam, Alexander G. Kozorezov, Matthew D. Shaw, and Karl K. Berggren. Demonstration of sub-3 ps temporal resolution with a superconducting nanowire single-photon detector. *Nat. Photonics*, 14(4):250–255, 2020. 29

[202] Alexander Dorodnyy, Yannick Salamin, Ping Ma, Jelena Vukajlovic Plestina, Nolan Lassaline, Dmitry Mikulik, Pablo Romero-Gomez, Anna Fontcuberta i Morral, and Juerg Leuthold. Plasmonic photodetectors. *IEEE Journal of Selected Topics in Quantum Electronic*, 24(6):4600313, 2018. 30, 34, 112

[203] Chee Leong Tan and Hooman Mohseni. Emerging technologies for high performance infrared detectors. *Nanophotonics*, 7(1):169–197, 2018. 30

[204] Yih-Guei Wey, Kirk Giboney, John Bowers, Mark Rodwell, Pierre Silvestre, Prabhu Thiagarajan, and Gary Robinson. 110-ghz galnaslinp double heterostructure p-i-n photodetectors. *Journal of Lightwave Technology*, 13(7):1490–1499, 1995. 31

[205] C.C. Barron, C.J. Mahon, B.J. Thibeault, G. Wang, W. Jiang, L.A. Coldren, and J.E. Bowers. Resonant-cavity-enhanced pin photodetectorwith 17ghz bandwidth-efficiency product. *Electronics Letters*, 30(21):1796–1797, 1994. 31

[206] K. Kato, A. Kozen, Y. Muramoto, Y. Itaya, T. Nagatsuma, and M. Yaita. 110-ghz, 50a 1.55-um wavelength. *IEEE Photonics Technology Letters*, 6(6):719 –721, 1994. 31

[207] Kirk S. Giboney, Radhakrishnan L. Nagarajan, Thomas E. Reynolds, Scott T. Allen, Richard P. Mirin, Mark J. W. Rodwell, and John E. Bowers. Travelling-wave photodetectors with 172-ghz bandwidth and 76-ghz bandwidth-efficiency product. *IEEE Photon. Technol. Lett.*, 7(4):412–414, 1995. 31

[208] Tadao Ishibashi and Hiroshi Ito. Uni-traveling-carrier photodiodes. *J. Appl. Phys.*, 127(3):031101, 2020. 31

[209] H. Ito, T. Furuta, S. Kodama, and T. Ishibashi. Inp/lngaas uni-travelling-carrier photodiodewith 310ghz bandwidth. *Electronics Letters*, 36(21):1810, 2000. 31

[210] Y. Hirota, T. Hirono, T. Ishibashi, and H. Ito. Traveling-wave photodetector for 1.55 um wavelength fabricated with unitraveling-carrier photodiodes. *Appl. Phys. Lett.*, 78(24):3767–3769, 2001. 31

[211] B. Kasper and J. Campbell. Multigigabit-per-second avalanche photodiode lightwave receivers. *Journal of Lightwave Technology*, 5(10):1351 – 1364, 1987. 32

[212] L. E. Tarof, J. Yu, R. Bruce, D. G. Knight, T. Baird, and B. Oosterbrink. High-frequency performance of separate absorption grading, charge, and multiplication inp/ingaas avalanche photodiodes. *IEEE Photon. Technol. Lett.*, 5(6):672–674, 1993. 32

[213] C. Lenox, H. Nie, P. Yuan, G. Kinsey, A. L. Homles Jr., B. G. Streetman, and J. C. Campbell. Resonant-cavity ingaas-inalas avalanche photodiodes with gain-bandwidth product of 290 ghz. *IEEE Photon. Technol. Lett.*, 11(9):1162–1164, 1999. 32

[214] T. Nakata, T. Takeuchi, I. Watanabe, K. Makila, and T. Torikai. 10 gbit/s high sensitivity, low-voltage-operation avalanche photodiodes with thin inalas multiplication layer and waveguide structure. *Electron. Lett.*, 36(24):2033, 2000. 32

[215] Daoxin Dai, Molly Piels, and John E. Bowers. Monolithic germanium/silicon photodetectors with decoupled structures: Resonant apds and utc photodiodes. *IEEE J. Select. Topics Quantum Electron.*, 20(6):43–56, 2014. 32

[216] Jae H. Kim, H. Torsten Griem, Robert A. Friedman, Eric Y. Chan, and Sankar Ray. High-performance back-illuminated ingaas/inalas msm photodetector with a record responsivity of 0.96 a/w. *IEEE Photon. Technol. Lett.*, 4(11):1241–1244, 1992. 32

[217] Wei Gao, Al-Sameen Khan, Paul R. Berger, R. G. Hunsperger, George Zydzik, H. M. O'Bryan, D. Sivco, and A. Y. Cho. In0.53ga0.47as metal-semiconductor-metal photodiodes with transparent cadmium tin oxide schottky contacts. *Appl. Phys. Lett.*, 65(15):1930–1932, 1994. 32

[218] Stephen Y. Chou, Yue Liu, and Paul B. Fischer. Fabrication of sub-50 nm finger spacing and width high-speed metal-semiconductor-metal photodetectors using high-resolution electron beam lithography and molecular beam epitaxy. *J. Vac. Sci. Technol. B*, 9(6):2920, 1991. 32

[219] Jin-Wei Shi, Kian-Giap Gan, Yi-Jen Chiu, Yen-Hung Chen, Chi-Kuang Sun, Ying-Jay Yang, and John E. Bowers. Metal–semiconductor–metal traveling-wave photodetectors. *IEEE Photon. Technol. Lett.*, 16(6):623–625, 2001. 32

[220] Chu-Hsuan Lin and Chee Wee Liu. Metal-insulator-semiconductor photodetectors. *Sensors*, 10(10):8797–8826, 2010. 32

[221] T.-H. Cheng, M. H. Liao, Lingyen Yeh, T.-L. Lee, M.-S. Liang, and C. W. Liu. Digital communication using ge metal-insulator-semiconductor light-emitting diodes and photodetectors. *J. Appl. Phys.*, 103(1):016103, 2008. 33

[222] C.-H. Lin, Y.-T. Chiang, C.-C. Hsu, C.-H. Lee, C.-F. Huang, C.-H. Lai, T.-H. Cheng, and C. W. Liu. Ge-on-glass detectors. *Appl. Phys. Lett.*, 91(4):041105, 2007. 33

[223] W.K. Chan, G.-K. Chang, R. Bhat, and C.K. Schlotter, N.E.and Nguyen. High-speed ga/sub 0.47/in/sub 0.53/as misim photodetectors with dielectric-assisted schottky barriers. *IEEE Electron Device Letters*, 10(9):417–419, 1989. 33

[224] Maurizio Casalino, Giuseppe Coppola, Mario Iodice, Ivo Rendina, and Luigi Sirleto. Near-infrared sub-bandgap all-silicon photodetectors: State of the art and perspectives. *Sensors*, 10(12):10571–10600, 2010. 33, 56

[225] M. W. Geis, S. J. Spector, M. E. Grein, R. T. Schulein, J. U. Yoon, D. M. Lennon, C. M. Wynn, S. T. Palmacci, F. Gan, F. X. Kartner, and T. M. Lyszczarz. All silicon infrared photodiodes: photo response and effects of processing temperature. *Opt. Express*, 15(25):16886, 2007. 33

[226] T. Baehr-Jones, M. Hochberg, and A. Scherer. Photodetection in silicon beyond the band edge with surface states. *Opt. Express*, 16(3):1659, 2008. 33

[227] Takasumi Tanabe, Hisashi Sumikura, Hideaki Taniyama, Akihiko Shinya, and Masaya Notomi. All-silicon sub-gb/s telecom detector with low dark current and high quantum efficiency on chip. *Appl. Phys. Lett.*, 96(10):101103, 2010. 33

[228] K. Kikuchi. Highly sensitive interferometric autocorrelator using si avalanche photodiodeas two-photon absorber. *Electron. Lett.*, 34(1):123, 1998. 33

[229] Yannick Salamin, Ping Ma, Benedikt Baeuerle, Alexandros Emboras, Yuriy Fedoryshyn, Wolfgang Heni, Bojun Cheng, Arne Josten, and Juerg Leuthold. 100 ghz plasmonic photodetector. *ACS Photonics*, 5(8):3291–3297, 2018. 34, 106

[230] Yunhong Ding, Zhao Cheng, Xiaolong Zhu, Kresten Yvind, Jianji Dong, Michael Galili, Hao Hu, N. Asger Mortensen, Sanshui Xiao, and Leif Katsuo Oxenlowe. Ultracompact integrated graphene plasmonic photodetector with bandwidth above 110 ghz. *Nanophotonics*, 9(2):317–325, 2020. 35

[231] S. C. Lee, S. Krishna, and S. R. J. Brueck. Quantum dot infrared photodetector enhanced by surface plasma wave excitation. *Opt. Express*, 17(25):23160, 2009. 35

[232] T. K. Liang, H. K. Tsang, I. E. Day, J. Drake, A. P. Knights, and M. Asghari. Silicon waveguide two-photon absorption detector at 1.5 um wavelength for autocorrelation measurements. *Appl. Phys. Lett.*, 87(7):1323, 2002. 35

[233] Daniel Schall, Emiliano Pallecchi, Guillaume Ducournau, Vanessa Avramovic, Martin Otto, and Daniel Neumaier. Record high bandwidth integrated graphene photodetectors for communication beyond 180 gb/s. *Optical Fiber Communication Conference*, 2018. 35

[234] Haining Wang, Changjian Zhang, Weimin Chan, Sandip Tiwari, and Farhan Rana. Ultrafast response of monolayer molybdenum disulfide photodetectors. *Nature Communications*, 6(8831), 2015. 35

[235] Arash Dehzangi, Ryan McClintock, Donghai Wu, Jiakai Li, Stephen M. Johnson, Emily Dial, and Manijeh Razeghi. High speed antimony-based superlattice photodetectors transferred on sapphire. *Applied Physics Express*, 12:116502, 2019. 35

[236] Michael Hakl, Quyang Lin, Sylvie Lepillet, Maximilien Billet, Jean-Francois Lampin, Stefano Pirotta, Raffaele Colombelli, Wenjian Wan, J. C. Cao, Hua Li, Emilien Peytavit, and Stefano Barbieri. Ultrafast quantum-well photodetectors operating at 10 um with a flat frequency response up to 70 ghz at room temperature. *ACS Photonics*, 8(2):464–471, 2021. 35

[237] Kengo Nozaki, Shinji Matsuo, Takuro Fujii, Koji Takeda, Masaaki Ono, Abdul Shakoor, Eiichi Kuramochi, and Masaya Notomi. Photonic-crystal nanophotodetector with ultrasmall capacitance for on-chip light-to-voltage conversion without an amplifier. *Optica*, 3(5):483–492, 2016. 35

[238] Jacob Pettine, Sean M. Meyer, Fabio Medeghini, Catherine J. Murphy, and David J. Nesbitt. Controlling hot electron spatial and momentum distributions in nanoplasmonic systems: Volume versus surface effects. *arXiv*, 2020. 37

[239] Yukina Takahashia and Tetsu Tatsuma. Solid state photovoltaic cells based on localized surface plasmon-induced charge separation. *Applied Physics Letters*, 99(18):182110, 2011. 37, 109

[240] Syed Mubeen, Joun Lee, Nirala Singh, Stephan Kramer, Galen D. Stucky, and Martin Moskovits. An autonomous photosynthetic device in which all charge carriers derive from surface plasmons. *Nature Nano*, 8(4):247–251, 2013. 37

[241] Thomas W. Ebbesen, Cyriaque Genet, and Sergey I. Bozhevolnyi. Surface-plasmon circuitry. *Physics Today*, 61(5):44–50, 2008. 38

[242] Zhenglong Zhang, Yurui Fang, Wenhui Wang, Li Chen, and Mengtao Sun. Propagating surface plasmon polaritons: Towards applications for remote-excitation surface catalytic reactions. *Advanced Science*, 3(1):1500215, 2016. 38, 52, 107

[243] Hangyong Shan, Ying Yu, Xingli Wang, Yang Luo, Shuai Zu, Bowen Du, Tianyang Han, Bowen Li, Yu Li, Jiarui Wu, Feng Lin, Kebin Shi, Beng Kang Tay, Zheng Liu, Xing Zhu, and Zheyu Fang. Direct observation of ultrafast plasmonic hot electron transfer in the strong coupling regime. *Light Science and Applications*, 8(1):9, 2019. 38, 106

[244] A. Giugni, B. Torre, A. Toma, M. Francardi, M. Malerba, A. Alabastri, R. Proietti Zaccaria, M. I. Stockman, and E. Di Fabrizio. Hot-electron nanoscopy using adiabatic compression of surface plasmons. *Nature Nanotechnology*, 8:845, 2013. 38, 50

[245] Andrea Giugni, Bruno Torre, Marco Allione, Gobind Das, Zhenwei Wang, Xin He, Husam N. Alshareef, and Enzo Di Fabrizio. Experimental route to scanning probe hot-electron nanoscopy (hens) applied to 2d material. *Advanced Optical Materials*, 5(15):1700195, 2017. 38, 50

[246] Olga Lozan, Ravishankar Sundararaman, Buntha Ea-Kim, Jean-Michel Rampnoux, Prineha Narang, Stefan Dilhaire, and Philippe Lalanne. Increased rise time of electron temperature during adiabatic plasmon focusing. 8(1):1656, 2017. 38, 50

[247] Charlotte I. Evans and Douglas Natelson. Remote excitation of hot electrons via propagating surface plasmons. *The Journal of Physical Chemistry C*, 123(15):10057–10064, 2019. 38

[248] Sviatlana Viarbitskaya, Olivier Demichel, Benoit Cluzel, Gerard Colas des Francs, and Alexandre Bouhelier. Delocalization of nonlinear optical responses in plasmonic nanoantennas. *Physical Review Letters*, 115:197401, 2015. 38, 50, 54

[249] Adrian Agreda, Deepak K. Sharma, Sviatlana Viarbitskaya, Romain Hernandez, Benoit Cluzel, Olivier Demichel, Jean-Claude Weeber, Gerard Colas des Francs, G.V. Pavan Kumar, and Alexandre Bouhelier. Spatial distribution of the nonlinear photoluminescence in au nanowires. *ACS Photonics*, 6:1240–1247, 2019. 38, 54

[250] Jean-Sebastien G. Bouillard, S. Vilain, Wayne Dickson, and Anatoly V. Zayats. Hyperspectral imaging with scanning near-field optical microscopy: applications in plasmonics. *Opt. Express*, 18(16):16513–16519, 2010. 39

[251] Jean Dellinger, K. Van Do, Xavier Le Roux, Frederique de Fornel, Eric Cassan, and Benoit Cluzel. Hyperspectral optical near-field imaging: Looking graded photonic crystals and photonic metamaterials in color. *Applied Physics Letters*, 101(14):141108, 2012. 39, 49

[252] Jean-Sebastien G. Bouillard, Wayne Dickson, Gregory A. Wurtz, and Anatoly V. Zayats. Near-field hyperspectral optical imaging. *ChemPhysChem*, 15(4):619–629, 2014. 39

[253] R. Sachan, V. Ramos, A. Malasi, S. Yadavali, B. Bartley, H. Garcia, G. Duscher, and R. Kalyanaraman. Oxidation-resistant silver nanostructures for ultrastable plasmonic applications. *Adv. Mater.*, 25:2045–2050, 2013. 39

[254] Yun Wang, Han Yun, Zeqin Lu, Richard Bojko, Wei Shi, Xu Wang, Jonas Flueckiger, Fan Zhang, Michael Caverley, Nicolas A. F. Jaeger, and Lukas Chrostowski. Apodized focusing fully etched subwavelength grating couplers. *IEEE Photonics Journal*, 7(3):2400110, 2015. 39

[255] Purnima Sethi, Anubhab Haldar, and Shankar Kumar Selvaraja. Ultra-compact low-loss broadband waveguide taper in silicon-on-insulator. *Optics Express*, 25(9):10196, 2017. 39

[256] Frederik Van Laere, Tom Claes, Jonathan Schrauwen, Stijn Scheerlinck, Wim Bogaerts, Dirk Taillaert, Liam O'Faolain, Dries Van Thourhout, and Roel Baets. Compact focusing grating couplers for silicon-on-insulator integrated circuits. *IEEE Photonics Technology Letters*, 19(23):1919, 2007. 39

[257] P. Hauer, J. Grand, A. Djorovic, G. R. Willmott, and E. C. Le Ru. Spot size engineering in microscope-based laser spectroscopy. *The Journal of Physical Chemistry C*, 120(37):21104–21113, 2016. 44, 87

[258] Aurelien Drezet and Cyriaque Genet. Imaging surface plasmons: From leaky waves to far-field radiation. *Physical Review Letters*, 110(21):213901, 2013. 45

[259] Junjun Shi, Yang Li, Meng Kang, Xiaobo He, Naomi J. Halas, Peter Nordlander, Shunping Zhang, and Hongxing Xu. Efficient second harmonic generation in a hybrid plasmonic waveguide by mode interactions. *Nano Lett.*, 19:3838–3845, 2019. 47

[260] Bert Voigtlander. *Scanning Probe Microscopy - Atomic Force Microscopy and Scanning Tunneling Microscopy*. Springer, 2015. 49

[261] A. Bouhelier and G. P. Wiederrecht. Excitation of broadband surface plasmon polaritons: Plasmonic continuum spectroscopy. *Physical Review B*, 71(19):195406, 2005. 51

[262] Neil W. Ashcroft and N. David Mermin. *Physique des solides*. EDP Sciences, 2002. 52

[263] Jiyong Wang, Aurelien Coillet, Olivier Demichel, Zhiqiang Wang, Davi Rego, Alexandre Bouhelier, Philippe Grelu, and Benoit Cluzel. Saturable plasmonic metasurfaces for laser mode locking. *Light:Science & Applications*, 9:50, 2020. 53

[264] J. K. Doylend, P. E. Jessop, and A. P. Knights. Silicon photonic resonator-enhanced defectmediated photodiode for sub-bandgap detection. *Opt. Express*, 18(14):14671–14678, 2010. 56

[265] Maurizio Casalino, Giuseppe Coppola, Richard M. De La Rue, and Dylan F. Logan. State-of-the-art all-silicon sub-bandgap photodetectors at telecom and datacom wavelengths. *Laser Photonics Rev.*, 10(6):895–921, 2016. 56

[266] Rana Nicolas, Gaetan Leveque, Joseph Marae-Djouda1, Guillame Montay, Yazid Madi, Jerome Plain, Ziad Herro, Michel Kazan, Pierre-Michel Adam, and Thomas Maurer. Plasmonic mode interferences and fano resonances in metal-insulator-metal nanostructured interface. *Sci. Rep.*, 5(14419), 2015. 56

[267] Shiyang Zhu, M. B. Yu, G. Q. Lo, and D. L. Kwong. Near-infrared waveguide-based nickel silicide schottky-barrier photodetector for optical communications. *Appl. Phys. Lett.*, 92(8):081103, 2008. 56

[268] M. Casalino, L. Sirleto, M. Iodice, N. Saffioti, M. Gioffre, I. Rendina, and G. Coppola. Cu/p-si schottky barrier-based near infrared photodetector integrated with a silicon-on-insulator waveguide. *Appl. Phys. Lett.*, 96(24):241112, 2010. 56

[269] S.M. Sze, D.J. Coleman Jr., and A. Loya. Current transport in metal-semiconductor-metal (msm) structures. *Solid-State Electronics*, 14(12):1209–1218, 1971. 57, 103, 105

[270] U. Fano. Zur theorie der intensitätsanomalien der beugung. *Ann. Phys.*, 32:393, 1938. 58

[271] D. Maystre and R. Petit. Brewster incidence for metallic gratings. *Opt. Comm.*, 17(2):196–200, 1976. 58

[272] M.C. Hutley and D. Maystre. The total absorption of light by a diffraction grating. *Opt. Comm.*, 19(3):431–436, 1976. 58

[273] N Bonod, G Tayeb, D Maystre, S Enoch, and E Popov. Total absorption of light by lamellar metallic gratings. *Opt. Express*, 16(20):15431–8, 2008. 58, 64

[274] A Wirgin and T Lopez-Rios. Can surface-enhanced raman scattering be caused by waveguide resonances? *Opt. Commun.*, 48(6):416–420, 1984. 58

[275] A Barbara, P Quemerais, E Bustarret, T Lopez-Rios, and T Fournier. Electromagnetic resonances of subwavelength rectangular metallic gratings. *Eur. Phys. J. D*, 23:143–154, 2003. 58

[276] Trevon Badloe, Jungho Mun, and Junsuk Rho. Metasurfaces-based absorption and reflection control:perfect absorbers and reflectors. *Journal of Nanomaterials*, 2017. 58

[277] J.P. Hugonin and P. Lalanne. Reticolo software for grating analysis. *Institut d'Optique, Orsay, France*, 2005. 59

[278] Drew A. Pommet M. G. Moharam, Eric B. Grann and T. K. Gaylord. Formulation for stable and efficient implementation of the rigorous coupled-wave analysis of binary gratings. *J. Opt. Soc. Am. A*, 12(5):1068–1076, 1995. 59

[279] Philippe Lalanne and G. Michael Morris. Highly improved convergence of the coupled-wave method for tm polarization. *J. Opt. Soc. Am. A*, 13(4):779–784, 1996. 59

[280] J. N. Reddy. *An Introduction to The Finite Element Method - Solutions Manual*. McGraw-Hill, 3rd edition edition, 2005. 59

[281] Dmitry I. Yakubovsky, Aleksey V. Arsenin, Yury V. Stebunov, Dmitry Yu. Fedyanin, and Valentyn S. Volkov. Optical constants and structural properties of thin gold films. *Opt. Express*, 25(21):25574–25587, 2017. 59

[282] H. H. Li. Refractive index of silicon and germanium and its wavelength and temperature derivatives. *Journal of Physical and Chemical Reference Data*, 9:561, 1980. 59

[283] Y. Todorov, A. M. Andrews, I. Sagnes, R. Colombelli, P. Klang, G. Strasser, and C. Sirtori. Strong light-matter coupling in subwavelength metal-dielectric microcavitiesat terahertz frequencies. *Phys. Rev. Lett.*, 102(18):186402, 2009. 61, 65

[284] Y. Todorov, L. Tosetto, J. Teissier, A. M. Andrews, P. Klang, R. Colombelli, I. Sagnes, G. Strasser, and C. Sirtori. Optical properties of metal-dielectric-metal microcavities in the thz frequency range. *Opt. Express*, 18(13):13886–13907, 2010. 64

[285] Lihong Gao, Fabien Lemarchand, and Michel Lequime. Exploitation of multiple incidences spectrometric measurements for thin film reverse engineering. *Opt. Express*, 20(14):15734–15751, 2012. 65

[286] I. D. Mash and G. P. Motulevich. Optical constants and electronic characteristics of titanium. *SOVIET PHYSICS JETP*, 36(3):516, 1973. 69

[287] P. B. Johnson and R. W. Christy. Optical constants of transition metals: Ti, v, cr, mn, fe, co, ni, and pd. *Phys. Rev. B*, 9(12):Phys. Rev. B, 1974. 69

[288] Mark A. Ordal, Robert J. Bell, Ralph W. Alexander, Lawrence A. Newquist, and Marvin R. Querry. Optical properties of al, fe, ti, ta, w, and mo at submillimeter wavelengths. *Appl. Opt.*, 27(6):1203–1209, 1988. 69

[289] Wolfgang S. M. Werner. Optical constants and inelastic electron-scattering data for 17 elemental metals. *Journal of Physical and Chemical Reference Data*, 38:1013, 2009. 69

[290] K. J. Palm, J. B. Murray, T. C. Narayan, and J. N. Munday. Dynamic optical properties of metal hydrides. *ACS Phot*, 5(11):4677–4686, 2018. 69

[291] Mario Lodari, Paolo Biagioni, Michele Ortolani, Leonetta Baldassarre, Giovanni Isella, and Monica Bollani. Plasmon-enhanced ge-based metal-semiconductor-metal photodetector at near-ir wavelengths. *Opt. Express*, 27(15):20516–20524, 2019. 82

[292] Muhammad Umar Khan and Brian Corbett. Bloch surface wave structures for high sensitivity detection and compact waveguiding. *Science and Technology of Advanced Materials*, 17(1):398–409, 2016. 87

[293] Guillaume Baffou, Ivan Bordacchini, Andrea Baldi, and Romain Quidant. Simple experimental procedures to distinguish photothermal from hot-carrier processes in plasmonics. *Light Sci Appl*, 9(108), 2020. 92, 93, 96

[294] Michael Bass, Casimer DeCusatis, Jay Enoch, Vasudevan Lakshminarayanan, Guifang Li, Carolyn Macdonald, Virendra Mahajan, and Eric Van Stryland. *Handbook of Optics, Third Edition Volume II: Design, Fabrication and Testing, Sources and Detectors, Radiometry and Photometry*. McGraw-Hill, 3rd edition edition, 2009. 101, 102, 103, 115

[295] Yu Chin Lim and R.A. Moore. Properties of alternately charged coplanar parallel strips by conformal mappings. *IEEE Transactions on Electron Devices*, 15(3):173–180, 1968. 101

[296] G.W. Farnell, I.A. Cermak, P. Silverster, and S.K. Wong. Capacitance and field distributions for interdigital surface-wave transducers. *IEEE Transactions on Sonics and Ultrasonics*, 17(3):188–195, 1970. 101

[297] S.V. Averine, Y.C. Chan, and Y.L Lam. Geometry optimization of interdigitated schottky-barrier metal–semiconductor–metal photodiode structures. *Solid-States Electronics*, 45(3):441–446, 2001. 101, 102

[298] Gerd Keiser. *Optical Fiber Communications*. McGraw-Hill, New York, 4th edition edition, 2010. 103, 105

[299] C.R. Crowell. The richardson constant for thermionic emission in schottky barrier diodes. *Solid-State Electronics*, 8(4):395–399, 1965. 104

[300] Heinz Beneking. Gain and bandwidth of fast near-infrared photodetectors: A comparison of diodes, phototransistors, and photoconductive devices. *IEEE Transactions on electron devices*, 29(9):1420–1431, 1982. 105

[301] Luchao Du, Akihiro Furube, Kohjiro Hara, Ryuzi Katoh, and Masanori Tachiya. Ultrafast plasmon induced electron injection mechanism in gold-tio2 nanoparticle system. *Journal of Photochemistry and Photobiology C: Photochemistry Reviews*, 15:21–30, 2013. 107

[302] Yang Tian and Tetsu Tatsuma. Mechanisms and applications of plasmon-induced charge separation at tio2 films loaded with gold nanoparticles. *J. AM. CHEM. SOC.*, 127:7632–7637, 2005. 109

[303] M. A. Noginov, Lei Gu, J. Livenere, G. Zhu, A. K. Pradhan, R. Mundle, M. Bahoura, Yu. A. Barnakov, and V. A. Podolskiy. Transparent conductive oxides: Plasmonic materials for telecom wavelengths. *Appl. Phys. Lett.*, 99:021101, 2011. 109

[304] Urcan Guler, Vladimir M. Shalaev, and Alexandra Boltasseva. Nanoparticle plasmonics: going practical with transition metal nitrides. *Materials Today*, 18(4):227–237, 2015. 109

[305] Adela Habib, Fred Florio, and Ravishankar Sundararaman. Hot carrier dynamics in plasmonic transition metal nitrides. *J. Opt.*, 20(6):064001, 2018. 109

[306] Paul R. West, Satoshi Ishii, Gururaj V. Naik, Naresh K. Emani, Vladimir M. Shalaev, and Alexandra Boltasseva. Searching for better plasmonic materials. *Laser Photonics Rev.*, 4(6):795–808, 2010. 109

[307] Marco P. Fischer, Aaron Riede, Kevin Gallacher, Jacopo Frigerio, Giovanni Pellegrini, Michele Ortolani, Douglas J. Paul, Giovanni Isella, Alfred Leitenstorfer, Paolo Biagioni, and Daniele Brida. Plasmonic mid-infrared third harmonic generation in germanium nanoantennas. *Light: Science & Applications*, 7(106), 2018. 109

[308] Thomas P. White and Kylie R. Catchpole. Plasmon-enhanced internal photoemission for photovoltaics: Theoretical efficiency limits. *Appl. Phys. Lett.*, 101:073905, 2012. 109

[309] Anagnostis Tsiatmas, Vassili A. Fedotov, F. Javier Garcia de Abajo, and Nikolay I. Zheludev. Low-loss terahertz superconducting plasmonics. *New Journal of Physics*, 14:115006, 2012. 109